

**Constitutive Behaviour of Ice Under Compressive  
States of Stress and its Application to  
Ice-Structure Interactions**

by

© Joshua Turner

A thesis submitted to the  
School of Graduate Studies  
in partial fulfilment of the requirements for the degree of

**Doctor of Philosophy**  
**Faculty of Engineering and Applied Science**  
Memorial University of Newfoundland

**May, 2018**

St. John's

Newfoundland and Labrador

## Abstract

In this work the multiaxial constitutive theory for the viscoelastic deformation of ice developed by Jordaan and others is examined and modified. The microstructural changes undergone by the material while under deformation have been modelled via a finite collection of state variables which represent the average “damage” within a region (originally coined to describe the degradation of mechanical components, damage is here used to refer to any change in microstructure). The accumulation of damage causes an enhancement in creep deformation via the process of microcracking at low pressures, or dynamic recrystallization and pressure melting at high pressures. The damage evolution is modelled based on Schapery’s approach, modified to include the effects of low- and high-pressure damage separately. The damage rate is influenced by confining pressure, axial stress, and temperature, with a pressure-temperature shift function introduced to define the relationship between pressure and temperature.

An exploratory series of triaxial tests was carried out in the laboratory at Memorial University; a description of the program, sample preparation, testing equipment, and procedure are provided. These tests were designed to investigate the deformation of ice under high shear and confining pressure. The ice samples were found to have an upper limit to their strength, failing at a stress difference (which is equivalent to the von Mises stress for a traditional triaxial test) of  $26.0 \pm 1.6$  MPa. Thin sections of the samples showed the region along the fault to be highly recrystallized. The amount of recrystallization was found to decrease with distance from the fault line, with nearly half of the failed sample being practically undamaged in some cases.

The role of numerous properties on ice-structure interactions have been investi-

gated via a numerical scheme and the finite element program ABAQUS. The properties examined include: the effect of elastic damage; the inclusion of power-law breakdown; the implementation of a non-linear damage exponent; the effect of the high-shear elastic failure discovered in the above experiments, and; the use of a pressure-temperature shift function for high-pressure damage.

Constant elastic properties were found to most closely resemble the results of indentation experiments, particularly with the addition of the non-linear damage exponent. Power-law breakdown was found to be suppressed under confining pressure, and had little effect upon the qualitative behaviour of an ice-structure interaction.

Implementing the high-shear elastic limit of 26.0 MPa on the von Mises stress was found to produce plastic deformation, instead of the expected viscoelastic behaviour; the internal stress along the fault-line of a sample is likely higher by a factor of five, leading to the discrepancy in behaviour. Applying the limit via a reduction in elastic modulus led to results more consistent with experimental evidence.

A pressure-temperature shift function based on the process of pressure melting was used to enhance or inhibit the accumulation of recrystallization damage; pressures at one temperature were translated to the corresponding pressure at the reference temperature of  $-10\text{ }^{\circ}\text{C}$  by assuming either a constant distance from melting point or a constant homologous temperature. The results were promising, producing the expected differences in loading and layer development. Extension to a reference temperature of  $-22\text{ }^{\circ}\text{C}$ , the temperature limit for pressure melting, is worth consideration.

## Acknowledgements

I am very grateful to the Faculty of Engineering and Applied Science for the opportunity to complete this project. In particular, I am indebted to Dr. Ian J. Jordan, who supervised this process and helped at every stage of development. Thanks also to the members of my supervisory committee: Dr. Rocky Taylor, Faculty of Engineering and Applied Science, MUN, and Dr. Ivan Saika-Voivod, Department of Physics and Physical Oceanography, MUN, for their support.

I would like to acknowledge the financial support I received from the School of Graduate Studies, MUN, and the Research and Development Corporation of Newfoundland, without which this would have been a much more difficult process.

Special thanks to Brian O'Rourke and Mark Kavanagh for their assistance and suggestions on both the laboratory and theoretical aspects of this project from start to finish. Further thanks to Matt Curtis for his assistance with the laboratory experiments.

Finally, thanks to my wife, Serena Turner, for putting up with me during this whole process, and to my daughter, Alexis, for lighting up my life.

# Contents

<b>Abstract</b>	<b>ii</b>
<b>Acknowledgements</b>	<b>iv</b>
<b>List of Tables</b>	<b>ix</b>
<b>List of Figures</b>	<b>x</b>
<b>List of Appendices</b>	<b>xvii</b>
<b>Nomenclature</b>	<b>xviii</b>
<b>1 Introduction</b>	<b>1</b>
1.1 Purpose of Investigation . . . . .	1
1.2 Methodology . . . . .	3
1.2.1 Experimental Background . . . . .	3
1.2.2 Model Development . . . . .	4
1.3 Scope of Thesis . . . . .	4
<b>2 Ice Mechanics</b>	<b>6</b>
2.1 Viscoelastic Deformation . . . . .	10
2.1.1 Linear Viscoelasticity . . . . .	11

2.1.2	Viscoelastic Modelling . . . . .	13
2.1.3	Non-Linear Viscoelasticity . . . . .	16
2.2	Thermodynamic Constitutive Theory . . . . .	20
2.2.1	Strain Energy and Work . . . . .	21
2.2.2	Entropy . . . . .	23
2.2.3	Thermodynamics of Irreversible Processes . . . . .	26
2.3	Molecular Theory of Deformation . . . . .	29
2.3.1	Absolute Rate Theory . . . . .	34
2.3.2	The Rate Theory of Viscoelastic Deformation . . . . .	36
2.3.3	The Experimental Activation Energy and Volume . . . . .	39
2.4	Fracture Mechanics . . . . .	43
2.4.1	Linear Elastic Fracture Mechanics . . . . .	43
2.4.2	J-Integral Theory . . . . .	46
2.5	Damage Mechanics . . . . .	47
2.6	Properties of Ice . . . . .	52
2.6.1	Basic Properties . . . . .	52
2.6.2	Hydrogen Bonding and Crystal Structure . . . . .	54
2.6.3	Mechanical Behaviour . . . . .	56
2.6.4	Ice Strength . . . . .	57
2.6.5	Microstructure . . . . .	58
2.6.6	Strain Localization . . . . .	61
2.6.7	Pressure-Temperature Effects . . . . .	65
2.6.8	Activation Energy . . . . .	72
2.7	Modelling Ice . . . . .	76

<b>3</b>	<b>Experimentation</b>	<b>79</b>
3.1	Specimen Preparation . . . . .	80
3.2	Equipment and Procedure . . . . .	81
3.3	Large Deviatoric Stress Tests . . . . .	83
3.4	Corrections and Calibrations . . . . .	85
3.5	Results and Observations . . . . .	88
3.5.1	Microstructure . . . . .	94
<b>4</b>	<b>Constitutive Modelling</b>	<b>101</b>
4.1	Mechanical Model . . . . .	101
4.2	Damage Evolution . . . . .	107
4.2.1	Rate Equation Based Shift Function . . . . .	115
4.2.2	Temperature-Dependence of Damage . . . . .	117
4.3	Elastic Damage . . . . .	125
4.4	Power Law Breakdown . . . . .	128
4.5	Summary of Additions to Model . . . . .	135
<b>5</b>	<b>Validation of Finite Element Model</b>	<b>137</b>
5.1	Validation . . . . .	137
5.1.1	Creep-Relaxation Simulations . . . . .	138
5.1.2	Delayed Elastic Recovery . . . . .	152
5.2	Indentation Validation . . . . .	153
5.2.1	Elastic Validation . . . . .	154
5.2.2	Validation of Indentation With Cylindrical Indentor . . . . .	159
5.2.3	Geometry of Indentation . . . . .	164

<b>6</b>	<b>Further Development of Finite Element Model</b>	<b>168</b>
6.1	Model Implementation . . . . .	173
6.1.1	Establishing Baseline Parameters for Simulations . . . . .	174
6.1.2	Normalized Velocity Testing . . . . .	180
6.2	Further Development . . . . .	189
6.2.1	Recalibration of Microcracking Damage Function . . . . .	189
6.2.2	Power Law Breakdown . . . . .	191
6.2.3	High-Shear Elastic Failure . . . . .	193
6.2.4	Non-Linear High-Pressure Damage Exponent . . . . .	199
6.2.5	Temperature-Dependent Damage Model . . . . .	203
6.3	Summary of Results . . . . .	209
<b>7</b>	<b>Conclusions</b>	<b>213</b>
	<b>Bibliography</b>	<b>221</b>
<b>A</b>	<b>Validation of Model</b>	<b>243</b>

# List of Tables

2.1	Variation in pre-exponential term and activation energy with increasing hydrostatic pressure. . . . .	76
3.1	Latest test series. . . . .	84
3.2	Shear stress and loading rate at elastic breakdown, strain rate post-failure. . . . .	93
4.1	Calibration constants. . . . .	111
4.2	Constants for elastic damage models. . . . .	126
5.1	Amalgamated damage constants. . . . .	147
6.1	Summary of indentation simulations. . . . .	172
6.2	Indenter velocities simulated. . . . .	182
A.1	Triaxial validation results for case of no damage. . . . .	245
A.2	Total damage. . . . .	246
A.3	Elastic strain with damage. . . . .	247
A.4	Delayed elastic equivalent strain with damage. . . . .	251
A.5	Viscous equivalent strain with damage. . . . .	253

# List of Figures

2.1	<i>hpz</i> distributions. . . . .	8
2.2	Creep response to constant stress. . . . .	10
2.3	Linear viscoelastic response to cumulative increases in applied stress. . . . .	12
2.4	Basic models of viscoelastic behaviour. . . . .	13
2.5	Example viscoelastic response. . . . .	15
2.6	Complementary strain energy density. . . . .	25
2.7	Endothermic vs. exothermic reactions. . . . .	31
2.8	Effect of stress on activation energy. . . . .	33
2.9	Change in activation energy with homologous temperature. . . . .	41
2.10	Illustration of Green's theorem. . . . .	47
2.11	Illustration of the crack-tip process zone . . . . .	48
2.12	Transition from ductile to brittle behaviour with increasing strain rate. . . . .	57
2.13	Thin sections of ice samples at ice-indenter interface. . . . .	59
2.14	Thin sections of ice samples at ice-indenter interface. . . . .	60
2.15	Thin sections of triaxial ice samples. . . . .	62
2.16	Failure behaviour of ice under triaxial compression with increasing confining pressure. . . . .	64
2.17	Pressure melting curve. . . . .	66

2.18	Load and temperature results from indentation experiments at Hobson's Choice ice island. . . . .	69
2.19	Strain rate at increasing levels of axial strain for a wide range of temperatures. . . . .	75
3.1	Triaxial equipment. . . . .	81
3.2	Example of shear faulting during triaxial compression. . . . .	85
3.3	Damage rates . . . . .	89
3.4	Nominal von Mises and axial stresses during test 7. . . . .	91
3.5	Nominal von Mises and axial stresses during testing. . . . .	92
3.6	Engineering and true strain during test 7. . . . .	94
3.7	Microstructure of untested sample. . . . .	95
3.8	Microstructure of sample 6. . . . .	96
3.9	Microstructure of sample 5. . . . .	98
3.10	Microstructure of sample 8. . . . .	99
3.11	Microstructure of sample 9. . . . .	100
4.1	Basic composition of Burgers model for viscoelastic behaviour. . . . .	102
4.2	Basic response of the non-linear Burgers model to a constant uniaxial stress. . . . .	103
4.3	Transition from microcracking to dynamic recrystallization and pressure melting with increasing hydrostatic pressure. . . . .	110
4.4	Recalibration of microcracking pressure-dependent damage function. . . . .	113
4.5	A comparison of the three formulations used to describe the von Mises stress component of high-pressure damage function. . . . .	114

4.6	Pressure-dependent shift function parameters. . . . .	118
4.7	Natural logarithm of minimum strain rates at increasing temperatures and pressures. . . . .	119
4.8	Li's damage rate vs. inverse temperature plots. . . . .	121
4.9	High-pressure damage rates. . . . .	122
4.10	High pressure damage rates. . . . .	124
4.11	Normalized elastic axial and lateral strains under uniaxial compression for three elastic damage models. . . . .	127
4.12	Normalized elastic strains under hydrostatic pressure for three elastic damage models. . . . .	127
4.13	Delayed elastic strain for three models of elastic damage under a con- fining pressure of 30 MPa and a von Mises stress of 15 MPa. . . . .	128
4.14	Example behaviour of sinh function and its limits over relevant $\alpha\sigma$ range.	130
4.15	Internal true stress and true strain during test IT960812. . . . .	131
4.16	Meglis strain rate vs stress data at increasing levels of strain. . . . .	132
4.17	Strain rate data at range of % strains. . . . .	133
4.18	Sinh fits to Meglis data at 40 % strain. . . . .	134
4.19	Meglis data at 40 % strain color-coded based on hydrostatic pressure.	135
5.1	General state of stress during validation. . . . .	140
5.2	Elastic strain with no damage. . . . .	141
5.3	Delayed elastic and viscous responses to generalized stress state. . . .	144
5.4	Volumetric strain with no damage. . . . .	145
5.5	Response of damage functions. . . . .	146

5.6	Elastic strain with damage. . . . .	149
5.7	Viscous strain with damage. . . . .	150
5.8	Total strain with no damage. . . . .	151
5.9	Theoretical surface pressures. . . . .	155
5.10	Normalized surface pressures on indentors from finite element simulations. . . . .	156
5.11	Force on indentors. . . . .	156
5.12	Elastic von Mises stresses. . . . .	157
5.13	Theoretical hydrostatic pressure within an elastic medium. . . . .	159
5.14	Numerical hydrostatic pressure within an elastic medium. . . . .	160
5.15	Basic simulation geometry. . . . .	162
5.16	Damage layer. . . . .	164
5.17	Force data from Hobson’s Choice test NRC07. . . . .	165
5.18	Model geometries. . . . .	166
6.1	Basic simulation geometry. . . . .	174
6.2	Load traces under various elastic damage formulations. . . . .	176
6.3	Load trace for increasing high-pressure exponents with constant elastic properties. . . . .	177
6.4	Damage layer development at approximately peak load for increasing values of $r_2$ . . . . .	178
6.5	Load traces for increasing high-pressure exponents with elastic damage. . . . .	179
6.6	Load traces for examined indenter velocities. . . . .	183

6.7	Damage layer development at approximately peak load for high, medium, and low indenter velocities. . . . .	183
6.8	Thin sections for normalized velocities of 0.3, 0.043, and 0.003 s <sup>-1</sup> under polarized light. . . . .	184
6.9	Development of surface stresses over the course of indentation simulation with indenter velocity of 68 mm/s. . . . .	185
6.10	Energy flux at peak load. . . . .	186
6.11	Development of surface stresses over the course of indentation simulation with indenter velocity of 0.68 mm/s. . . . .	187
6.12	Scaled ice geometries. . . . .	188
6.13	Layer development, $v_n = 0.34 \text{ s}^{-1}$ . . . . .	188
6.14	Layer development, $v_n = 0.034 \text{ s}^{-1}$ . . . . .	188
6.15	Damage layer development for recalibrated and original $f_1(p)$ . . . . .	190
6.16	Comparison of indenter loads produced by new and old calibrations. . . . .	190
6.17	Stress conditions near peak-load with and without power law breakdown. . . . .	192
6.18	Resulting indenter load from varying normalization constants for power law breakdown. . . . .	193
6.19	Damage distributions with and without power law breakdown. . . . .	194
6.20	von Mises stress distribution for two different indenter velocities when von Mises stress is limited to 26.0 MPa. . . . .	195
6.21	Damage distribution for two different indenter velocities when von Mises stress is limited to 26.0 MPa. . . . .	195
6.22	Load vs. indentation depth for two different indenter velocities when von Mises stress is limited to 26.0 MPa. . . . .	197

6.23	Load traces with and without elastic failure assuming microcracking elastic damage. . . . .	198
6.24	Damage layers before and after load drop when elastic failure is assumed.	198
6.25	Load traces with high-shear elastic failure separated from effect of damage. . . . .	200
6.26	Load traces produced for non-linear $r_2$ values. . . . .	202
6.27	Total damage produced by non-linear $r_2$ value at peak load. . . . .	203
6.28	Load traces at temperatures of -5, -10, and -15 °C with rate theory-based shift function included. . . . .	205
6.29	Damage layers at temperatures from -15 to -5 °C. . . . .	206
6.30	Microcracking damage layers at temperatures from -15 to -5 °C. . . . .	207
6.31	Recrystallization damage layers at temperatures from -15 to -5 °C. . . . .	207
6.32	Load traces produced for three temperatures and and two indenter velocities. . . . .	208
6.33	Experimental load traces at temperatures of -5 and -15 °C. . . . .	209
A.1	Comparison of total strains with the constant bulk modulus elastic damage formulation and power-law high-pressure damage. . . . .	254
A.2	Comparison of total strains with the constant bulk modulus elastic damage formulation and exponential high-pressure damage. . . . .	255
A.3	Comparison of total strains with the constant bulk modulus elastic damage formulation and normalized exponential high-pressure damage. . . . .	256
A.4	Comparison of total strains with the constant bulk modulus elastic damage formulation and geometric high-pressure damage. . . . .	257

A.5	Comparison of total strains with the Kachanov elastic damage formulation and power-law high-pressure damage. . . . .	258
A.6	Comparison of total strains with the Kachanov elastic damage formulation and exponential high-pressure damage. . . . .	259
A.7	Comparison of total strains with the Kachanov elastic damage formulation and normalized exponential high-pressure damage. . . . .	260
A.8	Comparison of total strains with the Kachanov elastic damage formulation and geometric high-pressure damage. . . . .	261
A.9	Comparison of total strains with the constant Poisson's ratio elastic damage formulation and power-law high-pressure damage. . . . .	262
A.10	Comparison of total strains with the constant Poisson's ratio elastic damage formulation and exponential high-pressure damage. . . . .	263
A.11	Comparison of total strains with the constant Poisson's ratio elastic damage formulation and normalized exponential high-pressure damage. . . . .	264
A.12	Comparison of total strains with the constant Poisson's ratio elastic damage formulation and geometric high-pressure damage. . . . .	265
A.13	Comparison of total strains with microcracking damage only using the calibration of Li. . . . .	266
A.14	Comparison of total strains with microcracking damage only using the calibration of Xiao. . . . .	267

# List of Appendices

A Validation of Model	243
-----------------------	-----

# Nomenclature

$\alpha_{w/i}$	Coefficient of thermal expansion for water and ice . . . . .	123
$\bar{v}_f$	Average velocity of the activated complexes moving along $\Delta_f$ . . . . .	35
$\Delta\epsilon$	Step increase in strain . . . . .	11
$\delta\epsilon_{ij}^e$	Recoverable (elastic) strain increment . . . . .	26
$\delta\epsilon_{ij}^p$	Non-recoverable (plastic) strain increment . . . . .	26
$\Delta\sigma(t)$	Stress difference during stress-relaxation cycle . . . . .	138
$\Delta E_f^0$	Activation energy at absolute zero . . . . .	35
$\Delta E_i^t$	True activation energy . . . . .	39
$\Delta E_e$	Empirical activation energy (J) . . . . .	30
$\Delta E_i$	Apparent activation energy . . . . .	39
$\Delta G^0$	Gibbs free energy at absolute zero . . . . .	36
$\Delta H$	Enthalpy change . . . . .	31
$\Delta H^0$	Enthalpy at absolute zero . . . . .	36
$\Delta S$	Equilibrium entropy . . . . .	32
$\Delta S^0$	Entropy at absolute zero . . . . .	36
$\Delta T_m$	Thermal distance from melting point . . . . .	122
$\Delta\sigma$	Step increase in stress . . . . .	11

$\Delta\sigma_1$	Stress difference prior to time $t_1$ . . . . .	138
$\Delta\sigma_2$	Stress difference after time $t_1$ . . . . .	138
$\delta_{ij}$	Kronecker delta . . . . .	104
$\dot{\epsilon}$	Strain rate . . . . .	13
$\dot{\epsilon}'_{ij}$	Damage-enhanced strain rate tensor . . . . .	108
$\dot{\epsilon}^c$	Uniaxial secondary creep strain rate . . . . .	103
$\dot{\epsilon}^d$	Uniaxial delayed elastic strain rate . . . . .	103
$\dot{\epsilon}^v$	Volumetric strain rate . . . . .	107
$\dot{\epsilon}_0$	Reference strain rate . . . . .	18
$\dot{\epsilon}_0^c$	Uniaxial secondary creep strain rate at reference stress . . . . .	104
$\dot{\epsilon}_0^d$	Uniaxial delayed elastic strain rate at reference stress . . . . .	104
$\dot{\epsilon}_t$	Axial true strain rate . . . . .	87
$\dot{\epsilon}_{est}$	Estimated true strain rate for constant stress . . . . .	87
$\dot{\epsilon}_{ij}$	Strain rate tensor . . . . .	107
$\dot{\epsilon}_{ij}^e$	Elastic strain rate tensor . . . . .	107
$\dot{\epsilon}_{min}$	Minimum strain rate . . . . .	73
$\dot{\epsilon}_{sc}$	Secondary creep strain rate . . . . .	73
$\dot{\gamma}$	Shear strain rate . . . . .	40
$\dot{a}$	Crack growth rate . . . . .	50
$\dot{\epsilon}$	Equivalent strain rate . . . . .	107
$\dot{\epsilon}^c$	Equivalent secondary creep strain rate . . . . .	107
$\dot{\epsilon}^d$	Equivalent delayed elastic strain rate . . . . .	107
$\dot{\epsilon}^e$	Equivalent elastic strain rate . . . . .	107
$\dot{\epsilon}_{ij}^c$	Deviatoric secondary creep strain rate tensor . . . . .	107

$\dot{\epsilon}_{ij}^d$	Deviatoric delayed elastic strain rate tensor . . . . .	107
$\dot{N}$	Change in crack density . . . . .	107
$\dot{N}_0$	Change in crack density for reference stress . . . . .	108
$\dot{Q}$	Heat transfer rate . . . . .	23
$\dot{S}$	Entropy production rate . . . . .	23
$\epsilon$	Strain . . . . .	11
$\epsilon^c$	Uniaxial secondary creep strain . . . . .	102
$\epsilon_v^c$	Secondary creep volumetric strain . . . . .	105
$\epsilon_{ij}^c$	Secondary creep strain tensor . . . . .	104
$\epsilon^d$	Uniaxial delayed elastic strain . . . . .	102
$\epsilon_v^d$	Delayed elastic volumetric strain . . . . .	105
$\epsilon_{ij}^d$	Delayed elastic strain tensor . . . . .	104
$\epsilon^e$	Uniaxial elastic strain . . . . .	102
$\epsilon_{ij}^e$	Elastic strain tensor . . . . .	104
$\epsilon^{ps}$	Pseudo-strain . . . . .	19
$\epsilon_K$	Kelvin-Voigt strain . . . . .	14
$\epsilon_M$	Maxwell strain . . . . .	14
$\epsilon_v$	Volumetric strain . . . . .	105
$\epsilon_{eng}$	Axial engineering strain . . . . .	86
$\epsilon_{ij}$	Multi-axial strain tensor . . . . .	21
$\gamma_m$	Surface energy per unit area of the $m^{th}$ crack . . . . .	22
$\gamma_s$	Surface energy per unit area . . . . .	44
$\kappa_f$	Transmission coefficient in forward direction . . . . .	35
$\kappa_{w/i}$	Compressibility of water and ice . . . . .	123

$k$	Rate constant for thermally-activated process . . . . .	30
$\mu$	Viscosity . . . . .	13
$\mu_K$	Kelvin-Voigt viscosity . . . . .	14
$\mu_M$	Maxwell viscosity . . . . .	14
$\nu$	Poisson's ratio . . . . .	44
$\nu_0$	Initial Poisson's ratio . . . . .	49
$\psi$	Reduced time . . . . .	17
$\rho_i$	Density of ice . . . . .	70
$\rho_m$	Mobile dislocation density . . . . .	40
$\rho_w$	Density of water . . . . .	70
$\sigma$	Stress . . . . .	11
$\sigma_1^a$	Applied axial stress prior to time $t_1$ . . . . .	138
$\sigma_2^a$	Applied axial stress after time $t_1$ . . . . .	138
$\sigma^d$	Stress in Kelvin dashpot . . . . .	104
$\sigma_0$	Reference stress . . . . .	18
$\sigma_1$	Axial stress . . . . .	114
$\sigma_a$	Applied stress . . . . .	49
$\sigma_c$	Stress required for crack nucleation . . . . .	108
$\sigma_m$	Magnitude of stress . . . . .	14
$\sigma_n$	Nominal stress . . . . .	48
$\sigma_t$	Axial true stress . . . . .	86
$\sigma_c$	Desired constant true stress . . . . .	87
$\sigma_{eff}$	Effective stress . . . . .	48
$\sigma_{eng}$	Axial engineering stress . . . . .	86

$\sigma_{ij}$	Multi-axial stress tensor . . . . .	21
$\sigma_{kk}$	Sum of normal stresses . . . . .	126
$\tau_a$	Applied shear stress . . . . .	39
$\tau_d$	Dummy time variable . . . . .	11
$\tau_i$	Internal shear stress . . . . .	42
$\tau_j$	Relaxation times . . . . .	15
$\tau_{eff}$	Effective shear stress . . . . .	41
$A$	Cross-sectional area . . . . .	48
$a$	Half crack length . . . . .	44
$A_0$	Initial cross-sectional area . . . . .	86
$A_e$	Empirical frequency factor or pre-exponential term . . . . .	30
$A_f$	Pre-exponential factor . . . . .	73
$A_m$	Surface area of the $m^{th}$ crack . . . . .	22
$A_n$	Nominal cross-sectional area . . . . .	48
$A_{w/i}$	Integral of the coefficient of thermal expansion with respect to temperature for water and ice . . . . .	123
$b$	Burgers vector . . . . .	40
$C_f$	Concentration of activated complexes per unit volume along length $\Delta_f$ . .	35
$c_i$	Specific heat of ice . . . . .	69
$C_p$	Concentration of products . . . . .	36
$C_r$	Concentration of reactants . . . . .	35
$c_w$	Specific heat of water . . . . .	69
$C_{w/i}$	Integration constants for water and ice . . . . .	123
$D$	Kachanov damage parameter . . . . .	48

$D_N$	Bounded damage parameter . . . . .	108
$da$	Virtual crack extension . . . . .	46
$ds$	Contour interval . . . . .	46
$E$	Elastic modulus . . . . .	13
$e_{ij}^c$	Deviatoric secondary creep strain tensor . . . . .	105
$e^d$	Equivalent delayed elastic strain . . . . .	106
$e_{ij}^d$	Deviatoric delayed elastic strain tensor . . . . .	105
$E_0$	Initial elastic modulus . . . . .	48
$E_K$	Kelvin-Voigt elastic modulus . . . . .	14
$E_M$	Maxwell elastic modulus . . . . .	14
$E_R$	Reference modulus . . . . .	19
$E_{eff}$	Effective elastic modulus . . . . .	48
$e_{ij}$	Deviatoric strain tensor . . . . .	105
$F$	Applied axial load . . . . .	86
$f$	Damage function . . . . .	108
$F(p)$	Pressure hardening function of Liu (1994) . . . . .	109
$F_0$	Initial applied axial load . . . . .	88
$f_1(p)$	Microcracking damage function . . . . .	111
$f_2(p)$	Dynamic recrystallization damage function . . . . .	111
$f_k$	Thermodynamic forces associated with internal variables . . . . .	22
$G$	Shear modulus . . . . .	125
$G(p)$	Pressure softening function of Liu (1994) . . . . .	109
$g(S)$	Schaperly damage enhancement factor . . . . .	51
$G_k$	Energy release rate for crack growth . . . . .	22

$H$	Heaviside step-function . . . . .	14
$h$	Planck's constant . . . . .	35
$J$	Creep compliance . . . . .	11
$J_f$	J-Integral . . . . .	46
$J_{ijkl}$	Compliance tensor . . . . .	26
$K$	Bulk modulus . . . . .	125
$k_B$	Boltzmann constant . . . . .	31
$K_{w/i}$	Integral of the compressibility with respect to pressure for water and ice .	123
$L$	Sample length . . . . .	86
$L_0$	Initial sample length . . . . .	86
$L_f$	Latent heat of fusion . . . . .	65
$m$	Secondary creep exponent . . . . .	141
$m_i$	Mass of ice . . . . .	69
$m_w$	Mass of water . . . . .	69
$N$	Crack density . . . . .	49
$n$	Delayed elastic exponent . . . . .	142
$P$	Pressure . . . . .	28
$p$	Hydrostatic pressure . . . . .	42
$p_1^h$	Hydrostatic pressure prior to time $t_1$ . . . . .	138
$p_2^h$	Hydrostatic pressure after time $t_1$ . . . . .	138
$p_0$	Reference hydrostatic pressure . . . . .	109
$P_c$	Confining pressure . . . . .	114
$Q_e$	Empirical activation energy (J/mol) . . . . .	30
$Q_i$	Generalized force conjugates associated with thermodynamic variables . . .	26

$q_i$	Generalized thermodynamic variables . . . . .	26
$R$	Relaxation modulus . . . . .	11
$r_2$	High-pressure damage exponent . . . . .	171
$R_g$	Universal gas constant . . . . .	31
$S$	Schapery damage parameter . . . . .	47
$s$	von Mises stress . . . . .	105
$S'$	Entropy production of reference equilibrium state . . . . .	27
$s^d$	von Mises stress in Kelvin dashpot . . . . .	105
$s_1^v$	von Mises stress prior to time $t_1$ . . . . .	139
$s_2^v$	von Mises stress after time $t_1$ . . . . .	139
$s_0$	Reference von Mises stress . . . . .	109
$S_1$	Microcracking damage parameter . . . . .	175
$S_2$	High-pressure damage parameter . . . . .	171
$S_{\%00}$	Salinity . . . . .	53
$S_i$	Internal microstructural (or damage) parameters . . . . .	19
$S_k$	Internal variables . . . . .	21
$s_L$	Laplace transform variable . . . . .	12
$S_t$	Damage under constant load . . . . .	87
$S_u$	Entropy production of universe . . . . .	27
$S_c$	Damage under constant stress . . . . .	87
$s_{ij}$	Deviatoric stress tensor . . . . .	105
$T$	Temperature . . . . .	23
$t$	Time . . . . .	11
$t'$	Start time of relaxation . . . . .	14

$t_1$	Time at stress reduction . . . . .	138
$T_h$	Homologous temperature . . . . .	37
$T_m$	Melting temperature . . . . .	37
$T_n$	Traction normal to $ds$ . . . . .	46
$u$	displacement . . . . .	46
$U_\epsilon$	Strain energy . . . . .	44
$U_i$	Internal energy density . . . . .	24
$U_p$	Potential energy . . . . .	46
$v$	Volume . . . . .	28
$V^t$	Theoretical activation volume . . . . .	42
$V_e$	Experimental activation volume . . . . .	42
$V_h$	Volume swept out by vacancy . . . . .	38
$v_l$	Specific volume of liquid phase . . . . .	65
$V_m$	Volume swept out by atom or molecule . . . . .	38
$v_n$	Normalized velocity . . . . .	171
$v_s$	Specific volume of solid phase . . . . .	65
$V_w$	Volume of melt water . . . . .	69
$V_{ice}$	Volume of ice . . . . .	69
$W$	Strain energy density function . . . . .	21
$W'$	Complementary strain energy density . . . . .	24
$W^c$	Complementary pseudo-strain energy density . . . . .	19
$W_0$	Initial work state . . . . .	23
$W_I$	Irreversible energy density . . . . .	23
$W_s$	Surface energy per unit area of the $m^{th}$ crack . . . . .	22

$W_s$	Surface energy . . . . .	44
$W_T$	Total work per unit volume . . . . .	22
$W'_T$	Total complementary work per unit volume . . . . .	25
$Z$	Partition functions for ground state activated complexes . . . . .	35
$Z_f$	Partition functions for activated complexes in forward direction . . . . .	35
$Z_r$	Partition functions for reactants . . . . .	35

# Chapter 1

## Introduction

The deformation of a solid often results in changes in the structure of the material. The nature and extent of these changes depend upon the factors involved, from the geometry of the interaction and the loads applied to the environmental temperature at which the deformation takes place. The accumulation of these changes, often referred to as “damage”, will generally result in changes in the mechanical and energy dissipation behaviour of the material. In some cases, such as ice, the accumulation of damage will lead to truly dramatic changes in material behaviour. Understanding damage processes is thus a key component to understanding ice-structure interactions, the main focus of this work.

### 1.1 Purpose of Investigation

Canada’s northern oceans cover a vast area, stretching from the iceberg packed waters off the coast of Newfoundland to the Beaufort Sea, terminating at the Yukon-Alaska border. The presence of ice in the northern oceans has always been the major

challenge facing development within the region. Only in the last century has the application of scientific knowledge and engineering methods enabled transportation pathways and certain development activities to proceed - albeit with significantly higher costs than those found in more agreeable climes.

Standard construction and design practices form only the baseline knowledge necessary for development in Arctic oceans. The core of Arctic offshore engineering lies in the understanding of ice mechanics, particularly with regards to how ice generates loads on platforms and vessels; local and global ice pressure estimates are necessary for the safe design of both. Several offshore platforms have already been constructed for the sub-Arctic conditions found off the coast of Newfoundland and Labrador. The knowledge and expertise gained during their construction and operation will be used to inform the design of the next generation of offshore platforms, which will have to contend with deeper waters and more severe Arctic weather conditions. Understanding ice-structure interactions is vital in determining ice loads and for the safe and efficient design of offshore structures under both Arctic and sub-Arctic conditions.

The form of ice failure observed during an ice-structure interaction depends upon the conditions involved. Contact with vertical walled structures will predominantly lead to crushing failure, while ice in contact with a sloped surface will often fail via some combination of bending or buckling. This work will primarily focus on the mechanics of ice crushing, a complex process characterized by the development and subsequent failure of high pressure zones (*hpzs*), which limit ice failure pressures and are of great importance to the design of offshore structures.

The main objective of this research is to improve the modelling of ice-structure interactions via the study of *hpzs*. This requires the analysis of ice under conditions

relevant to an ice-structure interaction, particularly at large compressive and shear stresses under a range of hydrostatic pressures. While spalling and other fracture events are a component of ice-structure interactions, this study is primarily interested in the continuum behaviour of the *hpz* itself, and will focus on loading rates and stresses that do not produce primarily brittle failure.

## 1.2 Methodology

This project focused on the study of the high-pressure, high-shear regions within a *hpz* via a series of triaxial experiments. The experiments examined the deformation of ice under a range of confining pressures and shear stresses, with the objective of gaining a deeper understanding of *hpz* failure behaviour and its relative importance during ice-structure interactions. Finite element modelling was used to simulate both the latest test series and the earlier triaxial and indentation experiments of other researchers. The results of these simulations are used to improve the constitutive model used to describe the behaviour of ice during an ice-structure interaction.

### 1.2.1 Experimental Background

To accomplish these goals, a number of triaxial experiments were conducted. The test series examined the failure behaviour of ice under increasing deviatoric stress, extending the earlier work of Meglis et al. (1999) to higher deviatoric stresses and hydrostatic pressures. This set of experiments was designed to help clarify the conditions necessary for failure to occur in a high-pressure zone and whether there are changes in failure behaviour with increasing deviatoric and hydrostatic stresses.

A wide range of experimental data from earlier investigators was also studied and analysed in an effort to improve the finite element model, including: the triaxial damage study of Stone et al. (1997); the constant strain rate triaxial tests of Melanson et al. (1999b); the triaxial experiments used by Barrette and Jordaan (2003) to develop a pressure-dependent activation energy; and the deformation, loading, microstructure, and temperature data gathered from the indentation experiments of Wells et al. (2011), Browne (2012), and O'Rourke et al. (2015).

## 1.2.2 Model Development

The results from the test series are used to refine the constitutive equations of ice, allowing for more accurate estimates of ice loads and more efficient structural design. The constitutive relations are refined to ensure that delayed elastic recovery occurs and expanded to include the effects of temperature-dependent damage and power-law breakdown. Finite element models implementing the refined constitutive relations are used to simulate the evolution and failure of *hpzs* during compression, with direct comparisons to experimental results being used to validate the model.

## 1.3 Scope of Thesis

This thesis focuses primarily on the temperature-dependence of ice deformation and its interdependence with hydrostatic pressure. The scope of this work can be outlined as follows:

1. Review of fundamental theories on viscoelasticity, thermodynamics, damage mechanics, and fracture.

2. Review of the relevant ice mechanics, particularly focused on the results of extensive triaxial and indentation experiments.
3. Experimental results from triaxial experiments used to guide theoretical modelling.
4. Outline of constitutive model and introduction of new factors, including temperature-dependent damage and power-law breakdown.
5. Validation of constitutive model as implemented by finite element program Abaqus via single element and indentation simulations.
6. Results of new developments in constitutive modelling for ice indentation experiments using finite element modelling.
7. Summary of conclusions and recommendations.

# Chapter 2

## Ice Mechanics

Ice-structure interactions pose a very real challenge to ships and structures in Arctic and sub-Arctic conditions (Lehmann, 2010), necessitating a range of “ice-strengthening” design techniques. This has provoked a thorough examination of the ice loads produced during such an interaction, from ship ramming tests (Cowper and Edgecombe, 1987; Edgecombe et al., 1992; Glen and Blount, 1984; Riska et al., 1990), and full-scale measurements on fixed structures (Blenkarn, 1970; Brown, 2001; Jefferies and Wright, 1988; Määttänen, 1978; Morsy and Brown, 1996; Yue and Bi, 2000), to medium- (Frederking et al., 1990; Masterson et al., 1993) and small-scale indentation tests (Barrette et al., 2002; Browne, 2012; Browne et al., 2013; O’Rourke et al., 2015; 2016a;b; Wells et al., 2011).

These tests found that while the measured global pressure was relatively low, on the order of one MPa at all scales, local pressures were drastically greater; pressures of 70 MPa in areas of 1 cm<sup>2</sup> have been observed during medium-scale indentation experiments (Frederking et al., 1990) while pressures of over 100 MPa have been

observed in laboratory-scale experiments in areas on the order of a few  $\text{mm}^2$  (Wells et al., 2011).

The stark difference between the observed global and local pressures can be explained by the development of high pressure zones (*hpzs*), which, due to the geometry of the interaction or some pre-existing flaw in the ice, localize the load into a number of small regions, as illustrated in Figure 2.1. Note that a sufficiently large interaction rate is required to produce *hpzs*, the size of which will be dependent upon the ice and structure involved. *Hpzs* have been observed to transfer more than 90 % of the load to the structure (Johnston et al., 1998) in regions that cover less than 10 % of the global interaction area (Taylor et al., 2008); summing the *hpzs* over the nominal contact area leads to the small measured global pressures. Understanding the behaviour of *hpzs* is thus a key component to understanding ice-structure interactions. Jordaan (2001) provides a thorough review of the mechanics of ice-structure interactions, with a focus on the behaviour of *hpzs*.

Of particular relevance to this work are the medium-scale indentation experiments that took place at the Hobson’s Choice ice island in 1989 (Frederking et al., 1990) and 1990 (Masterson et al., 1993), as they provided an early examination of *hpz* (referred to as the failure zone at the time) structure and behaviour. The two experimental programs examined the failure behaviour of ice during indentation with eight indentors of different design, including:

1. A rigid, spherical end-cap indenter with a surface area of  $0.8 \text{ m}^2$ . Unlike flat indentors, the geometry of indentation produced by a spherical end-cap indenter avoids the loading singularity at the edge of the indenter, minimizing plastic

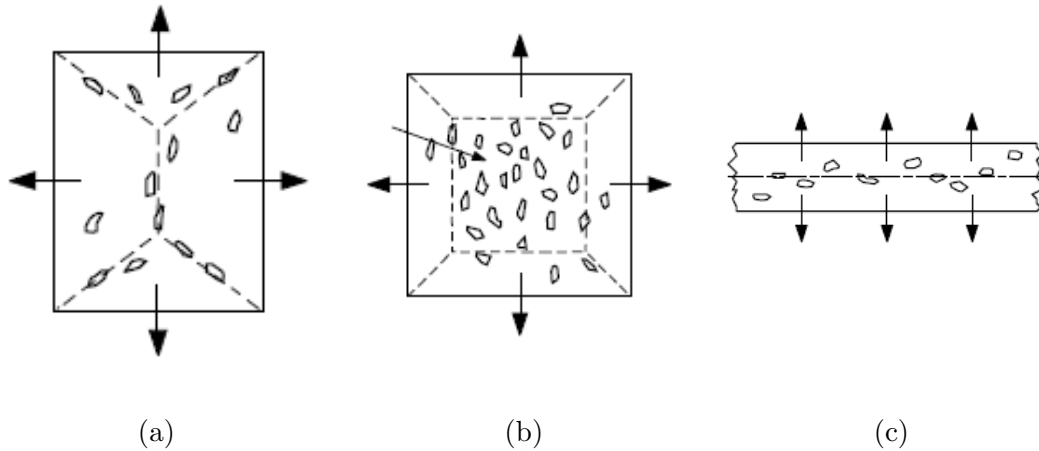


Figure 2.1: Illustration of *hpz* distributions for common ice-structure interaction geometries. (a) shows the distribution for a small, stationary rectangular area, (b) represents the distribution for a larger rectangular area, where the *hpzs* have become densely packed within the centre of the interaction zone, while (c) illustrates the distribution for a continuous ice sheet, where the *hpzs* occur predominantly along the centre line.

deformation.

2. Three flat, compliant indentors 1.8, 0.8, and 0.7 m<sup>2</sup> in area, designed to test contemporary revisions to shipping regulations. These indentors were designed to yield under the expected pressures, to simulate a section of a ship's hull.
3. Two rigid, flat indentors with total areas of 1.8 and 0.375 m<sup>2</sup>. These indentors were used as both a comparison to the results of the compliant tests and a mount for special purpose sensors.
4. Two wedge indentors with included angles of 90° and 143° were designed to test a design concept for use on fixed offshore structures.

Note that the ice face was shaped into one of three forms for indentations involving the flat indentors, to reduce the load necessary to induce crushing failure; both horizontally and vertically aligned, truncated wedges, as well as truncated pyramids of various initial contact areas, were tested.

In total, 26 indentation tests were performed, covering indenter velocities ranging from 0.3 mm/s to 400 mm/s and contact areas from 0.2 m<sup>2</sup> to 1.5 m<sup>2</sup>. Peak nominal pressures of  $6.2 \pm 3.4$  MPa were observed, with the highest local pressures of 70 MPa being observed at the centre of the indenter. Changes in failure mode were observed with increasing indenter velocity; low velocities produced a smooth loading curve indicative of creep deformation, while higher velocities produced saw-tooth loading. Examination of the the ice post-deformation showed a clear distinction between the highly damaged layer of ice near the contact surface and the practically undamaged ice beneath. The clear, intact ice beneath the centre of the indenter is here mistakenly labelled as undamaged; analysis of the relevant thin-sections has since shown this region to be highly recrystallized.

These tests sparked a wide range of laboratory-scale indentation and triaxial experiments designed to determine the parameters that contribute to *hpz* development. The results of these tests will be discussed in detail later, starting in Section 2.6.3. To fully understand the development of *hpzs*, an in-depth knowledge of the properties of ice is required. To facilitate understanding, brief introductions to viscoelastic theory, molecular deformation theory, thermodynamic constitutive theory, fracture mechanics, and damage mechanics are provided.

## 2.1 Viscoelastic Deformation

Ice, like many materials at high homologous temperatures, deforms viscoelastically; when subjected to a constant stress it will continue to deform after an initial elastic response, proceeding through three phases of deformation commonly termed primary, secondary, and tertiary creep (da Costa Andrade, 1910), as illustrated in Figure 2.2. Conversely, a constant strain will result in a gradual reduction in stress. The mechanical processes behind this behaviour are described in detail by Sinha (1978; 1982), who developed an early viscoelastic theory for ice under uniaxial conditions. A thorough review of viscoelasticity is provided to aid in understanding the deformation behaviour of ice.

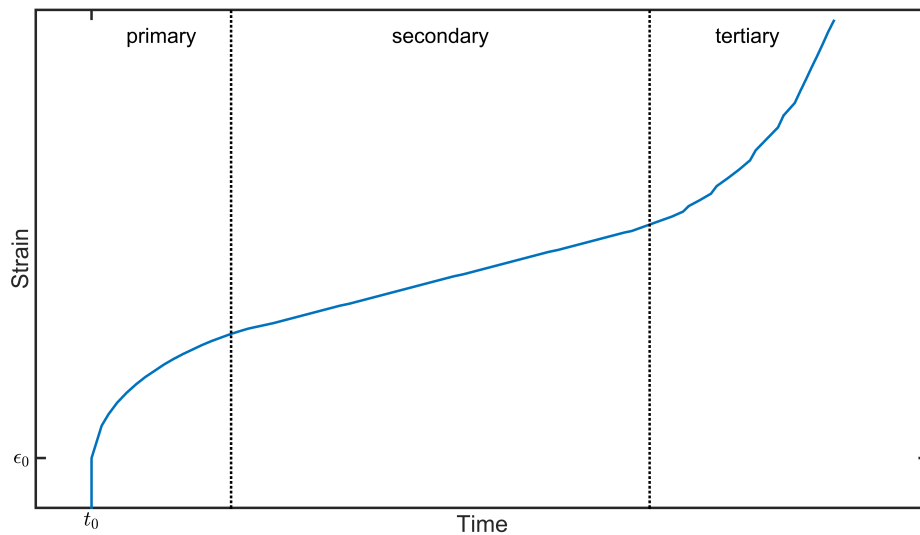


Figure 2.2: Creep response to constant stress.  $\epsilon_0$  represents the instantaneous elastic response to the application of a constant stress  $\sigma_0$  applied at time  $t_0$ .

### 2.1.1 Linear Viscoelasticity

The simplest viscoelastic model assumes that stress and strain are linearly dependent. The stress response of such a material to the successive application of strain (or vice versa) is then additive; a series of changes, each at a different time, will have a cumulative effect on the stress or strain state, which can be represented mathematically by:

$$\epsilon(t) = \sum_{i=1}^N J(t - t_i) \Delta\sigma(t_i) \quad (2.1)$$

$$\sigma(t) = \sum_{i=1}^N R(t - t_i) \Delta\epsilon(t_i) \quad (2.2)$$

where  $\sigma$  and  $\epsilon$  are the total stress and strain resulting from the application of a series of step increases in strain and stress, represented by  $\Delta\epsilon$  and  $\Delta\sigma$ , respectively, at times  $t_i$ ,  $J$  and  $R$  are the creep compliance and relaxation modulus, respectively, and  $t$  is the time. An example viscoelastic response is illustrated in Figure 2.3. If these changes occur continuously then the sum can be reduced to an integral, producing the general representation of linear viscoelasticity:

$$\epsilon(t) = \int_0^t J(t - \tau_d) \frac{d\sigma(\tau_d)}{d\tau_d} d\tau_d \quad (2.3)$$

$$\sigma(t) = \int_0^t R(t - \tau_d) \frac{d\epsilon(\tau_d)}{d\tau_d} d\tau_d \quad (2.4)$$

where  $\tau_d$  is a dummy integration variable. This is generally referred to as the Boltzmann superposition principle. Due to the nature of convolution integrals,  $J$  and  $R$  are related simply by:

$$\int_0^t J(t - \tau_d) R(\tau_d) d\tau_d = \int_0^t R(t - \tau_d) J(\tau_d) d\tau_d = t \quad (2.5)$$

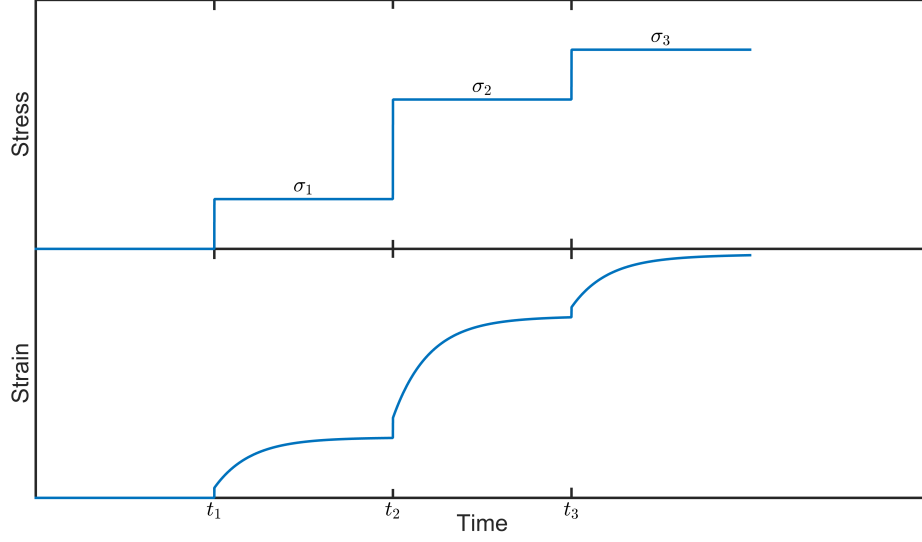


Figure 2.3: Linear viscoelastic response to cumulative increases in applied stress. Note that there is no viscous component in this example.

or, in the Laplace space:

$$s_L^2 \bar{J}(s_L) \bar{R}(s_L) = 1 \quad (2.6)$$

where  $s_L$  is the transform variable and the over-bars indicate the Laplace transform.

Biot (1954) used the thermodynamics of irreversible processes to derive the following relations for the creep compliance and relaxation modulus:

$$J(t) = \frac{1}{E_1} + \frac{t}{\mu_1} + \sum_{i=2}^n \frac{1}{E_i} \left(1 - e^{-E_i t / \mu_i}\right) \quad (2.7)$$

$$R(t) = E_1 + \sum_{i=2}^n E_i' e^{-E_i' t / \mu_i'} \quad (2.8)$$

where  $E_i$ ,  $\mu_i$ ,  $E_i'$ , and  $\mu_i'$  are material constants, which can be theoretically represented by arrays of springs and dashpots.

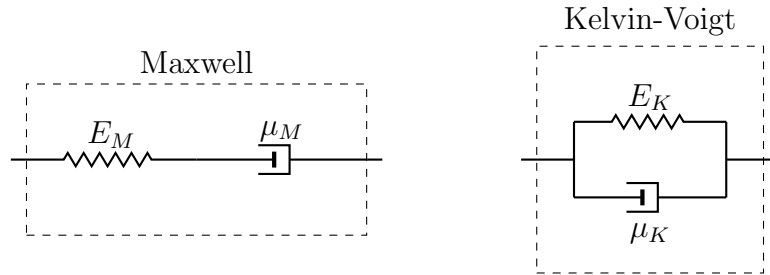


Figure 2.4: Basic models of viscoelastic behaviour.

### 2.1.2 Viscoelastic Modelling

Springs and dashpots provide the basic elements of viscoelastic analysis; springs are used to describe the instantaneous elastic response of a material, while dashpots can be used to model the time-dependent, viscous deformation. The linear, uniaxial constitutive relations for these elements are given by:

$$\sigma = E\epsilon \quad (\text{spring}) \quad (2.9)$$

$$\sigma = \mu\dot{\epsilon} \quad (\text{dashpot}) \quad (2.10)$$

where  $\sigma$  is the stress,  $E$  is the elastic modulus of the spring,  $\mu$  is the viscosity of the dashpot, and  $\epsilon$  and  $\dot{\epsilon}$  are the strain and strain rate, respectively. These elements can be arranged to describe the behaviour of various viscoelastic materials. The most basic arrangements are known as the Maxwell (spring and dashpot in series) and Kelvin-Voigt (spring and dashpot in parallel) materials. These arrangements are illustrated in Figure 2.4.

While both arrangements describe viscoelastic materials, their responses are actually quite different. For example, consider the application of a generalized uniaxial

stress-relaxation cycle:

$$\sigma = \sigma_m \left[ 1 - H(t - t') \right] \quad (2.11)$$

where  $\sigma_m$  is a constant representing the magnitude of stress,  $t'$  is the time at which relaxation begins, and  $H(t - t')$  is the Heaviside step function, which is defined as:

$$H(t - t') = \begin{cases} 0, & \text{if } t < t' \\ 1, & \text{if } t \geq t' \end{cases} \quad (2.12)$$

The normalized responses of the Maxwell and Kelvin-Voigt materials, respectively, are then:

$$\frac{\epsilon_M}{\sigma_m} = \frac{t - (t - t') H(t - t')}{\mu_M} + \frac{1 - H(t - t')}{E_M} \quad (2.13)$$

$$E_K \frac{\epsilon_K}{\sigma_m} = 1 - e^{-E_K t / \mu_K} - H(t - t') \left( 1 - e^{-E_K (t - t') / \mu_K} \right) \quad (2.14)$$

An example of this response is shown in Figure 2.5. The Kelvin-Voigt material represents what is known as a delayed elastic response; a recoverable strain that rises to a plateau based on the applied stress. The Maxwell material represents both an instantaneous elastic response (due to the spring) and a non-recoverable, viscous strain. This is an example of irrecoverable strain; while elasticity implies the storage of energy, viscous flow implies its dissipation, as well as the generation of heat.

To properly represent creep behaviour, chains of Maxwell or Kelvin units with a spectrum of moduli and viscosities are required. This is known as the Broad-Spectrum Approach (BSA). Schapery (1962) proposed a collocation method for fitting experimental data to such a spectrum. For example, consider the relaxation modulus

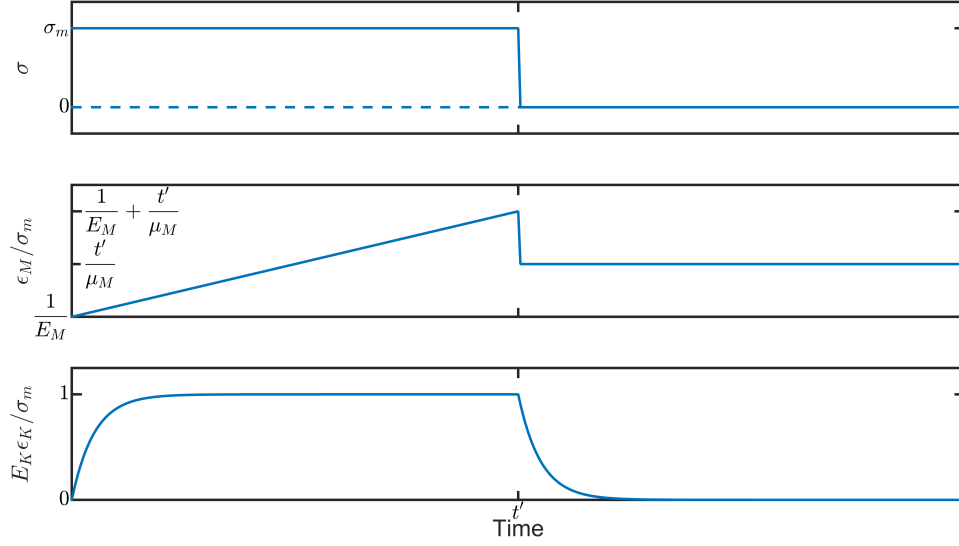


Figure 2.5: Example viscoelastic response. From top to bottom is shown: the idealized stress state; the normalized strain response of a Maxwell material, with an instantaneous elastic strain response of  $\sigma_m/E_M$  and a time-dependent viscous strain of  $\sigma_m t'/\mu_M$  that is non-recoverable; and finally, the fully recoverable normalized strain response of the Kelvin material, which plateaus at a strain of  $\sigma_m/E_K$ .

of Equation 2.8:

$$R(t) = E_1 + \sum_{j=2}^N E_j e^{-E_j t/\mu_j} \quad (2.15)$$

$$R(t) - E_1 = \sum_{j=2}^N E_j e^{-t/\tau_j} \quad (2.16)$$

where  $\tau_j = \mu_j/E_j$  and  $E_1 = R(\infty)$ . An arbitrary set of collocation points for  $\tau_j$  and  $t_k$  that coincide with available experimental data are then chosen, reducing the problem to a set of linear algebraic equations:

$$\{b_k\} = \{a_{jk}\} \{E_j\} \quad (2.17)$$

where  $\{b_k\} = R(t_k) - E_1$  and  $\{a_{jk}\} = e^{-t_k/\tau_j}$ . The response of the model can then be evaluated by solving for  $E_j$  and comparing the result of Equation 2.8 to experimental results. Multiple iterations may be necessary to locate suitable values of  $t_k$  and  $\tau_j$ . Some values of  $E_j$  may be significantly smaller than others and will contribute little to the total response. These values can be safely ignored to reduce computation time. This method was successfully applied to ice in Xiao (1997).

### 2.1.3 Non-Linear Viscoelasticity

While linear viscoelasticity is a useful starting point for the analysis of some viscoelastic materials, solids such as ice exhibit highly non-linear behaviour, and require more robust modelling tools. A generalization of linear viscoelastic theory for such cases is possible by using multiple integrals (Green and Rivlin, 1957). To illustrate, consider the application of an initial constant stress,  $\Delta\sigma_0$ , at time  $t = 0$ , followed by an additional stress,  $\Delta\sigma_1$ , at time  $t = t_1$ . The resulting non-linear strain can be represented in polynomial form by:

$$\begin{aligned} \epsilon(t) = \Delta\sigma_0 J_1(t) + \Delta\sigma_0^2 J_2(t, t) + \Delta\sigma_1 J_1(t - t_1) + \Delta\sigma_1^2 J_2(t - t_1, t - t_1) \\ + 2\Delta\sigma_0 \Delta\sigma_1 J_2(t, t - t_1) \end{aligned} \quad (2.18)$$

where  $J_2$  represents the second-order terms of the creep compliance; terms greater than second-order have been ignored. If  $N$  such load steps are applied, then the strain becomes:

$$\epsilon(t) = \sum_{i=0}^N \Delta\sigma_i J_1(t - t_i) + \sum_{i=0}^N \sum_{j=0}^N \Delta\sigma_i \Delta\sigma_j J_2(t - t_i, t - t_j) \quad (2.19)$$

which reduces to an integral form in the limit that  $dt \rightarrow 0$ , as per the Boltzmann superposition principle used to derive the linear viscoelastic relations. A similar process gives the non-linear, time-dependent stress:

$$\epsilon(t) = \int_0^t J_1(t - \tau_1) \frac{d\sigma(\tau_1)}{d\tau_1} d\tau_1 + \int_0^t \int_0^t J_2(t - \tau_1, t - \tau_2) \frac{d\sigma(\tau_1)}{d\tau_1} \frac{d\sigma(\tau_2)}{d\tau_2} d\tau_1 d\tau_2 \quad (2.20)$$

$$\sigma(t) = \int_0^t R_1(t - \tau_1) \frac{d\epsilon(\tau_1)}{d\tau_1} d\tau_1 + \int_0^t \int_0^t R_2(t - \tau_1, t - \tau_2) \frac{d\epsilon(\tau_1)}{d\tau_1} \frac{d\epsilon(\tau_2)}{d\tau_2} d\tau_1 d\tau_2 \quad (2.21)$$

Additional terms can be added as necessary. This formulation can be used to approximate the behaviour of all classes of materials to the desired level of non-linearity. For generality, higher order terms are necessary to effectively model creep behaviour. The difficulty lies in the determination of the functions  $J_i$  and  $R_i$  from experimental data, which becomes prohibitive for strongly non-linear materials such as ice.

A more cost-effective method for describing a non-linear viscoelastic response was developed by Schapery (1969) using the concept of reduced time; by folding the non-linearities into the time formulation, Schapery found it was possible to reduce a non-linear problem to a formulation identical to a linear response. The general result for a uniaxial stress state is given by:

$$\epsilon(t) = \int_0^t J[\psi(t) - \psi(\tau_d)] \frac{d\sigma(\tau_d)}{d\tau_d} d\tau_d \quad (2.22)$$

$$\sigma(t) = \int_0^t R[\psi(t) - \psi(\tau_d)] \frac{d\epsilon(\tau_d)}{d\tau_d} d\tau_d \quad (2.23)$$

where:

$$\psi(t) = \int_0^t \frac{d\tau_d}{a_d} \quad (2.24)$$

is the reduced time and  $a_d$  is a function of the desired non-linearities, such as stress, temperature, or ageing.

This theory was successfully applied to the creep of ice by Jordaan and McKenna (1988a). In their formulation,  $a_d$  took the form of a non-linear, stress-dependent viscosity, given by:

$$a_d = \mu(\sigma) = \frac{\sigma_0^n}{\sigma^{n-1} \dot{\epsilon}_0} \quad (2.25)$$

where  $\sigma_0$  and  $\dot{\epsilon}_0$  are a reference stress and strain rate, respectively. This formulation is suitable for materials which do not undergo substantial changes in microstructure during deformation. To account for such changes, other methods are required.

The modified superposition principle (MSP) is another generalization of the linear theory of viscoelasticity (Findley et al., 1976). For a uniaxial stress-state, this generalization is given by:

$$\epsilon = \int_0^t L(\sigma, t - \tau_d) \frac{dF(\sigma, \tau_d)}{d\tau_d} d\tau_d \quad (2.26)$$

where  $L$  and  $F$  are empirically determined functions. This is an approximate method that uses the results from a unit step creep test to describe the function  $L$  under arbitrary stress conditions. The accuracy of this formulation is highly variable, and is not general enough to describe all materials and stress histories.

Schapery (1981; 1991) proposed a model that isolated non-linearities within the stress function,  $F$ . In this formulation, the function  $L$  takes the form of the linear creep compliance,  $J$ , and the uniaxial strain becomes:

$$\epsilon = \int_0^t J(t - \tau_d) \frac{dF(\sigma, \tau_d)}{d\tau_d} d\tau_d \quad (2.27)$$

When generalized to three-dimensional loading, this provides a simple method for predicting viscoelastic solutions from elastic ones. Schapery (1981) applied this concept to the inclusion of microstructural changes during deformation. Assuming that the stress function is also a function of the internal microstructural parameters ( $S_i, i = 1, 2, \dots$ ), the uniaxial constitutive relation becomes:

$$\epsilon = E_R \int_0^t J(t - \tau_d) \frac{d\epsilon^{ps}(\sigma, S_i)}{d\tau_d} d\tau_d \quad (2.28)$$

where  $\epsilon^{ps}$  is an explicit function of stress, time, and microstructural parameters, referred to as the pseudostrain. The coefficient  $E_R$  is the reference modulus introduced to produce the correct units for strain. In effect,  $\epsilon^{ps}$  is the strain that exists in an elastic material with the same set of microstructural parameters,  $S_i$ . For many cases, a single microstructural parameter is sufficient. More complex materials such as ice require at least two parameters, one to describe the effect of microcracking at low pressures, the other dynamic recrystallization, pressure melting, and other relevant phenomenon at high pressures. Inverting Equation 2.28 provides the general form of the pseudostrain, given by:

$$\epsilon^{ps}(t) = \frac{1}{E_R} \int_0^t R(t - \tau_d) \frac{d\epsilon}{d\tau_d} d\tau_d \quad (2.29)$$

Extended to multi-axial deformation, the constitutive relation becomes:

$$\epsilon_{ij} = E_R \int_0^t J(t - \tau_d) \frac{d}{d\tau_d} \left( \frac{\partial W^c}{\partial \sigma_{ij}} \right) d\tau_d \quad (2.30)$$

where  $W^c$  is the complementary pseudo-strain energy density used to define the pseudostrain:

$$\epsilon_{ij}^{ps} = \frac{\partial W^c}{\partial \sigma_{ij}} \quad (2.31)$$

As the creep compliance and relaxation modulus are independent of state variables and the coefficient  $E_R$  is a constant, this theory imposes the restriction that the elastic properties, such as the Young's Modulus and Poisson's ratio, remain constant during the process. The use of a single function to represent non-linearities poses some restrictions on the types of materials that can be represented. Ice, for example, displays a combination of linear elastic, delayed elastic, and secondary creep deformation, with the later two following separate power laws; the application of a single power law does not satisfactorily model these features simultaneously, except at large strains where the elastic components become negligible.

It should be noted that Laplace transforms can often be used to reduce viscoelastic problems to mathematically equivalent elastic solutions. Known as the correspondence principle (Findley and Davis, 2013; Findley et al., 1976), this provides a simple method to perform a linear viscoelastic analysis, provided the boundaries are independent of time and inertial terms are neglected. Additional restrictions apply for non-linear analyses; the time and space dependence of creep and relaxation functions must appear as separate factors. Jordaan et al. (1992a) provide validation for this theory with respect to the deformation of ice.

## 2.2 Thermodynamic Constitutive Theory

Many viscoelastic materials are history dependent, particularly at high stresses and temperatures, both of which are common conditions during ice-structure interactions. Internal variable theories represent history-dependent materials with structural variables, such as microcrack density or void ratio. These theories are based upon the

thermodynamics of irreversible processes.

In a thermodynamic system, internal energy and force are state functions defined by state variables such as temperature, strain, etc. Reversible systems can be explicitly defined using external variables, but are insufficient to define an irreversible system; these systems require internal variables to account for the loss of energy during deformation (Biot, 1954; Bridgman, 1950; Coleman and Gurtin, 1967; Schapery, 1969). These internal variable theories postulate that a free energy function exists that is dependent upon all external and internal variables.

A similar theory, proposed by Kestin and Rice (1970) and Rice (1971), supposes that it is possible to define a finite set of internal variables with which to approximate a non-equilibrium state under investigation sufficiently close to the thermodynamic equilibrium state. Under most conditions, these theories will produce identical results. A review of the necessary thermodynamic theory is provided here.

### 2.2.1 Strain Energy and Work

To describe viscoelastic behaviour, we first assume that a strain energy density function,  $W$ , exists for all processes of interest.  $W$  is a function of all external variables (strain, temperature, etc.) and independent internal variables,  $S_k$ :

$$W = W(\epsilon_{ij}, S_k) \tag{2.32}$$

The stress tensor can then be derived by taking the partial derivative of the strain energy function with respect to strain:

$$\sigma_{ij} = \frac{\partial W}{\partial \epsilon_{ij}} \tag{2.33}$$

The internal variables  $S_k$  generally define changes in microstructure (crack geometry, void volume, grain boundary sliding, etc.). Constant  $S_k$  imply a hyperelastic material (Malvern, 1969); the theory is not limited to linear elastic materials.

The strain energy is equivalent to the work done during a reversible process ( $\Delta S_k = 0$ ). Most real processes will be partially or entirely irreversible, producing some form of change in internal state variables. The energy lost due to dissipation includes frictional energy, creep, plastic flow, etc. The total work per unit volume is then given by:

$$W_T = \int \sigma_{ij} d\epsilon_{ij} \quad (2.34)$$

$W_T$  includes the surface energy (Rice, 1977),  $W_s$ , given by:

$$W_s = 2\gamma_m A_m \quad (2.35)$$

where  $\gamma_m$  is the surface energy per unit area of the  $m^{\text{th}}$  crack and  $A_m$  is the corresponding surface area. This surface energy is both reversible and often negligible.

The strain energy density and total work done per unit volume are interrelated; consider an infinitesimal change in strain energy density:

$$\delta W = \frac{\partial W}{\partial \epsilon_{ij}} \delta \epsilon_{ij} + \frac{\partial W}{\partial S_k} \delta S_k = \sigma_{ij} \delta \epsilon_{ij} - f_k \delta S_k \quad (2.36)$$

where  $f_k$  are the thermodynamic forces involved; see Schapery (1997a) for more detail on the thermodynamic forces involved in viscoelastic and viscoplastic deformation. These forces produce changes in the microstructure parameters  $S_k$  that effect the storage of energy within the material. For example, if  $A_k$  is the surface area of a crack,  $f_k$  is a function of the energy release rate,  $G_k$ , for crack propagation:

$$f_k = G_k - \frac{\partial W_s}{\partial A_k} \quad (2.37)$$

The change in total work per unit volume obtained through integration from an arbitrary initial state,  $W_0$ , is given by:

$$\Delta W_T = W - W_0 + \int_0^1 f_k dS_k \quad (2.38)$$

The total work per unit volume can then be separated into reversible strain energy density and irreversible energy density,  $W_I = W_I(S_k)$ . A process starting from the reference state with zero strain energy then gives:

$$W_T = W + W_I \quad (2.39)$$

## 2.2.2 Entropy

Thermodynamic theory stipulates that a material must satisfy entropy requirements in addition to equilibrium equations and constitutive relations. Entropy is a function of all state variables, including non-observable internal variables. The rate of entropy production per unit mass of the universe,  $\dot{S}$ , is zero for a reversible process and positive for an irreversible one; it can never be negative:

$$\dot{S} = \dot{S}_{sys} + \dot{S}_{sur} \geq 0 \quad (2.40)$$

where  $S_{sys}$  is the entropy production of the system under consideration, while  $S_{sur}$  is the entropy production of the surroundings. We assume that the system is in contact with a heat reservoir that maintains a constant temperature,  $T$ . If  $\dot{Q}$  is the rate of heat transfer to the reservoir, then the entropy production rate of the reservoir is  $\dot{S}_{sur} = \dot{Q}/T$  and the total entropy production becomes:

$$\dot{S} = \dot{S}_{sys} + \frac{\dot{Q}}{T} \geq 0 \quad (2.41)$$

The first law of thermodynamics states that the rate of work done per unit volume,  $\dot{W}_T = \sigma_{ij}\dot{\epsilon}_{ij}$  and the rate of change in internal energy density,  $\dot{U}_i$ , are related to the rate of heat transfer via:

$$\dot{U}_i = \sigma_{ij}\dot{\epsilon}_{ij} - \frac{\dot{Q}}{V} \quad (2.42)$$

where  $V$  is the volume under consideration. Noting that the change in strain energy density can also be defined as  $\dot{W} = \dot{U}_i - \frac{T\dot{S}_{sys}}{V}$ , the rate of entropy production then becomes:

$$\dot{S} = \frac{V}{T} \left( \sigma_{ij}\dot{\epsilon}_{ij} - \dot{W} \right) = f_k \dot{S}_k \frac{V}{T} \quad (2.43)$$

$$f_k \dot{S}_k \frac{V}{T} \geq 0 \quad (2.44)$$

The above formulation is suitable for constant strain-rate testing. Some test procedures call for force-control, due to the hardness of the sample, flexibility of test frame, or simply the goals of the test. The complementary strain energy density,  $W'$ , is then used:

$$W' = \sigma_{ij}\epsilon_{ij} - W \quad (2.45)$$

As illustrated in Figure 2.6, the complementary strain energy density can be thought of simply as the area to the left of the stress-strain curve. The differential is then:

$$\delta W' = \delta\sigma_{ij}\epsilon_{ij} + \sigma_{ij}\delta\epsilon_{ij} - \delta W = \epsilon_{ij}\delta\sigma_{ij} + f_k\delta S_k \quad (2.46)$$

which implies that the strain and thermodynamic forces are given by:

$$\epsilon_{ij} = \frac{\partial W'}{\partial \sigma_{ij}}, \quad (2.47)$$

$$f_k = \frac{\partial W'}{\partial S_k} \quad (2.48)$$

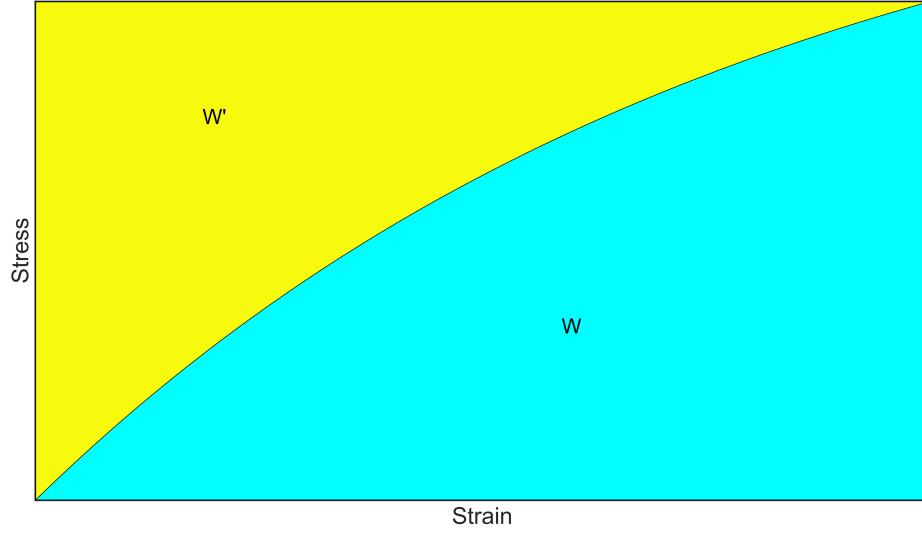


Figure 2.6: Illustration of complementary strain energy density.

The total complementary work per unit volume,  $W'_T$ , is then:

$$W'_T = \sigma_{ij}\epsilon_{ij} - W_T \quad (2.49)$$

Like the total work per unit volume defined in Equation 2.39, the total complementary work can also be separated into a reversible complimentary strain energy density term,  $W'$ , and the irreversible energy density term  $W'_I$ :

$$W'_T = W' + W'_I \quad (2.50)$$

To separate the recoverable strain from non-recoverable, we first examine the incremental form of Equation 2.47:

$$\delta\epsilon_{ij} = \frac{\partial\epsilon_{ij}}{\partial\sigma_{kl}}\delta\sigma_{kl} + \frac{\partial\epsilon_{ij}}{\partial S_m}\delta S_m \quad (2.51)$$

where:

$$\frac{\partial \epsilon_{ij}}{\partial \sigma_{kl}} = \frac{\partial^2 W'}{\partial \sigma_{ij} \partial \sigma_{kl}} = J_{ijkl} \quad (2.52)$$

$$\frac{\partial \epsilon_{ij}}{\partial S_m} = \frac{\partial f_m}{\partial \sigma_{ij}} \quad (2.53)$$

where  $J_{ijkl}$  is the compliance tensor. The recoverable strain,  $\delta \epsilon_{ij}^e$ , and non-recoverable strain,  $\delta \epsilon_{ij}^p$ , are then:

$$\delta \epsilon_{ij}^e = J_{ijkl} \delta \sigma_{kl} \quad (2.54)$$

$$\delta \epsilon_{ij}^p = \frac{\partial f_m}{\partial \sigma_{ij}} \delta S_m \quad (2.55)$$

The selection of internal variables should be based on experimental observations and theoretical considerations. The number of variables should be large enough (within reasonable limits) to represent the material being studied, and should all have some physical significance such that they can be derived from measurable quantities. At least one internal variable is necessary to represent a history-dependent material; two if the response is also non-linear. A general description of such a system is provided by the thermodynamics of irreversible processes.

### 2.2.3 Thermodynamics of Irreversible Processes

Physical systems undergoing deformation tend towards increasing entropy, which can be thought of as moving towards a more probable state. Consider a system in the vicinity of its equilibrium state, defined by  $n$  thermodynamic variables  $q_i$  and their generalized force conjugates  $Q_i$  (See Alberty (2009) for an example application of

conjugate variables). The entropy production of such a system is given by:

$$dS_u = dS_{sys} - \frac{dU}{T} + \sum_i \frac{Q_i}{T} dq_i \quad (2.56)$$

where  $S_u$  is the entropy production of the universe and  $dU$  is the change in internal energy. The reference equilibrium state, represented by  $S'$ , occurs at a constant  $T$  with  $q_i = Q_i = 0$  and is given by:

$$TS' = TS_{sys} - U = -\frac{1}{2} \sum_{ij} a_{ij} q_i q_j \quad (2.57)$$

where  $a_{ij}$  is a matrix of constants. Since we are describing an equilibrium state, the entropy  $S'$  is a maximum and can be represented by the quadratic function,  $V$ :

$$V = \frac{1}{2} \sum_{ij} a_{ij} q_i q_j \quad (2.58)$$

which is a positive-definite variable with a symmetric matrix of coefficients  $a_{ij}$ . Under external forces, the entropy is then:

$$TS_u = -V + \sum_i Q_i q_i \quad (2.59)$$

If the system is displaced from the reference state slowly and reversibly then it can be considered to follow a series of equilibrium states that produce maximum entropy, represented mathematically by  $\partial S_u / \partial q_i = 0$ . Otherwise, Onsager's principle (Onsager, 1931) applies:

$$T \frac{\partial S_u}{\partial q_i} = \sum_j b_{ij} \dot{q}_j \quad (2.60)$$

where the matrix of coefficients,  $b_{ij}$ , is symmetric. The basic relationship for irreversible processes is then:

$$\sum_j a_{ij} q_j + \sum_j b_{ij} \dot{q}_j = Q_i \quad (2.61)$$

It is useful to introduce the quadratic form:

$$D = \frac{1}{2} \sum_{ij} b_{ij} \dot{q}_i \dot{q}_j \quad (2.62)$$

which is equivalent to:

$$D = \frac{1}{2} T \sum_i \dot{q}_i \frac{\partial S_u}{\partial \dot{q}_i} = \frac{1}{2} T \frac{\partial S_u}{\partial t} \quad (2.63)$$

This shows that the function  $D$  must be positive-definite due to its dependence on the entropy production rate. Equation 2.61 may then be rewritten in the Lagrangian form using the quadratic expressions for  $V$  and  $D$ :

$$\frac{\partial V}{\partial q_i} + \frac{\partial D}{\partial \dot{q}_i} = Q_i \quad (2.64)$$

The invariant  $V$  is seen to play the role of a potential energy while  $D$  that of a dissipation function. Consider the case of a constant external pressure,  $P$ , acting on a system. The conjugate variable is then the volume of the system,  $-v$ , giving:

$$\sum_i Q_i dq_i = -P dv \quad (2.65)$$

Integrating Equation 2.56 gives:

$$-TS_u = U - TS_{sys} + Pv \quad (2.66)$$

which, for a uniform temperature, represents the Gibbs free energy of the system. Equation 2.56 can thus be thought of as an extension of the Gibbs free energy to non-equilibrium conditions, while the quadratic function  $V$  is the Helmholtz free energy at equilibrium, since:

$$V = U - TS_{sys} \quad (2.67)$$

Biot (1955) notes that these formulae for systems in the vicinity of equilibrium apply to a large class of phenomena, including mechanical dissipation and elastic forces, heat transfer, etc., as well as the coupling between these phenomena. Biot also notes that these expressions may be represented by a network of springs and dashpots, as per the viscoelastic models described in Section 2.1.

Schapery (1966) successfully applied these principles to the description of non-linear viscoelastic material behaviour; a viscoelastic material element was considered to be a closed thermodynamic system defined by  $n$  state variables  $q_i$  and an absolute temperature  $T$ . Generalized force conjugates were defined such that  $Q_i \delta q_i$  represented an infinitesimal amount of external work,  $\delta W$ , done on the system, which in this case correspond to the stresses induced by infinitesimal changes in strain. Schapery (1966) also successfully proved that this generalized formulation could be represented by a Maxwell chain with non-linear springs and dashpots. This description was later expanded (Schapery, 1981; 1991; 1997a) to include the effect of microstructural changes in the material; the resulting viscoelastic equations were presented in Section 2.1.3.

For a more in-depth review of the basic principles of the thermodynamics of irreversible processes, refer to De Groot (1951); for an example of its application to a viscoelastic medium, see Schapery (1991).

## 2.3 Molecular Theory of Deformation

The molecular theory of deformation (Krausz and Eyring, 1975) has been successfully used to describe the behaviour of ice within a particular deformation regime; a review

is provided to enhance understanding of the constitutive models introduced in Chapter 4. The theory posits that the thermally-activated, time-dependent deformation of a solid can be described via the same methods used to describe a chemical reaction, which, in general, obey an equation of the following form:

$$\dot{\epsilon} = A \exp \left[ -\frac{B}{T} \right] \quad (2.68)$$

where  $\dot{\epsilon}$  is the rate constant,  $T$  is the absolute temperature, and  $A$  and  $B$  are reaction- and material-dependent constants. Arrhenius (1889) established that a reacting system consists of both ordinary and “active” molecules, with only the latter being energetically capable of reacting. Arrhenius suggested the following rate constant, based on the van’t Hoff (1884) description of the chemical equilibrium constant:

$$\dot{\epsilon} = A_e \exp \left[ -\frac{\Delta E_e}{k_B T} \right] = A_e \exp \left[ -\frac{Q_e}{R_g T} \right] \quad (2.69)$$

where  $A_e$  is the empirically obtained frequency factor, which represents the number of times a possible reaction occurs per unit time; the frequency factor can be thought of as the maximum possible rate constant. It generally takes the form of a collision between molecules for a chemical reaction, or the breaking of atomic bonds during creep flow.

$\Delta E_e$  and  $Q_e$  are the empirically obtained activation energies in units of joules and joules per mole, respectively; for a reaction to occur, there has to be enough kinetic energy to overcome the potential energy barrier and form the products. The height of that barrier is the activation energy. There are two types of reactions, endothermic and exothermic, that differ only in the enthalpy change of the system; endothermic reactions produce a positive enthalpy change, absorbing heat from the surroundings,

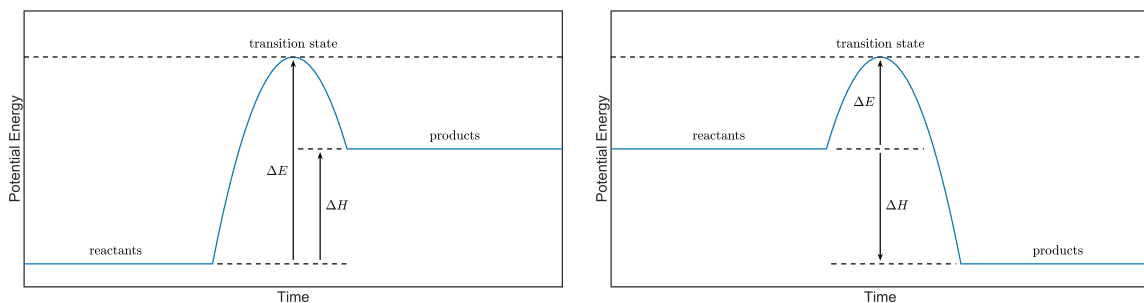


Figure 2.7: Examples of endothermic (left) and exothermic (right) reactions. Endothermic reactions are defined by absorption of energy by the system, represented by a positive enthalpy change ( $\Delta H$ ), while exothermic reactions release energy (negative  $\Delta H$ ).

while exothermic reactions release heat into their surroundings, leading to a negative enthalpy change. This is illustrated in Figure 2.7.

$k_B$  and  $R_g$  are the Boltzmann and universal gas constants, which relate the average kinetic energy of particles to their average temperature, as per the equipartition theorem (Pathria, 1972). While initially developed to describe the behaviour of gases, the equipartition theorem is broadly applicable and provides a useful approximation for both solids and liquids. For a solid, this may represent a measure of the vibrational motion of atoms or molecules within the crystal lattice. The higher the temperature, the higher the likelihood that inter-atomic or inter-molecular bonds will be broken.

The exponential term,  $e^{-Q_e/R_gT}$ , is a number between 0 and 1, representing the fraction of molecules with kinetic energy high enough to make it over the activation barrier during a given interaction. For a small number of collisions, this energy is large enough for the reaction or process to occur. This proportion follows the Boltzmann principle; it is larger at higher temperatures and lower activation energies.

Multiplying the frequency factor by the exponential term, we get the rate constant, which is the rate of successful collisions.

Scheffer and Kohnstamm (1911) introduced the concept of activation entropy to account for the dynamic nature of chemical equilibrium, which had been noted previously by van't Hoff (1884). Using equilibrium theory, it was supposed that molecules go both in the “forward” direction, from reactants to products, and vice versa in the “backward” direction. This is written formally as:

$$\kappa_f = A_f \exp \left[ \frac{\Delta S_f}{k_B} \right] \exp \left[ -\frac{\Delta H_f}{k_B T} \right] \quad (2.70)$$

$$\kappa_b = A_b \exp \left[ \frac{\Delta S_b}{k_B} \right] \exp \left[ -\frac{\Delta H_b}{k_B T} \right] \quad (2.71)$$

where  $\Delta S$  and  $\Delta H$  are the entropy and enthalpy of the transition state, respectively; equilibrium is achieved when the forward and backward rates are equal.

The effect of work on the rate constant must also be considered; deformation generally occurs under the effect of some external force acting on the material. The work done by these forces is found to change the height of activation barrier as follows:

$$\kappa_f = A_f \exp \left[ -\frac{Q_f - W_f}{k_B T} \right] = \kappa'_f \exp \left[ \frac{W_f}{k_B T} \right] \quad (2.72)$$

$$\kappa_b = A_b \exp \left[ -\frac{Q_b + W_b}{k_B T} \right] = \kappa'_b \exp \left[ -\frac{W_b}{k_B T} \right] \quad (2.73)$$

where  $W_f$  and  $W_b$  are the work in the forward and backward directions, respectively. The forward activation barrier is thus decreased by  $W_f$ , while the backwards barrier increases by  $W_b$ , as illustrated in Figure 2.8 for a symmetrical barrier. The net rate constant observed is then:

$$\kappa = \kappa_f - \kappa_b \quad (2.74)$$

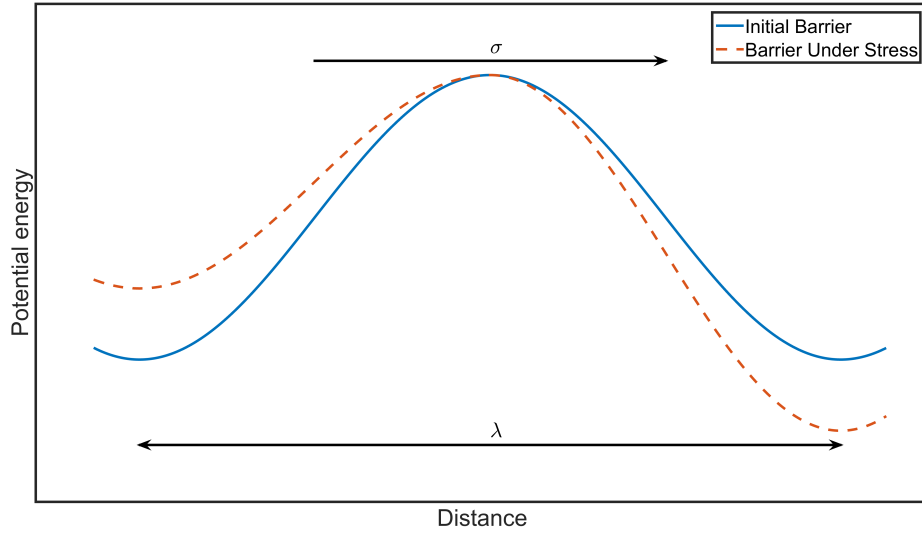


Figure 2.8: Effect of stress on activation energy. The activation barrier is reduced (or increased) by an amount equal to the total work done,  $W = \sigma A\lambda/2$ , where  $A$  is the effective cross-sectional area of the flow unit.

The work done is partly dissipated as heat and partly converted into the new product configuration. If the material is brittle, part of the work may also be dissipated via fracture.

Assuming that each activation results in an average contribution to strain of  $\delta$  and that the number of activations is  $\rho$ , then the strain rate is given by:

$$\dot{\epsilon} = \delta k \rho \quad (2.75)$$

While Equation 2.69 is sufficient for the analysis of many systems, a more in-depth description will be provided to assist in understanding the connection between molecular interactions and viscoelastic deformation.

### 2.3.1 Absolute Rate Theory

Simply put, the absolute rate theory is the application of statistical mechanics to the description of reaction kinetics. This requires a quantum mechanical calculation of the potential energy surface for a given reaction or process, which, as with any quantum mechanical description of a macroscopic process, involves a truly staggering number of dimensions to define the configuration space; approximately  $3n$ , where  $n$  is the number of particles, for a solid subjected to stress. This does not take into account the possibly infinite number of higher energy excited surfaces. Eyring and Polanyi (1931) provide a description of the semi-empirical methods used to calculate these surfaces.

The potential energy surface consists of a series of maxima and minima, hereafter referred to as peaks and valleys. Molecules can be considered to be within a stable configuration while within the potential energy valleys, each of which are connected to its neighbouring valleys by a saddle point. Molecules in a metastable position within a saddle point are said to be in the transition or activated state. A reaction corresponds to the system moving from one valley to another; the system is stable when in valleys. The lowest pass determines the ambient temperature at which stability is lost; larger barriers require high temperatures.

The rate of reaction can be calculated via statistical mechanics if we assume that equilibrium exists between initial and activated states; the rate is then equal to the concentration of activated complexes multiplied by the rate at which they pass through the transition state. The rate of forward reaction over a single barrier is

given by (Eyring, 1935):

$$\text{Rate}_f = \kappa_f C_f \frac{\bar{v}_f}{\Delta_f} = \kappa_f C_f \frac{k_B T}{h} \quad (2.76)$$

where  $\kappa_f$  is the transmission coefficient in the forward direction,  $C_f$  is the concentration of activated complexes per unit volume along length  $\Delta_f$ ,  $h$  is Planck's constant, and  $\bar{v}_f$  is the average velocity of the activated complexes moving along  $\Delta_f$ . The ratio  $\bar{v}_f/\Delta_f$  therefore represents the frequency at which the path  $\Delta_f$  is emptied.

The transmission coefficient is introduced to account for both the possibility of an activated complex being reflected back to its initial state and for a reactant to tunnel through the potential energy barrier to the product state, which is known as quantum tunnelling. Both effects are generally negligible during creep flow and plastic deformation; the additive binding is generally greater than the exchange binding in these cases, and the masses, temperatures, and potential energy barriers considered are large (or wide in the case of the energy barrier) enough that tunnelling is unlikely. The transmission coefficient can be calculated via the methods of Eyring (1935).

Applying the Boltzmann statistics of equilibrium, Eyring (1935) showed that  $C_f$  could be related to the concentration of reactants by:

$$C_f = \frac{Z_f}{Z_r} C_r = \frac{Z}{Z_r} \exp \left[ -\frac{\Delta E_f^0}{k_B T} \right] C_r \quad (2.77)$$

where  $Z_f$ ,  $Z_r$ , and  $Z$  represent the partition functions for various groups of molecules; the activated complexes in the forward direction, the reactants, and the ground state activated complexes, respectively.  $C_r$  is the concentration of reactants, and  $\Delta E_f^0$  is the activation energy at absolute zero. The rate constant can then be defined generally

as:

$$\kappa = \kappa \frac{k_B T}{h} \frac{Z}{Z_r} \exp \left[ -\frac{\Delta E^0}{k_B T} \right] \quad (2.78)$$

or, alternatively, either in terms of the Gibbs free energy needed for the system to reach the activated state,  $\Delta G^0$ , or the activation entropy,  $\Delta S^0$ , and heat of activation,  $\Delta H^0$ , as:

$$\kappa = \kappa \frac{k_B T}{h} \exp \left[ -\frac{\Delta G^0}{k_B T} \right] \quad (2.79)$$

$$\kappa = \kappa \frac{k_B T}{h} \exp \left[ \frac{\Delta S^0}{k_B} \right] \exp \left[ -\frac{\Delta H^0}{k_B T} \right] \quad (2.80)$$

The forward and backward reaction rates are then:

$$\text{Rate}_f = \kappa_f C_r \quad (2.81)$$

$$\text{Rate}_b = \kappa_b C_p \quad (2.82)$$

where  $C_p$  is the concentration of products. The net rate of flow is thus:

$$\text{Rate} = \kappa_f C_r - \kappa_b C_p \quad (2.83)$$

Rate theory not only applies to chemical reactions, but to any transition that is due to some underlying quantum process, such as the deformation of solids. To describe the highly non-linear deformation of a material such as ice, the rate theory of viscoelastic deformation is necessary.

### 2.3.2 The Rate Theory of Viscoelastic Deformation

As discussed in Section 2.1, viscoelastic deformation is the combination of time-independent (elastic) and time-dependent (viscous) deformation. This behaviour is

observed in both crystalline and polymeric materials, particularly at high homologous temperatures,  $T_h = T/T_m$ , where  $T$  and  $T_m$  are the absolute temperature and the melting point of the material, respectively.

The statistical description of the behaviour of an elastic material is relatively simple; an applied stress displaces atoms slightly from their equilibrium positions within valleys, such that the atoms do not reach the product state. These atoms return to their equilibrium positions upon the removal of stress. The elastic moduli are then a function of the steepness of the potential energy surface.

During viscous deformation, old neighbours are exchanged for new ones. Even with no stress, the breaking and forming of bonds takes place at some equilibrated rate; these processes are only accelerated by the application of an external stress. Movements can only occur where there are loose or empty spaces in the atomic structure, since molecules cannot occupy the same space. These empty sites are provided by dislocations or vacancies in crystal structures, which will be the focus of discussion here.

Empty sites can be assumed to occur at average intervals of  $\lambda_1$  along the direction of force. If stress is denoted as  $\sigma$ , then the force is given by  $\sigma\lambda_2\lambda_3$ , where  $\lambda_2\lambda_3$  is the cross-section being acted on by said force. Assuming a symmetrical energy barrier, the flow unit will go through the transition energy state at a distance of  $\lambda/2$ . The applied stress contributes work proportional to  $\sigma(\lambda_2\lambda_3\lambda/2)$  toward surmounting the barrier. As a result, the movement of the flow unit in the forward and backward

directions is:

$$\ell \exp \left[ \frac{\sigma \lambda_2 \lambda_3 \lambda}{2k_B T} \right] \quad (2.84)$$

$$\ell \exp \left[ -\frac{\sigma \lambda_2 \lambda_3 \lambda}{2k_B T} \right] \quad (2.85)$$

times per second, giving a net forward movement per second of:

$$\ell \left( \exp \left[ \frac{\sigma \lambda_2 \lambda_3 \lambda}{2k_B T} \right] - \exp \left[ -\frac{\sigma \lambda_2 \lambda_3 \lambda}{2k_B T} \right] \right) = 2\ell \sinh \left[ \frac{\sigma \lambda_2 \lambda_3 \lambda}{2k_B T} \right] \quad (2.86)$$

The forward velocity is simply the net forward movement per second times the distance moved,  $\lambda$ :

$$2\lambda\ell \sinh \left[ \frac{\sigma \lambda_2 \lambda_3 \lambda}{2k_B T} \right] \quad (2.87)$$

The strain rate can then be obtained by dividing this velocity by the distance between empty sites:

$$\dot{\epsilon} = 2 \frac{\lambda}{\lambda_1} \ell \sinh \left[ \frac{\sigma \lambda_2 \lambda_3 \lambda}{2k_B T} \right] \quad (2.88)$$

The vacancy volume swept out by this movement is given by  $V_h = \lambda\lambda_2\lambda_3$ , while the volume swept out by the atom or molecule is  $V_m = \lambda_1\lambda_2\lambda_3$ , so that the strain rate becomes:

$$\dot{\epsilon} = 2 \frac{V_h}{V_m} \ell \sinh \left[ \frac{\sigma V_h}{2k_B T} \right] \quad (2.89)$$

Finally, applying Equation 2.79, the strain rate becomes:

$$\dot{\epsilon} = 2 \frac{V_h}{V_m} \frac{k_B T}{h} \exp \left[ -\frac{\Delta G^0}{k_B T} \right] \sinh \frac{\sigma V_h}{2k_B T} \quad (2.90)$$

It should be noted that this section describes only the simplest kind of viscous behaviour, controlled by a single, symmetrical barrier that is independent of both time

and the state of deformation. While never fully valid, it is a good approximation for most situations. Frequently the effect of time, stress, deformation, and the presence of multiple processes cannot be ignored. The modifications necessary to adequately describe some of these effects can be found in Ree and Eyring (1955) and Ree and Eyring (1958).

### 2.3.3 The Experimental Activation Energy and Volume

For a given deformation step, the rate constant can be described by either the apparent activation energy,  $\Delta E_i$ , measured via experiment, or the true activation energy,  $\Delta E_i^t$ , which accounts for the energy lost due to work being done on the system:

$$\dot{\epsilon}_i = A_i \exp \left[ -\frac{\Delta E_i}{k_B T} \right] = A_i \exp \left[ -\frac{\Delta E_i^t - W_i(\tau_a)}{k_B T} \right] = \dot{\epsilon}_i^t \exp \left[ \frac{W_i(\tau_a)}{k_B T} \right] \quad (2.91)$$

where  $\tau_a$  is the applied shear stress. The activation volume plays a similar role as the activation energy; the activation energy describes the necessary energy for a transformation, while the activation volume is the local volume required for molecular rearrangements. Both are characteristic of the bond breaking and atomic rearrangement process associated with the transition. These are important indicators of the atomic processes involved in the deformation. While both the activation energy and volume can theoretically be determined exactly from the relevant wave equation, it is rarely practical to do so. Instead, approximate theoretical and empirical results must be compared to discover the identity of the mechanism associated with the elementary process under investigation.

The experimental activation energy can be calculated from strain rate data gathered at different temperatures. Early studies in metals based on Becker (1925) gave

the following relation:

$$\text{Rate} = A_e \exp\left(\frac{\Delta E_e}{k_B T}\right) \quad (2.92)$$

Dorn (1957) and Seeger (1958) suggest that the strain rate equation of Orowan (1940) can be redefined as:

$$\dot{\gamma} = \alpha b \rho_m A_e \exp\left(-\frac{\Delta E_e}{k_B T}\right) \quad (2.93)$$

where  $\dot{\gamma}$  is the shear strain rate,  $\alpha$  is a geometric factor,  $\rho_m$  is the mobile dislocation density, and  $b$  is the Burgers vector, which represents the magnitude and direction of the lattice distortions produced during deformation. Over a temperature range where other variables remain constant, strain rates can then be compared via the standard Arrhenius shift function:

$$\frac{\dot{\gamma}_1}{\dot{\gamma}_2} \simeq \exp\left[-\frac{\Delta E_e}{k_B} \left(\frac{1}{T_1} - \frac{1}{T_2}\right)\right] \quad (2.94)$$

The experimental activation energy is thus proportional to the slope of a standard Arrhenius type plot:

$$\Delta E_e = -k_B \frac{d \ln \dot{\gamma}}{d(1/T)} \quad (2.95)$$

Variations in slope indicate a change in the rate controlling mechanism. Many materials undergo multiple changes in rate controlling mechanism as the temperature is increased. In general, the activation energy of solids is seen to increase as the melting temperature is approached, as shown in Figure 2.9. Note that a corresponding increase in the frequency factor is also observed, otherwise the deformation rate of solids would decrease due to the increase in activation energy; the opposite behaviour is observed experimentally.

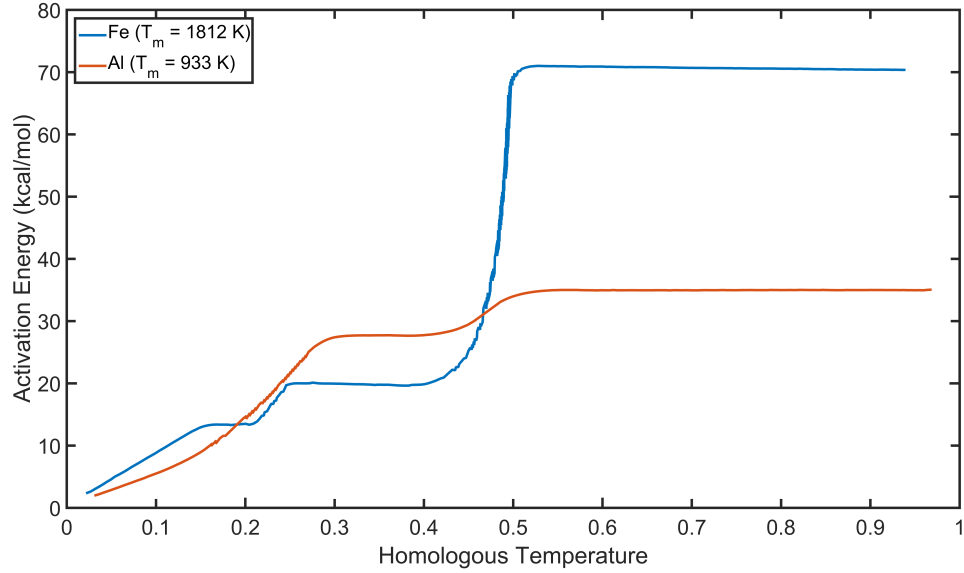


Figure 2.9: Change in activation energy with homologous temperature for iron and aluminium. Recreated from Krausz and Eyring (1975).

The correlation between the experimental and theoretical activation energies is quite complex in cases where the backward movement over the activation barrier cannot be ignored, as noted by Eyring (1936), Orowan (1936), and Kauzmann (1941). The simplest case, where temperatures are low and stresses are high, was examined by Krausz (1970) and Suzuki and Kojima (1966). Further refinements to the determination of the Arrhenius activation energy were made by Schoeck (1965), Osborne (1963), Hirsch and Warrington (1961), and Makin (1964).

While Equation 2.91 implies that the work supplied by the applied shear stress is independent of changes in temperature, Conrad and Wiedersich (1960) noted that since it is the effective shear stress,  $\tau_{\text{eff}}$ , given by:

$$\tau_{\text{eff}} = \tau_a - \tau_i \quad (2.96)$$

that produces the work necessary to overcome the energy barrier, and that the internal stress,  $\tau_i$ , is temperature dependent, so too are the work done and the apparent activation energy.

The theoretical activation volume,  $V^t$ , has been shown to be (Laidler, 1965):

$$V^t = -k_B T \left( \frac{\partial \ln \dot{\epsilon}}{\partial p} \right)_T \quad (2.97)$$

where  $p$  is the hydrostatic pressure. The activation volume is related to the amount of work necessary to change the volume of the system, and is generally negligible at low pressures; high pressures are necessary to measure sufficiently accurate values of the activation volume. Most measurements of activation volume are carried out by varying the applied shear stress. The experimental activation volume,  $V_e$ , is then:

$$V_e = -k_B T \left( \frac{d \ln \dot{\gamma}}{d \tau_a} \right)_{T,struct} \quad (2.98)$$

As per the earlier discussion of the activation energy, the measured activation volume must be related to the activation volume of the correct kinetics equation, which must then be compared to the theoretical value. Approximate solutions are once again used, as the theoretical calculation from the atomic configuration is impractical.

The key point is that experimental values gain significance only when correlated with true values from the kinetics equations. Validity must be established first, by comparing effects of observable experimental values to the predictions of the kinetics equation.

## 2.4 Fracture Mechanics

Fracture plays a significant role in the behaviour of an ice-structure interaction, generally acting as a limiting factor on the strength of ice. Here, we examine only the aspects of fracture mechanics that are related to the continuum behaviour of ice, particularly with regards to the development of microcracks.

Fracture can be generally categorized into three modes based on the relative movement of the upper and lower crack surfaces (Liebowitz, 1968). Different approaches to modelling fracture are employed depending upon both the material characteristics and crack mode. All approaches must deal with the difficulty of modelling the material behaviour near the crack tip stress singularity; a common shortcoming of elastic fracture theories is that they predict infinite stresses in this region, even at low stresses. In reality, this is not physically possible and energy near the crack tip must be dissipated through some local mechanism, such as creep or microstructural change.

### 2.4.1 Linear Elastic Fracture Mechanics

Griffith (1921) studied crack extension from the point of view of energy balance, avoiding the stress singularity at the crack tip. He compared the energy released from crack extension to the energy required for the creation of new surfaces. The analysis required that a strain energy potential,  $W$ , exists where:

$$\sigma_{ij} = \frac{\partial W}{\partial \epsilon_{ij}} \quad (2.99)$$

and that stress is either monotonically increasing or constant. Since cracks cannot support stress, we assume that there is a stress-free area above and below the crack

of height  $na$ , where  $a$  is half the crack length. The strain energy,  $U_\epsilon$ , released by the stress-free volume for a material under plane stress conditions is then:

$$U_\epsilon = \frac{n\sigma^2 a^2}{2E} \quad (2.100)$$

Griffith (1921) found that  $n \approx \pi$ . The strain energy release rate per increase in crack length is then:

$$\frac{dU_\epsilon}{da} = \frac{\pi\sigma^2 a}{E} \quad (2.101)$$

Crack growth occurs when the critical energy release rate is achieved; this may be expressed as:

$$\frac{dU_\epsilon}{da} \geq \frac{dW_s}{da} \quad (2.102)$$

where  $W_s = 4a\gamma_s$  is the surface energy and  $\gamma_s$  is the surface energy per unit area. Equation 2.102 then becomes:

$$\frac{\pi\sigma^2 a}{E} \geq 4\gamma_s \quad (2.103)$$

The plane strain expression differs only slightly, requiring the addition of a  $(1 - \nu)$  term in the denominator of the left-hand term, where  $\nu$  is the Poisson's ratio of the material. Early comparisons between the theoretical results of Griffith (1921) and the total work required to induce crack growth were generally found to differ by orders of magnitude, with glass and ice having the smallest difference, at factors between 5 and 10. This reflects the additional work being done in the region around the crack tip (sometimes referred to as the process zone) due to inelastic deformation within the process zone, such as plastic flow, viscoelastic creep, etc., as well as changes in the internal microstructure, generally referred to as damage.

All such processes consume additional energy, greatly exceeding the work required to produce new crack surfaces; these processes must be accounted for if accurate predictions of the critical energy release rate are to be made. For metals, which generally have well defined yield strength, Irwin (1958) developed a correction for the plastic deformation within the process zone based on the material yield strength. Other developments in the description of the process zone include the strip yield model of Dugdale (1960) and the work on crack tip cohesion by Barenblatt (1962), which were later tied to the theory of Griffith by Willis (1967) and shown to be equivalent during brittle fracture by Rice (1968); these developments are summarized in Kanninen and Popelar (1985).

The use of linear elastic fracture mechanics (LEFM) is appropriate when the process zone at the crack tip is much smaller than the crack size; such a material will exhibit brittle failure behaviour and can be treated as entirely elastic. The work of Dempsey (1996), Abdel-Tawab and Rodin (1995), and others has shown that LEFM may only be applied to the description of ice deformation when two conditions are met: 1) when brittle behaviour dominates, generally observed at high loading rates, and; 2) when samples are of sufficient size that heterogeneities can be treated as a continuum, with their effects distributed throughout the sample. At lower strain or loading rates, where creep and damage processes dominate, the more involved, time-dependent, methods developed by Schapery (1981) and others are required. This approach is based upon the J-Integral method of Cherepanov (1967) and Rice (1968); a basic review of the theory is provided here. For a recent investigation into the time-dependent fracture of ice, see Kavanagh et al. (2015) and Kavanagh (2018).

## 2.4.2 J-Integral Theory

J-Integral theory is used to calculate the energy release rate due to crack extension within a material subjected to a two-dimensional deformation field. The theory is based on the path-independent contour integrals of Eshelby (1956; 1951). In this case, the contour of interest for crack extension (Rice, 1968) is given by:

$$J_f = \int_{\Gamma} \left( W dy - T_n \frac{\partial u}{\partial x} ds \right) \quad (2.104)$$

where  $ds$  is an increment along the contour,  $T_n$  is the traction normal to  $ds$ ,  $u$  is the displacement, and  $W$  is the strain energy density, given by:

$$W(x, y) = \int_0^\epsilon \sigma_{ij} d\epsilon_{ij} \quad (2.105)$$

The integral makes use of Green's theorem, which notes that the double integral over a region bounded by a simply connected, closed contour with no singularities is equivalent to the line integral around the boundary. In other words, assuming there are no cracks within or on the contour (singularities) and no gaps within the region (simply connected), then:

$$\oint_C (Ldx + Mdy) = \iint_D \left( \frac{\partial M}{\partial x} - \frac{\partial L}{\partial y} \right) dxdy \quad (2.106)$$

where the path of integration for  $C$  is counter-clockwise, as illustrated in Figure 2.10.

The theoretical concept for the J-Integral was developed independently by Cherepanov (1967) and Rice (1968), who showed that an energetic (i.e. related to energy) contour path integral,  $J_f$ , was independent of the path around a crack; an example of such a path is provided in Figure 2.11. It was found that the J-Integral for a virtual crack extension,  $da$ , was equal to the change in potential energy,  $U_p$ :

$$J_f = -\frac{dU_p}{da} = \frac{\pi\sigma^2 a}{E} \quad (2.107)$$

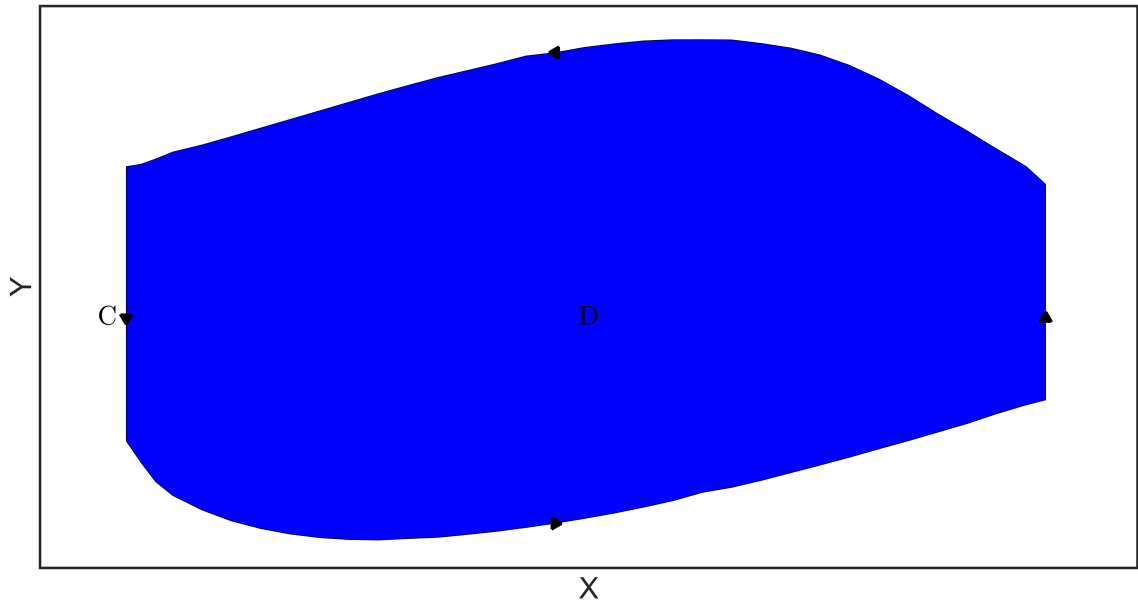


Figure 2.10: Illustration of Green's theorem.

Schapery (1981; 1984) extended the theory to larger process zones and used correspondence principles to obtain rigorous solutions to viscoelastic problems involving crack growth. The results were used to define a damage parameter,  $S$ , that accounts for the effect of distributed microcracks. To adequately describe this model, an introduction to damage mechanics is provided.

## 2.5 Damage Mechanics

An early exploration of damage and its effect on the material properties of a material was carried out by Kachanov (1958), who posited that the amount of damage within a material could be represented by a single scalar factor. Microcracks and voids were presented as a reduction in cross-sectional area, with the damage factor simply being

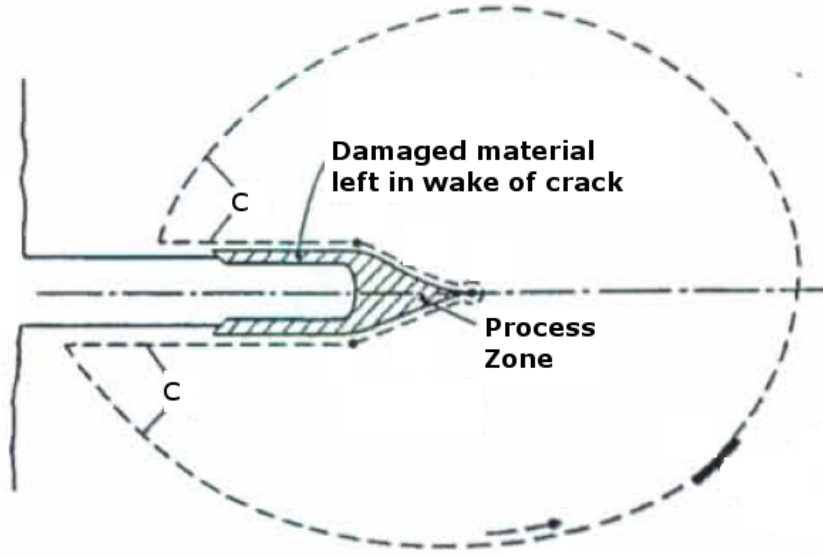


Figure 2.11: Illustration of the crack-tip process zone as defined by Schapery (1984).

the ratio of the damaged cross-section to the original, or total, cross section. This can be viewed as an increase in effective stress or a reduction in effective modulus:

$$D = \frac{A}{A_n} \quad (2.108)$$

$$\sigma_{eff} = \frac{\sigma_n}{1 - D} \quad (2.109)$$

$$E_{eff} = E_0(1 - D) \quad (2.110)$$

where  $D$  is the damage parameter,  $A_n$  and  $A$  are the nominal and damaged area,  $\sigma_n$  and  $\sigma_{eff}$  are the nominal and effective stress, and  $E_0$  and  $E_{eff}$  are the initial and effective elastic modulus.

Budiansky and O'Connell (1976) described the effect of microcracking on a material's elastic properties in three dimensions. Their approach was based on the strain

energy lost during crack nucleation in a brittle elastic material. The effect of crack interaction was included, but they did not account for the traction across crack surfaces, limiting its application to tensile regions. For an isotropic array of flat, circular cracks, they found that the damage parameter was related to the crack density,  $N$ , by  $D = a^3 N$ , where  $a$  is the crack radius (or half crack length).

Traction across crack surfaces cannot be ignored under compression, which effectively reduces the accumulation of microcracks by both closing existing cracks and reducing crack nucleation. Horii and Nemat-Nasser (1983) developed a general 2D solution for a compressive state of stress where plane strain conditions were enforced. The approach of Kachanov (1993) is applicable to both two and three dimensional configurations; assuming an elastic solid with  $N$  cracks per unit volume with an applied stress,  $\sigma_a$ , at the remote boundary, the problem becomes one of crack surfaces loaded with tractions of  $T = n_i \sigma_a$  and stresses vanishing at infinity. Under these conditions, Kachanov (1993) found that the effective moduli for non-interacting cracks with a random isotropic distribution becomes:

$$\frac{E_{eff}}{E_0} = \frac{1}{1 + C_1 N} \quad (2.111)$$

$$\frac{\nu_{eff}}{\nu_0} = \frac{1 + C_3 N}{1 + C_1 N} \quad (2.112)$$

where  $C_1$  and  $C_3$  are constants dependent upon the initial Poisson's ratio,  $\nu_0$ . The remaining moduli can be derived from the above equations through the basic equations for the shear and bulk moduli. These forms have been shown to provide accurate results for both low and high crack densities; crack interactions can, in general, be safely ignored.

Schaperly (1981; 1984; 1990; 1991) developed a continuum model based on J-

Integral theory, successfully estimating the energy flux into the process zone at the crack-tip (idealized previously in Figure 2.11) and using it to define a damage parameter,  $S$ , for microcracking.

The viscoelastic crack-growth analysis of Schapery begins with several assumptions: first, proportional loading is assumed; the stress,  $\sigma_{ij}$  at any point is given by:

$$\sigma_{ij} = \sigma \sigma'_{ij} \quad (2.113)$$

where  $\sigma'_{ij}$  is a constant tensor and  $\sigma$  is a scaling parameter. Power law material behaviour is also assumed, which produces a complementary strain energy,  $W'$ , of:

$$W'(\sigma \sigma'_{ij}) = \sigma^{r+1} W'(\sigma'_{ij}) \quad (2.114)$$

Schapery (1981; 1984) proved that not only could the J-Integral be defined in terms of the complementary strain energy function by:

$$J = \frac{\partial W'}{\partial a} \quad (2.115)$$

but also that a power law relationship existed between the J-Integral and crack-growth rate,  $\dot{a}$ , for non-linear viscoelastic materials that undergo power law stress-strain behaviour. Similar to the results observed experimentally by Atkins and Mai (1985) and others, this is usually expressed as:

$$\dot{a} = c_1 J^k \quad (2.116)$$

where  $c_1$  and  $k$  are constants. Combined, these results give a crack-growth rate of:

$$\dot{a} = c_1 \sigma^{k(r+1)} \left( \frac{\partial W'}{\partial a} \right)^k \quad (2.117)$$

where  $\partial W'/\partial a$  can be shown (Schapery, 1984) to be approximately equal to  $a$  for penny-shaped (flat, circular) cracks of the same radius. Equation 2.117 can then be rewritten in the form:

$$\dot{a} = c_1 (c_2 a)^k \sigma^q \quad (2.118)$$

where  $c_2$  is the proportionality constant and  $q = k(r + 1)$ . Integration yields:

$$\frac{a}{a_0} = \frac{1}{\left[1 - (k - 1) (c_2 a_0)^{k-1} S\right]^{1/(k-1)}} \quad (2.119)$$

where  $a_0$  is the initial crack length and  $S$  is the integral of the stress history:

$$S = \int_0^t c_1 c_2 \sigma^q d\tau \quad (2.120)$$

which is hereafter referred to as the Schapery damage measure. Assuming that each crack produces only a small decrease in strain energy (in other words, that a large spall does not occur) and that the stress history of the sample is known, then the cumulative damage from distributed microcracking can be estimated and its effect on viscoelastic deformation calculated. Schapery accounted for this total damage through the definition of a pseudostrain, discussed previously in Section 2.1.3, and a damage enhancement factor,  $g(S)$ , given by:

$$g(S) = e^{\lambda S} \quad (2.121)$$

where  $\lambda$  is also a positive constant. While the above method does not provide any insight into “damage” of other forms, such as dynamic recrystallization or pressure melting within ice, the formulation has been successfully extended to these conditions through the addition of additional damage parameters as required under such circumstances (Jordaan, 2001).

## 2.6 Properties of Ice

Snow and ice are familiar phenomena to those of us living within the Arctic and Northern Temperate Zones. Many questions remain to be settled about these common materials, particularly with regards to their interactions with ships and offshore structures. The study of ice is thus scientifically interesting and a matter of economic importance. A review of the relevant properties of water, in both liquid and solid form, as well as the literature regarding ice behaviour, is provided in the following sections.

### 2.6.1 Basic Properties

The properties of water have been used as a standard with which other materials are compared to due to its ubiquity; an unhappy coincidence given water's numerous anomalous properties. Indeed, it has been argued that without the anomalous properties of water that life as we know it would not be possible (Podgornik, 2011).

For our purposes, the vital property of water is its expansion upon freezing by a factor of almost 10 %; while this is not a unique property, the sheer extent of the expansion that occurs during the transition from water to ice is exceptional. The additional fact that fresh water has a maximum density at 4°C is quite extraordinary. The thermal properties of water are also anomalous, with an abnormally high specific heat and latent heat, which minimizes temperature variations in regions with abundant water and greatly affects climates around the world.

The majority of the world's water is contained within its oceans, which contain enormous quantities of salts. Fortunately, the composition of sea water is sufficiently

uniform to describe with a single parameter, the salinity,  $S$ , defined as the ratio of solid material to sea water. The salinity is usually reported in parts per thousand, ‰, with a value of  $S = 35‰$  being typical for ocean water.

The freezing of such solutions is a complicated problem. The freezing point and density inversion temperature are essentially linear functions of salinity, with the density inversion temperature disappearing at salinities greater than  $S = 24.7‰$ , which corresponds to a freezing point of  $-1.3\text{ }^{\circ}\text{C}$ . During the freezing process the majority of salts are rejected from the newly formed crystal lattice, leading to the formation of nearly pure ice. The freezing of salt water and fresh water can then be thought of to differ in degree but not in kind, though it must be noted that the expulsion of impurities during the freezing process leads an increase in salinity in the nearby sea water, which can prevent further freezing. These are known as brine pockets, which reduce sea ice strength through their inability to support stress.

Due to the density inversion temperature, water and ice produce interesting circulation behaviour. Cooled water sinks until the entire body of water reaches a uniform temperature at maximum density. Further cooling leads to a reduction in density, trapping the top layer of water and leading to the formation of a layer of ice. This layer of ice acts as heat insulator, reducing heat transfer to the water below. A considerable temperature gradient develops, from the ambient temperature at the surface of the ice sheet to the freezing point of water at the bottom. The water beneath the ice develops a separate temperature gradient, with the temperature increasing from the freezing point near the ice layer to the density inversion temperature at greater depths. This is referred to as a thermocline, the depth of which is dependent upon environmental conditions. Water and air currents modify this behaviour by varying

degrees, but the basic process remains the same.

The formation of ice around the world varies due to variations in climate. The primary division is between sea ice and fresh-water ice. The ice of interest in this work is fresh-water, granular ice, a form of polycrystalline ice with randomly oriented grains. This form of ice can be easily grown in the laboratory from seed ice crystals of a desired grain size and can be treated as a statistically isotropic material; see Section 3.5.1 for verification via experimental results. The results observed from experiments with granular ice can then be extrapolated out to other forms of ice based on saline content, age, or type of ice (iceberg, ice island, first year sea-ice, multi-year sea ice, etc.). See Pounder et al. (1965), Sanderson (1988), and others for an in-depth discussion of the numerous forms of naturally occurring ice and their properties.

## 2.6.2 Hydrogen Bonding and Crystal Structure

Almost all naturally occurring ice, as discussed throughout this text, is made up the hexagonal crystal form generally referred to as ice- $I_h$ , with the exception of only a small amount of the cubic form, ice- $I_c$ , that is occasionally present in the upper atmosphere. Other forms of solid  $H_2O$  are possible at very high pressures and very low temperatures, but these conditions do not occur naturally, at least terrestrially. These other solid forms require pressures greater than 2000 atm or temperatures of less than  $-200\text{ }^\circ\text{C}$ ; the largest ice sheet in the world, at over 4000 m, exerts a maximum pressure of only 350 atm, while the coldest surface temperature ever measured on earth was  $-89.2\text{ }^\circ\text{C}$ .

The forces which bind atoms into molecules, and ultimately into solid and liquid

aggregates, arise due to the internal structures of the atoms involved. A full review of the theories behind these forces would require a quantum mechanical treatment; a simplified discussion will be presented here (Pounder et al., 1965).

The binding forces holding a water molecule together are primarily of the covalent type; the hydrogen atoms “share” their electrons with the oxygen atom, forming a closed shell. The hydrogen ions form an angle of  $104.5^\circ$  with the central oxygen ion at a distance of approximately  $0.96 \text{ \AA}$ .

This is not an unusual atomic structure. The anomalous properties of water arise instead from the additional binding force provided by hydrogen bonding; as the separation between water molecules decreases, it becomes possible for the positive axis of hydrogen ions to align with the negative charge concentrations of the oxygen molecules, providing a small electrostatic attraction. The space between oxygen atoms containing a hydrogen bond is only  $3.10 \text{ \AA}$ , a little over three times the covalent bond length. While possible, it is highly unlikely for water molecules to form more than one hydrogen bond at temperatures above the freezing point.

Liquid water forms a random hydrogen-bonded network, with molecules having an ice-like local environment but lacking long-range periodic order. Near freezing, at temperatures below the inversion point, the number of hydrogen bonds per molecule approaches four, the same as in ice, and hence the liquid becomes less dense. The transition to ice forces the molecules into a rigid tetrahedral arrangement of oxygen atoms, resulting in a very open lattice structure. This explains the drop in density between water and ice; melting breaks some of the hydrogen bonds, allowing water molecules to pack more closely, increasing density.

While seemingly minor, these anomalous properties lead to very interesting side-

effects within the context of the mechanical behaviour of ice.

### **2.6.3 Mechanical Behaviour**

Investigators have examined the properties of ice under a wide range of conditions. Key parameters include temperature, confining pressure, deviatoric stress, and strain rate. Each follows a similar trend in behaviour while the others are held constant, from brittle to ductile failure (or vice versa). Under uniaxial stress or strain conditions, the differences in material behaviour are clear; at low strain rates ice fails in a ductile manner, reaching a peak stress and then decaying to a plateau and eventually failing. Low deviatoric stresses cause similar, though inverted, behaviour; a minimum strain rate is reached followed by an increase to a plateau. As strain rate/deviatoric stress increases the ice transitions to brittle behaviour, where failure occurs immediately upon reaching peak stress/minimum strain, as seen in Figure 2.12. The differences between ductile and brittle behaviour are more difficult to discern directly from the resulting stress or deformation history for ice under states of triaxial stress. Instead, the underlying microstructural changes within the ice must be examined to determine the failure regime (Melanson et al., 1999a; Mizuno, 1998; Rist et al., 1988).

The reverse trend is observed for temperature; at low temperatures ice is brittle and transitions to ductile behaviour as the melting temperature is approached (Durham et al., 1983). The same trend is observed for confining pressure, due to the onset of pressure melting (Meglis et al., 1999). The brittle-ductile transition has a notable effect upon the strength of ice, and must be accounted for during an ice-structure interaction.

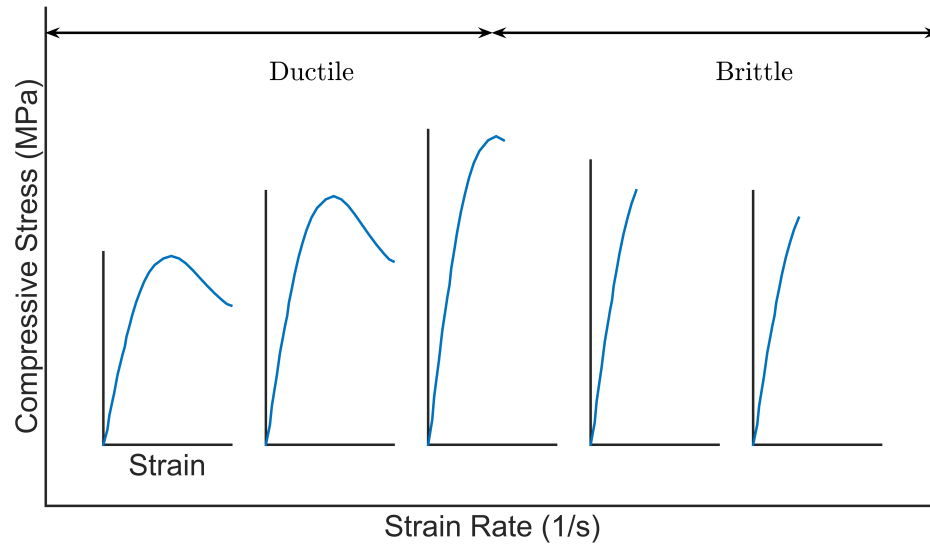


Figure 2.12: Transition from ductile to brittle behaviour with increasing strain rate. (Keegan et al., 2013)

### 2.6.4 Ice Strength

The practical purpose of ice testing is to determine the strength of ice during an interaction, which will provide a limit to the amount of force that can be transferred to the structure; ice will fail far in advance of the materials commonly used in the construction of offshore ships and structures. Simonson et al. (1974) examined the strength of cylindrical ice samples up to 0.2 GPa hydrostatic pressure at a temperature of  $-10^{\circ}\text{C}$ . They found that the strength of ice increased with increasing strain rate and decreased with increasing hydrostatic pressure. The application of pure hydrostatic pressure (no deviator) was found to reduce the porosity of ice, decrease the elastic modulus, and induce melting at approximately 100 MPa, which is consistent with the pressure-melting curve of Nordell (1990).

Jones (1978; 1982) and Jones and Chew (1983) studied the compressive strength of cylindrical ice samples up to confining pressures of 85 MPa and 60 MPa for constant strain rate and deviatoric stress, respectively. In both test series, they found that ice strength increased to a maximum between confining pressures of 20 and 30 MPa, then decreased. This behaviour was more pronounced at higher strain rates, with lower rates showing only small changes in strength. It is unclear why this behaviour was not observed in the results of Simonson et al. (1974), which examined ice strength at confining pressures of up to 200 MPa, though later work confirms the results of Jones and Chew (Barrette and Jordaan, 2003; Mizuno, 1998; Nadreau and Michel, 1986a;b).

Jones also noted a change in ice appearance between low and high confining pressures tests; at low pressures, ice became cracked and opaque after testing, while high pressure tests produced ice that was free of cracking and, in some cases, clearer than prior to testing due to a reduction in air content. Further study by Jones and Chew found that the activation volume of ice changed with increasing hydrostatic pressure, implying that more than one deformation mechanism was involved. To confirm this, an examination of the microstructure of ice post-deformation is required.

### **2.6.5 Microstructure**

Ice undergoes significant changes in microstructure when deformed. The type and extent of this microstructural change is primarily dependent upon the applied stress conditions and the temperature of the ice. Changes in microstructural behaviour have been observed in numerous indentation experiments, both with increasing loading

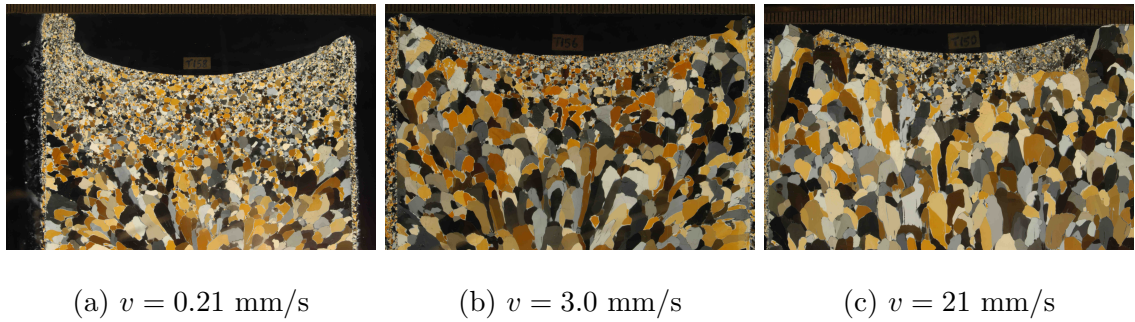
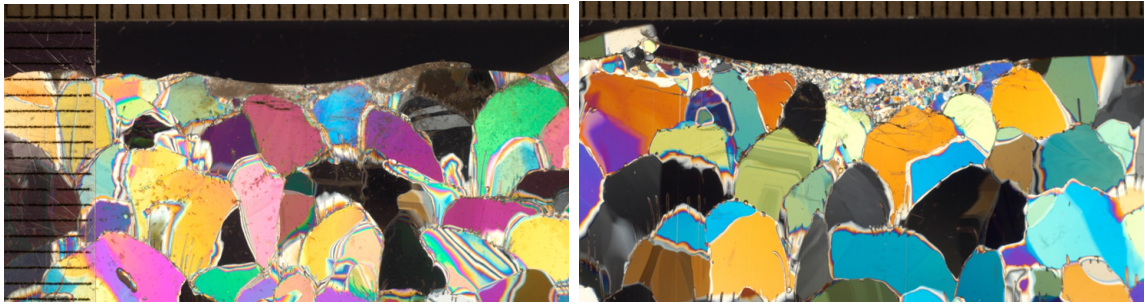


Figure 2.13: Thin sections of ice samples at ice-indentor interface, photographed between crossed polarizing film with back lighting. Varying levels of recrystallization near the interface are evident. Spherical end-cap indenter with a 70 mm diameter was used for all tests. Indentation proceeded to a depth of 12 mm for Figure c), 15 mm for the others.

rates (or velocity) (Turner et al., 2015), and with increasing temperature (Browne, 2012). Low speed creep tests produce a widespread damage zone which transitions to a thin damage layer of mixed composition (a recrystallized zone at the centre, microcracking at the edges) as the loading rate required to induce cyclic loading is reached. This layer becomes more dominated by microcracking damage with further increases in velocity, as illustrated in Figure 2.13.

Similarly, low temperature indentation experiments produce significantly more microcracking, transitioning to a thicker, more recrystallized layer in the central region at higher temperatures, as seen in Figure 2.14. It should be noted that some investigators (Gagnon, 2008) mistakenly label the central region of the *hpz* as “intact” ice. This is highly misleading, as the ice in this region has been found to deform at rates several orders of magnitude larger than that observed for virgin, undamaged ice.

Rist et al. (1988) observed changes in microstructure in cylindrical samples of



(a)  $T = -15^{\circ}C$ .

(b)  $T = -5^{\circ}C$ .

Figure 2.14: Thin sections of ice samples at ice-indentor interface, photographed between crossed polarizing film with back lighting. Varying levels of microcracking and recrystallization are evident. Results obtained from the indentation test series of Browne et al. (2013)

polycrystalline ice during constant strain rate tests with confining pressures up to 30 MPa. Both microcracking and recrystallization were observed, with recrystallization dominating at lower rates, then transitioning to microcracking at higher rates. Stone et al. (1997) discovered a similar trend with increasing confining pressure, observing that the application of a confining pressure suppressed microcracking in favour of recrystallization. These results were confirmed and greatly expanded by the work of Melanson et al. (1999a) and Meglis et al. (1999).

Melanson et al. (1999a) examined the microstructural response of cylindrical samples of polycrystalline ice for a constant confining pressure of 20 MPa at two different strain rates:  $10^{-4} \text{ s}^{-1}$  and  $10^{-2} \text{ s}^{-1}$ . By stopping tests at increasing levels of total axial strain and examining the resulting thin sections they were able to investigate the progress of microstructural change during deformation. Their results confirmed those of Rist et al. (1988); ice was found to transition from recrystallization at low

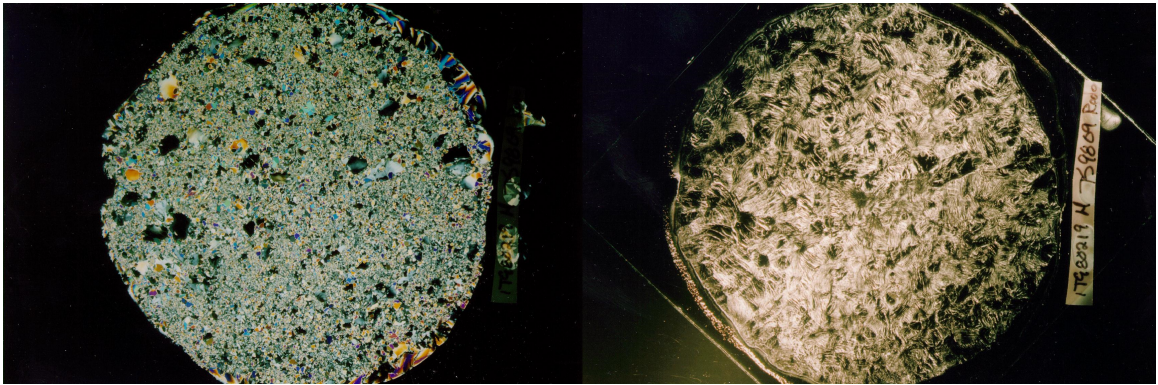
rates to microcracking at high. They also observed a reduction in grain size in all tests where the peak stress was reached; no change in microstructure was observed prior to this point. This corresponds to a strain of approximately 1 %. The grain size was found to stabilize after approximately 10 % strain to an average size that was consistent across all tests.

Meglis et al. (1999) examined the response of cylindrical samples of cylindrical ice to confining pressures ranging from 5 to 60 MPa and deviatoric stresses up to 25 MPa. They confirmed the results of Stone et al. (1997); microcracking dominates at low confining pressures, is suppressed as confining pressure increases, and transitions to dynamic recrystallization with further increases in pressure, as seen in Figures 2.15.

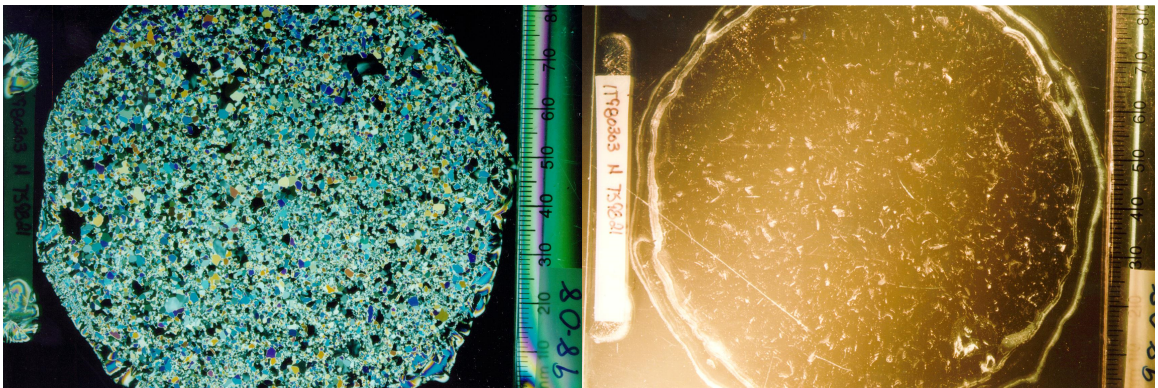
Interestingly, the reduction in grain size appears to depend more on total axial strain than the applied confining pressure; while higher confining pressures initially produce smaller grains at low strains, grain size appears to plateau at similar levels for true strains greater than approximately 30 %. This contradicts the results of Kuon and Jonas (1973) for polycrystalline ice during extrusion, who found that the grain size decreased with increasing strain rate and decreasing temperature, or, in other words, that brittle deformation led to a smaller average grain size. This contradiction may be due to differences in testing method.

### **2.6.6 Strain Localization**

Rist et al. (1988) first studied the variation of failure mode with confinement. They found that axial splitting occurred at low confining pressures, as expected for nearly uniaxial conditions. As confining pressure was increased, ice began failing along  $45^\circ$



(a)  $P_c = 6$  MPa



(b)  $P_c = 51$  MPa

Figure 2.15: Thin sections of triaxial ice samples, photographed between crossed polarizing film (left) and side lighting (right), respectively. Applied von Mises stress was 12 MPa in all cases.

shear faults, while only softening occurred under still higher confining pressures. Similar results were found by Sammonds and Murrell (1989) and Sammonds et al. (1989; 1998). The faulting behaviour of ice was further examined by Barrette and Jordaan (2001) and Li et al. (2003; 2005) for columnar and granular ice respectively. Both applied significantly higher confining pressures. Both observed that shear faulting occurred at an angle of  $45^\circ$ . Barrette and Jordaan found that the fault plane consisted

of a highly microcracked (or pulverized) layer at low confining pressures while the bulk of the columnar ice remained unchanged. At higher confining pressures, recrystallization occurred throughout the entire specimen but was greatly enhanced near the fault plane. Li et al. (2005) observed that faulting, here termed strain localization, was generally confined to hydrostatic pressures less than 10 MPa and greater than 50 MPa, as well as temperatures of  $-10^{\circ}\text{C}$  or higher. They also studied iceberg ice under the same conditions and found that, while strain localization most often occurred under the same restrictions, some samples faulted at medium confining pressures and low temperatures. They concluded that strain localization is largely dependent upon initial flaws in the ice. Jordaan and Barrette (2014) discuss the relevance of this behaviour with regards to the load oscillations commonly observed during ice-structure interactions. They conclude that strain localization is practically guaranteed to occur under the stress conditions observed within a *hpz*. The various types of faulting behaviour are summarized in Figure 2.16.

Blair (1987) was the first to note the effect strain localization had on ice strength. He compared the results of uniaxial and triaxial tests for first-year sea ice at different strain rates. Strength was found to dramatically increase with strain rate during triaxial testing but decrease slightly during uniaxial testing. At high strain rates, ice strength at failure varied from 10 MPa to over 200 MPa, with the low strength samples faulting along well-defined,  $45^{\circ}$  planes with little deformation and the high strength samples deforming uniformly. A later analysis by Barrette (2014) showed a similar trend with increasing hydrostatic pressure; the strength of samples where strain localization occurred decreased dramatically while the strength of other samples increased. Samples which did not fail via strain localization were said to have

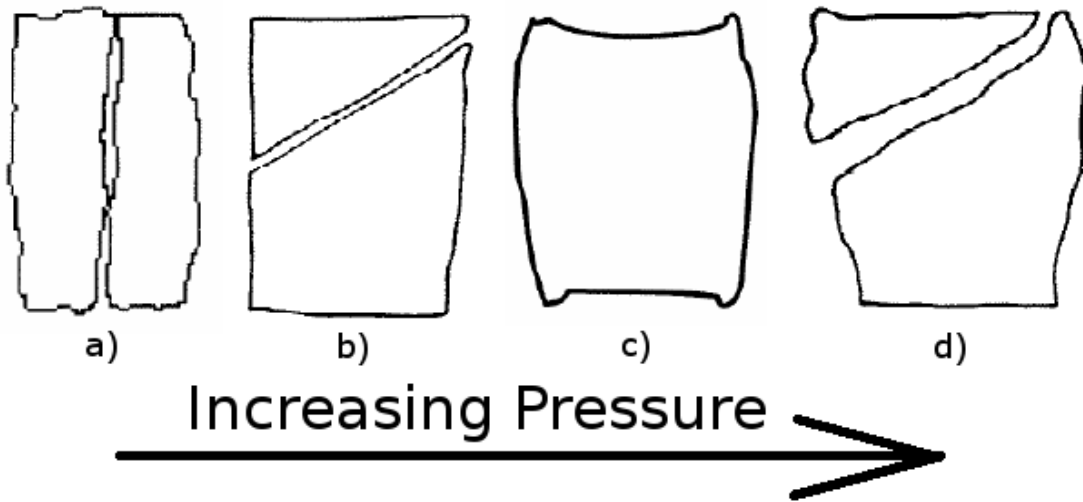


Figure 2.16: Failure behaviour of ice under triaxial compression with increasing confining pressure. From left to right we have: (a) axial splitting at little to no confining pressure; (b)  $45^\circ$  fault at low confining pressures. Damage is localized in a heavily microcracked failure plane; (c) Softening only. Possible at all confining pressures, but most common at medium pressures; (d)  $45^\circ$  fault at high confining pressures. Recrystallization present throughout sample, though highly localized in fault plane.

undergone uniform grain refinement (UGR) and could be up to an order of magnitude stronger.

It is interesting to contrast these seemingly similar results. Blair (1987) noted the drastic difference in strength while increasing the applied strain rate, or, in other words, while transitioning to more brittle-like behaviour. Barrette (2014), on the other hand, noted the strength difference while transitioning from brittle to ductile behaviour, though Li et al. (2005) had earlier noted that strain localization also occurs at low confining pressures under brittle conditions. The exact conditions required for,

as well as the outcome of, strain localization requires further attention.

### 2.6.7 Pressure-Temperature Effects

One of the essential, and almost unique, properties of ice (shared by some elements and compounds that form spacious crystal lattices with tetrahedral coordination, such as Be, Mg, Ca, Sr, Ba (Wax et al., 2001), SiO<sub>2</sub>, P, Se, Ce, Cs, Rb, Co, and Ge (Debenedetti, 1996)) is that the density of its solid phase is less than the density of its liquid phase, which is most easily seen in the fact that ice floats on water.

An important consequence of this property, in terms of the analysis of ice-structure interactions, is the process of pressure melting; as the applied hydrostatic pressure increases, the melting point of ice actually decreases. This is represented by the Clausius–Clapeyron relation:

$$\frac{dT}{T} = \frac{(v_l - v_s)}{L_f} dP \quad (2.122)$$

where  $T$  is the absolute temperature,  $L_f$  is the latent heat of fusion,  $P$  is the pressure, and  $v_l$  and  $v_s$  are the specific volume of the liquid and solid phases, respectively, which are simply the inverted densities. Nordell (1990) determined the pressure required for melting at temperatures as low as -22 °C, as recreated in Figure 2.17. At temperatures lower than -22 °C the trend reverses due to the transition to other forms of crystalline ice, all of which have higher densities than water. Note that the combinations of pressure and temperature required to produce these high density forms of ice do not occur terrestrially.

In this way, changes in pressure can be considered equivalent to changes in temperature, and vice-versa. One of the earliest triaxial tests on ice was performed by

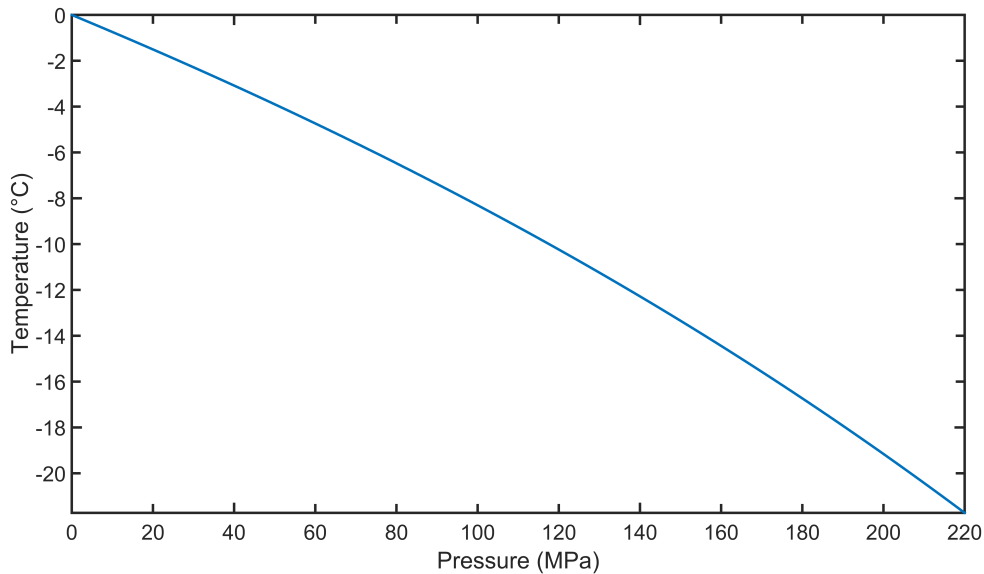


Figure 2.17: Pressure melting curve. The pressure required to induce melting decreases as the temperature increases. Recreated from Nordell (1990).

Rigsby (1958) and confirmed that the effect of hydrostatic pressure was equivalent to an increase in temperature for monocrystalline ice; the creep behaviour at  $-3\text{ }^{\circ}\text{C}$  and 1 atm (0.1 MPa) of pressure was shown to be practically identical to the behaviour at  $-5\text{ }^{\circ}\text{C}$  and 270 atm (27 MPa), a pressure which Nordell (1990) had shown decreased the melting point of ice to  $-2\text{ }^{\circ}\text{C}$ . Thus, the two tests occurred at an identical ‘distance’ from the melting point, and also at similar homologous temperatures,  $T_h$ , which is defined as the ratio between the current temperature,  $T$ , of a material and its melting point,  $T_m$ :

$$T_h = \frac{T}{T_m} \quad (2.123)$$

The homologous temperatures of Rigsby’s tests were thus quite similar, at 0.9890 and 0.9889 respectively.

Haefeli et al. (1968) proved that this pressure-temperature equivalence did not strictly hold for polycrystalline ice. They observed that an increase in hydrostatic pressure combined with a corresponding drop in temperature produced a slightly lower strain rate. This must be attributed to the presence of grain boundaries within polycrystalline ice, and, more specifically, the stress concentrations that accompany them; Raj and Ashby (1971) theorized that the applied shear stress at a grain boundary can be magnified by a factor of five or more, depending on the geometry of the boundary. It has since been shown that the presence of grain boundaries greatly affect the behaviour of ice (Barnes et al., 1971; Mae and Azuma, 1989; Mizuno, 1992).

It is clear that the behaviour of ice is highly dependent upon the ambient temperature. This has motivated the study of the temperature-dependence of ice during ice-structure interactions. Several studies of the surface temperature of ice during indentation testing have been undertaken (Gagnon, 1994b; Gagnon and Sinha, 1991; Turner et al., 2015). They show that temperature near the indentation surface can increase by several degrees, increasing the probability of pressure melting.

The observed temperature fluctuations can also be used to confirm changes in the deformation regime; low speed creep tests produce temperature changes that are smaller than those observed at higher speeds. The average temperature change increases dramatically as cyclic loading conditions begin to dominate at higher speeds; the “medium” speed tests of Turner et al. (2015) correspond to a regime dominated by cyclic loading and consistently measured an average temperature change of 4.49 degrees over a range of speeds and maximum loads. It is interesting to note that a temperature increase of this magnitude would reduce the pressure required for melting from approximately 110 MPa (at  $T = -10^{\circ}\text{C}$ ) to approximately 55 MPa.

With a maximum contact area of  $4000 \text{ mm}^2$  the indenter used produced an average nominal pressure at maximum load of 26.7 MPa. Given that higher than average pressures are present in the *hpz* it seems likely that pressure melting occurred under these conditions.

Turner et al. (2015) also showed that the temperature traces provided by the thermocouples during indentation could be used to infer changes in the contact conditions; initial rapid increases in temperature were noted where contact with each thermocouple was made, and, more interestingly, some load drops could be correlated with large temperature drops in one or more thermocouples followed by an increase in others. This is likely due to a shift in *hpz* position after spalling, leading to the loss of contact with some thermocouples and a redistribution of pressure on others. Heat transfer at the centre of a *hpz* also has some interesting characteristics, with many tests displaying a similar pattern of a rapid increase in temperature followed by a plateau that lasts until some later layer failure. A notable deviation from this behaviour can occur prior to a failure event; a significant temperature drop can be observed leading up to some load drops. These are the moments when pressure in the *hpz* is largest, making it likely that pressure melting is involved. While the data is inconclusive, it seems likely that these thermocouples happened to be within a very short range of the point of failure; with more information, it may be possible to correlate failure events with surface temperature fluctuations.

Finally, the results show that, under certain conditions, the loading and temperature traces oscillate inversely to one another, as seen in Figure 2.18. This can be explained by pressure melting within the ice; as the load increases, ice melts at internal grain boundaries, drawing heat away from the surface. When the load is removed,

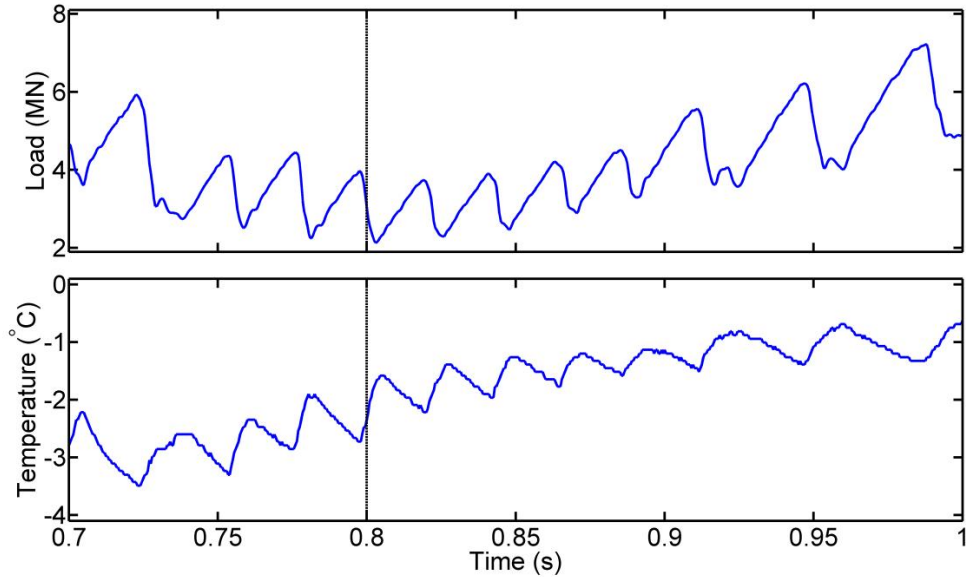


Figure 2.18: Load and temperature results from indentation experiments at Hobson's Choice ice island. Temperature decreases as load increases, and vice-versa. Recreated from Gagnon and Sinha (1991)

the ice recrystallizes and heat is transferred back to the surface. The amount of melt required to cause this temperature drop can be estimated from basic thermodynamic relations:

$$m_i c_i \Delta T = m_w L_f \quad (2.124)$$

where  $m_{i/w}$  and  $c_{i/w}$  are the mass and specific heat of ice and water, respectively, and  $\Delta T$  is the temperature change.

Rearranging in terms of the volume of melt water,  $V_w$ , per volume of ice,  $V_{ice}$ , gives:

$$\frac{V_w}{V_{ice}} = \frac{\rho_i c_i \Delta T}{\rho_w L_f} \quad (2.125)$$

where  $\rho_{i/w}$  are the densities of ice and water, respectively. This produces a melt volume of approximately 0.5 % for temperature drops of 1 °C, as seen in Figure 2.18.

This basic model makes several assumptions, including:

1. That the density of ice remains constant. Not only does the density change with temperature, but also with damage. The reduction in ice density also depends upon position within the *hpz*; ice near the centre has the same density as undamaged ice, while ice near the edge is less dense by  $\approx 0.06 \text{ g/cm}^3$  (Meaney et al., 1991). These changes in density have relatively little effect on the melt volume results, for two reasons:
  - (a) The change in ice density from 0 to -25 °C, the range over which standard pressure-melting can be considered to hold, is minor, amounting to only  $3.4 \text{ kg/m}^3$ , less than 0.4 % of the average density.
  - (b) Pressure-melting is believed to occur primarily within the centre of the *hpz*, where no change in density due to damage is known to occur.
2. That heat transfer within the layer is uniform. Experiments have shown that the surface temperature varies across a *hpz*. Pressure melting must therefore be confined to a relatively small region within the layer. It is interesting to note that Equation 2.125 describes an arbitrary volume and can be used to model a region of any size; with sufficient information it should be possible to extend the analysis to the correct regions within the *hpz*.
3. That the mass of ice and water remain constant. The mass of water is initially zero and increases as pressure melting continues, causing an equal drop in ice

mass. Heat can then be drawn from this newly created melt water during later occurrences of pressure melting. Additionally, mass is often lost to spalling events during ice-structure interactions. These effects are negligible over the course of a single load cycle.

Other estimates agree that the internal melt volume amounts to less than 1 % of the layer volume (Jordaan, 2001; Jordaan et al., 2005; 1999). It should be noted that the mechanism behind the temperature changes observed during indentation experiments are disputed; Gagnon (1994a; 2008) posits that viscous heating produced by a layer of melt water at the ice-indentor interface is the root cause of the observed temperature increases. The supposed proof of the existence of a layer of melt water comes from conductance measurements at the ice-indentor interface; no attempt is made to isolate this increase in conductance due to melt water thickness from the standard increase in conductance observed from any solid under pressure. Indeed, Gagnon (1994a) notes an immediate increase in conductance at contact, at pressures well below those necessary to induce pressure melting, indicating that some, if not all, of the observed changes in conductance may be due simply to fluctuations in pressure.

The viscous heating hypothesis also conflicts with numerous pieces of experimental evidence, including:

1. The temperature plateaus observed in Turner et al. (2015); a continuous viscous flow of melt water would produce a corresponding continuous increase in temperature.
2. The cyclic temperature drops with sawtooth loading observed in Gagnon and

Sinha (1991) and Turner et al. (2015); assuming viscous flow, an increase in load should lead to a corresponding increase in temperature at the ice-indentor interface, not a decrease as is observed.

Finally, from a theoretical standpoint, the energy dissipated via the viscous flow of water is simply insufficient to produce significant heating; the energy balance equation for viscous heating (in one dimension for simplicity) would be:

$$\rho c \frac{\partial T}{\partial t} = \mu \left( \frac{\partial v}{\partial y} \right)^2 \quad (2.126)$$

where  $\rho$ ,  $c$ , and  $\mu$  are the density, specific heat capacity, and dynamic viscosity of water, respectively, while  $T$ ,  $t$ ,  $v$ , and  $y$  represent the temperature, time, velocity, and layer thickness, respectively. Since water is a low viscosity, high specific heat capacity liquid, the velocity gradient necessary to produce significant viscous heating is truly excessive, on the order  $10^6 \text{ s}^{-1}$  for a single temperature cycle.

### 2.6.8 Activation Energy

As described in Section 2.3, the activation energy is the minimum amount of energy necessary for a reaction or process to overcome the corresponding energy barrier. Originally developed to describe the temperature dependence of chemical reaction rates, the description has been shown to extend to many other thermally activated processes, such as the creep strain rates of metals (Zener and Hollomon, 1944) and ice (Glen, 1955). In effect, the strain rates are controlled by an underlying thermally activated process, such as dislocation glide.

In general, the strain rate,  $\dot{\epsilon}$ , produced by an applied stress can be represented by

an Arrhenius formulation:

$$\dot{\epsilon} = A_f e^{\frac{-Q}{R_g T}} \quad (2.127)$$

where  $A_f$  is the pre-exponential or frequency factor. The activation energy of ice has been examined under many conditions. Glen (1955) demonstrated that, for uniaxial compressive stresses between 0.1 MPa and 1 MPa and temperatures between 260.15 K and 273.15 K, the creep of ice followed an Arrhenius rate equation of the form:

$$\dot{\epsilon}_{min} = A_f \sigma^n e^{-\frac{Q}{R_g T}} \quad (2.128)$$

where  $\dot{\epsilon}_{min}$  is the minimum strain rate,  $\sigma$  is the uniaxial stress, and  $n$  is an exponential factor of approximately 3.2. He found that, for these conditions,  $A_f$  and  $Q$  had values of  $7 \times 10^{24}$  bar <sup>$n$</sup> /years ( $2 \times 10^{17}$  bar <sup>$n$</sup> /s) and 134 J/mol, respectively. These experiments also demonstrated that creep results at different temperatures could be compared using a shift function; the stress dependence of Equation 2.128 can be eliminated by taking the ratio of two strain rates, assuming that both the activation energy and the pre-exponential term remain constant:

$$\dot{\epsilon}(T_1) = \dot{\epsilon}(T_2) \exp \left[ \frac{Q}{R_g} \left( \frac{1}{T_2} - \frac{1}{T_1} \right) \right] \quad (2.129)$$

Barnes et al. (1971) extended the rate equation to higher stresses (up to 10 MPa) using the formulation Garofalo (1963) proposed for high-temperature metals:

$$\dot{\epsilon}_{sc} = A_f \sinh^n(\alpha\sigma) e^{-\frac{Q}{R_g T}} \quad (2.130)$$

where  $\dot{\epsilon}_{sc}$  is the secondary creep strain rate and  $\alpha$  is a normalization constant. This simplifies to the form of Equation 2.128 at low stresses:

$$\text{For } 0 < \alpha\sigma \ll 1, \sinh^n(\alpha\sigma) \approx (\alpha\sigma)^n = A_f \sigma^n \quad (2.131)$$

Barnes found that there was a clear change in behaviour as the temperature approached the melting point of ice that was not noted by Glen; the activation energy jumped from 78 kJ/mol to 120 kJ/mol, while the pre-exponential factor increased by eight orders of magnitude, from  $2.58 \times 10^{10} \text{ s}^{-1}$  to  $4.60 \times 10^{18} \text{ s}^{-1}$ .

Sinha (1978) examined the activation energy of ice during creep. He found that the activation energy for the delayed elastic strain rate was 67 kJ/mol, which compared well to the 65 kJ/mol activation energy for the secondary creep strain rate found by Gold (1973).

Barrette and Jordaan (2003) examined the effect of hydrostatic pressure on the activation energy of ice. They found that the activation energy remained constant for low confining pressures but increased dramatically at the highest confining pressures studied, from 80 kJ/mol to 130 kJ/mol, similar to the increase in activation energy with increasing temperature found by Barnes et al. (1971) and others (Mellor and Testa, 1969). Taken together, these results would seem to indicate that the dominant deformation process of polycrystalline ice at both high pressures and high temperatures is similar, if not identical. This is likely the result of pressure melting; in the case of ice, an increase in pressure is equivalent to an increase in temperature, as noted by Jordaan et al. (2005).

Mizuno (1992) examined the deformation behaviour of ice as temperature was increased at two different hydrostatic pressures and found that, while the activation enthalpy of ice at low temperatures was identical for the two hydrostatic pressures, it was slightly larger for the higher hydrostatic pressure at temperatures above  $-6 \text{ }^\circ\text{C}$ .

This change was not reported by Barrette and Jordaan (2003), who performed few tests at temperatures above  $-6 \text{ }^\circ\text{C}$ . However, the strain rate data acquired from the

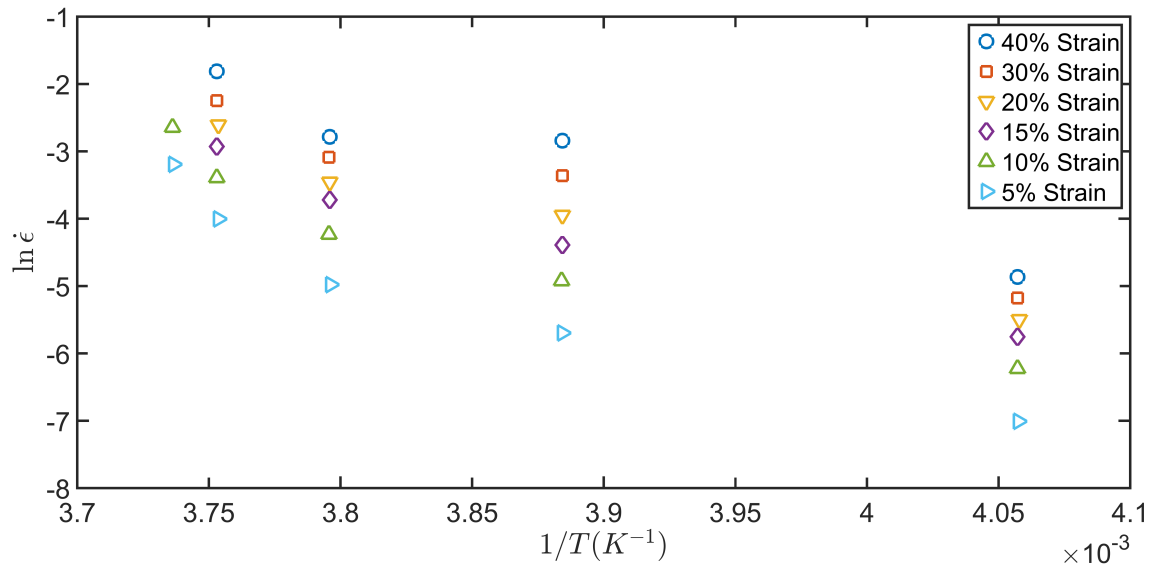


Figure 2.19: Strain rate at increasing levels of axial strain for a wide range of temperatures. A noticeable change in slope occurs in the 5 % and 10 % axial strain curves at a temperature of approximately -6 °C. Recreated from Barrette (2014).

tests that took place at -5 °C do lend some support to the result, as seen in Figure 2.19.

Recently, Jordaan and Barrette (2014) expanded upon their earlier results, reporting a change in the pre-exponential term of the Arrhenius equation by nearly nine orders of magnitude, as reproduced in Table 2.1. This explains how strain rate increases by several orders of magnitude while activation energy increases, which would normally cause a reduction in rate were the pre-exponential term to remain constant.

Table 2.1: Variation in pre-exponential term,  $A_f$ , and activation energy,  $Q$ , with increasing hydrostatic pressure,  $p$ , obtained at the minimum strain rate.

$p$ (MPa)	15	35	55	65	70
$A_f$ ( $s^{-1}$ )	6.98E+12	2.46E+12	2.41E+11	1.46E+16	1.81E+23
$Q$ (J)	1.33E-19	1.30E-19	1.22E-19	1.60E-19	2.16E-19

## 2.7 Modelling Ice

The preceding Chapter provided the background necessary to understand the constitutive model developed by Jordaan and McKenna (1988a;b) and others for the compressive deformation of ice, which will be presented in full in Chapter 4. The model was chosen due to the fact that it includes the effect of both viscoelasticity and damage on the deformation of ice, which have been shown to be key components of the development of *hpzs*. A brief introduction to other constitutive models is presented and discussed here for completeness.

Numerous constitutive models have been proposed, generally for the case of ice subjected to increasing loads only (Santaoja, 1990; Sinha, 1978); these models do not effectively simulate the observed load drops during cyclic or saw-tooth loading. Several models have been proposed which attempt to rectify this omission.

One of the more promising such models, developed in Derradji-Aouat (1992; 2000; 2003) and Derradji-Aouat et al. (2000), sought to describe the deformation behaviour of ice under any loading scenario. The total strain was composed of elastic, viscoelastic, and viscoplastic terms, similar to the delayed elastic and viscous creep terms used

elsewhere, along with an additional term representing the effect of microcracking development. The effect of strain rate, temperature, hydrostatic pressure, salinity, and grain size on the various strain terms was also accounted for. Good agreement with experimental evidence was found under a variety of scenarios, particularly after the addition of a brittle failure envelope for ice subjected to high strain rates ( $> 10^{-3} \text{ s}^{-1}$ ), which accounted for the transition to purely brittle deformation. The model lacks for only a term to describe the extensive dynamic recrystallization observed in most ice-structure interactions; as such, the model of Jordaan and others, which already possessed such a term, was used as the basis for this work.

Gagnon (2011) describes a numerical model for ice crushing where the ice has been modelled as a crushable foam, a material with a Poisson's ratio of practically zero (i.e. no lateral expansion will occur under a uniaxial stress), a decision unsupported by experimental evidence; studies of ice properties report a Poisson's ratio of approximately 0.3 during elastic deformation, while a value of 0.5 is generally assumed for plasticity models after yielding has occurred. Two main assumptions are made in the development of this model: 1) that rapid melting due to the viscous flow of melt water at the surface of the centre of the *hpz*, here referred to as a "hard" zone, plays a significant role in the deformation behaviour of ice, and; 2) that spalling controls the size and shape evolution of the hard zones and that they occur at regular intervals.

The viscous heating hypothesis was previously discussed in Section 2.6.7 and its shortcomings highlighted. To summarize, viscous heating is generally inconsequential for a low viscosity, high heat capacity liquid such as water, and no credible evidence has been presented to the contrary for the case of ice-structure interactions.

As for the second assumption, while spalling does play a significant role in the

development and failure of *hpzs*, the occurrence of spalling is highly probabilistic in nature while also not the sole cause of the load drops observed during saw-tooth loading; the pressure scans of Wells et al. (2011), O'Rourke et al. (2016a), and O'Rourke et al. (2016b) show that there is little to no change in *hpz* area during the majority of load drops, indicating that most load drops are due to the failure and extrusion of the damage layer. In this case, spalling, if it occurs at all, occurs outside the contact area, and plays an insignificant role in the observed load.

Finally, the model is independent of both time and damage; viscoelastic deformation and changes in microstructure are not considered. Combined with the use of unproven underlying assumptions, this model is deemed inappropriate for the study of ice-structure interactions.

# Chapter 3

## Experimentation

Triaxial compression tests are used to examine a particular region of interest within a *hpz*, from the high-pressure region at the centre of the *hpz* to the low-pressure, high-shear regions on the periphery. While the failure behaviour of triaxially compressed specimens may differ from that which is observed during a full indentation experiment, possibly due to the absence of the intense stress gradient present during indentation experiments, the results of triaxial compression tests have been found to closely resemble the material behaviour observed within specific regions of a *hpz*, particularly with regards to the accumulation of microstructural damage.

The exploratory test series described in the following sections was focused on the examination of ice deformation behaviour under excessive shear. The results of these tests are used to improve the damage model of ice described in Chapter 4.

### 3.1 Specimen Preparation

Ice was prepared as per Stone et al. (1989), with some modifications. Granular blocks of ice were grown from 2 – 3.35 mm seed ice that had been flooded with distilled, deionized, and deaerated water. The seed ice was obtained by crushing and sifting sculptors ice (growth process minimizes air content and grain volume) via a commercial ice crusher and copper sieves of the appropriate mesh size. The remaining crushed ice of size greater than 3.35 mm was also flooded with distilled, deionized, and deaerated water, frozen into ice blocks, then crushed to obtain further seed ice. This process produced ice blocks with grains of approximately 3 – 5 mm, slightly larger than the seed ice itself.

The resulting ice block was machined into cylinders approximately 150 mm in length and 70 mm in diameter using a bandsaw and lathe installed in the cold room. Efforts were made to test samples immediately after machining, so as not to expose them to the cold room defrost cycles. If this was not possible, the samples were stored in a separate insulated cooler within the cold room at temperatures of -10 °C until testing, to prevent significant changes in the sample microstructure.

Ice samples were mounted to hardened-steel end platens with a matching diameter (approximately 70 mm) within a Structural Behaviour Engineering Laboratories Model 10 triaxial cell. The specimen assembly was enclosed in a latex membrane to exclude the confining fluid, as seen in Figure 3.1. Silicone oil was chosen as the confining fluid, as per the earlier studies of Barrette and Jordaan (2003) and others. The fluid was supplied by a pressure intensifier that could apply confining pressures of up to 70 MPa. The entire test series took place at an environmental temperature



Figure 3.1: Triaxial equipment prior to testing.

of  $-10\text{ }^{\circ}\text{C}$ .

## 3.2 Equipment and Procedure

A Materials Testing Systems (MTS) test frame was used to supply the axial load necessary to deform the samples. The system was rated for a maximum applied load of 500 kN, which corresponds to a nominal stress on the ice samples of approximately 130 MPa. Two load cells were used to measure the axial load applied to the ice

samples, one inside the triaxial cell, the other out; the internal cell is used to measure the difference between the applied axial load and the axial load supplied by the confining pressure, while the external cell measures the total applied load. Both cells are rated for a maximum load of 500 kN, to match the test frame. The confining pressure, ram displacement, and loads were all recorded via the test frame's data acquisition software.

Contact between the ice sample and ram was made prior to the start of testing to ensure that the ram displacement would proceed in the desired direction; previous investigators found that the ram would sometimes proceed in the opposite direction otherwise. The confining pressure was then applied slowly at a rate of 18 MPa/hr to minimize heating of the ice sample. This is consistent with the time necessary to maintain temperature equilibrium in the work of Barrette and Jordaan (2003), although in that study the confining pressure was applied in a series of steps instead of at a constant rate. Force control was then used to apply a near-instantaneous, constant axial load (corresponding to the desired nominal von Mises stress) until the desired total engineering strain was reached or sample failure occurred. The axial load was then quickly removed and the confining pressure slowly reduced to ambient pressure.

The samples were immediately examined post-testing to check for signs of failure and leakage through the latex membrane. Samples were photographed, numbered, and packaged within plastic bags, then stored within an insulated cooler in an external freezer at a temperature of -30 °C for later thin sectioning.

To examine the microstructure of samples, thin sections were prepared using a bandsaw and microtome. A bandsaw was used to make an initial section approxi-

mately one cm thick. This section was then frozen to a clean glass slide using beads of supercooled water. The exposed surface was then shaved down to produce a flat surface for further microtoming. This surface was securely frozen to another slide with additional water. The sample was then microtomed down to the desired thickness. A thickness of approximately 0.3 mm was found to be necessary to produce the highest quality thin section photographs under both polarized- (used to highlight grains and grain boundaries) and side-lighting (used to highlight cracking).

### **3.3 Large Deviatoric Stress Tests**

This test series was designed to extend the constant hydrostatic pressure data of Meglis et al. (1999) to higher deviatoric stresses. As per their work, a hydrostatic pressure of 55 MPa was examined for the majority of tests, with a single exploratory test at a higher pressure of 70 MPa. The test parameters are listed in Table 3.1. Note that repeat tests were used to assess the capabilities of the test system and the data acquisition software.

Each test was designed to deform to an axial engineering strain of 40% under a constant axial load and confining pressure. The majority of the samples failed via shear faulting within a few percent axial strain, prior to reaching the desired von Mises stress or hydrostatic pressure. An example failure is shown in Figure 3.2.

Table 3.1: Planned nominal stress conditions for latest test series.

Test	Confining Pressure (MPa)	von Mises Stress (MPa)	Hydrostatic Pressure (MPa)
1 <sup>1</sup>	49	18	55
1a <sup>1</sup>	49	18	55
2 <sup>1</sup>	49	18	55
3 <sup>1</sup>	49	18	55
4	45	30	55
5	45	30	55
6 <sup>1</sup>	53	6	55
7	40	45	55
8	40	45	55
9	60	30	70

<sup>1</sup> Repeat test of conditions studied by Meglis et al. (1999)

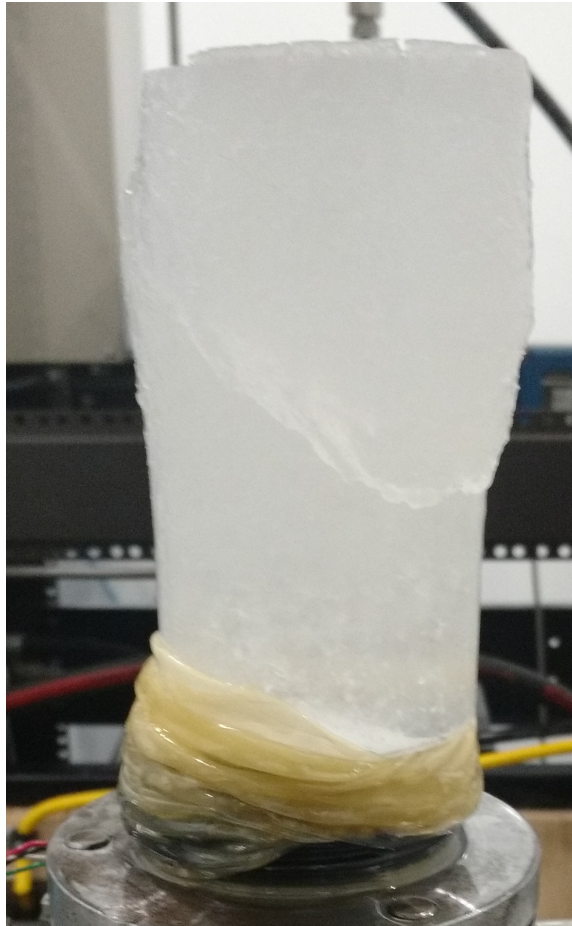


Figure 3.2: Example of shear faulting during triaxial compression. Deformation took place under a confining pressure of 40 MPa and a nominal axial stress of 85 MPa.

### 3.4 Corrections and Calibrations

The standard triaxial compression experiment takes place under a constant axial load and confining pressure. As such, the applied axial stress actually decreases with increasing deformation as the cross-sectional area of the sample increases. Fortunately, ice has been shown to maintain an approximately constant volume (measured at atmospheric pressure) under triaxial compression (Melanson, 1998) with some minor

deviations due to extrusion around the platens. With the further assumption that the sample deforms uniformly (i.e. barrelling of the samples is ignored), the cross-sectional area,  $A$ , is given by:

$$A = A_0 \frac{L_0}{L} \quad (3.1)$$

where  $A_0$  is the initial cross-sectional area, while  $L$  and  $L_0$  are the current and initial sample lengths. Note that some deviation from the constant volume assumption is to be expected; the application of a hydrostatic pressure,  $p$ , will cause a reduction in volume approximately equal to the inverse bulk modulus,  $K^{-1}$  per MPa of applied pressure, or:

$$\frac{\Delta V}{V} \approx \frac{p}{K} \quad (3.2)$$

where  $\Delta V$  is the change in volume and  $V$  is the initial volume. Under a hydrostatic pressure of 70 MPa, the maximum hydrostatic pressure applied here, the elastic change in volume amounts to less than a percent, and can be safely ignored.

Under these assumptions the true axial stress during deformation is estimated to be:

$$\sigma_t = \frac{F}{A} = \frac{FL}{A_0 L_0} = \sigma_{eng} \frac{L}{L_0} = \sigma_{eng}(1 + \epsilon_{eng}) \quad (3.3)$$

where  $F$  is the applied axial load,  $\sigma_t$  and  $\sigma_{eng}$  are the axial true and engineering stresses, respectively, and  $\epsilon_{eng}$  is the engineering strain in the axial direction.

The fact that the true stress does not remain constant complicates the damage analysis slightly; the constant axial load results must be used to estimate the true strain that would have resulted from the desired constant stress test. A constitutive

relation is necessary; in this case, the true strain rate in the axial direction,  $\dot{\epsilon}_t$ , is assumed to obey Glen's law:

$$\dot{\epsilon}_t = B\sigma_t^n \quad (3.4)$$

where  $B$  and  $n$  are constants that are assumed to be independent of stress. The estimated true strain is then:

$$\dot{\epsilon}_{est} = \dot{\epsilon}_t \left( \frac{\sigma_c}{\sigma_t} \right)^n \quad (3.5)$$

where  $\dot{\epsilon}_{est}$  is the true strain that would result from the application of a constant stress,  $\sigma_c$ . Note that this estimate does not take into account the effect of damage on the strain rate. Assuming that the creep enhancement factor can be accurately applied to Glen's law:

$$\dot{\epsilon}_t = B\sigma_t^n e^{\beta S_t} \quad (3.6)$$

$$\dot{\epsilon}_{est} = \dot{\epsilon}_t \left( \frac{\sigma_c}{\sigma_t} \right)^n e^{\beta(S_c - S_t)} \quad (3.7)$$

where  $S_t$  is the damage accumulated during the constant load test and  $S_c$  is the damage that would have accrued under a constant stress test.

$S_t$  can be estimated from Equation 3.6 by taking the natural logarithm:

$$\ln(\dot{\epsilon}_t) = \beta S_t + \ln B + n \ln \sigma_t \quad (3.8)$$

which, for the special case of a constant damage rate,  $\dot{S}_t$ , becomes:

$$\ln(\dot{\epsilon}_t) = \beta \dot{S}_t t + \ln B + n \ln \sigma_t \quad (3.9)$$

The damage rate can therefore be acquired from the slope of the natural logarithm of the strain rate vs. time curve. At this stage the initial transitory behaviour of the

ice has ended but runaway creep has not yet begun, after which the model no longer applies.  $S_c$  is currently estimated using the same process applied to Equation 3.5.

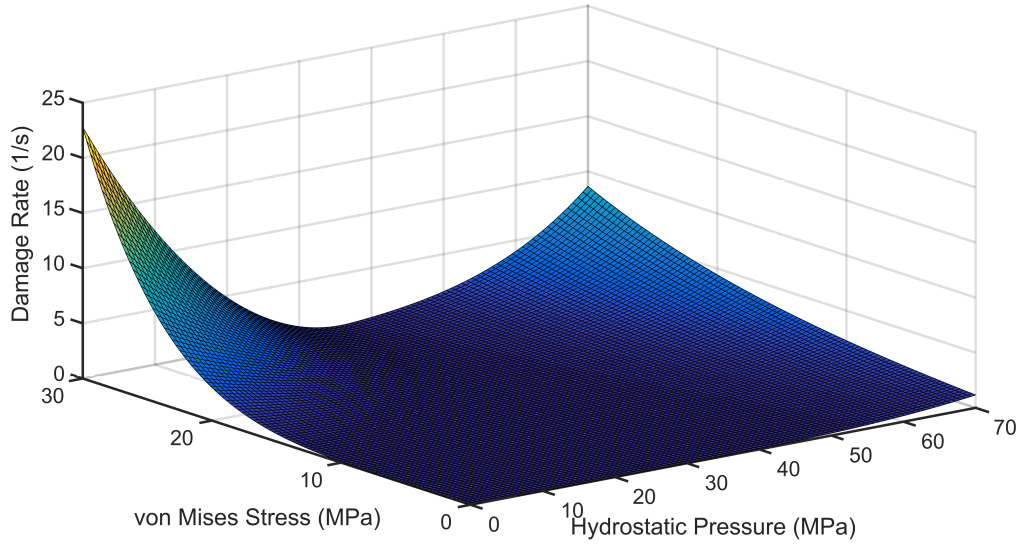
The above process has been used by Xiao (1997) and Li (2002) to calibrate the damage model. The resulting damage rates are plotted in Figures 3.3a and 3.3b for reference. It would be preferable to conduct constant axial stress tests, and thus avoid the calibration process. To accomplish this, the axial load would have to be modified with increasing strain as:

$$F = \frac{F_0}{1 + \epsilon_{eng}} \quad (3.10)$$

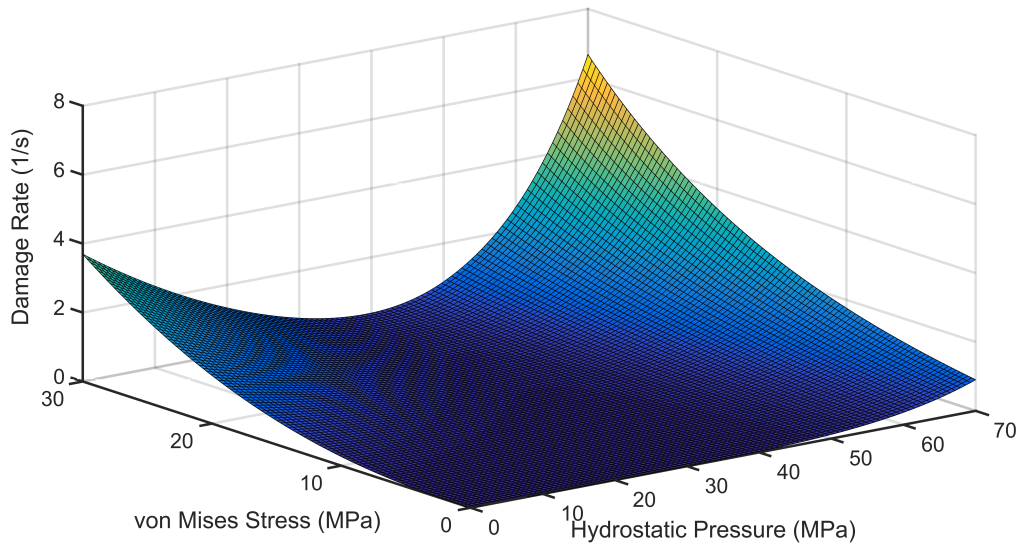
where  $F$  and  $F_0$  are the current and initial applied axial loads, respectively. The damage parameters could then be calculated directly, without the need for calibrations, and used when calibrations are required in later tests. Unfortunately, this option was not available during this test series; it was not possible to define the load command in terms of other variables due to limitations in the test software.

### 3.5 Results and Observations

Previous investigators (Li et al., 2005) found that samples under triaxial compression were more likely to fail via strain localization at both low and high confining pressures than at medium confining pressure, as well as high temperatures. This is consistent with the general observation that ice becomes stronger at confining pressures between the two extremes, where microcracking is suppressed but dynamic recrystallization and pressure melting have yet to become a significant factor in the deformation behaviour of ice.



(a)



(b)

Figure 3.3: Damage rates of a) Xiao (1997) and b) Li (2002)

The tests of Meglis et al. (1999) took place at nominal von Mises stresses ( $\sigma_1 - \sigma_3$  for a standard triaxial test) ranging from 6 MPa to 18 MPa. The new test series was designed to examine von Mises stresses of 30 and 45 MPa. It was found that, unlike the work of Meglis et al. (1999), the ice samples failed due to strain localization, without exception, producing a  $45^\circ$  shear fault similar to the one shown in Figure 3.2 in all cases. The loading conditions for each test, converted to nominal stresses for ease of analysis, are provided in Figures 3.5. None of the tested samples are able to reach the desired axial load, as seen more clearly in Figure 3.4; the ice appears to be unable to elastically support a von Mises stress greater than approximately 26 MPa. This point will hereafter be referred to as sample failure for ease of communication. The plateaus observed after the application of the axial load are actually post sample failure; the samples can no longer maintain the previous loading rate, but the DAQ attempts to reach the desired load until the failure is detected some time later, at 80 % of the maximum axial load.

Similar behaviour is observed for all other high shear tests. Table 3.2 lists the observed von Mises stress at failure for each test, along with the loading rates observed prior to failure and the strain rates observed post-failure. The failure stresses are remarkably consistent, with a mean failure stress of 26.0 MPa and a standard deviation of only 1.6 MPa. The minor differences between tests are likely due to changes in confining pressure, with the stress at failure decreasing with increasing confining pressure. The loading rate appears to have no bearing upon the observed failure stress; the loading rate was found to be insufficient to produce a near-instantaneous load during test 4, and was subsequently increased in further tests. Comparing tests 4 and 5, an increase in loading rate of a factor of 30 produced an increase in stress

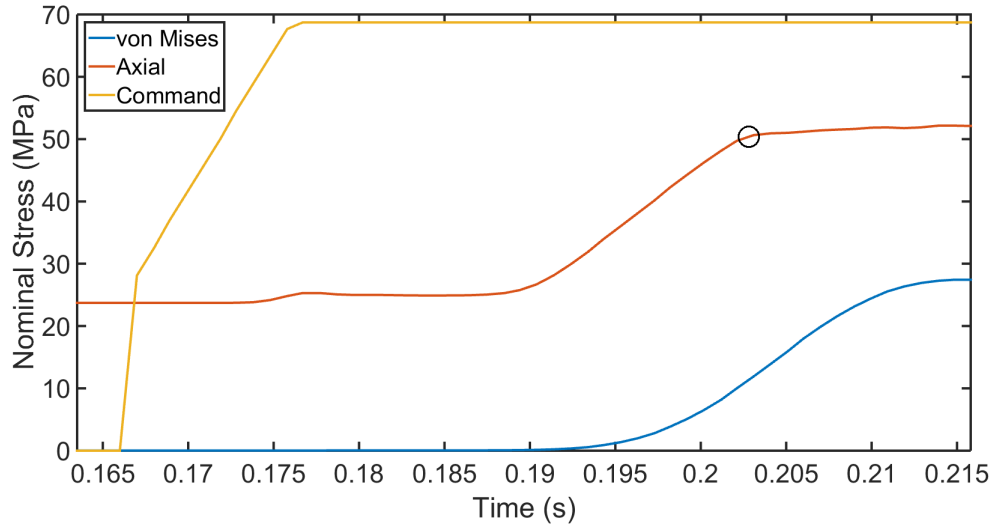


Figure 3.4: Nominal von Mises and axial stresses during test 7. The load command issued by the DAQ software, converted to the corresponding nominal stress on the ice sample, is plotted for comparison. The sample is seen to have failed within 15 ms of the application of stress, as noted by the black circle. Note that there is a minor delay between the readings of the external and internal load cells

difference at failure of 0.14 MPa, an increase of approximately half a percent.

With failure occurring in such a short amount of time, it is reasonable to assume that the deformation is mostly elastic in nature; for example, the amount of damage enhanced creep strain produced by the loading conditions of test 7 is estimated to be approximately  $7 \times 10^{-6}$ , or less than one thousandth of a percent. Figure 3.6 shows the engineering and true strain for test 7, along with the expected elastic strain at sample failure, assuming isotropic material behaviour with an elastic modulus of 9.5 GPa (theoretical upper limit on elastic modulus of ice, generally only observed during high-frequency vibration tests) and a Poisson's ratio of 0.3. The expected

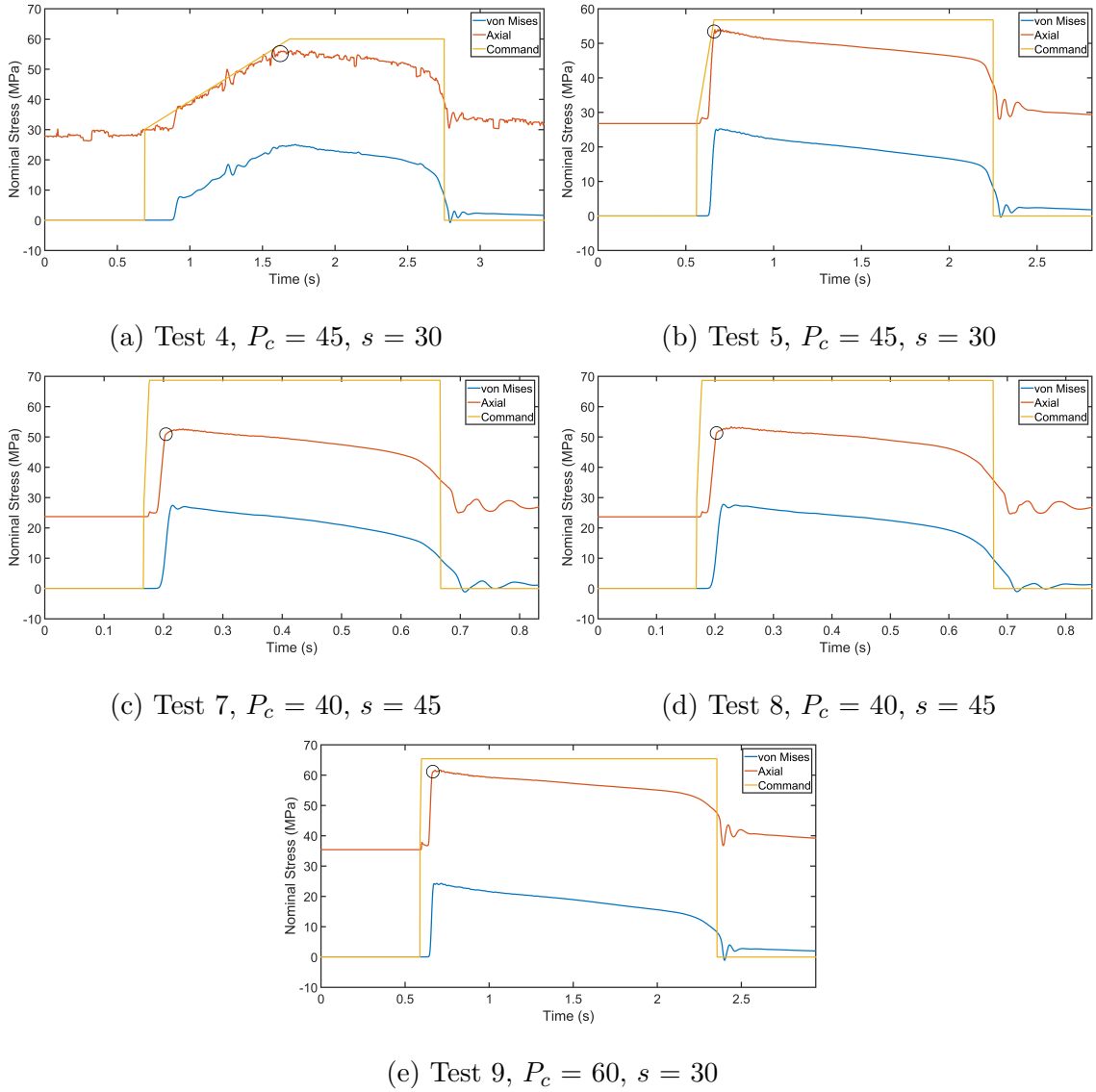


Figure 3.5: Nominal von Mises and axial stresses during testing. The tests were programmed to maintain confining pressures ranging from 40 to 60 MPa and to reach nominal von Mises stresses of 30 or 45 MPa. The load command issued by the DAQ software, converted to the corresponding nominal stress on the ice sample, is plotted for comparison. Loss of elastic strength in each sample is observed to occur at a von Mises stress of approximately 26 MPa, noted by the black circles, prior to reaching the desired axial stress.

Table 3.2: Shear stress and loading rate at elastic breakdown, strain rate post-failure.

Test	4	5	7	8	9
Confining Pressure (MPa)	45	45	40	40	60
Maximum Stress Difference (MPa)	25.08	25.22	27.44	27.77	24.30
Loading Rate (MN/s)	0.11	3.4	7.7	7.5	5.1
Axial Strain Rate ( $s^{-1}$ )	0.105	0.109	0.281	0.273	0.114

elastic strain makes up only a third of the observed strain; an elastic modulus of less than 0.8 GPa is necessary to produce the observed elastic strain at failure. The samples continued to deform after the apparent loss of elastic strength in a manner consistent with viscous deformation, following a power law relationship with a power of approximately  $n = 3$ .

These results indicate that strain localization is heavily dependent upon the applied shear stress; the majority of these tests took place at a hydrostatic pressure of 55 MPa, a pressure that Li et al. (2005) found to suppress strain localization at temperatures less than  $-6^{\circ}\text{C}$  when a von Mises stress of 15 MPa was applied. Here, each sample failed due to strain localization at a von Mises stress of approximately 26 MPa, above which the ice could no longer sustain elastic stress (stress is still supported via viscous components, as seen in Figures 3.5). Further experimentation is necessary, as five samples are insufficient to confirm these results. Further studies may also wish to determine the relation between stress at elastic failure and the applied confining pressure and axial stress.

The implications of this high-pressure elastic softening will be discussed further

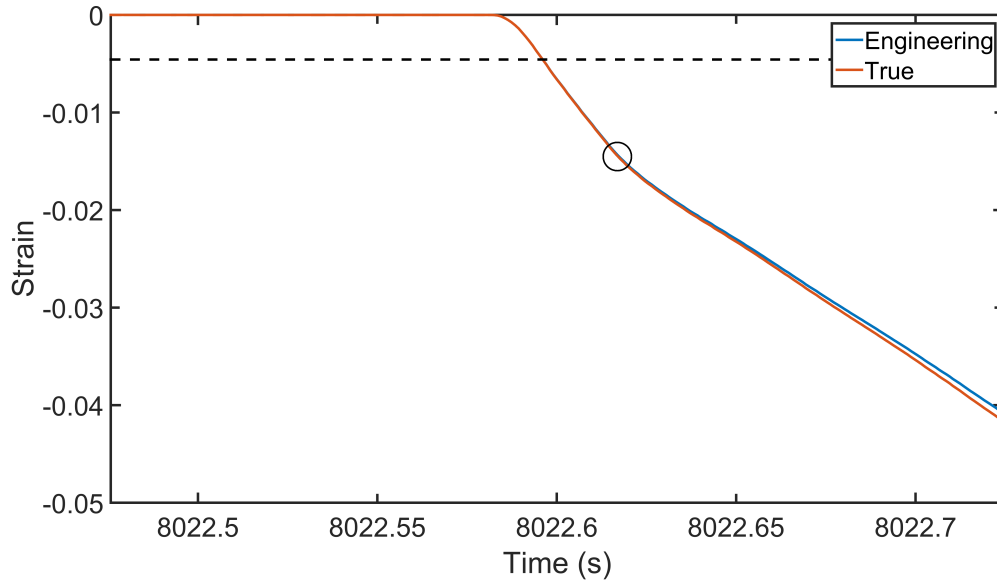


Figure 3.6: Engineering and true strain during test 7. The test was conducted under a confining pressure of 40 MPa and was programmed to reach a nominal von Mises stress of 45 MPa. The expected elastic strain (--) assuming linear isotropic elasticity for the stress conditions at sample failure is added for comparison. Note that failure occurs when the slope changes, at approximately  $t = 8022.62$  s.

in Chapter 4.

### 3.5.1 Microstructure

Thin sectioning of some of the test samples was undertaken to examine the resulting microstructure. Due to unforeseen delays, thin sectioning could not be completed for several months post-testing. Samples were stored at  $-30$  °C for this period of time, to minimize static recrystallization, which refers to any process by which grains may grow and/or rearrange to reduce internal energy while not undergoing deformation.

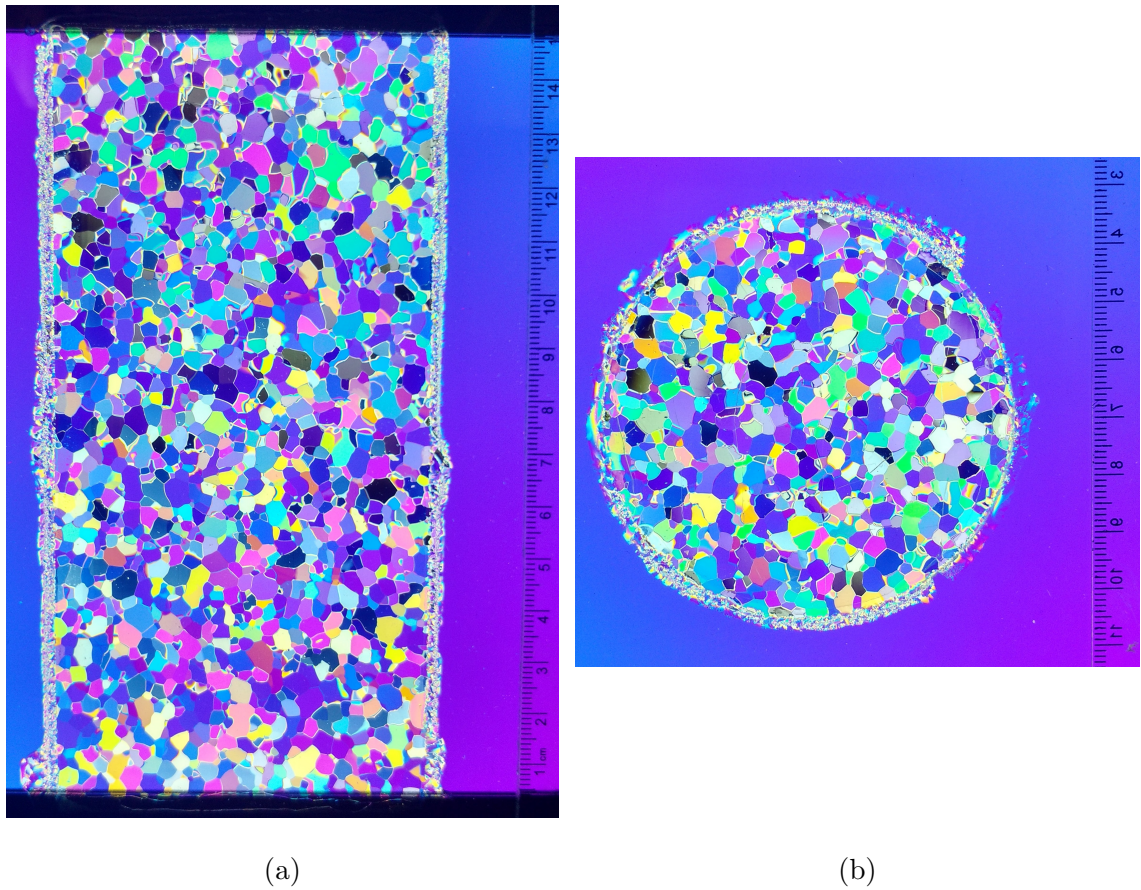


Figure 3.7: Microstructure of untested sample under polarized lighting.

Thin sections of an untested sample are provided in Figure 3.7 to serve as a baseline for comparison. The majority of the grains are seen to be only a couple millimetres in diameter, comparable to the size of the initial seed ice, with the largest grains being approximately five millimetres in diameter. This is unsurprising, given both the growth process and the extended period of time prior to thin sectioning.

By comparison, the thin sections of tested samples show little sign of static recrystallization, as seen in Figure 3.8a, indicating that the observed microstructure should indeed correlate to the deformation processes produced during testing of the samples. This test was also used as a comparison to the experiments of Meglis et al.

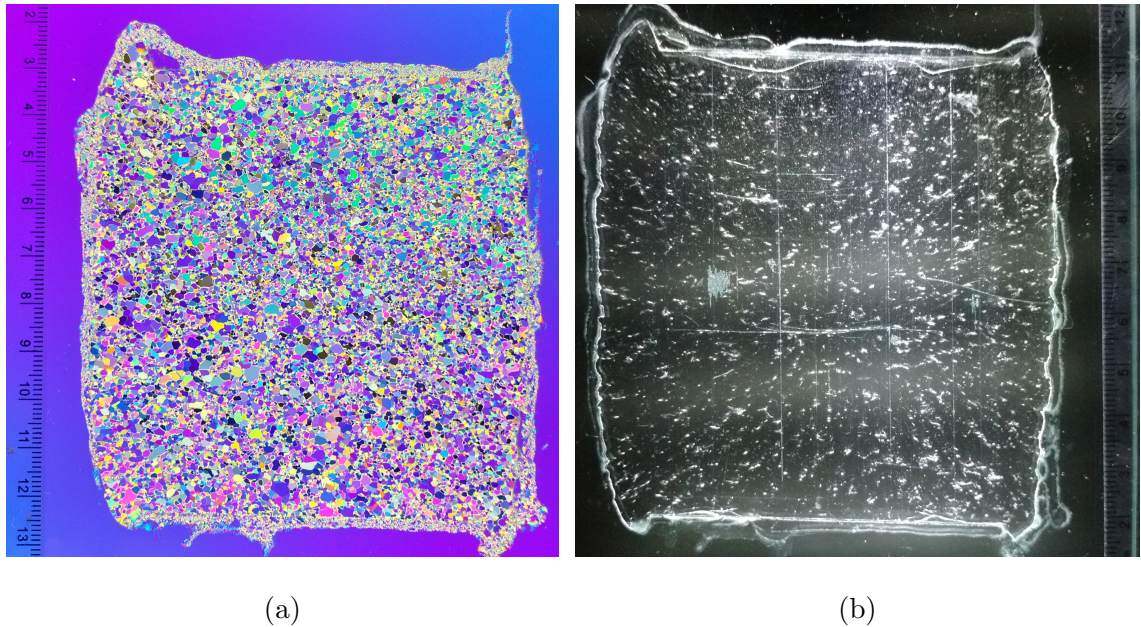


Figure 3.8: Microstructure of sample 6, in its entirety. Sample was deformed under a confining pressure of 53 MPa at a nominal von Mises stress of 6 MPa. a) uses polarized lighting conditions to highlight the grain structure, while b) uses side-lighting to highlight microcracking. The observed extensive dynamic recrystallization is common for samples that undergo uniform grain refinement.

(1999). Unfortunately, the matching thin sections for these test conditions are not available. However, the resulting microstructure is as one would expect, with high levels of dynamic recrystallization and comparatively little microcracking, which has been suppressed by the high confining pressure.

As the von Mises stress is increased a new failure regime is observed; a large region around the fault line is observed to be highly damaged, while the remainder of the sample is practically undamaged, comparable to the microstructure of the untested sample. This is shown in Figures 3.9a, 3.10a, and 3.11a. The corresponding im-

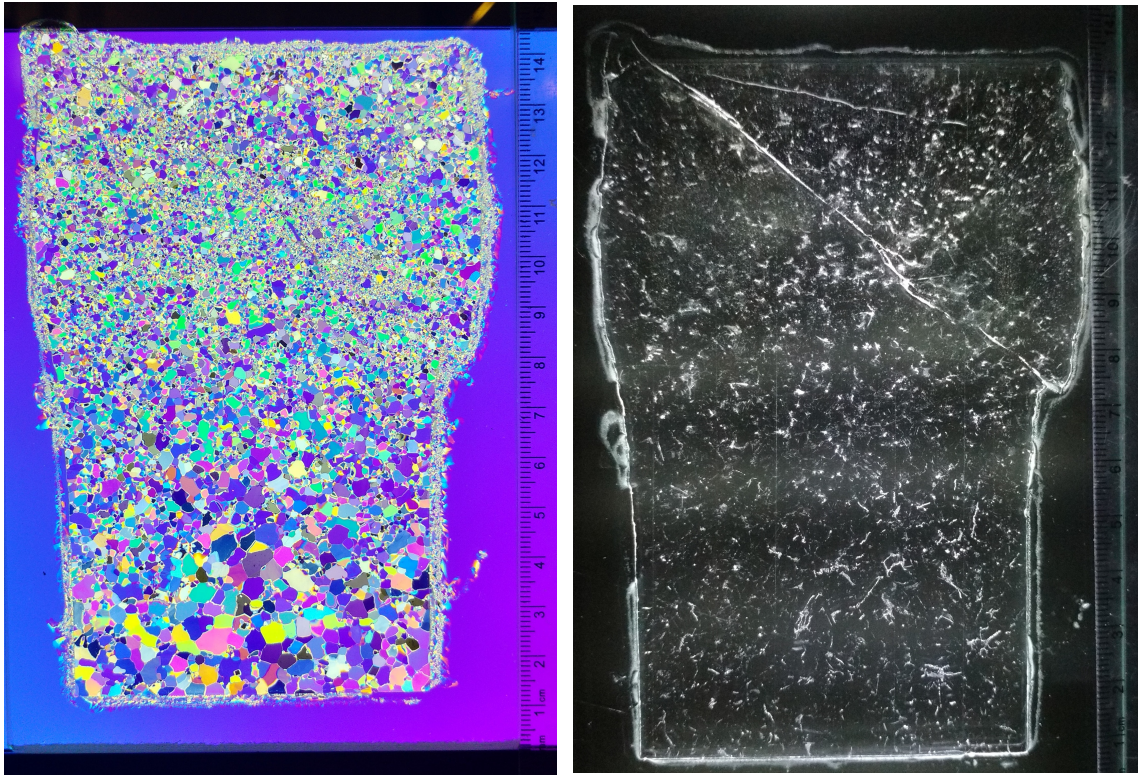
ages under side-lighting show that less and less microcracking occurs with increasing confining pressure, indicating that the majority of the damage is due to dynamic recrystallization.

The faults are observed to occur in the topmost region of each sample, likely due to differences in the end-platens; the bottom platen is fixed to the base of the triaxial cell, while the top platen rests on the ice sample and is free to rotate. Imperfections, due to scratching, corrosion, etc., at the contact surfaces of the plunger and/or top platen may then lead to the uneven application of stress within the topmost region of the ice samples.

There are some interesting differences between the samples. The damage in Figure 3.9a forms an x-shaped shear band, with relatively undamaged regions between, as found in the triaxial simulations of Li (2002); the other samples form only a single, large shear band.

The topmost region in Figure 3.10a was found to be relatively undamaged, indicating that the regions near the end-platen are not always zones of high damage; it is likely in this case that some internal stress concentration immediately focused a significant amount of damage within the sample, away from the ice surface.

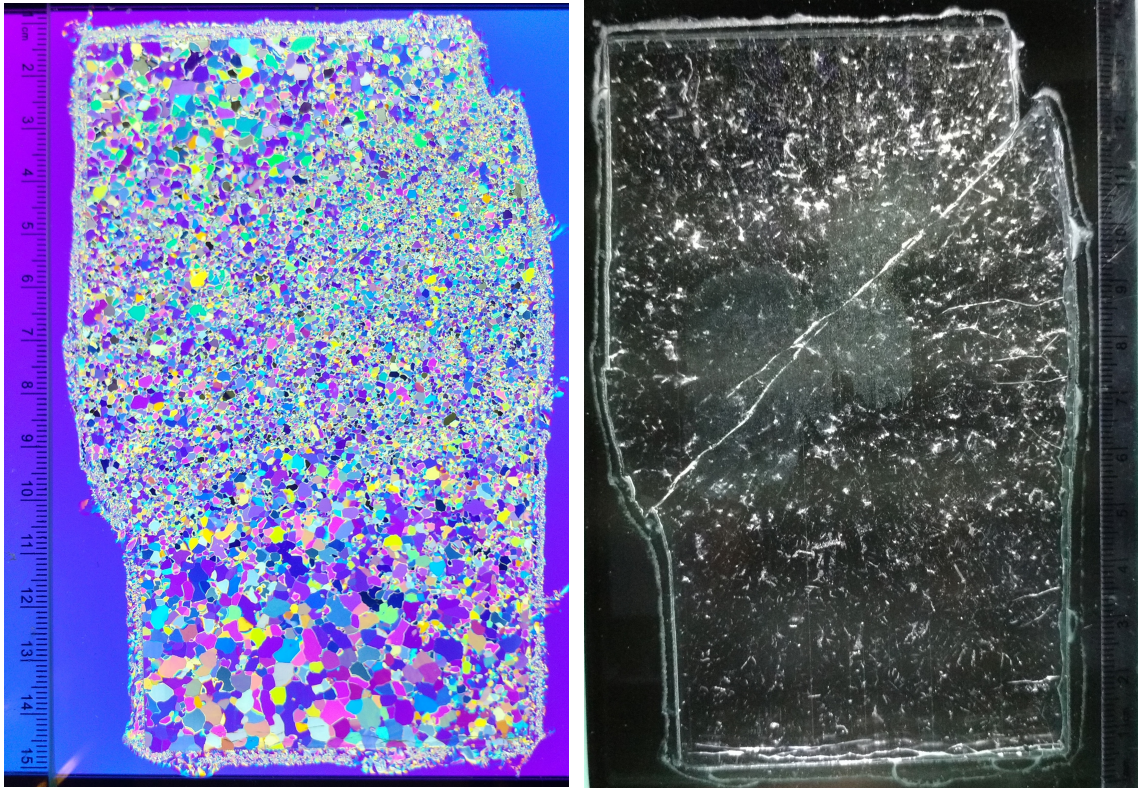
Finally, the tests show that higher confining pressures lead to recrystallization being dispersed throughout the sample, as seen in 3.11a. This is also consistent with the results of earlier investigators, who found that samples that failed under high confining pressure were likely to be highly recrystallized throughout.



(a)

(b)

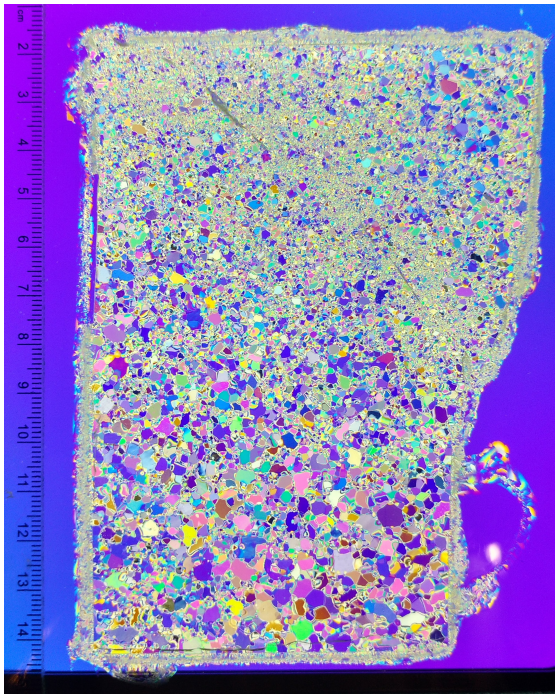
Figure 3.9: Microstructure of sample 5, deformed under a confining pressure of 45 MPa.



(a)

(b)

Figure 3.10: Microstructure of sample 8, deformed under a confining pressure of 40 MPa.



(a)



(b)

Figure 3.11: Microstructure of sample 9, deformed under a confining pressure of 60 MPa.

# Chapter 4

## Constitutive Modelling

In this chapter a constitutive model for the compressive deformation of ice is presented and examined. Originally published by Jordaan and McKenna (1988a;b), the model is based on the power law relation of Glen (1955) and the non-linear viscoelastic damage formulation of Schapery (1981; 1984; 1991; 1997a;b), and has been expanded by numerous authors (Li, 2002; Liu, 1994; Moore et al., 2013; Xiao, 1991; 1997) to include additional effects, particularly the hydrostatic pressure on the sample. The model is reproduced here for completeness. Modifications and additions, including a new, temperature-dependent damage function, are then introduced, and their effects examined.

### 4.1 Mechanical Model

The deformation of ice is a complex process whose properties are strongly influenced by the presence of damage. The non-linear Burgers model is considered a practical model for the primary and secondary creep response of many viscoelastic solids, in-

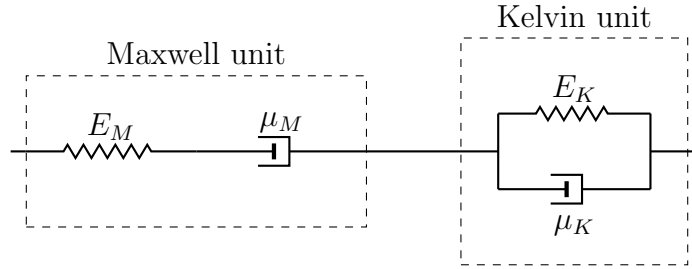


Figure 4.1: Basic composition of Burgers model for viscoelastic behaviour.

cluding ice. The model consists of a combination of the Maxwell and Kelvin units with non-linear dashpots aligned in series, as seen in Figure 4.1. The spring of the Maxwell unit models the initial elastic response of the sample while the dashpot models the creep response, which continually increases under stress. The Kelvin unit models the delayed elastic response of the sample, with strain increasing to a plateau under constant stress, as seen in the example response of Figure 4.2. It should be noted that an infinite series of Kelvin units with varying properties is required to accurately model the viscoelastic behaviour of real materials. Known as the Broad Spectrum Approach, this level of precision is both numerically intensive and, as noted by Xiao (1991) and Melanson (1998), unnecessary when viscous deformation dominates. Instead, a single Kelvin unit representing the average delayed elastic response was used for this model.

The response of the model to a uniaxial stress can be described by the combination of elastic, delayed elastic, and secondary creep strains:

$$\epsilon = \epsilon^e + \epsilon^d + \epsilon^c \quad (4.1)$$

The elastic component is given by:

$$\epsilon^e = \frac{\sigma}{E_M} \quad (4.2)$$

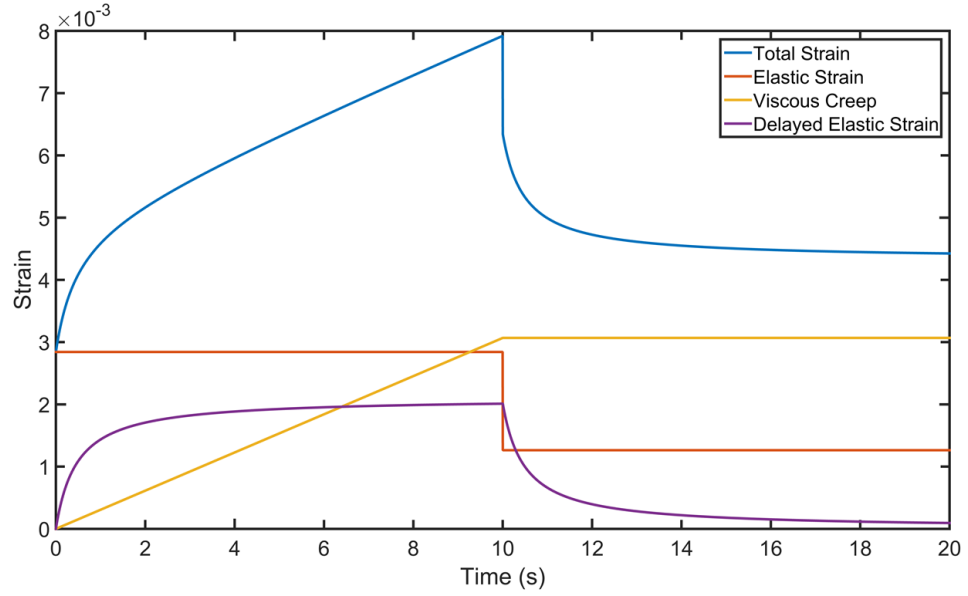


Figure 4.2: Basic response of the non-linear Burgers model to a constant uniaxial stress.

where  $\sigma$  is the axial stress and  $E_M$  is the elastic modulus of the Maxwell spring. The delayed elastic and secondary creep strains are derived from the strain rates of the Kelvin and Maxwell units, respectively:

$$\dot{\epsilon}^d = \frac{\sigma}{\mu_K} \quad (4.3)$$

$$\dot{\epsilon}^c = \frac{\sigma}{\mu_M} \quad (4.4)$$

where  $\mu_K$  and  $\mu_M$  are the viscosities of the Kelvin and Maxwell dashpots. Assuming both dashpots follow a power law relationship with stress, their strain rates can be

represented by:

$$\dot{\epsilon}^d = \dot{\epsilon}_0^d \left( \frac{\sigma^d}{\sigma_0} \right)^n \quad (4.5)$$

$$\dot{\epsilon}^c = \dot{\epsilon}_0^c \left( \frac{\sigma}{\sigma_0} \right)^m \quad (4.6)$$

where  $\dot{\epsilon}_0^d$  and  $\dot{\epsilon}_0^c$  are the delayed elastic and secondary creep strain rates at the reference stress,  $\sigma_0 = 1$  MPa,  $n$  and  $m$  are constants, and  $\sigma^d$  is the stress in the Kelvin dashpot, given by:

$$\sigma^d = \sigma - E_K \epsilon^d \quad (4.7)$$

where  $E_K$  is the elastic modulus of the Kelvin spring. The viscosities can therefore be represented by:

$$\mu_K = \frac{\sigma}{\dot{\epsilon}_0^d} \left( \frac{\sigma_0}{\sigma^d} \right)^n \quad (4.8)$$

$$\mu_M = \frac{\sigma}{\dot{\epsilon}_0^c} \left( \frac{\sigma_0}{\sigma} \right)^m \quad (4.9)$$

Extension to three dimensions follows a similar approach. The total strain is again described by a combination of elastic, delayed elastic, and secondary creep strain:

$$\epsilon_{ij} = \epsilon_{ij}^e + \epsilon_{ij}^d + \epsilon_{ij}^c \quad (4.10)$$

The elastic strain can be described by any desired formulation. Here the linear isotropic form is used for convenience:

$$\epsilon_{ij}^e = \frac{1 + \nu}{E_M} \sigma_{ij} - \frac{\nu}{E_M} \sigma_{kk} \delta_{ij} \quad (4.11)$$

where  $\delta_{ij}$  is the Kronecker delta, which is equal to one when  $i = j$  and zero otherwise.

The delayed elastic and secondary creep strains can be conveniently expressed in terms of their deviatoric components,  $e_{ij}$ , and volumetric components,  $\epsilon_v$ :

$$\epsilon_{ij}^d = e_{ij}^d + \epsilon_v^d \quad (4.12)$$

$$\epsilon_{ij}^c = e_{ij}^c + \epsilon_v^c \quad (4.13)$$

where the deviatoric components describe the change in shape of the sample, while the volumetric components describe the change in volume. Note that this volume change is due to the accumulation of damage within the sample and is not an inherent result of creep deformation.

Assuming that creep behaviour is isotropic and that the normal and shear viscosity coefficients are identical, the deviatoric strain rates can be described by:

$$\dot{e}_{ij}^d = \frac{3}{2} \left( \frac{s_{ij}}{\mu_K} \right) \quad (4.14)$$

$$\dot{e}_{ij}^c = \frac{3}{2} \left( \frac{s_{ij}}{\mu_M} \right) \quad (4.15)$$

where  $s_{ij} = \sigma_{ij} - \frac{1}{3}\sigma_{kk}$  is the deviatoric stress tensor. The von Mises stress,  $s$ , is used to define unique viscosity coefficients, given by:

$$\mu_K = \frac{s}{\dot{\epsilon}_0^d} \left( \frac{s_0}{s^d} \right)^n \quad (4.16)$$

$$\mu_M = \frac{s}{\dot{\epsilon}_0^c} \left( \frac{s_0}{s} \right)^m \quad (4.17)$$

where the von Mises stress is defined as:

$$s = \sqrt{\frac{3}{2}s_{ij}s_{ij}} \quad (4.18)$$

and  $s^d$  is the von Mises stress in the Kelvin dashpot, given by:

$$s^d = s - E_K e^d \quad (4.19)$$

where  $e^d$  is the equivalent delayed elastic strain, which can be shown to be equal to the strain when  $s_{ij} = s$ . Note that the absolute value of  $s^d$  must be taken and a sign function,  $\text{sgn}$ , applied as follows to ensure that delayed elastic recovery occurs:

$$\left(s^d\right)^n = \text{sgn}\left(s - E_K e^d\right) |s - E_K e^d|^n \quad (4.20)$$

Otherwise, any even value of  $n$  would always produce a positive value of  $e^d$ , which would lead to an increase in delayed elastic strain from a decrease in applied stress instead of the expected delayed elastic recovery.

Combining Equations 4.14, 4.15, 4.16, 4.17, and 4.20, it is found that:

$$\dot{e}_{ij}^d = \frac{3}{2} \dot{\epsilon}_0^d \text{sgn}\left(s - E_K e^d\right) \left(\frac{|s - E_K e^d|}{s_0}\right)^n \frac{s_{ij}}{s} \quad (4.21)$$

$$\dot{e}_{ij}^c = \frac{3}{2} \dot{\epsilon}_0^c \left(\frac{s}{s_0}\right)^m \frac{s_{ij}}{s} \quad (4.22)$$

which, assuming the volumetric components are negligible, reduces to the uniaxial formulation described in equations 4.1-4.9 under a uniaxial stress. Using the von Mises stress to define the viscosities is thus both consistent and convenient, though its positive-definite nature does produce some complications that must be accounted for, as discussed further in Section 4.2.

To obtain the volumetric strain component the dilation of ice under compression must be examined. Frederking et al. (1990) found that the density of ice at the indentation surface decreased with distance from the centre of the indenter, with the recrystallized ice at the centre having a density nearly identical to that of virgin ice. This indicates that dilation due to microcracking occurs during the compression of ice. Singh (1993) proposed an empirical equation for the volumetric strain rate of ice,

$\dot{\epsilon}^v$ , under triaxial compression, given by:

$$\dot{\epsilon}^v = -\frac{f_3}{p}s(\dot{\epsilon} - \dot{\epsilon}^e) = -\frac{f_3}{p}s(\dot{\epsilon}^d + \dot{\epsilon}^c) \quad (4.23)$$

where  $f_3$  is a constant,  $\dot{\epsilon}$  and  $\dot{\epsilon}^e$  are the total and elastic equivalent strain rates of the sample, respectively, while  $\dot{\epsilon}^d$ , and  $\dot{\epsilon}^c$  are the equivalent delayed elastic and secondary creep strain rates, which are represented by:

$$\dot{\epsilon}_{ij}^d = \frac{s_{ij}}{s}\dot{\epsilon}^d \quad (4.24)$$

$$\dot{\epsilon}_{ij}^c = \frac{s_{ij}}{s}\dot{\epsilon}^c \quad (4.25)$$

The total strain rate is then:

$$\dot{\epsilon}_{ij} = \dot{\epsilon}_{ij}^e + \dot{\epsilon}_{ij}^d + \dot{\epsilon}_{ij}^c + \dot{\epsilon}^v \delta_{ij} \quad (4.26)$$

## 4.2 Damage Evolution

The formulation of Section 4.1 does not account for enhanced creep due to the accumulation of damage; a damage evolution factor is necessary to describe the effect of microstructural change on the creep response of ice. The theory behind such damage factors has been described in detail in Section 2.5.

Early investigations focused on the effect of microcracking on the deformation of ice. An early model, developed by Xiao (1991) and Xiao et al. (1991), described the effect of microcracking on the creep response of ice via the crack density, as detailed in Jordaan and McKenna (1991) and Jordaan et al. (1990; 1992b). In short, the change in crack density,  $\dot{N}$ , was given by:

$$\dot{N} = \dot{N}_0 \left( e^{\frac{\sigma - \sigma_c}{\sigma_0}} - 1 \right) \quad (4.27)$$

and subsequently reduced to:

$$\dot{N} = \dot{N}_0 \left( \frac{\sigma - \sigma_c}{\sigma_0} \right)^m \quad (4.28)$$

where  $\dot{N}_0$  is a reference rate,  $\sigma$  is the applied stress,  $\sigma_c$  is the stress required for crack nucleation,  $\sigma_0$  is a reference stress, and  $m$  is a constant. This was used to estimate an isotropic, bounded damage parameter,  $D_N$ , as per the work of Budiansky and O'Connell (1976), given by:

$$D_N = a^3 N \quad (4.29)$$

where  $a$  is half the crack length and  $N$  is the crack density. The effect of crack density on the delayed elastic and creep response of ice was given as:

$$\dot{\epsilon}'_{ij} = \dot{\epsilon}_{ij} e^{\beta D_N} \quad (4.30)$$

where  $\dot{\epsilon}_{ij}$  and  $\dot{\epsilon}'_{ij}$  are the undamaged and enhanced strain rates, respectively, and  $\beta$  is a constant. This damaged enhanced creep formulation is similar to the approach of Schapery (1981; 1984; 1991; 1997a;b), which allows for the examination of numerous forms of damage within a similar format. Schapery defined an unbounded damage parameter, given by:

$$S = \int_0^t f \left( \frac{\sigma}{\sigma_0} \right)^q d\tau \quad (4.31)$$

where  $S$  is the accumulated damage,  $f$  is a function of the material properties, known as the damage function,  $\sigma$  and  $\sigma_0$  are the applied and reference stress, respectively, and  $q$  is a constant.

Singh (1993) extended the formulation to multi-axial stress states by defining the stress dependence in terms of the von Mises stress and included the effect of

hydrostatic pressure,  $p$ , on the damage function, redefining  $f$  as  $f/p$ . The model was refined in Singh and Jordaan (1996) to include the effect of porosity, based on earlier work on crushed ice (Singh et al., 1995). Xiao and Jordaan (1996) refined the model further, defining two damage factors; one for the creep response of ice, another for the delayed elastic:

$$S_{m,k} = \int_0^t \frac{f_{m,k}}{p} \left( \frac{s}{s_0} \right)^{q_{m,k}} d\tau \quad (4.32)$$

where the subscripts  $m$  and  $k$  represent the Maxwell dashpot (corresponding to the creep response) and Kelvin unit (corresponding to the delayed elastic response), respectively. Liu (1994) accounted for the effect of pressure hardening by defining the following pressure-dependent function,  $F(p)$ :

$$\dot{S} = S_0 \left( \frac{s}{s_0} \right)^q F(p) \quad (4.33)$$

$$F(p) = F_0 \left( \frac{p_0}{p} \right)^f \quad (4.34)$$

where  $S_0$ ,  $F_0$ ,  $q$ , and  $f$  are constants, while  $s_0$  and  $p_0$  are the reference von Mises stress and hydrostatic pressure, respectively. Liu (1994) further defined a separate pressure enhancement factor,  $G(p)$ , to describe the softening effect of pressure melting:

$$G(p) = e^{\alpha M} \quad (4.35)$$

$$\dot{M} = G_0 \left( \frac{p}{p_0} \right)^g \quad (4.36)$$

where  $\alpha$ ,  $G_0$ , and  $g$  are constants. Combined, these produce enhanced delayed elastic and viscous creep strain rates of:

$$\dot{\epsilon}'_{ij} = \dot{\epsilon}_{ij} e^{\beta S} G(p) = \dot{\epsilon}_{ij} e^{\beta S + \alpha M} \quad (4.37)$$

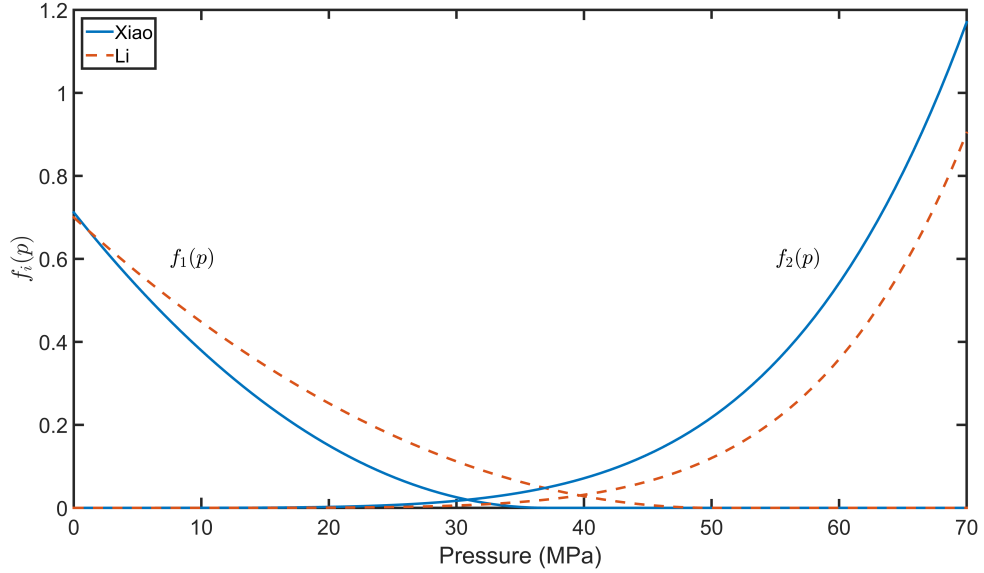


Figure 4.3: Transition from microcracking ( $f_1$ ) to dynamic recrystallization and pressure melting ( $f_2$ ) with increasing hydrostatic pressure ( $p$ )

which is mathematically equivalent to the addition of another damage function, as seen in Equation 4.37. Later models express this explicitly, defining separate damage functions for low and high hydrostatic pressures:

$$S = S_1 + S_2 = \int_0^t \left( f_1(p) + f_2(p) \right) \left( \frac{s}{s_0} \right)^q d\tau \quad (4.38)$$

This was done in an effort to model the transition from microcracking to dynamic recrystallization and pressure melting (Jordaan et al., 1999; Melanson et al., 1999b), which can be seen in Figure 4.3.

Xiao (1997) altered the stress dependence of the dynamic recrystallization and pressure melting damage function from a power law to an exponential, to better reflect the effects of dynamic recrystallization on the creep response of ice, as described by Jonas and Muller (1969). Simulations of the model have produced promising results,

Parameter	$a_1$	$a_2$	$p_1$	$p_2$	$r_1$	$r_2$	$q_1$
Xiao	0.712	0.1	37	42.8	2	5-7	5
Li	0.7	0.12	50	50	2	6	2.4
Recalibration	0.983	0.1	11.1	42.8	N/A	5-7	5

Table 4.1: Calibration constants used in damage models of Xiao and Li. Values used in recalibration of  $f_1(p)$  are provided for comparison.

exhibiting the expected rise to peak stress followed by a drop in stress, as well as the development of a highly damaged surface layer at the ice-indentor interface (Jordaan et al., 1999; Li, 2002; Melanson, 1998; Xiao, 1997). The model is given by:

$$S = S_1 + S_2 = \int_0^t \left\{ f_1(p) \left( \frac{s}{s_0} \right)^{q_1} + f_2(p) e^{s/s_0} \right\} d\tau \quad (4.39)$$

$$f_1 = a_1 \left( 1 - \frac{p}{p_1} \right)^2 [1 - H(p - p_1)] \quad (4.40)$$

$$f_2(p) = a_2 \left( \frac{p}{p_2} \right)^{r_2} \quad (4.41)$$

where  $f_1(p)$  is the microcracking damage function,  $f_2(p)$  the dynamic recrystallization damage function, and  $a_1$ ,  $a_2$ ,  $p_1$ ,  $p_2$ , and  $r_2$  are calibration constants.  $S$  is used to define the enhanced delayed elastic and viscous creep strain rates, as per Equation 4.30. The calibration parameters used by Xiao (1997) and Li (2002) are listed in Table 4.1; they are used extensively in the finite element simulations described in Chapters 5 and 6.

The latest model, developed by Moore et al. (2013), reproduced the pressure drop via the deletion of excessively damaged elements, simulating the effect of extrusion during ice-structure interactions. While interesting, the use of a deletion criterion was

deemed unsatisfactory due to difficulties defining the contact surfaces post-element deletion; element deletion was therefore not implemented here.

Several aspects of this model have been modified in the present program of work. Firstly, it was noted that the cut-off pressure,  $p_1$ , of the microcracking damage function was likely temperature dependent; ice is known to transition from dynamic recrystallization to microcracking with decreasing temperatures. The damage function was therefore remodelled to remove the temperature dependence of the cut-off pressure. Two models were considered; a power law formulation similar to the dynamic recrystallization damage function, and a decaying exponential. The exponential form was chosen to avoid a numerical singularity at zero pressure. The pressure-dependent microcracking damage function then becomes:

$$f_1(p) = a_1 e^{(-p/p_1)} \quad (4.42)$$

The strain rate data of Xiao (1997), Melanson (1998), and Li (2002) for hydrostatic pressures less than 30 MPa was used to perform the calibration, in an effort to isolate the microcracking damage function from the effects of recrystallization and pressure melting. The dynamic recrystallization pressure function was assumed to be consistent with the new microcracking pressure function and was left unmodified. The resulting calibration can be seen in Figure 4.4 and the fit parameters are found in Table 4.1. Note that the error on the high-pressure data points is significant due to the onset of runaway strain, as noted in Jordaan et al. (1999).

Secondly, the exponential function used to represent the effect of von Mises stress on dynamic recrystallization produces a non-zero damage under pure hydrostatic

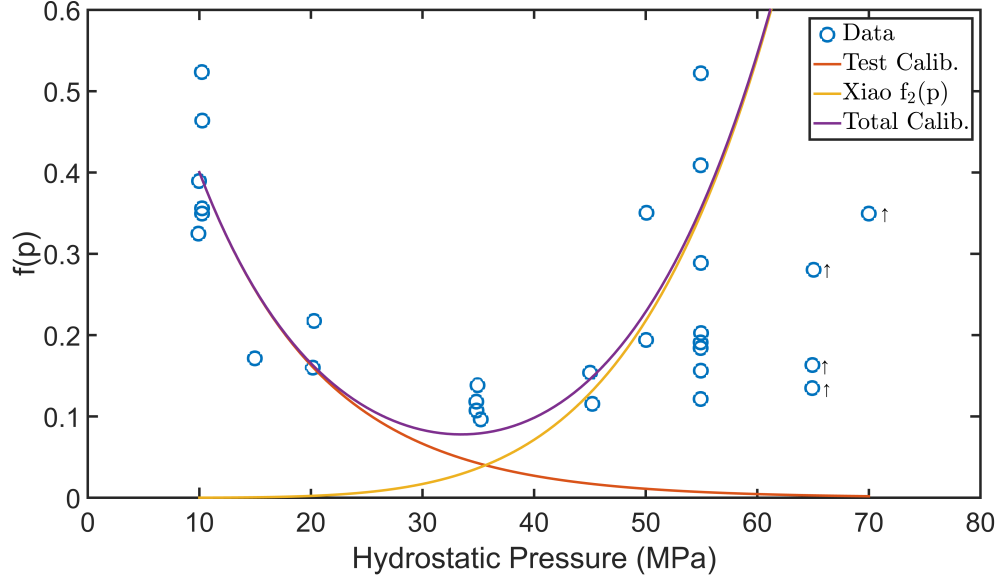


Figure 4.4: Recalibration of microcracking pressure-dependent damage function.

pressure. This behaviour was rectified by normalizing the exponential:

$$S = S_1 + S_2 = \int_0^t \left\{ f_1(p) \left( \frac{s}{s_0} \right)^{q_1} + f_2(p) \left( \frac{e^{s/s_0} - 1}{e - 1} \right) \right\} d\tau \quad (4.43)$$

where the divisor is implemented to insure that the von Mises stress function is equal to unity at the reference stress, similar to the power law behaviour of earlier models.

This can also be achieved by using a geometric function:

$$S = S_1 + S_2 = \int_0^t \left\{ f_1(p) \left( \frac{s}{s_0} \right)^{q_1} + f_2(p) \left( 2^{s/s_0} - 1 \right) \right\} d\tau \quad (4.44)$$

A comparison of the three formulations is provided in Figure 4.5. The original exponential formulation is non-zero at a von Mises stress of zero, as described, producing damage under a pure hydrostatic pressure. The normalized exponential and geometric forms correct this behaviour and are nearly identical, though the normalized exponential form does produce significantly higher damage at stresses much

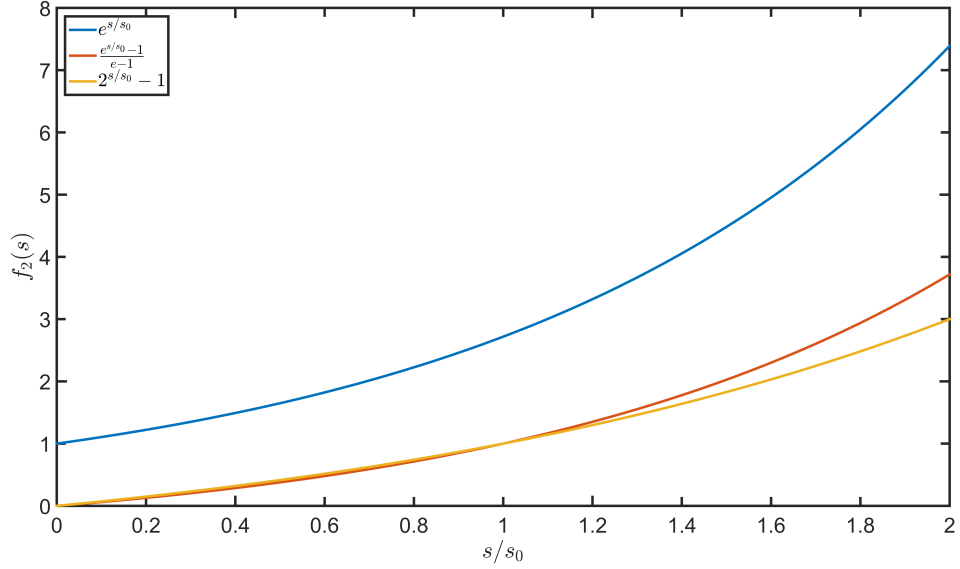


Figure 4.5: A comparison of the three formulations used to describe the von Mises stress component of high-pressure damage function.

greater than the reference stress,  $s_0$ .

Finally, it should be noted that, due to the positive definite nature of the von Mises stress, the model can produce identical damage rates under different combinations of confining pressure,  $P_c$ , and axial stress,  $\sigma_1$ , as outlined here:

$$\begin{aligned}\sigma_1 &= p \pm \frac{2}{3}s \\ P_c &= p \mp \frac{s}{3}\end{aligned}\tag{4.45}$$

In other words, there are stress states with axial stresses both above and below the desired hydrostatic pressure that produce identical amounts of damage. It is currently unclear whether this corresponds to physical results, as this author is unaware of any experiments examining this behaviour. However, it seems likely that the stress state with higher axial stress (and therefore a higher axial strain rate) would produce more

damage. Further examination of this behaviour is recommended.

### 4.2.1 Rate Equation Based Shift Function

As noted in Section 2.6.8, a shift function based on the rate equation can be used to compare the results of tests conducted at different temperatures, as per Barnes et al. (1971) and others. A review of the work of previous investigators is provided to highlight the need for a temperature-dependent damage function; the formulation of Barrette and Jordaan (2003) is given by:

$$\dot{\epsilon}_{ij}(T_1) = \dot{\epsilon}_{ij}(T_2) \exp \left[ \frac{Q(p)}{R_g} \left( \frac{1}{T_2} - \frac{1}{T_1} \right) \right] \quad (4.46)$$

where  $Q(p)$  is the pressure-dependent activation energy. While applicable at temperatures lower than approximately -8 °C, this formulation does not take into account the observed changes in either the pre-exponential or activation energy terms that occur at higher temperatures; to accurately apply the shift function to triaxial experiments, the effects of the hydrostatic pressure, von Mises stress, and temperature must be accounted for separately. Assuming that both the pre-exponential factor and the activation energy are dependent upon all three variables, we can represent the strain rate as:

$$\dot{\epsilon} = A_f(s, p, T) \exp \left[ -\frac{Q(s, p, T)}{R_g T} \right] = A_f(s) A_f(p) A_f(T) \exp \left[ -\frac{Q(s) Q(p) Q(T)}{R_g T} \right] \quad (4.47)$$

assuming that separation of variables is possible. The ratio of strain rates at different

temperatures can then be represented by:

$$\begin{aligned} \frac{\dot{\epsilon}(s, p, T)}{\dot{\epsilon}(s, p, T_0)} &= \frac{A_f(s)A_f(p)A_f(T)}{A_f(s)A_f(p)A_f(T_0)} \exp \left[ -\frac{Q(s)Q(p)Q(T)}{R_g T} + \frac{Q(s)Q(p)Q(T_0)}{R_g T_0} \right] \\ &= \frac{A_f(T)}{A_f(T_0)} \exp \left[ \frac{Q(s)Q(p)}{R_g} \left( \frac{Q(T_0)}{T_0} - \frac{Q(T)}{T} \right) \right] \end{aligned} \quad (4.48)$$

While the stress dependence of the pre-exponential factor cancels, the temperature dependence does not. To reproduce all experimental activation energy results,  $A_f(T)$  and  $Q(T)$  must increase at a transition temperature variably found to be -10, -8, or -6 °C by Glen (1955), Barnes et al. (1971), and Mizuno (1992), respectively, while  $A_f(p)$  and  $Q(p)$  must increase dramatically at very high pressures, as noted by Barrette and Jordaan (2003). It has also been shown (Mizuno, 1992) that the activation energy and pre-exponential term transition with increasing temperature occurs even under hydrostatic pressure, at least up to intermediate pressures; it is unclear if this behaviour extends to even higher pressures.

To model this behaviour, some assumptions about the form of  $A_f(p)$  and  $Q(p)$  are made. First, it is assumed that the results of Barrette and Jordaan (2003) represent the transition from one plateau to another; the low pressure results are averaged to provide a single value for all such pressures, while the values measured at 70 MPa (the limit of testing) are assumed to represent the high-pressure plateau. This corresponds to activation energies of 77.28 and 130.07 kJ/mol and pre-exponential terms of  $3.227 \cdot 10^{12}$  and  $1.81 \cdot 10^{23}$ , respectively. A linear extrapolation using the two high-pressure data points is then applied to bridge the plateaus; the complete functions can be seen in Figures 4.6. Finally,  $Q(T)$  is assumed to take the form of a step-function with values identical to those of  $Q(p)$  and a transition temperature of -8 °C. As per the results of Barnes et al. (1971), this is assumed to correspond to an increase in

$A_f(T)$  of approximately  $10^8$ .

While useful within temperature and pressure ranges where the activation energy remains constant, the shift function method generally fails otherwise; Figure 4.7 presents the natural logarithm of the minimum strain rate at temperatures from -5 to -15 °C using the parameters from Table 2.1. The strain rate should increase drastically as the depressed melting point is approached (at approximately 55 MPa), which the shift function fails to produce. Instead, a temperature-dependent damage function is necessary.

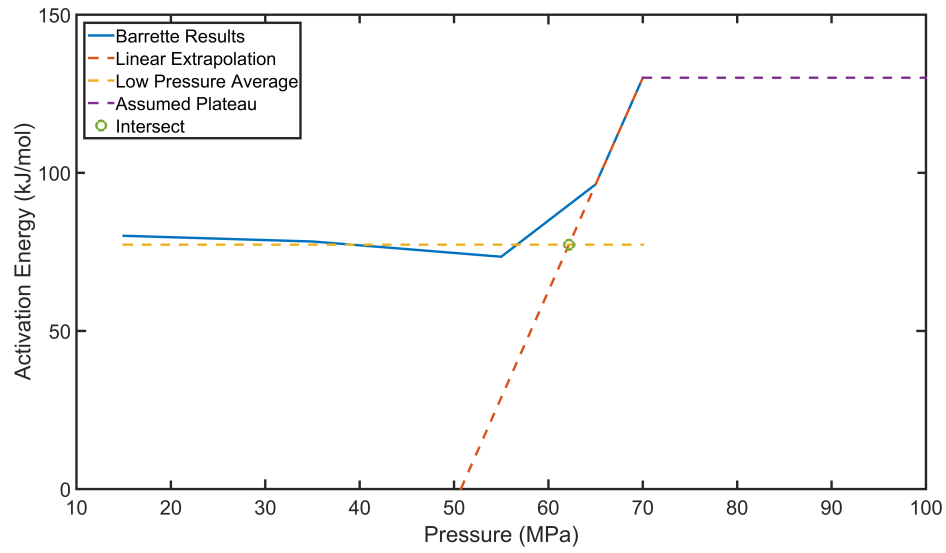
### 4.2.2 Temperature-Dependence of Damage

While useful when comparing the results of experiments performed at different ambient temperatures, the shift function does not model changing sample temperatures or elucidate the underlying relation between damage and temperature. Experiments have shown that the dominant microstructural change within an ice sample under identical stress conditions but different temperatures will differ; microcracking will dominate at low temperatures, while dynamic recrystallization dominates at high temperatures. To represent this, a temperature dependent damage function is necessary.

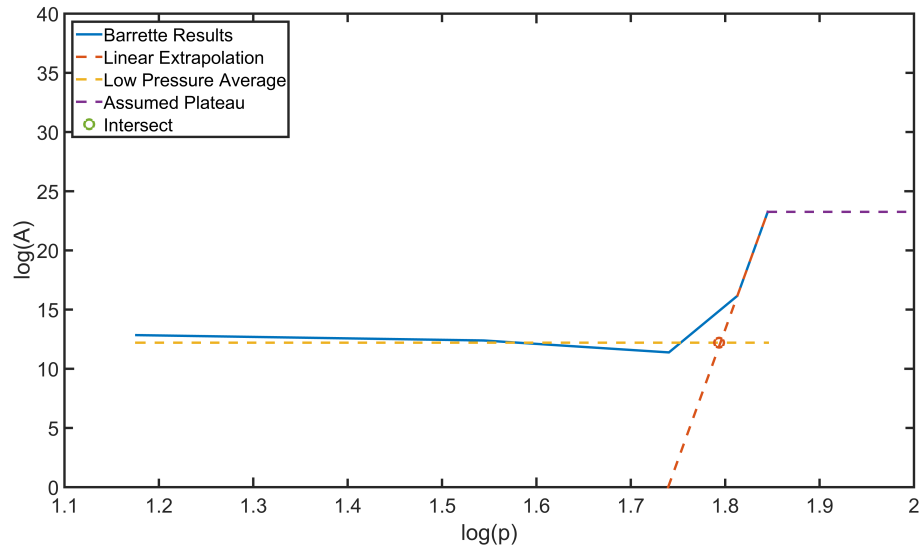
To illustrate, a brief exploration of the relevant material is provided. First, assuming that the temperature dependence is separable, the damage parameter can be represented generally by:

$$S = S_1 + S_2 = \int \{f_1(p)f_1(s)f_1(T) + f_2(p)f_2(s)f_2(T)\} dt \quad (4.49)$$

where  $S_1$  and  $S_2$  are the microcracking and dynamic recrystallization damage factors



(a) Activation energy



(b) Pre-exponential term

Figure 4.6: Pressure-dependent shift function parameters based on the results of Barrette (2014).

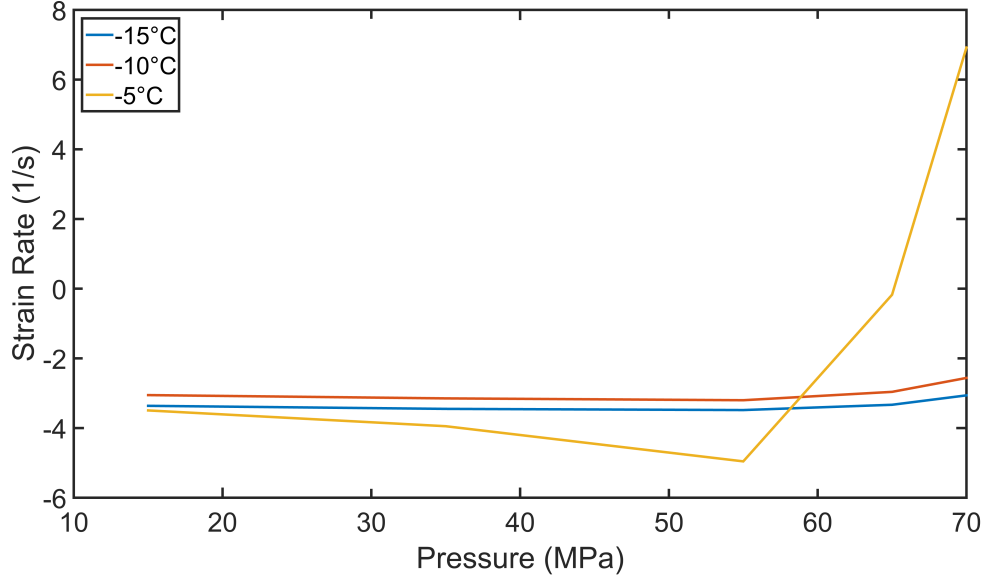


Figure 4.7: Natural logarithm of minimum strain rates at increasing temperatures and pressures recreated from the results of Jordaan and Barrette (2014) and Barnes et al. (1971).

respectively, and  $f(p)$ ,  $f(s)$ , and  $f(T)$  are functions dependent upon hydrostatic pressure, von Mises stress, and temperature respectively.

Li (2002) defined a shift function similar to the Arrhenius relation to compare the damage rate at different temperatures, given by:

$$\dot{S} = \{f_1(p)f_1(s) + f_2(p)f_2(s)\} e^{-\frac{Q}{R_g T}} \quad (4.50)$$

which is equivalent to defining the temperature-dependent damage functions of Equation 4.49 as:

$$f_1(T) = f_2(T) = e^{-\frac{Q}{R_g T}} \quad (4.51)$$

Taking the natural logarithm of the damage rate gives:

$$\ln(\dot{S}) = \ln(\dot{S}_0) - \frac{Q}{R_g T} \quad (4.52)$$

By taking the natural logarithm of the damage rate and plotting it versus the inverse temperature for a range of hydrostatic pressures, Li showed that this function produced a decent fit to his data. Two of these plots have been reproduced in Figure 4.8. Note that the straight line fit of the 70 MPa data appears to diverge at high temperatures, similar to the effect seen in Barnes et al. (1971); it is possible a change in activation energy occurs here as well.

It should also be noted that this formulation is incompatible with the standard shift function. Assuming that damage enhanced creep is given by:

$$\dot{\epsilon}' = \dot{\epsilon} e^S \quad (4.53)$$

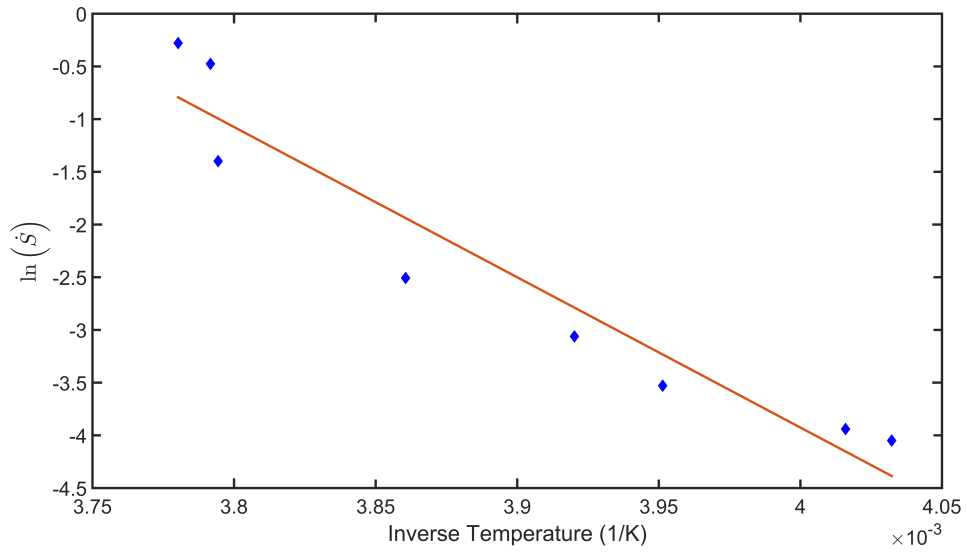
and that constant stress and temperature are applied, Li's shift function reduces to:

$$S = \dot{S}_0 \dot{S}_T t = \{f_1(p) f_1(s) + f_2(p) f_2(s)\} e^{-\frac{Q}{R_g T} t} \quad (4.54)$$

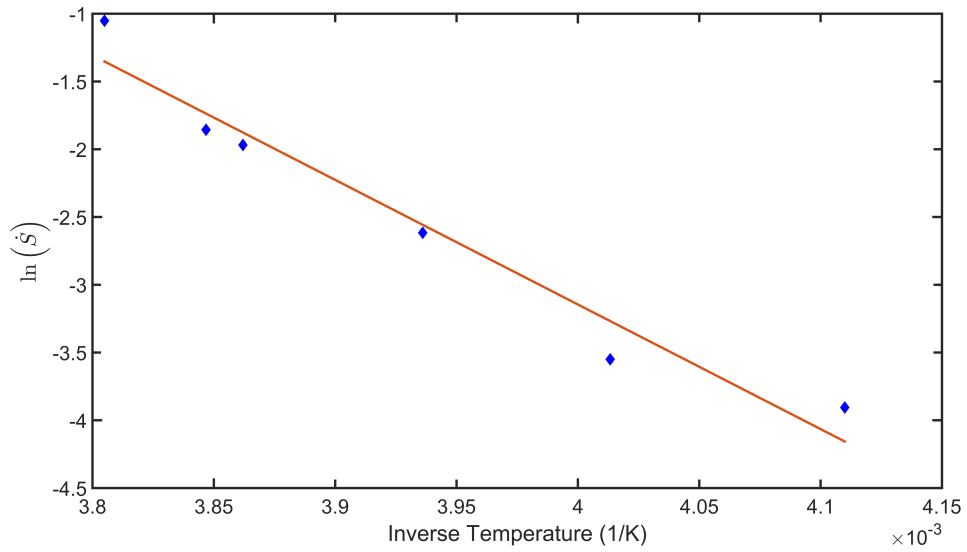
The ratio of strain rates under the same stress conditions but different temperatures is then given by:

$$\dot{\epsilon}'(T_1) = \dot{\epsilon}'(T_2) e^{\dot{S}_0 (\dot{S}_{T_1} - \dot{S}_{T_2}) t} = \dot{\epsilon}'(T_2) e^{\dot{S}_0 \left( e^{-\frac{Q}{RT_1}} - e^{-\frac{Q}{RT_2}} \right) t} \quad (4.55)$$

This form, while consistent with experimental results, does not describe the temperature dependence of the microcracking or dynamic recrystallization damage functions, and is thus of little interest. Instead, a damage function based on the thermal “distance” from the melting point was developed; in this case, the effect of pressure and temperature are inseparable.



(a)



(b)

Figure 4.8: Damage rate vs. inverse temperature plots. Above are the results for 70 MPa confining pressure, below are the 15 MPa results. Recreated from Li (2002).

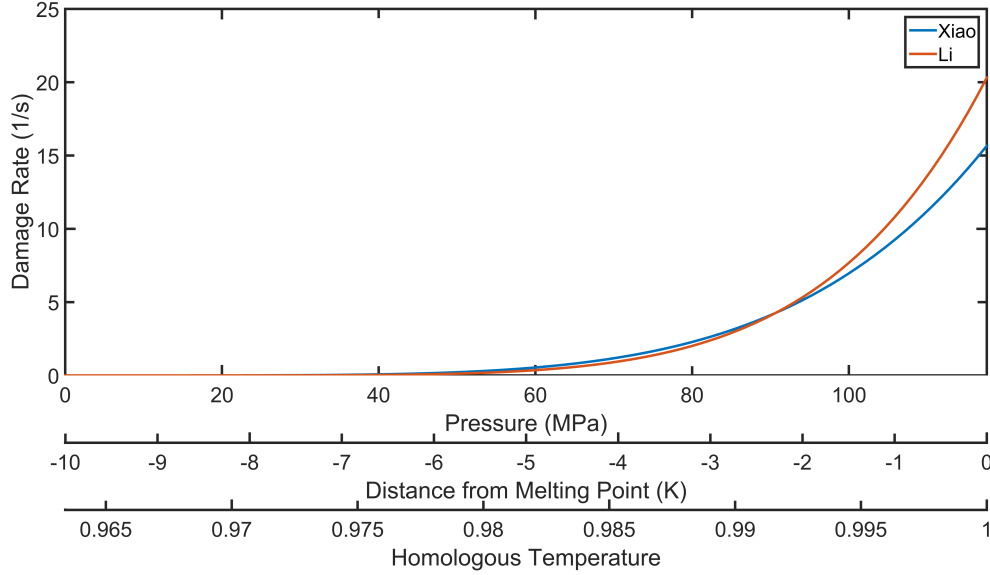


Figure 4.9: High-pressure ( $S_2$ ) damage rates of Xiao and Li compared to the pressure, distance from melting point, and homologous temperature. Environmental temperature is  $-10^\circ\text{C}$ .

In order to develop a temperature-dependent formulation for the high pressure damage rate of ice, two assumptions were made and their results compared:

1. That the damage rate vs thermal distance from the melting point,  $\Delta T_m = T - T_m$ , is constant, or
2. That the damage rate vs homologous temperature,  $T_h = \frac{T}{T_m}$ , is constant.

Under these assumptions, the pressure-dependent damage functions,  $f_2(p)$ , of Xiao (1997) and Li (2002), obtained from triaxial compression tests at  $-10^\circ\text{C}$ , become either  $f_2(\Delta T_m)$  or  $f_2(T_h)$ , as seen in Figure 4.9.

These functions can then be used as a master curve from which the damage

parameter at other combinations of pressure and temperature can be obtained, first by calculating the melting temperature,  $T_m$ , of ice at a given pressure,  $p$ , using:

$$\frac{\delta p}{\delta T} = \frac{L_f}{T (C_w e^{(A_w - K_w)} - C_i e^{(A_i - K_i)})} \quad (4.56)$$

where  $L_f$  is the latent heat of fusion,  $A_{w/i}$  and  $K_{w/i}$  are the integrals of the coefficient of thermal expansion,  $\alpha_{w/i}$ , with respect to temperature and the compressibility,  $\kappa_{w/i}$ , with respect to pressure, respectively, and  $C_{w/i}$  are the resulting integration constants:

$$A_{w/i} = \int \alpha_{w/i}(T) \delta T - C_{A_{w/i}} \quad (4.57)$$

$$K_{w/i} = \int \kappa_{w/i}(P) \delta P - C_{K_{w/i}} \quad (4.58)$$

$$C_{w/i} = \exp [C_{A_{w/i}} + C_{K_{w/i}}] \quad (4.59)$$

as outlined in the work of Nordell (1990).  $\Delta T_m$  or  $T_h$  can then be calculated, followed by the corresponding pressure at the reference temperature,  $T_0 = -10^\circ\text{C}$ . This pressure can then be used to calculate the damage rate from the master curves, as can be seen in Figure 4.10. Note that this relation only holds for pressures up to approximately 220 MPa, past which the melting temperature begins to increase due to the formation of other forms of crystalline ice. A numerical integration scheme is required to solve Equation 4.56, as all parameters are temperature and pressure dependent.

It should be noted that this formulation is limited by the range of possible pressures at  $-10^\circ\text{C}$ ; the damage rate is only defined for compressive forces, or pressures greater than 0 MPa, while sample-wide pressure melting will occur at hydrostatic pressures of approximately 117.6 MPa or greater. These limits correspond to a  $\Delta T_m$  of  $[-10, 0]$  and a  $T_h$  of  $[0.9634, 1]$ . If a wider range is desired, a series of experiments at

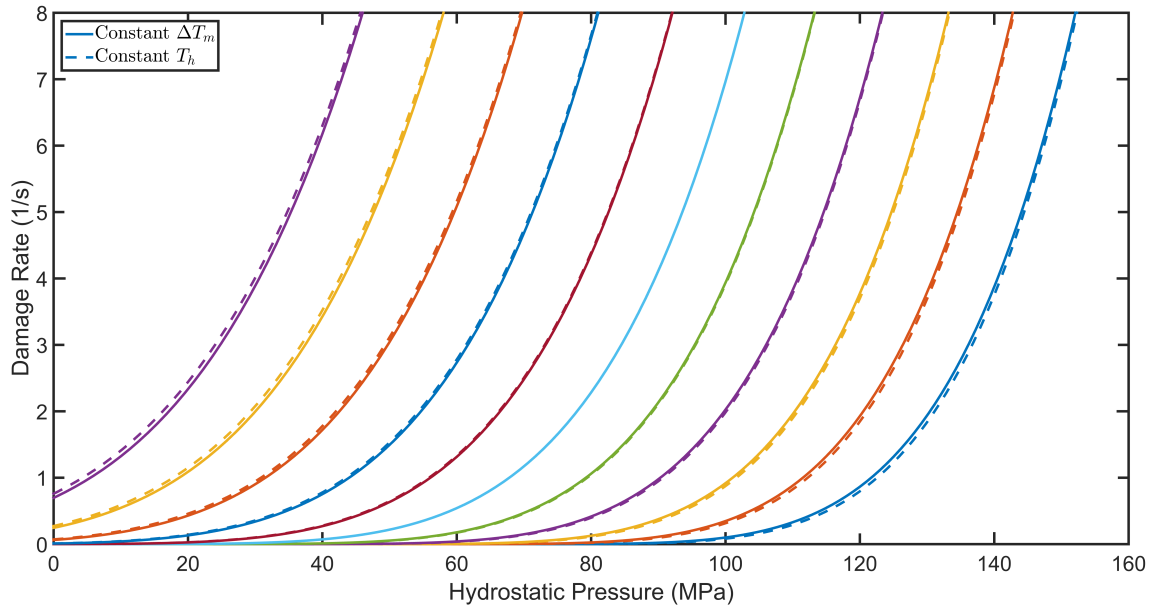


Figure 4.10: High pressure damage rates for temperatures ranging from  $-5^{\circ}\text{C}$  (left) to  $-15^{\circ}\text{C}$  (right). Solid lines represent the results assuming that the rate is constant with respect to the distance from the melting point, dashed the results assuming that the rate is constant with respect to the homologous temperature. The results differ only slightly, with the differences becoming more pronounced with distance from the reference temperature. While the non-zero damage at  $p = 0$  is unrealistic, damage is not calculated under such a stress condition, and as such can safely be ignored.

$-22^{\circ}\text{C}$  is recommended, which represents the lower limit of relation 4.56. The range of applicability would then extend from a  $\Delta T_m$  of  $[-22, 0]$  and a  $T_h$  of  $[0.9195, 1]$ . Currently,  $f_2(\Delta T_m)$  and  $f_2(T_h)$  are assumed to equal zero for values of  $\Delta T_m$  and  $T_h$  that are less than these lower limits.

An in-depth examination of the response of this temperature-dependent damage function is presented in Chapter 6.

### 4.3 Elastic Damage

The effect of damage on the elastic properties of the sample must also be taken into account to accurately model the compressive behaviour of ice. Multiple formulations for elastic damage have been implemented and examined; the constant Poisson's ratio model, the constant bulk modulus model, and the crack-based model of Kachanov (1993). Each can be defined in terms of a series of constants;  $C_1$ ,  $C_2$ ,  $C_3$ , and  $C_4$ :

$$\frac{E}{E_0} = \frac{1}{1 + C_1 S_1} \quad (4.60)$$

$$\frac{G}{G_0} = \frac{1}{1 + C_2 S_1} \quad (4.61)$$

$$\frac{\nu}{\nu_0} = \frac{1 + C_3 S_1}{1 + C_1 S_1} \quad (4.62)$$

$$\frac{K}{K_0} = \frac{1}{1 + C_4 S_1} \quad (4.63)$$

where  $G$  and  $K$  are the shear and bulk moduli, respectively, while  $_0$  represents the initial value for each elastic property. It is important to note that microcracking damage alone, represented by  $S_1$ , should be used to describe elastic damage; the model of Kachanov is based upon the presence of dilute microcracks, and does not provide a theoretical basis for the accumulation of dynamic recrystallization or pressure melting. The use of the full damage parameter,  $S = S_1 + S_2$ , in the elastic damage formulation is explored in the following sections only for the sake of completeness.

There is also some evidence to suggest that the elastic properties of ice do not change under compressive damage (Jordaan et al., 1992b; Kalifa et al., 1992; Stone et al., 1997), unlike the creep and delayed elastic behaviour. The effect of constant elastic properties can also be examined by setting the constants in equations 4.60-4.63 to zero. The constants for each model are listed in Table 4.2.

Model	$\nu = \nu_0$	$K = K_0$	Kachanov
$C_1$	1	1	$\frac{16(1 - \nu_0^2)(1 - 3\nu_0/10)}{9(1 - \nu_0/2)}$
$C_2$	$C_1$	$\frac{3C_1}{2(1 + \nu_0)}$	$\frac{16(1 - \nu_0)(1 - \nu_0/5)}{9(1 - \nu_0/2)}$
$C_3$	$C_1$	$\frac{C_1}{2\nu_0}$	$\frac{8(1 - \nu_0^2)}{45(1 - \nu_0/2)}$
$C_4$	$C_1$	0	$\frac{16(1 - \nu_0^2)}{9(1 - 2\nu_0)}$

Table 4.2: Constants for elastic damage models.

The effect of damage on elastic strain can be seen when applied to equation 4.11:

$$\epsilon_{ij}^e = \frac{1}{E_0} \left( (1 + \nu_0) \sigma_{ij} - \nu_0 \sigma_{kk} \delta_{ij} + S_1 \left( (C_1 + \nu_0 C_3) \sigma_{ij} - \nu_0 C_3 \sigma_{kk} \delta_{ij} \right) \right) \quad (4.64)$$

where  $\sigma_{kk}$  is the sum of the normal stresses, which is related to the hydrostatic pressure by the equation  $p = \sigma_{kk}/3$ . In terms of the deviatoric and volumetric components the elastic strain becomes:

$$\epsilon_{ij}^e = \frac{1}{E_0} \left( (1 + \nu_0) s_{ij} + (1 - 2\nu_0) p \delta_{ij} + S_1 \left( (C_1 + \nu_0 C_3) s_{ij} + (C_1 - 2\nu_0 C_3) p \delta_{ij} \right) \right) \quad (4.65)$$

The effect of damage on elastic strain under each model can be seen in Figures 4.11 and 4.12. All models produce an increase in elastic strain as damage accrues under a constant stress. Only the constant bulk modulus model produces a constant elastic strain with increasing damage under a constant hydrostatic pressure. Note that this is only a concern when the exponential form of the high-pressure damage function is used.

These damage forms are also used to describe the deterioration of the Kelvin spring of the Burgers model, represented by  $E_K$ . The results of different models

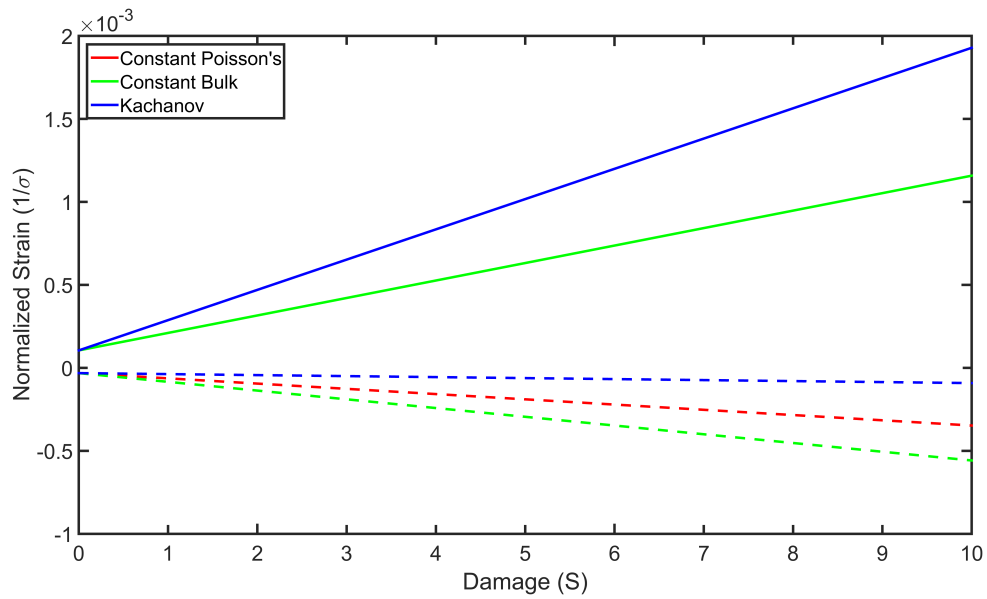


Figure 4.11: Normalized elastic axial (—) and lateral (---) strains under uniaxial compression for three elastic damage models. Note that the constant Poisson's and Bulk modulus models produce the same axial strain under these conditions.

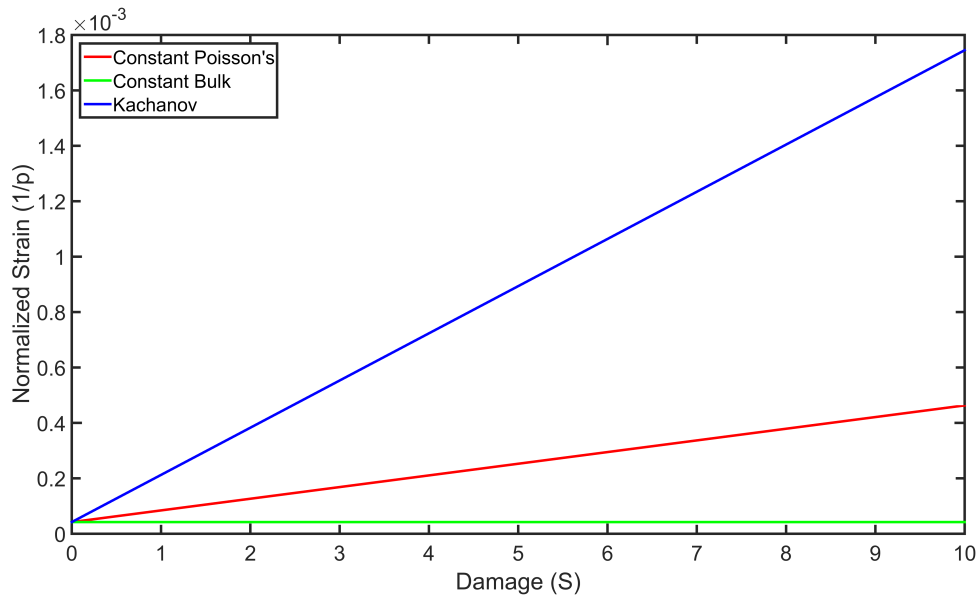


Figure 4.12: Normalized elastic strains under hydrostatic pressure for three elastic damage models.

under different conditions are shown in Figure 4.13. Unlike elastic strain, the delayed elastic strain results depend upon the chosen applied stress and calibration.

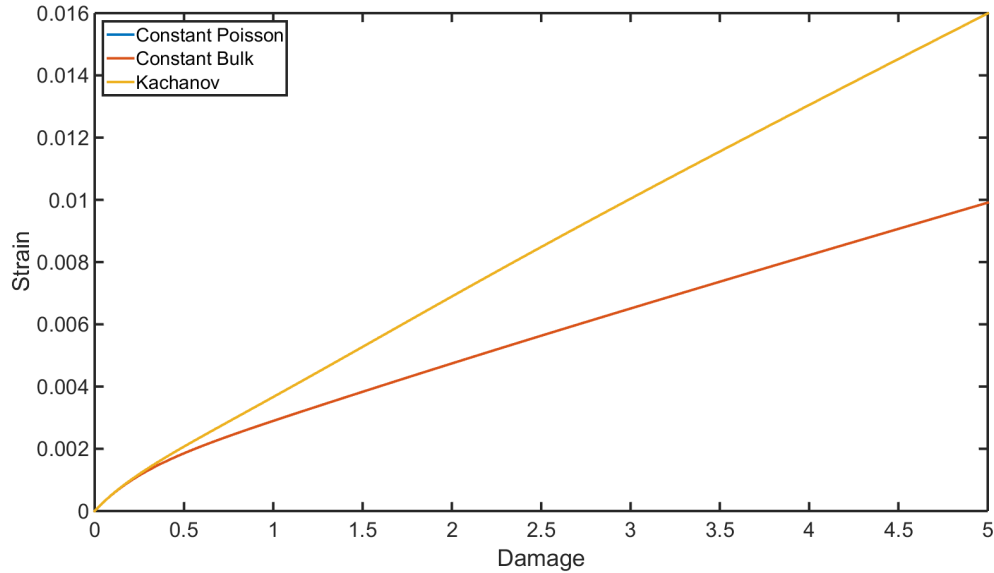


Figure 4.13: Delayed elastic strain for three models of elastic damage under a confining pressure of 30 MPa and a von Mises stress of 15 MPa. Note that the constant Poisson’s and Bulk modulus models produce identical results.

## 4.4 Power Law Breakdown

It has long been known that a material undergoing creep deformation diverges from power law behaviour under large uniaxial stresses. This is commonly referred to as power law breakdown. The source of this breakdown is still debated, though evidence suggests that the transition is one from a regime of homogeneous deformation to one dominated by grain boundary sliding (Nabarro, 2004).

Empirical modelling of this behaviour generally produces an exponential stress-dependence (see Jonas et al. (1969) for an example). Garofalo (1963) proposed the use of the hyperbolic sine function,  $\sinh$ , to accurately model the full range of stress behaviour in metals. The function was successfully applied to ice under uniaxial stress conditions by Barnes et al. (1971), using the following model:

$$\sinh^n \alpha\sigma \approx \begin{cases} (\alpha\sigma)^n & : \alpha\sigma < 0.8 \\ \frac{e^{n\alpha\sigma}}{2^n} & : \alpha\sigma > 1.8^1 \end{cases} \quad (4.66)$$

where  $n$  is the standard power law exponent,  $\alpha$  is a normalization factor, and  $\sigma$  is the applied uniaxial stress. The  $\alpha\sigma$  limits are chosen such that the results of the limit functions differ from the results of the  $\sinh$  function by less than 10 %, as can be seen in Figure 4.14.

To discern whether power law breakdown is a concern under the conditions of interest during an ice-structure interaction, the data Meglis et al. (1999) gathered from triaxial compression experiments on ice was inspected for signs of divergence from power law behaviour. As per that work, the stress and strain rates were examined at strains from 2 % to 40 %. The minimum strain rate and the corresponding true stress were also extracted from the available raw data. Data points where the sample could no longer support stress, hereafter referred to as outliers, were ignored during the data analysis. The outliers were isolated by comparing the ratio of current stress to initial stress; it was found that a ratio of less than 0.5 was always associated with the samples inability to support stress, as illustrated in Figure 4.15 for a total strain of 40 %.

---

<sup>1</sup>Note that the value of 1.2 printed in Barnes et al. (1971) appears to be a typo

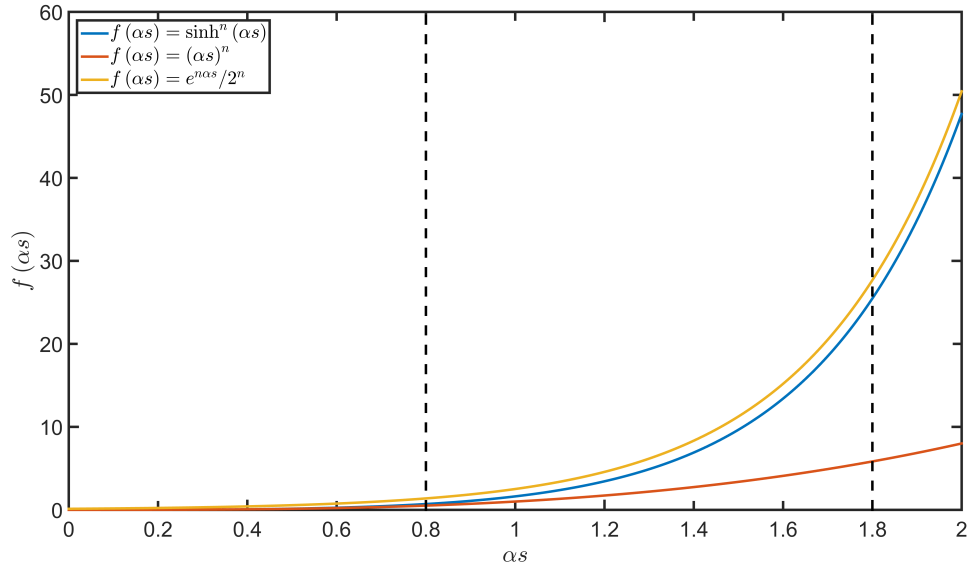


Figure 4.14: Example behaviour of sinh function and its limits over relevant  $\alpha\sigma$  range. A value of  $n = 3$  was used.

The full data set is recreated in Figures 4.16. A notable increase in strain rate is observed with increasing strain. Signs of divergence from power law behaviour are observed to begin at strains of 20 % and greater, which likely corresponds to the point at which secondary creep begins to dominate the strain rate behaviour.

All data sets show signs of a secondary trend consisting of significantly higher strain rates at low stresses, as seen in Figure 4.17. This appears to correspond to the data noted as outliers in Figure 4.15. These data points are likely associated with strain localization (SL) and are ignored during the analysis of power law breakdown; the remaining data points are assumed to undergo uniform grain refinement (UGR).

A linear fit to the natural logarithms of the strain rate and stress data at lower strains was used to provide a baseline comparison to the work of Meglis et al. (1999)

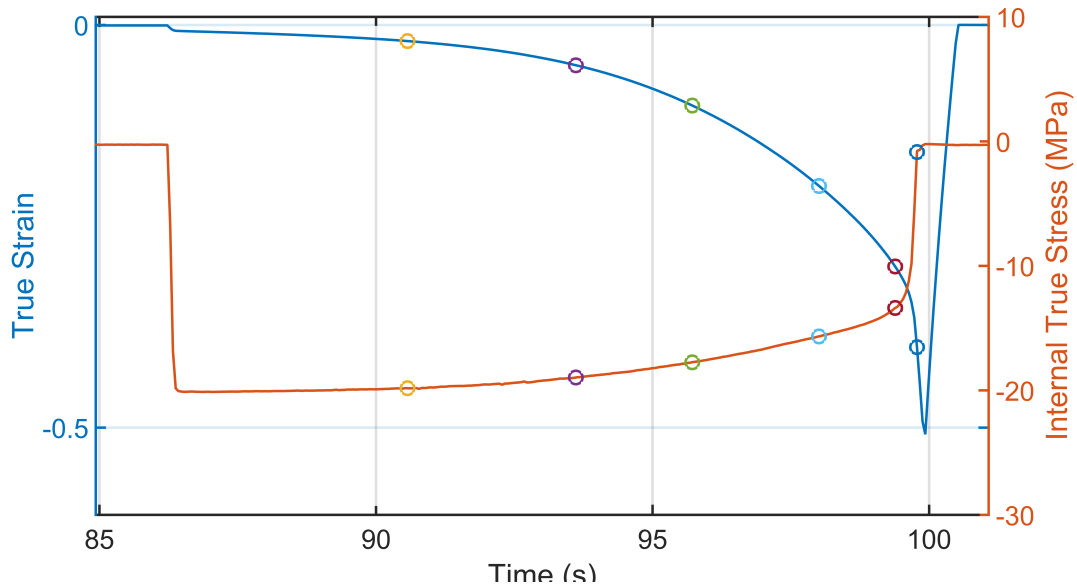


Figure 4.15: Internal true stress and true strain during test IT960812. The coloured circles represent increasing levels of strain, from 2 % up to 40 %.

and others; assuming a power law relation, the slope will provide the value for the exponent  $n$ , while the intercept,  $b$ , will provide a limiting function for the pre-exponential term,  $A$ , and the normalization constant,  $\alpha$ , of the form:

$$e^b = A\alpha^n. \quad (4.67)$$

The fit produces satisfactory results when applied to the data points that underwent UGR, with  $n$  ranging from 2.75 at 2 % strain up to 3.65 at 10 % strain and  $b$  ranging from -13.9 to -14.1, with adjusted  $R^2$  values of 0.76 or greater. Note that the results for  $n$  are significantly lower than those reported by Meglis et al. (1999), possibly due to the exclusion of data deemed associated with strain localization in this work.

While the linear fit fails to adequately describe the the full range of data, it can

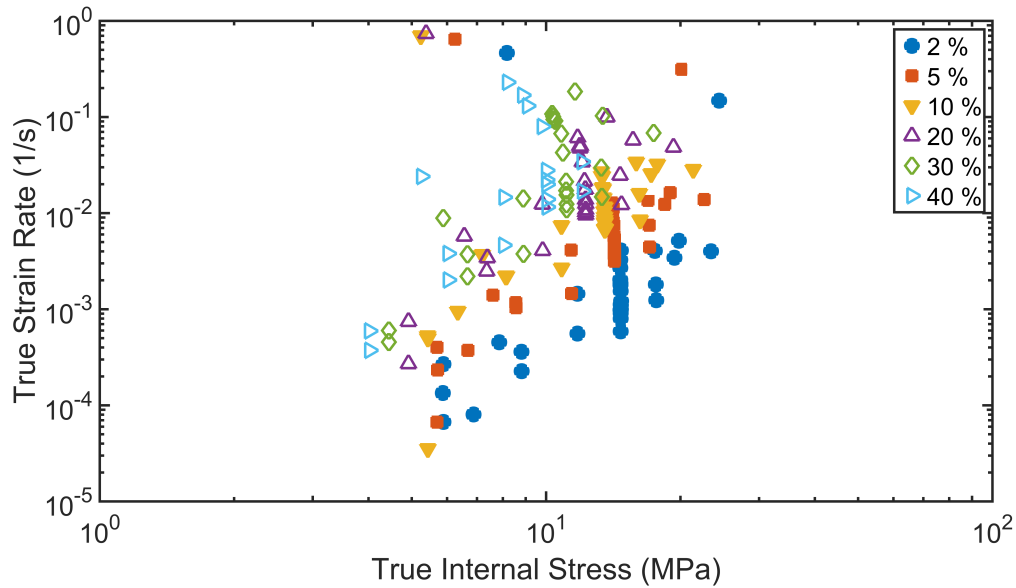


Figure 4.16: Meglis et al. (1999) strain rate vs stress data at increasing levels of strain.

be used to provide a suitable estimate of the parameters of Equation 4.66 if the data points associated with power law breakdown are ignored. Since the y-intercept provides only a limiting function for  $\alpha$  and  $A$ , assumptions on their form must be made. The average value of  $\alpha = 0.27$  from Barnes et al. (1971) was found to provide a satisfactory starting point, as seen in Figure 4.18.

Noting that deviations from power law behaviour appear only after reaching 20 % strain, it seems plausible that observed behaviour may be due to damage accumulation instead of power law breakdown. Sorting the data based on the hydrostatic pressure produces Figure 4.19; the data with strain rates significantly greater than the power-law fit line all correspond to either high or low hydrostatic pressures, which map to the conditions where strain localization and excessive damage are more likely.

Given these results, it would seem reasonable to conclude that power law break-

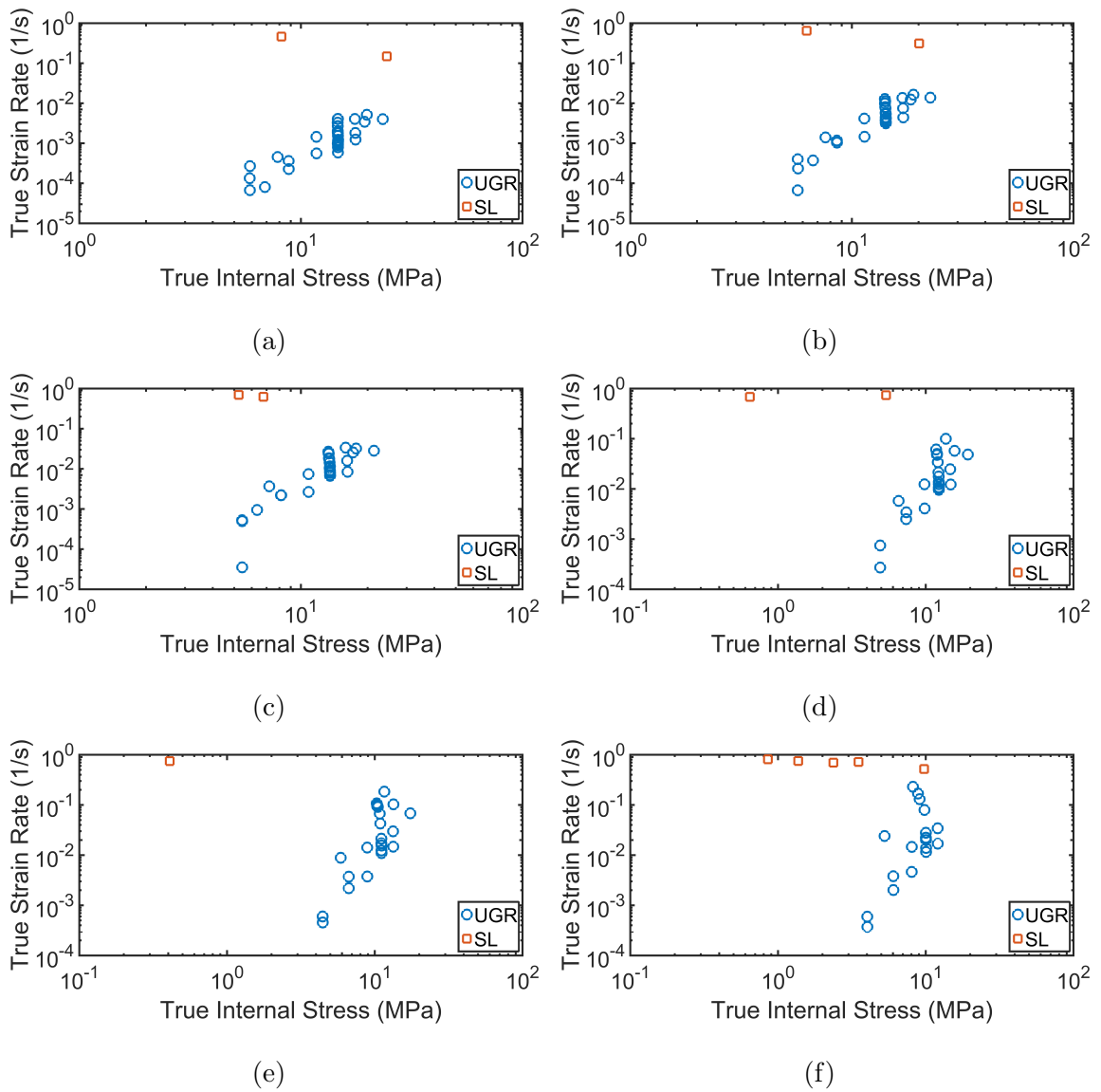


Figure 4.17: Strain rate data at range of % strains. The total strain increases from (a)-(f) as follows: 2 %, 5 %, 10 %, 20 %, 30 %, and 40 %.

down is suppressed during the triaxial compression of ice, at least for the von Mises stresses examined here. Since power law breakdown is known to occur under uniaxial test conditions, the calibration values of Barnes et al. (1971) should be thought of as

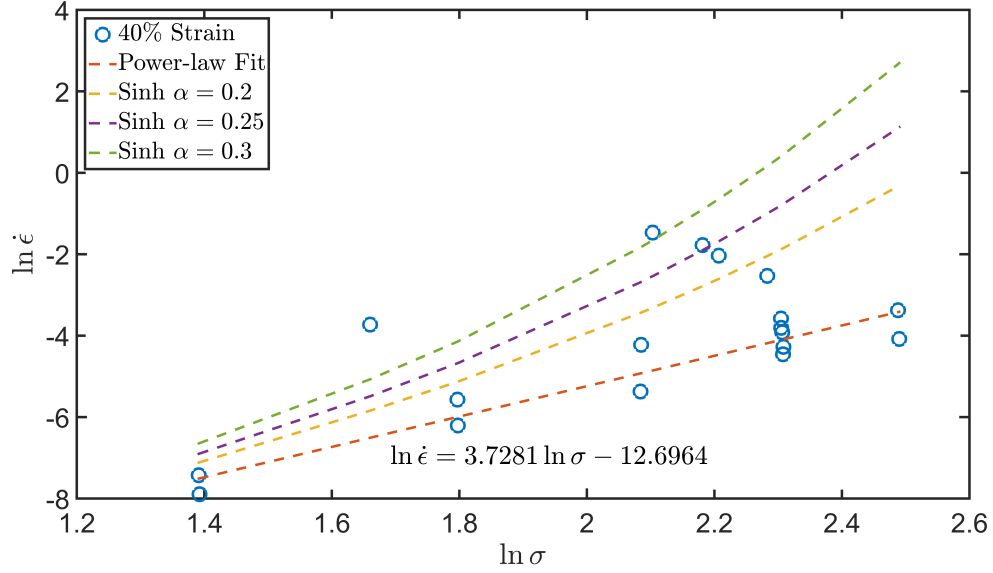


Figure 4.18: Sinh fits to Meglis et al. (1999) data at 40 % strain with  $\alpha$  ranging from 0.2 to 0.3.

a lower limit, with a pressure-dependent  $\alpha$  of the form:

$$\alpha(p) = 0.27e^{-\frac{p}{p_n}} \quad (4.68)$$

where  $p_n$  is some normalization constant. Taking power law breakdown into account, the modified formulation for secondary creep becomes:

$$\dot{\epsilon}_{ij}^c = \frac{3}{2}\dot{\epsilon}_0^c \left( \frac{\sinh \alpha(p)s}{\sinh \alpha(p)s_0} \right)^m \frac{s_{ij}}{s} \quad (4.69)$$

which reduces to the reference strain rate of Sinha (1978) under uniaxial conditions when  $s = s_0$ .

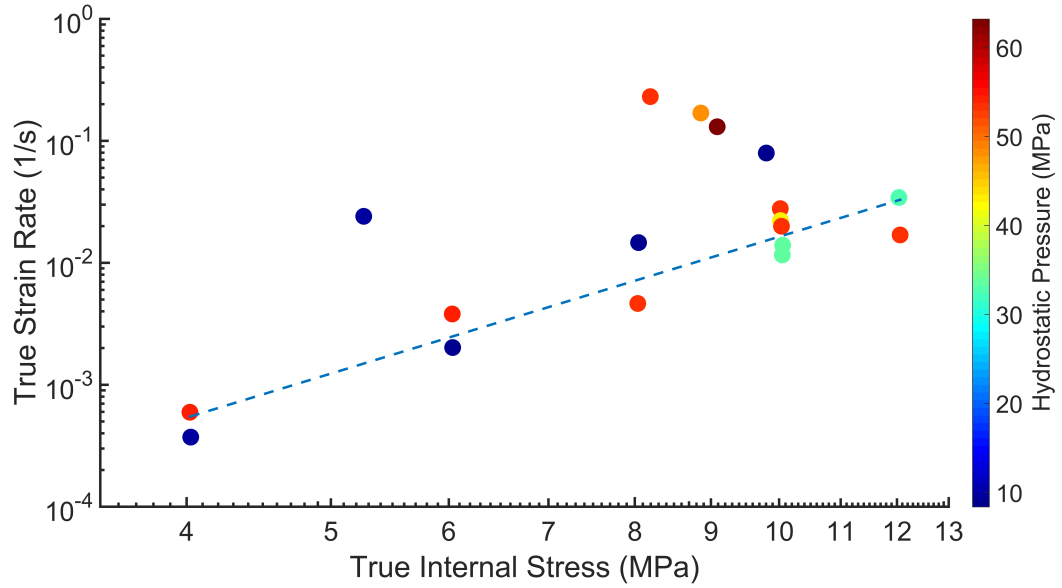


Figure 4.19: Meglis data at 40 % strain color-coded based on hydrostatic pressure. The dashed line represents the power-law fit to the data, as per Figure 4.18

## 4.5 Summary of Additions to Model

Numerous modifications and additions, both major and minor, to the constitutive model of earlier investigators have been presented in this Chapter; a brief summary of these changes is provided here for the sake of clarity:

1. The definition of the deviatoric delayed elastic strain rate,  $\dot{\epsilon}_{ij}^d$ , was modified to include the absolute value of the von Mises stress in the Kelvin dashpot,  $s^d$ , and apply the sign function to the same stress. Otherwise, delayed elastic recovery would never occur in cases where the power law exponent,  $n$ , was even.
2. The definition of the pressure-dependent microcracking damage function,  $f_1(p)$ , was changed from a quadratic relation to a decaying exponential. This was done

in order to remove its dependence on a cut-off pressure, which was highly likely to be temperature dependent; the transition from microcracking to dynamic recrystallization requires larger pressures at lower temperatures.

3. The exponential function used to describe the effect of von Mises stress on high-pressure damage,  $f_2(s)$ , was normalized such that  $f_2(0) = 0$  and  $f_2(s_0) = 1$ , as per the original power law expression.
4. The shift function previously used to describe delayed elastic and viscous creep strain rates at different temperatures was modified to include the noted increases in activation energy,  $Q$ , and pre-exponential factor,  $A_f$ , at increasing pressures and temperatures.
5. A temperature-dependent damage function was developed to describe the changes in damage evolution observed at different temperatures. Two versions of this function were developed; one assumes that the amount of dynamic recrystallization observed is dependent upon the thermal distance from the melting point,  $T_m$ , the other that homologous temperature,  $T_h$ , is the defining parameter. Both are found to produce similar results theoretically.
6. The definition of the deviatoric viscous creep strain rate,  $\dot{\epsilon}_{ij}^c$ , was modified to include a term accounting for power law breakdown; as discussed, power law breakdown appears to be suppressed at high hydrostatic pressures. As such, a decaying exponential form for the normalizing factor,  $\alpha(p)$ , was implemented such that power law breakdown would occur only at low hydrostatic pressures, as per Barnes et al. (1971).

# Chapter 5

## Validation of Finite Element Model

This chapter describes the steps taken to validate the finite element model prior to examining the additions and refinements to the constitutive model introduced in Chapter 4; the results of these changes can be found in Chapter 6.

### 5.1 Validation

To acquire useful information from any simulation a series of validation tests must first be completed. To be considered valid, the simulation must: a) output results that agree with theoretical calculations, and b) output results that reproduce experimental results. As mentioned in Chapter 4, there are a wide variety of potentially accurate models to simulate. To ensure that each model was accurately simulated, a series of single element creep-relaxation simulations were performed.

### 5.1.1 Creep-Relaxation Simulations

Single element triaxial creep-relaxation cycles were used to validate the implementation of the constitutive models described in Chapter 4. A creep-relaxation cycle can be represented in general by the following conditions: first, a confining pressure,  $P_c$ , is applied and held constant throughout the cycle. An axial stress,  $\sigma_1^a$ , is applied for a period of time ending at  $t = t_1$ , followed by a period of time at a reduced axial stress,  $\sigma_2^a$ . Such a state of stress is often presented in terms of its hydrostatic and deviatoric components as follows:

$$\sigma_{ij}(t) = p^h(t) \delta_{ij} + s_{ij}(t) \quad (5.1)$$

$$\sigma_{ij}(t) = \begin{bmatrix} P_c + \Delta\sigma(t) & 0 & 0 \\ 0 & P_c & 0 \\ 0 & 0 & P_c \end{bmatrix} = p^h(t) \begin{bmatrix} 1 & 0 & 0 \\ 0 & 1 & 0 \\ 0 & 0 & 1 \end{bmatrix} + \frac{\Delta\sigma(t)}{3} \begin{bmatrix} 2 & 0 & 0 \\ 0 & -1 & 0 \\ 0 & 0 & -1 \end{bmatrix} \quad (5.2)$$

with:

$$\Delta\sigma(t) = \Delta\sigma_1 + (\Delta\sigma_2 - \Delta\sigma_1)H(t - t_1) \quad (5.3)$$

$$\Delta\sigma_1 = \sigma_1^a - P_c, \quad \Delta\sigma_2 = \sigma_2^a - P_c \quad (5.4)$$

$$p^h(t) = P_c + \frac{\Delta\sigma(t)}{3} = p_1^h + (p_2^h - p_1^h)H(t - t_1) \quad (5.5)$$

$$p_1^h = P_c + \frac{\Delta\sigma_1}{3}, \quad p_2^h = P_c + \frac{\Delta\sigma_2}{3} \quad (5.6)$$

where the stress difference,  $\Delta\sigma(t)$ , has been simplified for convenience,  $\Delta\sigma_1$ ,  $\Delta\sigma_2$ ,  $p_1^h$ , and  $p_2^h$  are the stress differences and hydrostatic pressures before and after  $t_1$ , respectively, and  $H(t - t_1)$  is the Heaviside step function.  $\Delta\sigma(t)$  can be positive or negative, but the model is designed with a positive  $\Delta\sigma(t)$  in mind. In either case,

the von Mises stress is given by:

$$s(t) = |\Delta\sigma(t)| = s_1^v + (s_2^v - s_1^v) H(t - t_1) \quad (5.7)$$

$$s_1^v = |\Delta\sigma_1|, \quad s_2^v = |\Delta\sigma_2| \quad (5.8)$$

where  $s_1^v$  and  $s_2^v$  are the von Mises stresses before and after  $t_1$ , respectively. Under these conditions,  $s_{ij}/s$  is a constant (either  $\pm^2/3$ ,  $\mp^1/3$ , or 0) for all values of  $s$  save zero, where it is mathematically undefined. The  $\lim_{s \rightarrow 0} s_{ij}/s$  does exist, and retains the value  $s_{ij}/s$  had prior to reaching zero. This stress state is reproduced in Figures 5.1.

Analytical solutions exist for each component of the constitutive relation described in Chapter 4, save for the case of delayed elastic strain with damage. For the special case of no damage, the isotropic elastic strain is given by:

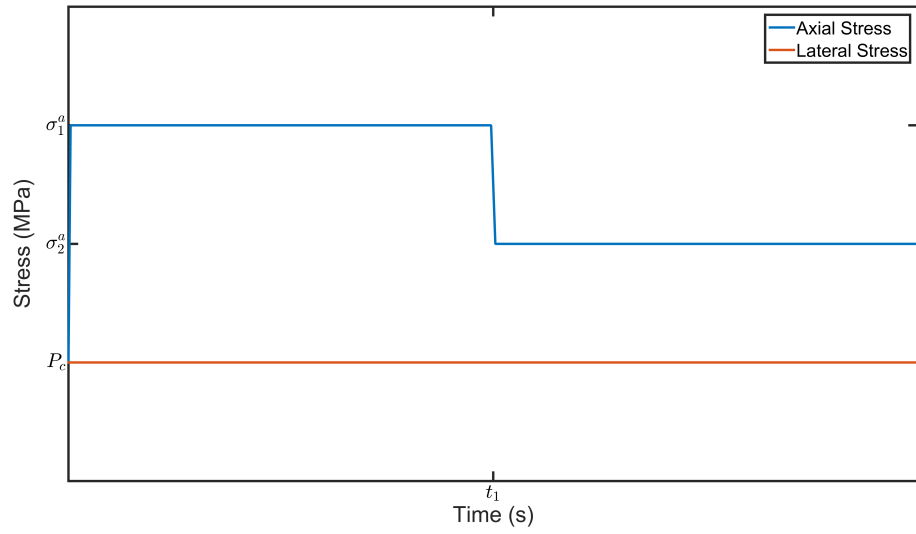
$$\epsilon_{ij}^e(t) = \frac{1}{E_0} \begin{bmatrix} (1 - 2\nu_0) P_c + \Delta\sigma(t) & 0 & 0 \\ 0 & (1 - 2\nu_0) P_c - \nu_0 \Delta\sigma(t) & 0 \\ 0 & 0 & (1 - 2\nu_0) P_c - \nu_0 \Delta\sigma(t) \end{bmatrix} \quad (5.9)$$

The resulting strain can be seen in Figure 5.2.

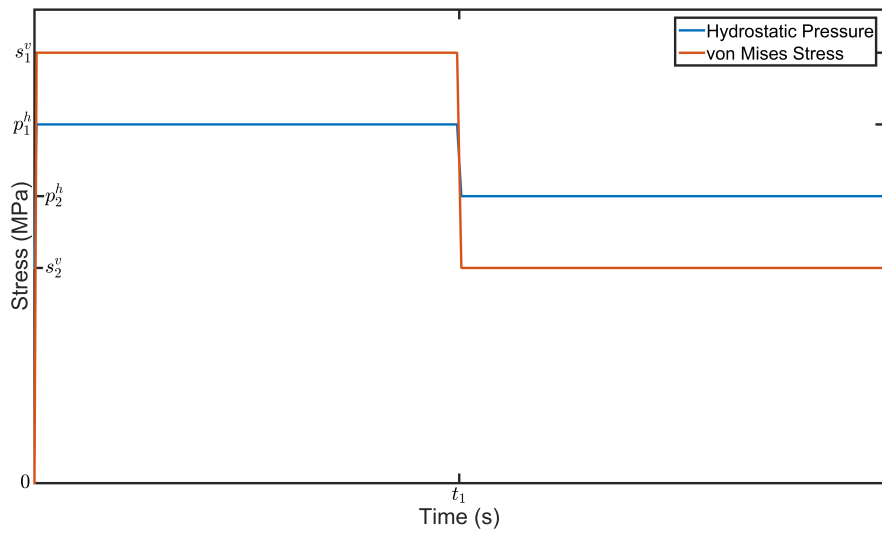
The deviatoric component of the secondary creep strain rate is given by:

$$\dot{\epsilon}_{ij}^c = \dot{\epsilon}^c \frac{s_{ij}}{s} = \frac{\dot{\epsilon}^c}{3} \begin{bmatrix} 2 & 0 & 0 \\ 0 & -1 & 0 \\ 0 & 0 & -1 \end{bmatrix} \quad (5.10)$$

where  $\dot{\epsilon}^c = \frac{3}{2} \dot{\epsilon}_0^c \left( \frac{s}{s_0^\mu} \right)^m$  is the equivalent secondary creep strain rate, the general



(a)



(b)

Figure 5.1: General state of stress during validation. (a) demonstrates the normal stresses, (b) the stress invariants.

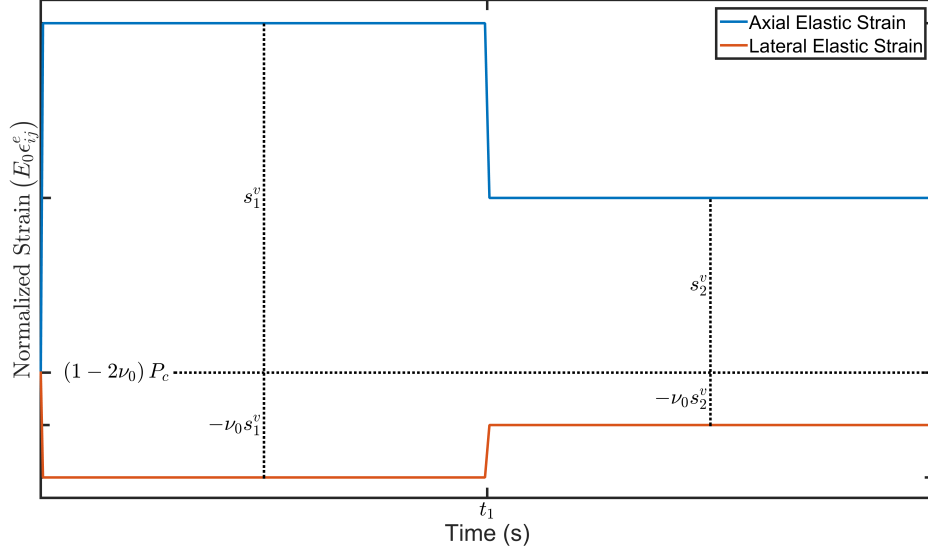


Figure 5.2: Elastic strain with no damage.

solution to which is simply:

$$e^c = A_c s^m t + C \quad (5.11)$$

$$A_c = \frac{3}{2} \frac{\dot{\epsilon}_0^c}{(s_0^\mu)^m} \quad (5.12)$$

where  $m$  is the secondary creep exponent and  $C$  is an integration constant. Applying a general creep-relaxation cycle produces an equivalent secondary creep strain of:

$$e^c = A_c \left[ (s_1^v)^m t + ((s_2^v)^m - (s_1^v)^m) (t - t_1) H(t - t_1) \right] \quad (5.13)$$

The deviatoric components of the delayed elastic strain rate have a similar formulation:

$$\dot{\epsilon}_{ij}^d = \dot{e}^d \frac{s_{ij}}{s} = \frac{\dot{e}^d}{3} \begin{bmatrix} 2 & 0 & 0 \\ 0 & -1 & 0 \\ 0 & 0 & -1 \end{bmatrix} \quad (5.14)$$

where  $\dot{\epsilon}^d = \frac{3}{2}\dot{\epsilon}_0^d \left(\frac{s^d}{s_0^\mu}\right)^n$  is the equivalent delayed elastic strain rate. The equivalent delayed elastic strain has one of two general solutions under a constant stress, depending on the exponent  $n$ :

$$E_0 e^d = \begin{cases} s - C e^{-A_d E_0 t} & : n = 1 \\ s - (A_d E_0 (n-1)t - C)^{\frac{1}{1-n}} & : n \neq 1 \end{cases}, \quad (5.15)$$

$$A_d = \frac{3}{2} \frac{\dot{\epsilon}_0^d}{(s_0^\mu)^n} \quad (5.16)$$

The solutions for a general creep-relaxation cycle are more complex. For  $n = 1$ , the equation is given by:

$$E_0 e^d = s_1^v (1 - e^{-A_E t}) + (s_2^v - s_1^v) (1 - e^{-A_E (t-t_1)}) H(t - t_1) \quad (5.17)$$

while the solution for  $n \neq 1$  is:

$$\begin{aligned} E_0 e^d = & \left( s_2^v - \left( A_n (t - t_1) \right. \right. \\ & \left. \left. + \left( s_2^v - s_1^v \left( 1 - \left( A_n (s_1^v)^{n-1} t_1 + 1 \right)^{\frac{1}{1-n}} \right) \right)^{1-n} \right)^{\frac{1}{1-n}} \right) H(t - t_1) \\ & + \left( s_1^v \left( 1 - \left( A_n \cdot (s_1^v)^{n-1} t + 1 \right)^{\frac{1}{1-n}} \right) \right) (1 - H(t - t_1)) \end{aligned} \quad (5.18)$$

where:

$$A_E = A_d E_0 \quad (5.19)$$

$$A_n = A_E (n - 1) \quad (5.20)$$

Note that for the case of simple uniaxial creep ( $s_1^v = \sigma$ ,  $t < t_1$ ) the solution when  $n \neq 1$  reduces to:

$$e^d = \frac{\sigma}{E_0} \left( 1 - \left( \frac{3}{2} \frac{\dot{\epsilon}_0^d}{(s_0^\mu)^n} E_0 (n-1) \sigma^{n-1} t + 1 \right)^{\frac{1}{1-n}} \right) \quad (5.21)$$

which is equivalent to the result of Jordaan and McKenna (1988a) when the initial viscosity of the Kelvin dashpot,  $\mu_{k_0}$ , is given by:

$$\mu_{k_0} = \frac{2}{3} \frac{(s_0^\mu)^n}{\sigma^{n-1} \dot{\epsilon}_0^d} \quad (5.22)$$

The delayed elastic and viscous strain components are shown in Figures 5.3.

Finally, the general solution for the non-elastic volumetric strain component under a constant stress is simply:

$$\epsilon^v = \frac{f_3 s}{p^h} (e^d + e^c) + C \quad (5.23)$$

where  $f_3$  is a constant. This results in the following solution for a creep-relaxation cycle:

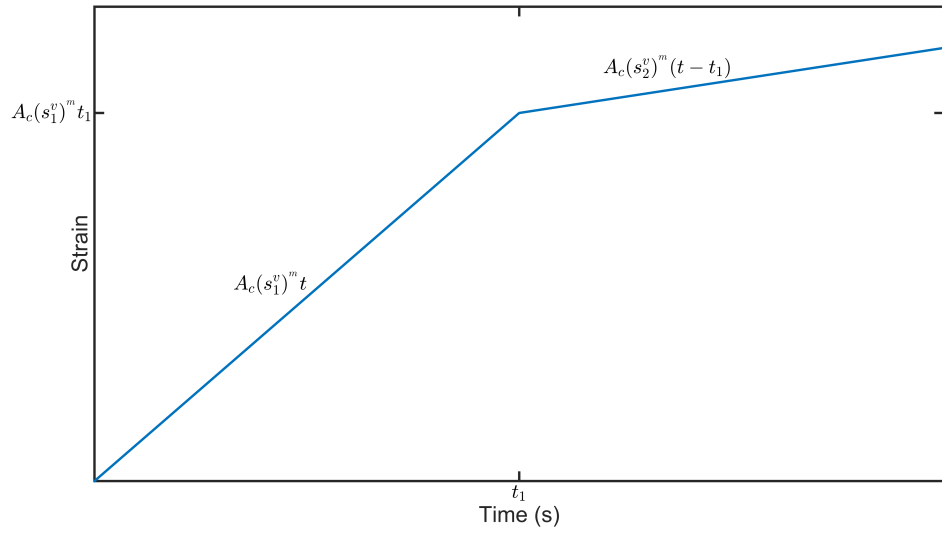
$$\begin{aligned} \epsilon^v = \frac{f_3 s_1^v}{p_1^h} \left[ (e^d + e^c) [1 - H(t - t_1)] + [e^d(t_1) + e^c(t_1)] H(t - t_1) \right] + \\ \frac{f_3 s_2^v}{p_2^h} \left[ (e^d + e^c) - [e^d(t_1) + e^c(t_1)] \right] H(t - t_1) \end{aligned} \quad (5.24)$$

An example of the volumetric response is given in Figure 5.4.

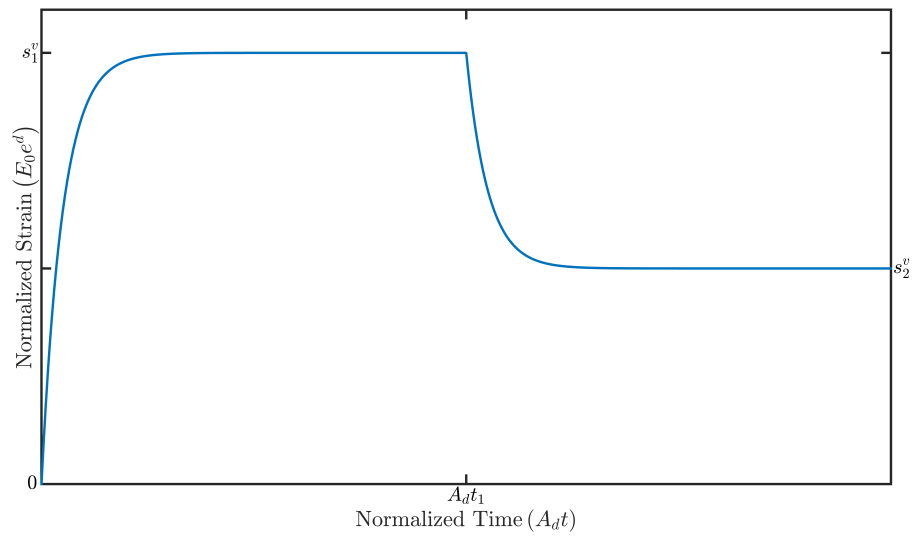
The accumulated damage,  $S_i$ , and damage rate,  $\dot{S}_i$ , for a given formulation can be represented generally by the following equations:

$$S_i = A_0 \left( A_1 (t - (t - t_1)) H(t - t_1) + A_2 (t - t_1) H(t - t_1) \right) \quad (5.25)$$

$$\dot{S}_i = A_0 \left( A_1 (1 - H(t - t_1)) + A_2 H(t - t_1) \right) \quad (5.26)$$



(a)



(b)

Figure 5.3: Delayed elastic and viscous responses to generalized stress state. (a) demonstrates the viscous strains, (b) the delayed elastic strains.

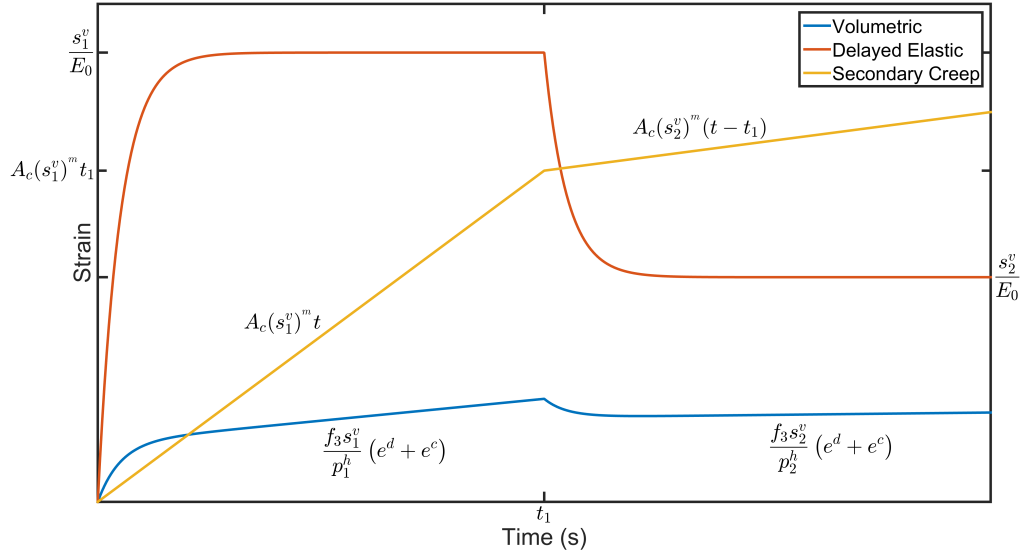
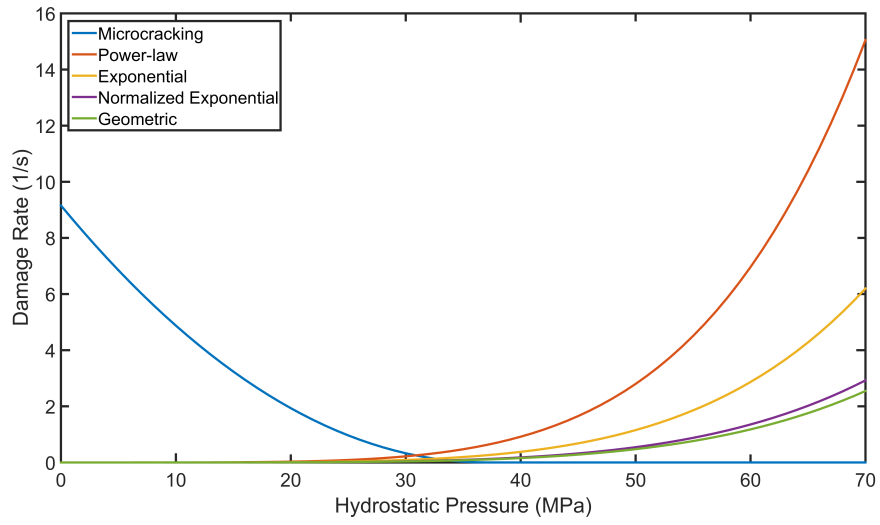


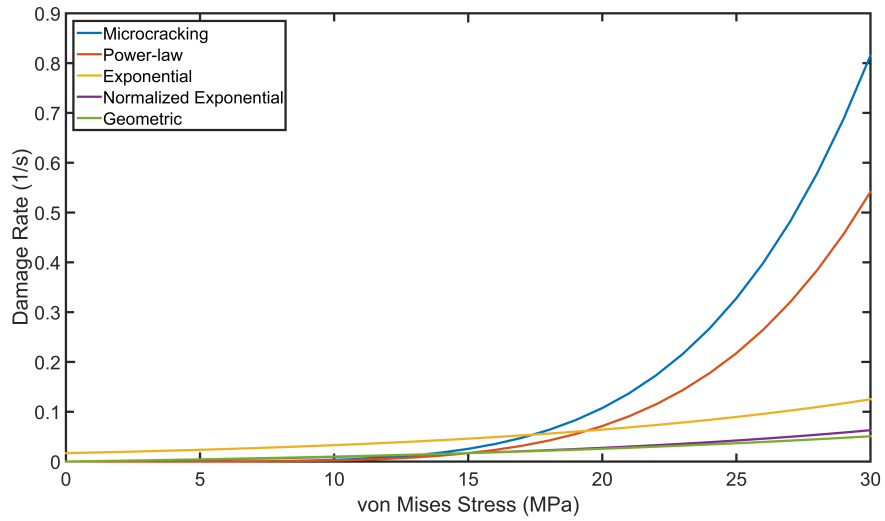
Figure 5.4: Volumetric strain with no damage. Note that the figure is presented as positive for ease of viewing. Volumetric strain represents dilation due to irreversible processes, and will have the opposite sign of compression, depending on sign convention.

where  $A_0$ ,  $A_1$ , and  $A_2$  are the simplified forms of the calibration constants of Xiao and Li, presented in Table 4.1. The differences between damage models are highlighted in Figures 5.5. The amalgamated constants can be found in Table 5.1. The accumulated damage and damage rate are cumulative; a simple summation is all that is required to obtain the full damage parameter,  $S$ , or damage rate,  $\dot{S}$ .

To represent elastic damage, the desired damage function is substituted into one



(a)



(b)

Figure 5.5: Response of damage functions using the calibration constants of Xiao (1997). (a) is the response to a constant von Mises stress of 10 MPa over a range of hydrostatic pressures, (b) is the response to a constant hydrostatic pressure of 30 MPa over a range of von Mises stresses.

Table 5.1: Amalgamated damage constants.

Damage Function	$A_0$	$A_1$	$A_2$
$S_1$	$\frac{a_1}{(p_1)^{r_1}} \left( \frac{1}{s_0^s} \right)^{q_1}$	$(s_1^v)^{q_1} (p_1 - p_1^h)^{r_1}$	$(s_2^v)^{q_1} (p_1 - p_2^h)^{r_1}$
$S_2^p$	$\frac{a_2}{(p_2)^{r_2}} \left( \frac{1}{s_0^s} \right)^{q_2}$	$(s_1^v)^{q_2} (p_1^h)^{r_2}$	$(s_2^v)^{q_2} (p_2^h)^{r_2}$
$S_2^e$	$\frac{a_2}{(p_2)^{r_2}}$	$e^{s_1^v/s_0^s} (p_1^h)^{r_2}$	$e^{s_2^v/s_0^s} (p_2^h)^{r_2}$
$S_2^{ne}$	$\frac{a_2}{(p_2)^{r_2}} \left( \frac{1}{e-1} \right)$	$(e^{s_1^v/s_0^s} - 1) (p_1^h)^{r_2}$	$(e^{s_2^v/s_0^s} - 1) (p_2^h)^{r_2}$
$S_2^g$	$\frac{a_2}{(p_2)^{r_2}}$	$(2^{s_1^v/s_0^s} - 1) (p_1^h)^{r_2}$	$(2^{s_2^v/s_0^s} - 1) (p_2^h)^{r_2}$

of the three elastic models detailed in Chapter 4:

$$\epsilon_{ij}^e(t) = \frac{1}{E} \begin{bmatrix} (1 - 2\nu) P_c + \Delta\sigma(t) & 0 & 0 \\ 0 & (1 - 2\nu) P_c - \nu\Delta\sigma(t) & 0 \\ 0 & 0 & (1 - 2\nu) P_c - \nu\Delta\sigma(t) \end{bmatrix} \quad (5.27)$$

where:

$$E = \frac{E_0}{1 + C_1 S} \quad (5.28)$$

$$\nu = \nu_0 \left( \frac{1 + C_3 S}{1 + C_1 S} \right) \quad (5.29)$$

Substituting in the values for  $C_1$  and  $C_3$  (which can be found in Table 4.2) pro-

duces:

$$\epsilon_{ij}^e(t, \nu = \nu_0) = \frac{(1+S)}{E_0} \begin{bmatrix} P_h + \Delta\sigma(t) & 0 & 0 \\ 0 & P_h - \nu_0\Delta\sigma(t) & 0 \\ 0 & 0 & P_h - \nu_0\Delta\sigma(t) \end{bmatrix} \quad (5.30)$$

$$\epsilon_{ij}^e(t, K = K_0) = \frac{1}{E_0} \begin{bmatrix} P_h + \Delta\sigma(t)(1+S) & 0 & 0 \\ 0 & P_h - \Delta\sigma(t)(1+S/2) & 0 \\ 0 & 0 & P_h - \Delta\sigma(t)(1+S/2) \end{bmatrix} \quad (5.31)$$

$$\epsilon_{ij}^e(t, \text{Kachanov}) = \frac{1}{E_0} \begin{bmatrix} P_h + \Delta\sigma(t) + K_1S & 0 & 0 \\ 0 & P_h - \nu_0\Delta\sigma(t) + K_2S & 0 \\ 0 & 0 & P_h - \nu_0\Delta\sigma(t) + K_2S \end{bmatrix} \quad (5.32)$$

where:

$$P_h = (1 - 2\nu_0) P_c \quad (5.33)$$

$$K_1 = P_K + \Delta\sigma_{K_1}(t) \quad (5.34)$$

$$K_2 = P_K - \nu_0\Delta\sigma_{K_2}(t) \quad (5.35)$$

$$P_K = \frac{16}{9}(1 - \nu_0^2)P_c \quad (5.36)$$

$$\Delta\sigma_{K_1}(t) = \frac{16(1 - \nu_0^2)(1 - 3\nu_0/10)}{9(1 - \nu_0/2)}\Delta\sigma(t) \quad (5.37)$$

$$\Delta\sigma_{K_2}(t) = \frac{8(1 - \nu_0^2)}{45(1 - \nu_0/2)}\Delta\sigma(t) \quad (5.38)$$

The response of each model to increasing damage is shown in Figure 5.6.

Secondary creep with damage requires a more complicated representation due to

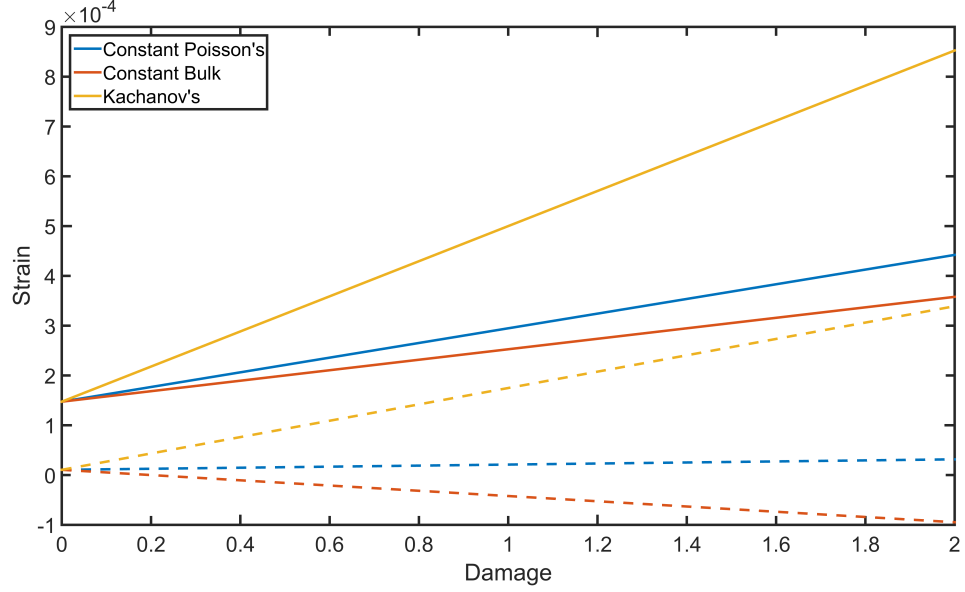


Figure 5.6: Elastic strain with damage for a unit hydrostatic pressure and von Mises stress under the three formulations examined. Note that compression is positive in this figure. Axial (—) elastic compression increases with damage for all three formulations. Lateral (---) expansion occurs under the constant Bulk Modulus formulation, while lateral compression increases under the Kachanov formulation.

its history dependence. The general solution for a constant stress state is given by:

$$e^c = \frac{A_c s^m}{\beta_c \dot{S}} e^{\beta_c \dot{S} t} + C \quad (5.39)$$

where  $C$  is a constant. For a creep-relaxation cycle this becomes:

$$e^c = A_c \left[ \frac{(s_1^v)^m}{\beta_1} \left( e^{\beta_1 t} - 1 - e^{\beta_1} [e^t - e^{t_1}] H(t - t_1) \right) + \frac{(s_2^v)^m}{\beta_2} e^{\beta_2} [e^t - e^{t_1}] H(t - t_1) \right] \quad (5.40)$$

where  $\beta_1 = \beta_c A_0 A_1$  and  $\beta_2 = \beta_c A_0 A_2$  are constants that depend upon the damage formulation used. An example response of Equation 5.40 to a creep-relaxation cycle

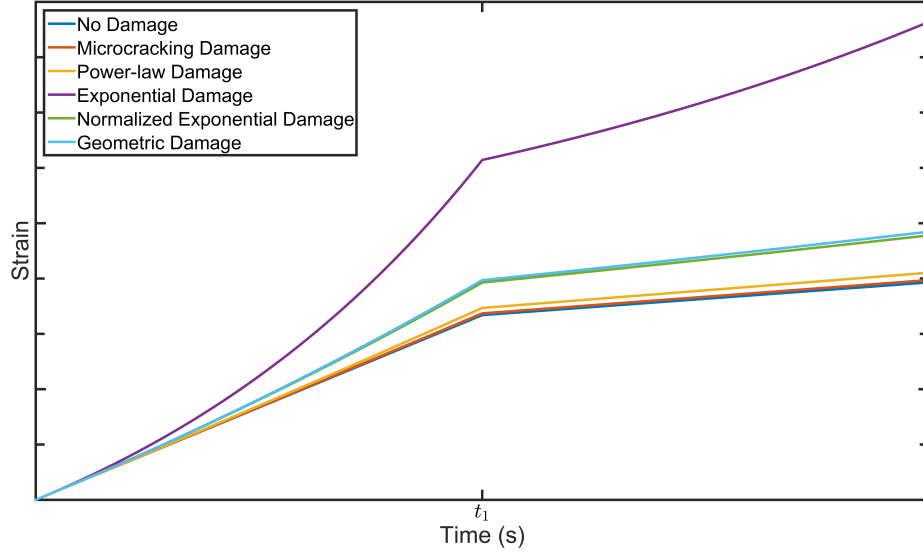


Figure 5.7: Viscous strain with damage for various damage formulations.

is given in Figure 5.7.

No analytical solution exists for delayed elastic strain with damage during loading. The forward Euler method was instead used to estimate the delayed elastic strain response to a creep-relaxation cycle; more accurate modelling techniques exist, but the increased confidence was deemed not worth the increased complexity.

Analytical solutions do exist for unloading to a stress of  $s = 0$ , and are given by:

$$e^d = \begin{cases} C e^{-A_d E_0 f(t)} & : n = 1 \\ (A_d E_0^n (n-1) f(t) + C)^{\frac{1}{1-n}} & : n \neq 1 \end{cases} \quad (5.41)$$

$$f(t) = \begin{cases} t & : \dot{S} = 0 \\ \frac{e^{-\beta_d / C_1}}{\beta_d \dot{S}} \left( -\frac{\beta_d}{C_1} \right)^n \Gamma \left[ 1 - n, -\beta_d C_1 \left( \dot{S} t + 1 / C_1 \right) \right] & : \dot{S} \neq 0 \end{cases} \quad (5.42)$$

where  $\Gamma$  is the incomplete gamma function. It should be noted that only the expo-

nential form of the high-pressure damage function produces a non-zero damage rate for a von Mises stress of zero. These forms are presented only for completeness; given that a numerical solution is required for the loading portion of a cycle it was deemed unnecessary to switch to a theoretical solution for unloading.

An example comparison between the theoretical and finite element results for the simple case of no damage is presented in Figure 5.8. The finite element model matches the theoretical results perfectly, lending credibility to the model implementation. Results of the creep-relaxation cycles for all other parameter combinations are presented in greater detail in Appendix 1. The majority are seen to match theoretical results, save for a handful of cases where some numerical instability at the sudden load drop created excessive, erroneous strain results.

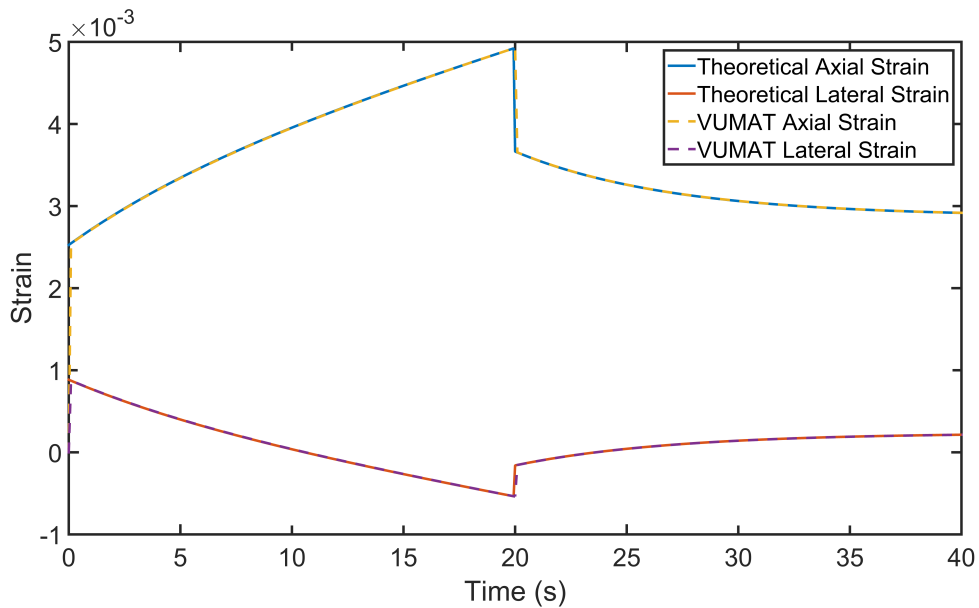


Figure 5.8: Total strain with no damage.

### 5.1.2 Delayed Elastic Recovery

A key component of the model is the presence of delayed elastic recovery, a common element of viscoelastic behaviour. It was discovered during the validation process that Equation 4.21 does not lead to delayed elastic recovery under all circumstances; a numerical singularity is encountered as hydrostatic pressure is approached due to the presence of the  $s_{ij}/s$  term. A theoretical limit for this term does not appear to exist. As the von Mises stress,  $s$ , approaches zero, so too do the components of the deviatoric stress tensor,  $s_{ij}$ , necessitating the application of L'Hospital's rule:

$$\lim_{s \rightarrow 0} \frac{s_{ij}}{s} = \lim_{s \rightarrow 0} \frac{\partial s_{ij}}{\partial s} / \frac{\partial s}{\partial s} = \lim_{s \rightarrow 0} \frac{\partial s_{ij}}{\partial s} \quad (5.43)$$

For reference, the von Mises stress is defined as:

$$s = \sqrt{\frac{3}{2} s_{ij} s_{ij}} \quad (5.44)$$

Taking the derivative with respect to the deviatoric stress components gives:

$$\frac{\partial s}{\partial s_{ij}} = \frac{3}{4} \frac{1}{\sqrt{\frac{3}{2} s_{kl} s_{kl}}} \frac{\partial (s_{kl} s_{kl})}{\partial s_{ij}} = \frac{3}{4s} \frac{\partial (s_{kl} s_{kl})}{\partial s_{ij}} \quad (5.45)$$

Since  $s^2 = \frac{3}{2} s_{ij} s_{ij}$ , Equation 5.45 reduces to:

$$\frac{\partial s}{\partial s_{ij}} = \frac{1}{2s} \frac{\partial s^2}{\partial s_{ij}} = \frac{3s_{ij}}{2s} \quad (5.46)$$

the limit of which remains undefined:

$$\lim_{s \rightarrow 0} \frac{s_{ij}}{s} = \lim_{s \rightarrow 0} \frac{1}{\frac{\partial s}{\partial s_{ij}}} = \lim_{s \rightarrow 0} \frac{2s}{3s_{ij}} \quad (5.47)$$

Applying L'Hospital's rule again reproduces the original limit, providing no useful information. Fortunately, numerical solutions have shown that the ratio will remain

constant as a hydrostatic pressure is approached from a randomly chosen stress state.

When applied to the delayed elastic strain rate we obtain:

$$\dot{\epsilon}_{ij}^d = \frac{s_{ij}}{s} \dot{\epsilon}^d \implies \frac{s_{ij}}{s} = \frac{\dot{\epsilon}_{ij}^d}{\dot{\epsilon}^d} = C \quad (5.48)$$

where C is a constant. Assuming that there is some time,  $t_0$ , at which the delayed elastic strain rate is defined and using the fact that the equivalent delayed elastic strain rate is defined for all stress states, the delayed elastic strain rate for some later time,  $t_1$ , where  $s_{ij}/s$  is undefined can be represented by:

$$\dot{\epsilon}_{ij}^d(t_1) = \frac{\dot{\epsilon}_{ij}^d(t_0)}{\dot{\epsilon}^d(t_0)} \dot{\epsilon}^d(t_1) = C \dot{\epsilon}^d(t_1) \quad (5.49)$$

We thus avoid the singularity as  $s \Rightarrow 0$  and successfully produce delayed elastic recovery under a pure hydrostatic pressure.

## 5.2 Indentation Validation

A variety of indentation finite element simulations were implemented to compare the results of the models to existing experimental evidence. There is a wide range of indentation data available for use in model validation. Two indentation geometries from the test series that took place on Hobson's Choice ice island (Frederking et al., 1990) are modelled here; one involving a cylindrical indentation into a truncated pyramidal ice face, the other a spherical end-cap indentation into a smooth ice face. The results of these simulations are compared to theoretical results and the simulation results of earlier investigators.

### 5.2.1 Elastic Validation

The first step in the validation process is to ensure that the finite element simulation reproduces known theoretical results where they are available. The stress-strain fields produced during the indentation of an elastic material are well known (Timoshenko and Goodier, 1951). Of interest here are the axisymmetric solutions for the indentation of rigid cylindrical and spherical indentors into smooth, elastic surfaces. The stress distributions along the contact surface during such an indentation are given by:

$$\frac{p_c}{p_m} = \frac{a}{2\sqrt{a^2 - r^2}} \quad (5.50)$$

$$\frac{p_s}{p_m} = \frac{3}{2a}\sqrt{a^2 - r^2} \quad (5.51)$$

where  $p_c$  and  $p_s$  are the pressure distributions for the cylindrical and spherical indentors, respectively,  $p_m$  is the mean pressures over the entire contact surface,  $a$  is the radius of the contact surface, and  $r$  is the radial coordinate. These distributions are presented in Figure 5.9. Note that the surface pressure outside the contact area is zero for both indentors.

These surface distributions provide the first validation check for the finite element model; they should hold for all stages of an elastic indentation, provided the stresses and radii are properly normalized. It must be noted that the contact area during a spherical indentation increases with time, unlike a cylindrical indentation which provides a constant contact surface. The surface stresses for pure elastic finite element analyses for both indenter geometries are provided in Figure 5.10. Both geometries show minor discrepancies from the theoretical curves at the centre node and the indenter edge, but otherwise provide a sufficiently accurate recreation of theoretical

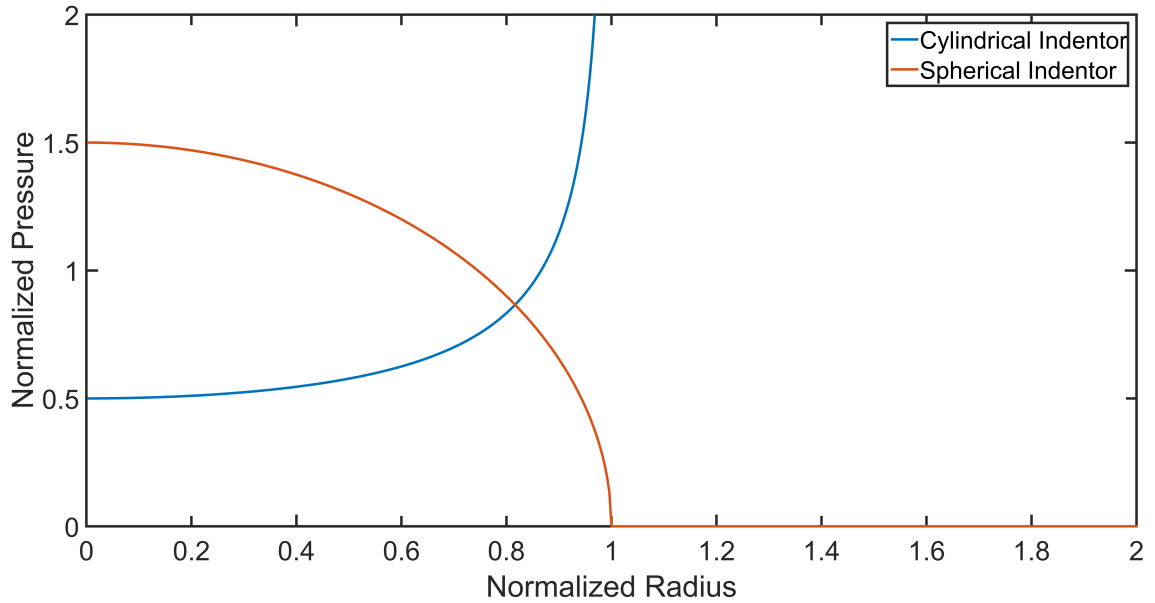


Figure 5.9: Theoretical surface pressures for cylindrical and spherical indentors in contact with a semi-infinite plane. Note the singularity at the edge of the cylindrical indenter. In practice, this region will undergo some plastic yielding.

results. The corresponding indenter displacements are given by:

$$d_c = \frac{F(1 - \nu^2)}{2aE} \quad (5.52)$$

$$d_s = \frac{3F(1 - \nu^2)}{4aE} \quad (5.53)$$

where  $d_c$  and  $d_s$  are the penetration depth of the cylindrical and spherical indentors, respectively,  $F$  is the total load on the indentors, while  $E$  and  $\nu$  are the elastic modulus and Poisson's ratio of the indented material, respectively. A comparison of the theoretical and numerical load vs. displacement curves is provided in Figure 5.11. The simulations slightly overestimate the load on the indentors in both cases, as is common with finite element models. The error in loading for the cylindrical indenter is on the order of 10 % for all displacements, while the error in loading for

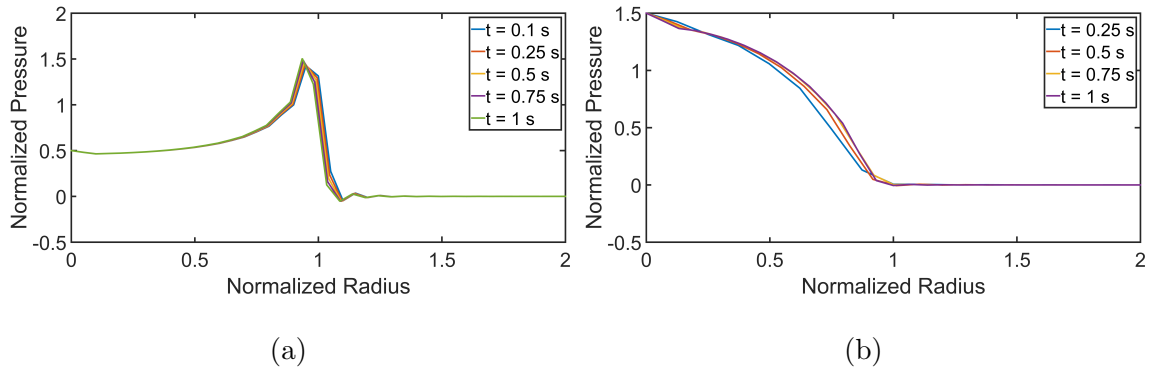


Figure 5.10: Surface pressure on rigid (a) cylindrical and (b) spherical indentors for an elastic medium across a number of time steps during a simulation. The pressure is normalized with respect to the total pressure on the indenter, while the radius is normalized with respect to the indenter radius.

the spherical indenter decreases from nearly 25 % to less than 5 % with increasing displacement, due to the increase in contact area.

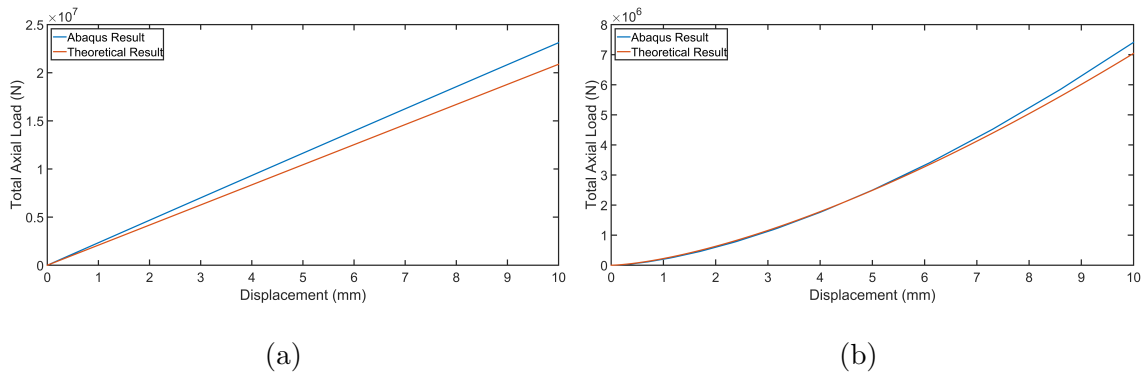


Figure 5.11: Force on rigid (a) cylindrical and (b) spherical indentors for given penetration depth within an elastic medium. Note that the contact radius during spherical indentation is dependent upon the penetration depth by  $a = \sqrt{r_c d_s}$ , where  $r_c$  is the radius of curvature of the indenter, which in this case is 256 mm.

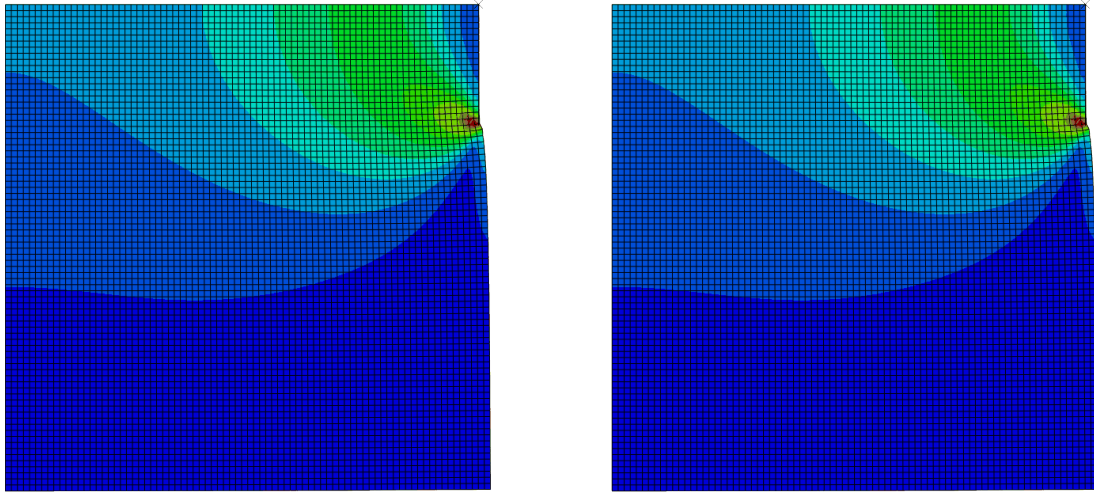


Figure 5.12: von Mises stress produced by a cylindrical indentation into an elastic medium for both the VUMAT (left) and built-in Abaqus (right) elastic definitions. Note that indentation proceeds from the top right corner of both structures.

On the practical end of validation, a simple and efficient check on the custom user subroutine (VUMAT) code is to ensure that its pure elastic results match the results from the built-in elastic definition provided by Abaqus. One such comparison for the von Mises stress produced by the cylindrical indenter is provided in Figure 5.12; the VUMAT result is seen to match Abaqus' built in elastic result perfectly under these conditions. The same is true for the spherical indenter.

Finally, only a direct comparison of the theoretical and numerical stress fields within the specimen remains. The theoretical formulations used are summarized in Fischer-Cripps (2000). The stresses within an elastic medium during indentation with

a rigid cylindrical indenter are given by:

$$\frac{\sigma_r}{p_m} = -\frac{1}{2} \left[ J_1^0 - \frac{z}{a} J_2^0 - (1 - 2\nu) \frac{a}{r} J_0^1 + \frac{z}{r} J_1^1 \right] \quad (5.54)$$

$$\frac{\sigma_\theta}{p_m} = -\frac{1}{2} \left[ 2\nu J_1^0 + (1 - 2\nu) \frac{a}{r} J_0^1 - \frac{z}{r} J_1^1 \right] \quad (5.55)$$

$$\frac{\sigma_z}{p_m} = -\frac{1}{2} \left[ J_1^0 + \frac{z}{a} J_2^0 \right] \quad (5.56)$$

$$\frac{\tau_{rz}}{p_m} = -\frac{z}{2a} J_2^1 \quad (5.57)$$

where:

$$J_1^0 = R^{-1/2} \sin \frac{\phi}{2} \quad (5.58)$$

$$J_0^1 = \frac{a}{r} \left( 1 - \sqrt{R} \sin \frac{\phi}{2} \right) \quad (5.59)$$

$$J_2^1 = \frac{r}{a} R^{-3/2} \sin \frac{3\phi}{2} \quad (5.60)$$

$$J_2^0 = \sqrt{1 + \frac{z^2}{a^2}} R^{-3/2} \sin \left( \frac{3\phi}{2} - \theta \right) \quad (5.61)$$

$$J_1^1 = \sqrt{1 + \frac{z^2}{a^2}} \frac{a}{r} R^{-1/2} \sin \left( \theta - \frac{\phi}{2} \right) \quad (5.62)$$

$$R = \sqrt{\left( \frac{r^2}{a^2} + \frac{z^2}{a^2} - 1 \right)^2 + 4 \frac{z^2}{a^2}} \quad (5.63)$$

$$\tan \phi = \frac{2za}{r^2 + z^2 - a^2} \quad (5.64)$$

$$\tan \theta = \frac{a}{z} \quad (5.65)$$

For comparison, the theoretical and numerical hydrostatic pressures are presented in Figures 5.13 and 5.14. The results are comparable, once the mean pressure is accounted for, save for the introduction of edge effects at the periphery. This is not unexpected, as the model is not truly infinite.

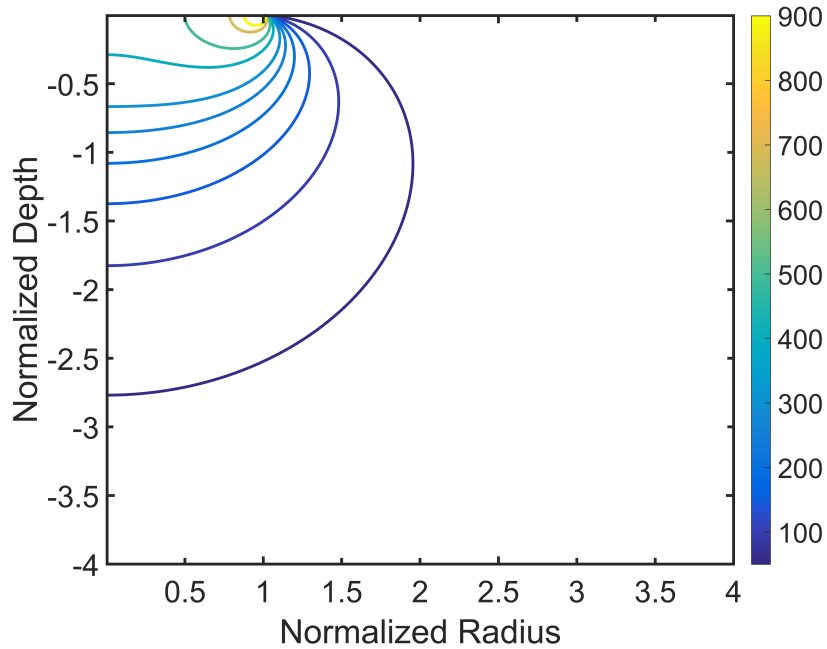


Figure 5.13: Theoretical hydrostatic pressures within an elastic medium. Both depth and radius are normalized to the radius of the indenter.

### 5.2.2 Validation of Indentation With Cylindrical Indentor

Test TFR07 from the Hobson’s Choice test series was used by previous investigators (Li, 2002; Moore et al., 2013; Xiao, 1997) to validate earlier constitutive models. Each found that they could reproduce both the expected load drop from pressure softening as well as the formation of the damage layer at the ice-indentor interface. Here, this test is simulated via a two-dimensional, axisymmetric model, which is used to reduce computation time; this symmetry will not hold perfectly during a true indentation experiment due to the random nature of *hpz* development and spalling failure. The results are then compared to the work of Li; the model of Xiao used a plane strain formulation, while the model of Moore requires element deletion. They are thus

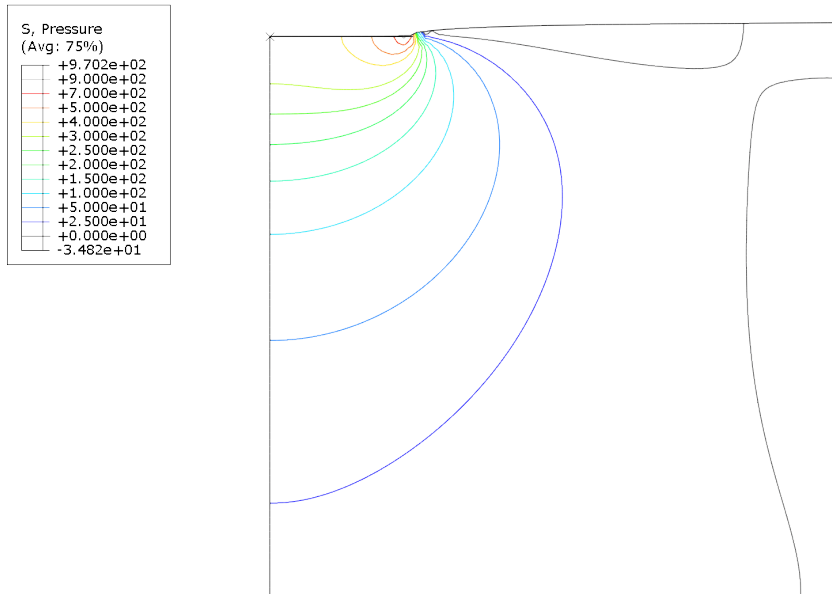


Figure 5.14: Numerical hydrostatic pressures within an elastic medium. Note that Abaqus always denotes compressive hydrostatic pressure as positive, opposite the common usage.

ignored.

The ice-indentation system, consisting of a servo-controlled hydraulic actuator, a back plate, and an indenter, was reduced to a single flat, rigid indenter for ease of modelling. The indenter was constrained to move only towards the ice surface, with a constant speed of 68 mm/s. Note that indenter velocity is not constant during the actual test referenced, as shown in Frederking et al. (1990); velocity increases dramatically for brief periods of time post-layer failure or spalling (i.e. during a load drop) before stabilizing at a constant rate once more. A constant speed is modelled here to reduce complexity.

Contact between the indenter and ice surface is modelled via the penalty contact

method so as to prevent conflicts with other constraints. The finite sliding option is also used to account for the possibility of large deformations at the contact interface. Note that this method introduces additional stiffness that must be accounted for during analysis and increases computation time. Contact was assumed to be frictionless to reduce complexity; stresses at the surface will thus be slightly lower than expected. An explicit analysis was chosen over implicit due to the inclusion of contact surfaces and the highly non-linear nature of ice, both of which are modelled better by an explicit analysis; the increased computation cost is made up elsewhere.

The simulation is designed to begin after initial spalling has occurred, which is assumed to have reduced the ice to a truncated pyramidal shape with an upper radius of 100 mm and a slope of 2:3. The region of interest near the ice-indentor interface is given a much finer mesh than the majority of the ice, which is modelled only to reduce the boundary effect (Xiao, 1991). The mesh size was reduced significantly (by a factor of 4) compared to the work of Xiao (1997) and Li (2002) while maintaining a run time of only a few hours; numerous runs with different combinations of model parameters were desired, so run time could not be excessive.

Linear quad elements with both distortion and combined hourglass control were used for all regions. Quadratic elements, which would likely have provided a significant increase in model accuracy, were not available for use with the axisymmetric model. Distortion control was used to prevent excessive distortion of the ice elements at the ice-indentor interface, which would otherwise extrude out from underneath the indenter, reaching aspect ratios of 1:20 or greater; the accuracy of such elements could not be verified and were thus prevented. The use of distortion control is expected to increase the stiffness of the ice slightly. Combined hourglass control was found to

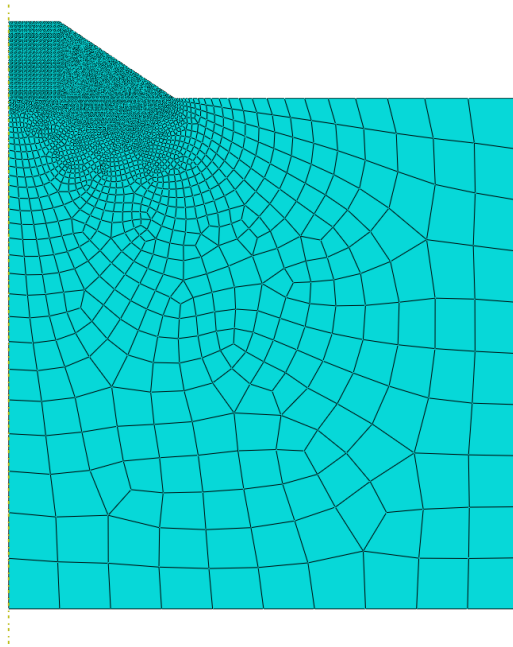


Figure 5.15: Basic simulation geometry used by earlier investigators.

be the only method capable of preventing hourglassing in this model, introducing an artificial stiffness and viscosity to the zero-energy deformation modes of each element.

The base of the ice is fixed in only the vertical direction; further constraints are unnecessary due to the distance from the contact surface. Strangely, an additional constraint was required to enforce contact between the reference node of the indenter and the top left-most node of the ice, otherwise the ice node would slip around the indenter. This produces higher than expected stresses at the node in question, as will be noted in later sections. This geometry is shown in Figure 5.15.

The modelled ice obeys the viscoelastic damage model outlined in Chapter 4, which is implemented via a custom user subroutine. The model of Li (2002) appears to use the following settings:

- The exponential high-pressure damage function,  $(f_2(p) = e^{s/s_0})$  must be used, along with;
- the elastic damage model of Kachanov,  $(C_1 = \frac{16(1 - \nu_0^2)(1 - 3\nu_0/10)}{9(1 - \nu_0/2)})$ , with;
- full elastic damage,  $(S = S_1 + S_2)$ , and;
- an initial damage of  $S_0 = S_1(0) = 1.2$ .

However, these settings did not produce the expected results; damage developed along a circular path from the top-right corner towards the centre of the sample, as seen in Figure 5.16, and no load drop was evident after a period of 0.2 s, four times the length of time required to produce a load drop in Li (2002), as seen in Figure 5.17.

Attempts to rectify this inconsistency led to the identification of the conditions necessary to induce a load drop and/or the development of a surface damage layer, as well as the possible parameter combinations that could be used to do so. The three main parameters are: 1) the elastic damage type; 2) the indenter velocity, and; 3) the high-pressure damage exponent,  $r_2$ . All three operate under the same principle; each increases the rate at which high-pressure damage accrues in its own way. It seems likely that the parameters of Li were misprinted, and that either the microcracking damage or constant elastic properties formulation was used. This, combined with a high-pressure exponent,  $r_2$ , greater than the calibration value of five, are sufficient to produce the expected damage layer and load drop.

A more detailed examination of the results under a wide range of parameters is provided in Section 6.1.

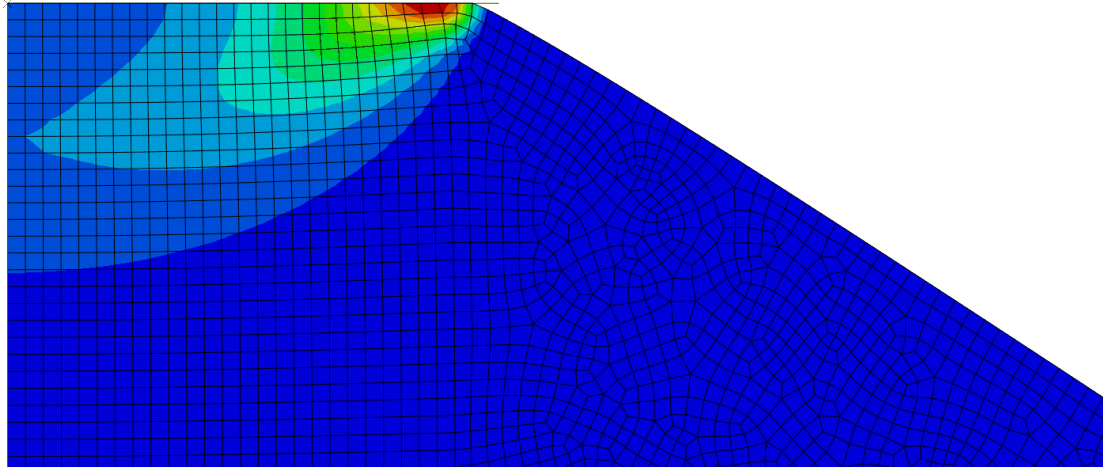


Figure 5.16: Damage layer resulting from best estimate of parameters implemented in Li (2002).

### 5.2.3 Geometry of Indentation

As noted in Chapter 3, a scaled down version of the spherical end-cap indenter used at Hobson’s Choice (Frederking et al., 1990) was tested in recent laboratory indentation experiments (Barrette et al., 2002; Browne, 2012; Browne et al., 2013; O’Rourke et al., 2015; 2016a;b; Wells et al., 2011). The spherical end-cap indenter provides several benefits over the cylindrical geometry, in particular the lack of a singularity at the edge of the contact region, while also complicating the analysis of the experimental results due to the non-constant contact area.

To study the effects of modelling a spherical end-cap indenter, three different geometries were implemented. The first simply replaced the cylindrical indenter with

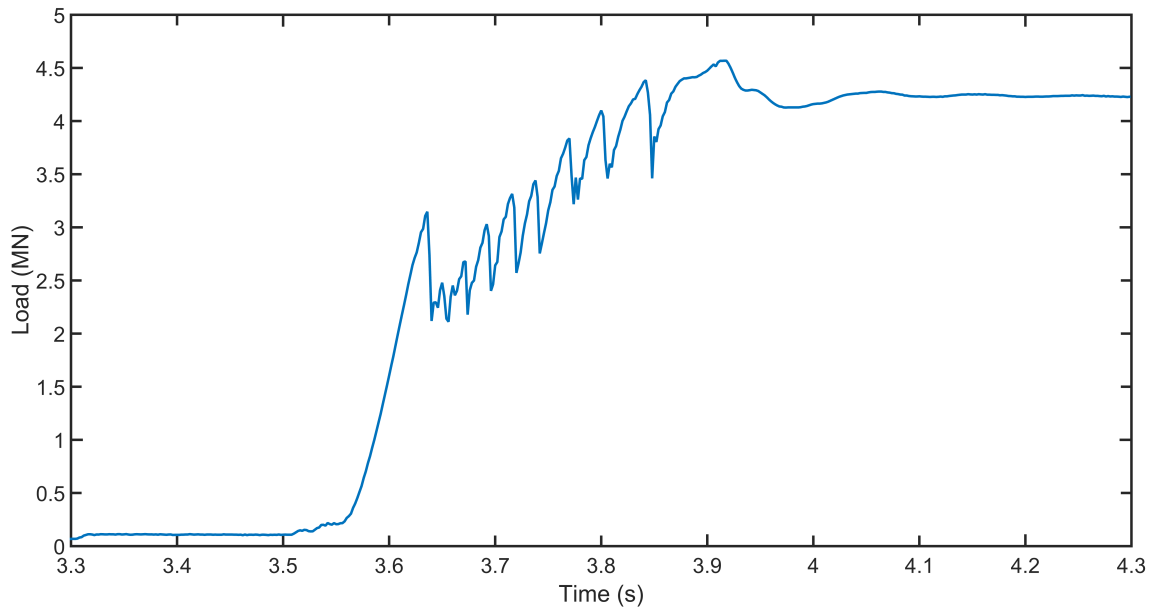
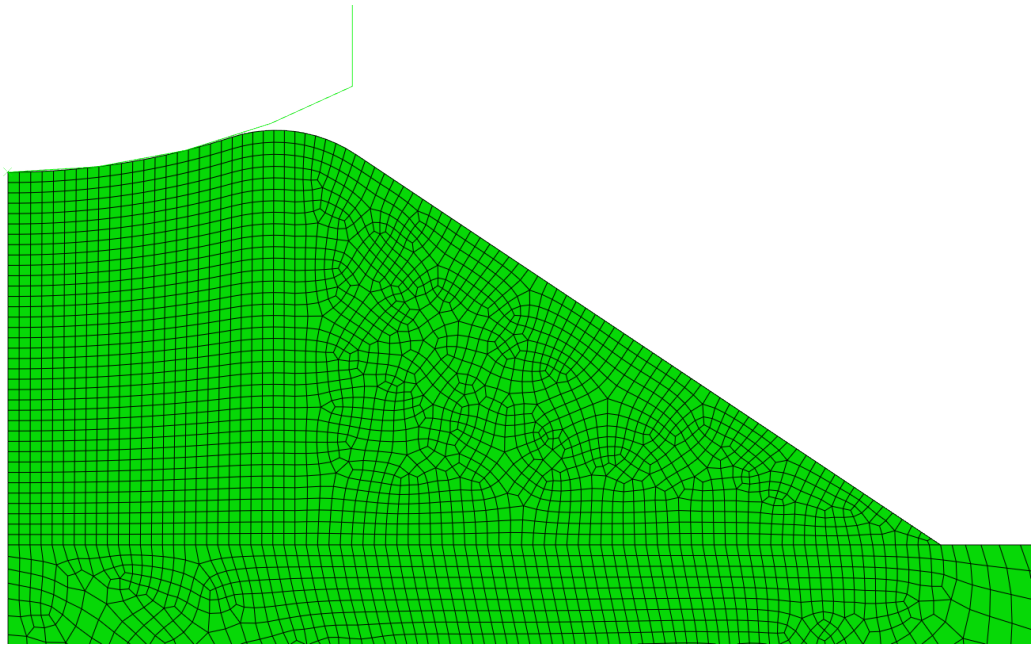


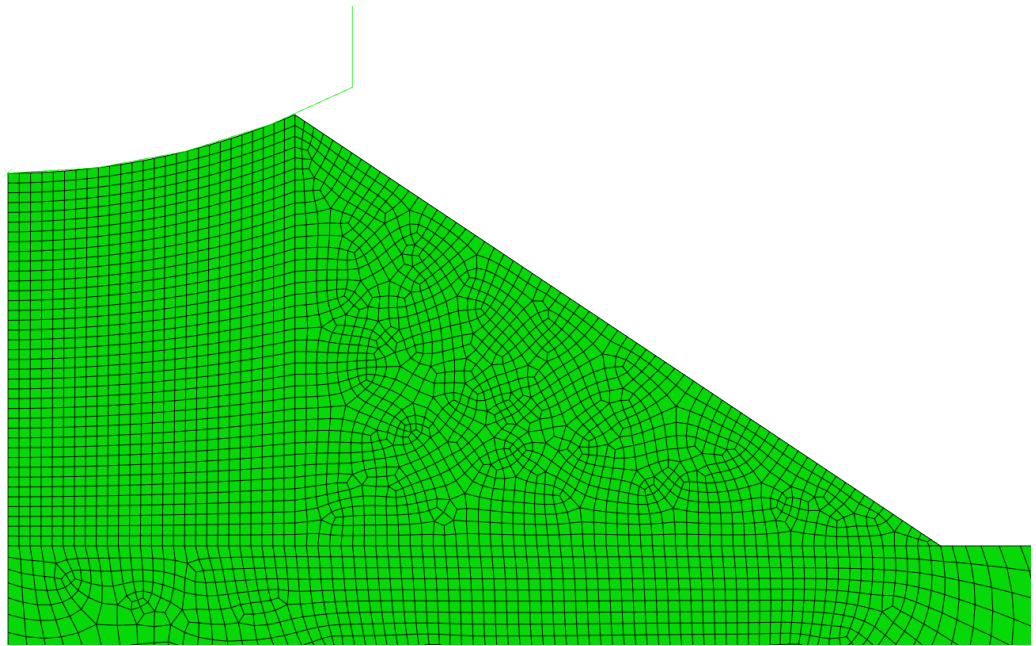
Figure 5.17: Force data from Frederking et al. (1990) test NRC07. Initial load drop occurs a little over 0.05 s after initial transitory loading behaviour ends (i.e. after slope becomes constant).

a spherical end-cap. This geometry was found to produce excessive element distortion and fail well before full contact with the indenter could be achieved. To compensate for this, the ice surface was grooved to match the radius of curvature of the indenter. Full contact was thus achieved from the start of the simulation, similar to the earlier cylindrical indentation simulations. Finally, the corner near the edge of the indenter was rounded to prevent stress concentrations in the corner elements. The region of interest for the two geometries are presented in Figure 5.18.

The results of the grooved geometry were promising, providing a smoother load drop and similar layer development, possibly due to lack of additional contact at larger strains. As such, it was chosen as the basis for all further investigations. It



(a)



(b)

Figure 5.18: Geometry used to model spherical end-cap indentations with (a) and without (b) a rounded corner near the edge of the contact region.

must be noted that the grooved geometry produces elastic stress fields similar to those of a cylindrical indentation; the cylindrical geometry can be thought of as an iso-parametrization of the grooved geometry.

# Chapter 6

## Further Development of Finite Element Model

This chapter describes the results of finite element simulations of ice indentation experiments using the constitutive relations described in Chapter 4 and the experimental results presented in Chapter 3 and earlier studies. Note that in all cases the desire is to match, as closely as possible, the saw-tooth loading cycle seen previously in Figure 5.17. The relevant relations include the strain rate equations, given by:

$$\dot{\epsilon}_{ij} = \dot{\epsilon}_{ij}^e + \dot{\epsilon}_{ij}^d + \dot{\epsilon}_{ij}^c + \dot{\epsilon}^v \delta_{ij} \quad (6.1)$$

$$\epsilon_{ij}^e = \frac{1 + \nu}{E_M} \sigma_{ij} - \frac{\nu}{E_M} \sigma_{kk} \delta_{ij} \quad (6.2)$$

$$\dot{\epsilon}_{ij}^d = \frac{3}{2} \dot{\epsilon}_0^d \operatorname{sgn}(s - E_K e^d) \left( \frac{|s - E_K e^d|}{s_0} \right)^n \frac{s_{ij}}{s} \quad (6.3)$$

$$\dot{\epsilon}_{ij}^c = \frac{3}{2} \dot{\epsilon}_0^c \left( \frac{s}{s_0} \right)^m \frac{s_{ij}}{s} \quad (6.4)$$

$$\dot{\epsilon}^v = -\frac{f_3}{p} s (\dot{e} - \dot{e}^e) = -\frac{f_3}{p} s (\dot{e}^d + \dot{e}^c) \quad (6.5)$$

the damage parameter and related damage functions:

$$S = S_1 + S_2 = \int_0^t \left\{ f_1(p) \left( \frac{s}{s_0} \right)^{q_1} + f_2(p) \left( 2^{s/s_0} - 1 \right) \right\} d\tau \quad (6.6)$$

$$f_1(p) = a_1 e^{(-p/p_1)} \quad (6.7)$$

$$f_2(p) = a_2 \left( \frac{p}{p_2} \right)^{r_2} \quad (6.8)$$

the elastic damage relations of Kachanov (1993):

$$\frac{E}{E_0} = \frac{1}{1 + C_1 S_1} \quad (6.9)$$

$$\frac{G}{G_0} = \frac{1}{1 + C_2 S_1} \quad (6.10)$$

$$\frac{\nu}{\nu_0} = \frac{1 + C_3 S_1}{1 + C_1 S_1} \quad (6.11)$$

$$\frac{K}{K_0} = \frac{1}{1 + C_4 S_1} \quad (6.12)$$

the equations used to describe power law breakdown:

$$\sinh^n \alpha \sigma \approx \begin{cases} (\alpha \sigma)^n & : \alpha \sigma < 0.8 \\ \frac{e^{n\alpha \sigma}}{2^n} & : \alpha \sigma > 1.8 \end{cases} \quad (6.13)$$

$$\alpha(p) = 0.27 e^{-\frac{p}{p_n}} \quad (6.14)$$

$$\dot{\epsilon}_{ij}^c = \frac{3}{2} \dot{\epsilon}_0^c \left( \frac{\sinh \alpha(p) s}{\sinh \alpha(p) s_0} \right)^m \frac{s_{ij}}{s} \quad (6.15)$$

the four relations used in an attempt to describe high-shear elastic failure:

$$\sigma_{ij} = \begin{cases} \sigma_{ij} & : s \leq 26.0\text{MPa} \\ \sigma_{ij} \frac{26.0}{s} & : s > 26.0\text{MPa} \end{cases} \quad (6.16)$$

$$S_1 = \begin{cases} S_1 & : s \leq 26.0\text{MPa} \\ S_{max} & : s > 26.0\text{MPa} \end{cases} \quad (6.17)$$

$$E_M = \begin{cases} E_M & : s \leq 26.0\text{MPa} \\ E_M \frac{26.0}{s} & : s > 26.0\text{MPa} \end{cases} \quad (6.18)$$

$$E_M = \begin{cases} E_M & : s \leq 26.0\text{MPa} \\ E_M/100 & : s > 26.0\text{MPa} \end{cases} \quad (6.19)$$

the non-linear high-pressure damage exponent described in this Chapter, given by:

$$r_2 = r_0 e^{s_2/s_0} \quad (6.20)$$

as well as the temperature and pressure relations used to define a master curve for the temperature dependent damage model:

$$f_2(p) = f_2(\Delta T_m) = f_2(T_h) \quad (6.21)$$

$$\Delta T_m = T - T_m \quad (6.22)$$

$$T_h = T/T_m \quad (6.23)$$

$$\frac{\delta p}{\delta T} = \frac{L_f}{T (C_w e^{(A_w - K_w)} - C_i e^{(A_i - K_i)})} \quad (6.24)$$

$$A_{w/i} = \int \alpha_{w/i}(T) \delta T - C_{A_{w/i}} \quad (6.25)$$

$$K_{w/i} = \int \kappa_{w/i}(P) \delta P - C_{K_{w/i}} \quad (6.26)$$

$$C_{w/i} = \exp [C_{A_{w/i}} + C_{K_{w/i}}] \quad (6.27)$$

The initial sections focus on determining the parameters that best reproduce the myriad experimental results obtained by previous investigators. This is accomplished primarily by: varying the elastic damage formulation and damage type; comparing the results of the microcracking damage formulation of Kachanov (1993) and the constant Poisson’s ratio model of Moore et al. (2013); as well as studying the effects of implementing constant elastic properties, microcracking elastic damage only, or high-pressure elastic damage ( $S_1 + S_2$ ); varying the high-pressure damage exponent,  $r_2$ , as per the work of Xiao (1997); and examining the results of simulations at constant normalized velocities,  $v_n$ , but for different scales.

The later sections explore the effect of entirely new parameters and models, including: the recalibration of the microcracking damage function,  $f_1(p)$ ; the inclusion of power law breakdown in the description of creep behaviour; the effect of the high-shear elastic failure observed in the test series described in Section 3.5; the outcome of implementing a non-linear high-pressure damage exponent,  $r_2(S_2)$ , that increases with damage; and the repercussions of assuming that high-pressure damage,  $S_2$ , is constant for a given thermal distance,  $\Delta T$ , or homologous temperature,  $T_h$ . The various studies are summarized in Table 6.1. It should be noted that all models are valid for compressive states of stress only, and over only a single load cycle; without some form of damage healing or layer extrusion it is impossible for the finite element model to describe the cyclic load failures commonly seen in indentation experiments. Further development is required in order to simulate multiple load cycles.

Table 6.1: Summary of indentation simulations.

Series	Purpose
Establishing Baseline Parameters	Examined three components: 1) elastic damage formulation; 2) elastic damage type, and; 3) high-pressure damage exponent
Normalized Velocity Testing	Show that model is scale-independent
$f_1(p)$ Recalibration	Ensure that new calibration approximates earlier results
Power Law Breakdown	Examine effect of pressure on power law breakdown
High-Shear Elastic Failure	Implement newly observed high-shear elastic failure
Non-Linear $r_2$	Cursory examination of effect of making high-pressure damage exponent increase with high-pressure damage
Temperature-Dependent Damage	Study effect of new temperature-dependent damage model

## 6.1 Model Implementation

Finite element simulations based on the Hobson’s Choice spherical end-cap indentation tests (Frederking et al., 1990) were developed to examine the behaviour of the constitutive model during indentation. The simulation is designed to examine the period some time after indentation begins. A portion of the ice is removed to ensure that full contact between the indenter and the ice surface occurs at the beginning of the simulation, forming a curved contact surface with a radius of curvature corresponding to that of the indenter. This avoids complications arising from infinitesimally small contact areas while better representing the conditions observed mid-indentation test. Nearby ice is assumed to be lost due to initial fracture behaviour, represented by a slope with a ratio of 2:3. In some simulations, ice in the region near the indenter is also assigned some initial microcracking damage, as per the work of Li (2002). The remaining bulk of ice is supplied to ensure semi-infinite conditions and remains largely unaffected by the majority of simulations. The indenter was based on a scaled down model of the Hobson’s Choice spherical end-cap indenter, with the diameter and radius of curvature reduced by a factor of five, to approximately match the contact radius modelled by earlier investigators (Li, 2002; Moore et al., 2013; Xiao, 1997) when investigating cylindrical indentations. The indenter was then extended to prevent excessive element distortion at the edge. The described geometry is presented in Figure 6.1. All remaining parameters, from contact controls to element type, are identical to those described in Section 5.2.2.

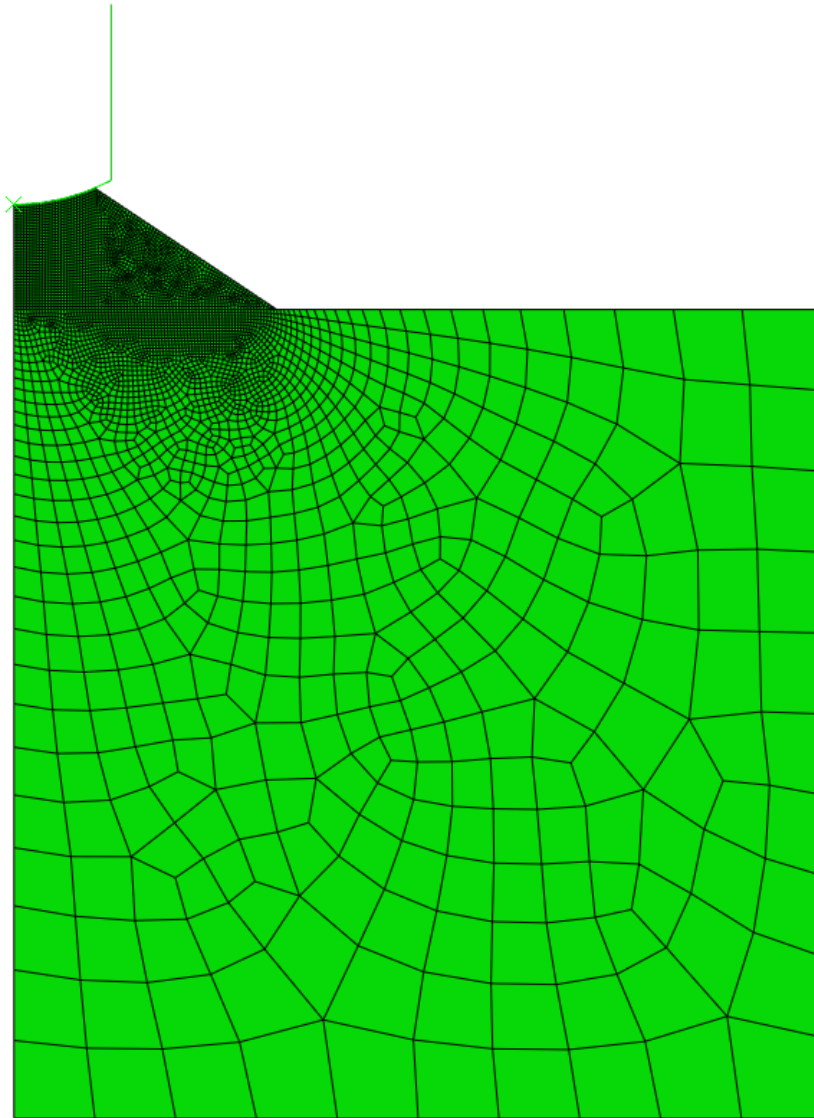


Figure 6.1: Basic simulation geometry.

### 6.1.1 Establishing Baseline Parameters for Simulations

Initial simulations were used to establish the set of parameters that best reproduce the results of experimental studies. The relevant parameters included: the elastic damage formulation (Kachanov's, constant Poisson's ratio, constant bulk modulus);

the elastic damage type (constant elastic properties, microcracking elastic damage, high-pressure elastic damage), and; the high-pressure damage exponent ( $r_2$ ). Each simulation enforced an indenter velocity of 68 mm/s, as per the work of Xiao (1997), Li (2002), and Moore et al. (2013).

As discussed in Section 4.3, several types of elastic damage were implemented and investigated. All were based on the microcracking ( $S_1$ ) damage formulation of Kachanov (1993), with constants modified to produce specific properties (either a constant Poisson's ratio or a constant Bulk modulus). The effects of using constant elastic properties (no elastic damage), as well as including high-pressure ( $S_2$ ) elastic damage, were also examined. It must be noted that including high-pressure elastic damage is a theoretically unsound approach; the formulation of Kachanov (1993) is based on the effects of dilute, distributed microcracking, and can make no extrapolations on the effect of dynamic recrystallization and pressure melting. Finally, a brief study of the effect of increasing  $r_2$  was undertaken to provide a baseline from which to examine the effect of implementing a damage dependent, non-linear  $r_2$  into the constitutive model.

The three elastic damage types were initially examined, with the calibration values of Xiao (1997) being used for the remaining parameters (See Table 4.1). The corresponding indenter loads produced by these conditions are shown in Figure 6.2. The load drop produced under constant elastic properties is much more pronounced than the other conditions. This result led to it being chosen as the baseline for all further testing, as significant load drops are one of the defining characteristics of indentation experiments. Time to failure and peak load are seen to differ between experimental and numerical data; numerous model properties (primarily the initial damage and

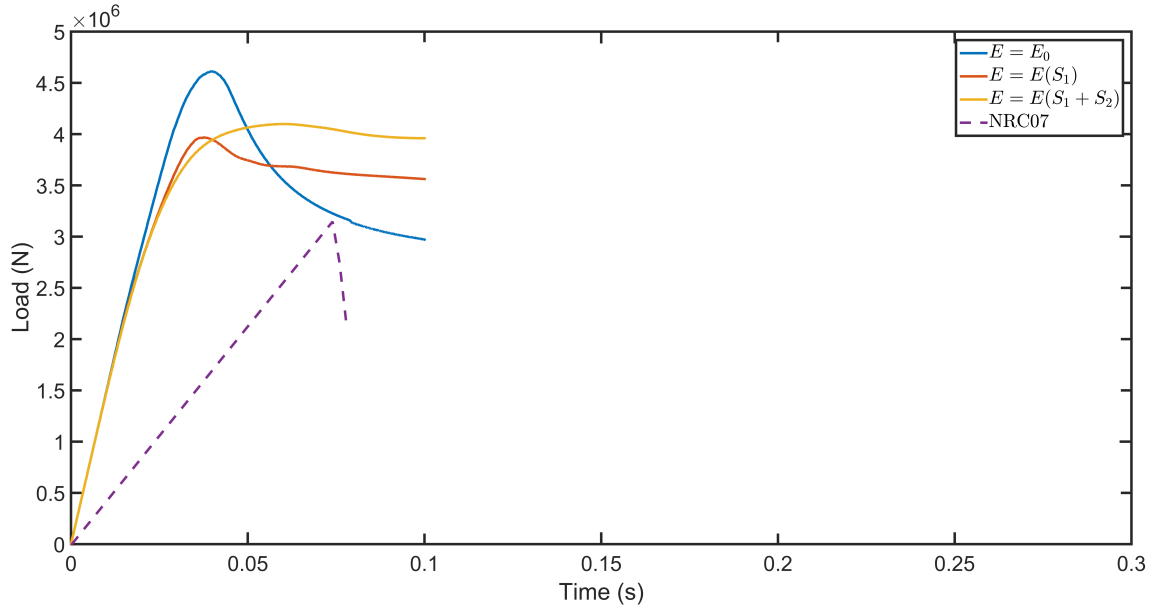


Figure 6.2: Load traces under various elastic damage formulations. The high-pressure exponent  $r_2$  is set to the calibration value used by Xiao (1997) and Li (2002) for all simulations. The first load cycle of test NRC07 from the Hobson’s Choice 1989 test series (Frederking et al., 1990) is plotted for comparison. Note that a constant slope was used to extrapolate load curve back to zero force, so as to ignore the initial transitory loading conditions.

the elastic properties chosen, respectively) combine to produce this discrepancy.

The case of constant elastic properties, which has some supporting experimental evidence under uniaxial and low triaxial stresses (Jordaan et al., 1992b; Kalifa et al., 1992; Stone et al., 1997), was then further examined to establish a baseline for material behaviour. The loading behaviour for increasing  $r_2$  values are shown in Figure 6.3. The results were as expected when constant elastic properties were enforced; increasing  $r_2$  values led to more pronounced load drops, as per the work of Xiao (1997), and

a highly localized damage layer composed predominantly of  $S_2$  damage, the evolution of which can be observed in Figures 6.4. This assumes that the velocity of the test is sufficient to induce dynamic recrystallization; within regimes where microcracking dominates, increasing  $r_2$  actually leads to a *reduction* in  $S_2$  damage.

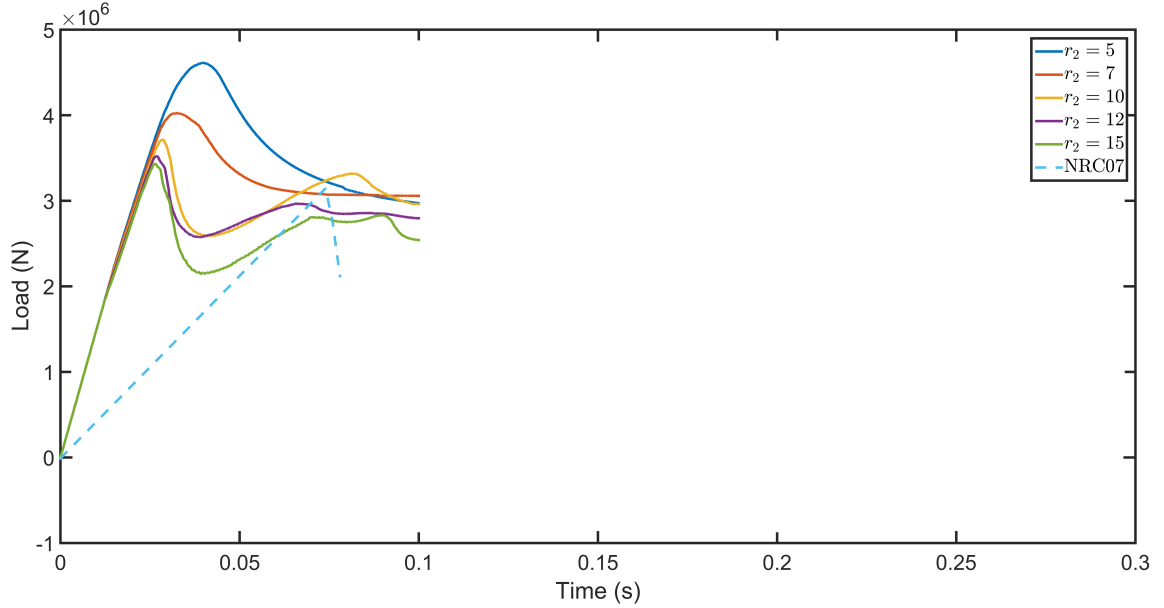


Figure 6.3: Load traces for increasing high-pressure exponents with constant elastic properties. The load drop becomes more sheer as  $r_2$  is increased, as noted by Xiao (1997). The first load cycle from test NRC07 (Frederking et al., 1990) is plotted for comparison; these results are seen to compare much more favourably to experimental results.

Including either type of elastic damage leads to undesired loading behaviour; microcracking elastic damage produces slight load drops with gentle slopes, while the inclusion of high-pressure elastic damage produces plastic-like loading behaviour, with

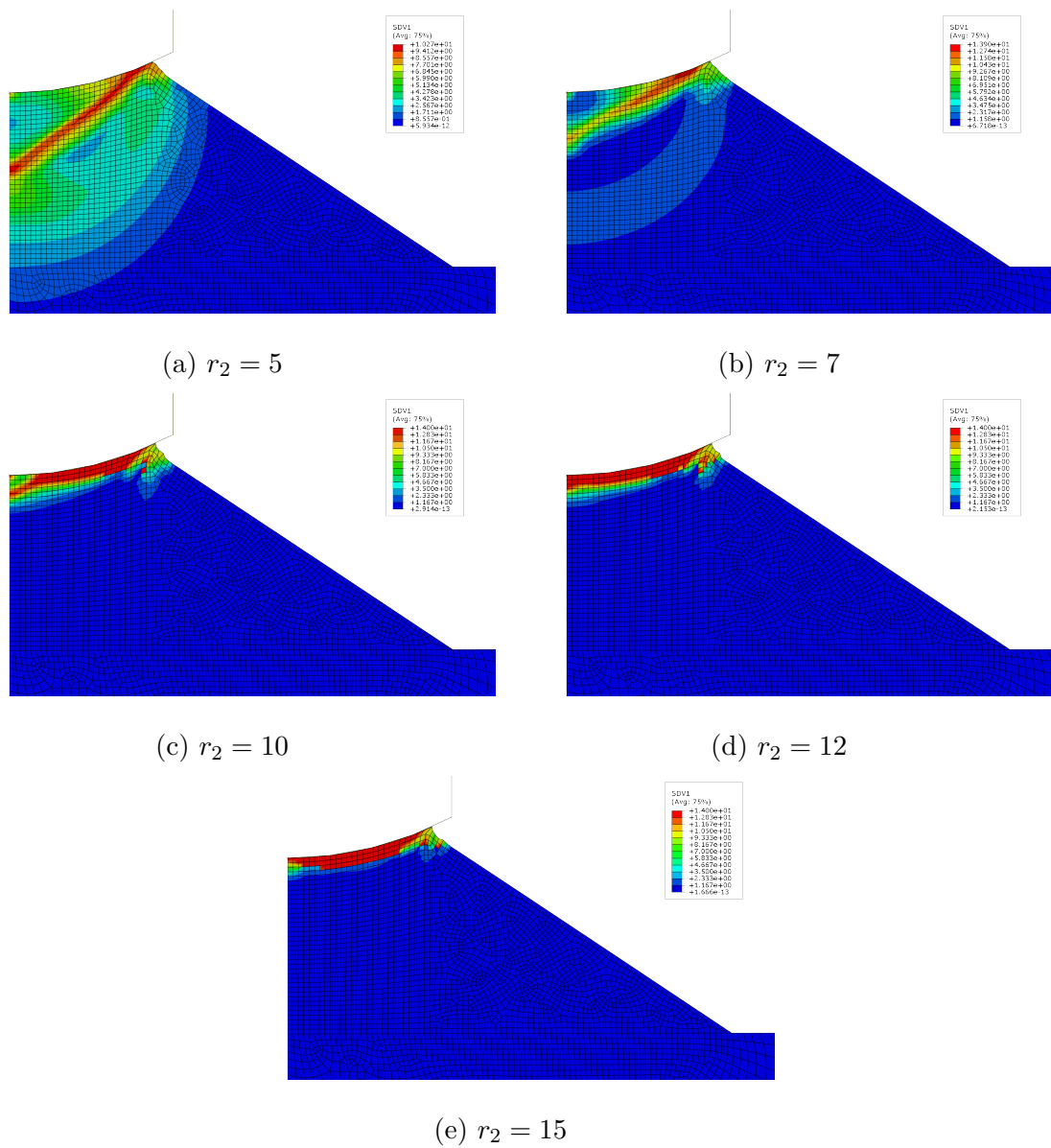


Figure 6.4: Damage layer development at approximately peak load for increasing values of  $r_2$ . The layer becomes highly localized, similar to experimental indentation results.

each  $r_2$  exponent producing a slightly different load plateau, as seen in Figures 6.5. It is therefore recommended that constant elastic properties be enforced while increasing

the high-pressure damage exponent ( $r_2$ ), as is done throughout the remainder of this work. Further experimental verification of this constant elastic modulus assumption would be highly valuable.

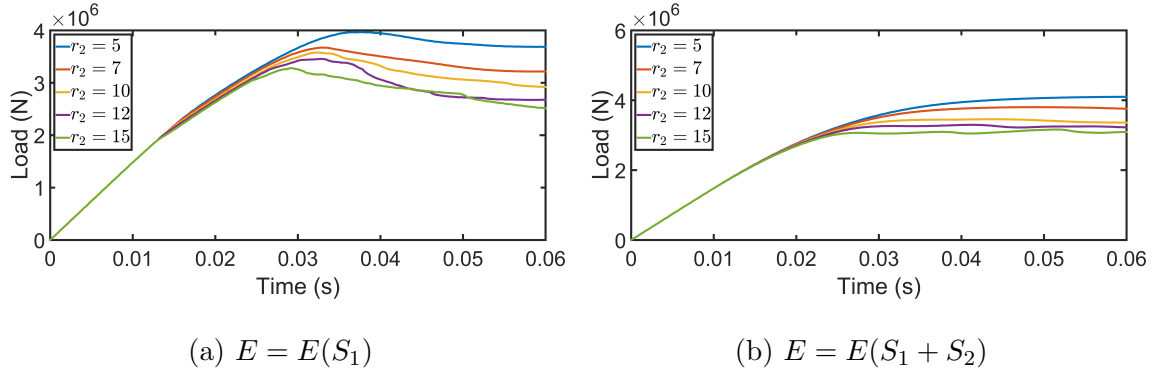


Figure 6.5: Load traces for increasing high-pressure exponents with elastic damage.

Finally, the effects of the constant Poisson ratio formulation of Moore et al. (2013) and the microcracking formulation of Kachanov (1993) on the elastic modulus of the Kelvin spring were compared (it should be noted that the constant Bulk modulus formulation introduced in Chapter 2 produces an elastic modulus identical to the constant Poisson's ratio formulation, and thus produces identical results when the remaining elastic properties are assumed to be constant). The differences are insignificant when constant elastic properties are assumed, which is to be expected; the delayed elastic spring decays very quickly and eventually disappears under both formulations. The effects are much more pronounced when microcracking or high-pressure elastic damage are assumed, though these results are of little interest here. The Kachanov model was chosen as a baseline for further simulations, as it has some theoretical basis.

### 6.1.2 Normalized Velocity Testing

The microstructural behaviour of ice during indentation has been shown to scale relatively well from small-scale laboratory testing up to medium-scale in-situ experiments and beyond. The normalizing factor appears to be the velocity; if the diameter of the indenter is reduced by a factor of ten, then the velocity must also be reduced to match. Note that while microstructural behaviour does appear to scale, fracture behaviour does not; as the interaction volume increases the probability of it including a flaw of sufficient size to act as a “weakest” link increases, leading to a decrease in global pressure with increasing contact area that is known as the scale effect. See Sanderson (1988), Jordaan and Pond (2001), Taylor and Jordaan (2015), and others for more detail.

Careful thought must be put into the comparison of results from indentation tests with different geometries. In this case, three geometries are of interest; the cylindrical indentation geometry of the Hobson’s Choice 1989 test series, which was used to verify the models of Xiao (1997) and Li (2002); the spherical end-cap geometry from the same series, which was used as a basis for the laboratory indentation tests of Browne (2012) and O’Rourke et al. (2015); and the simplified finite element model used to reproduce their results, as described in Section 6.1.

The Hobson’s Choice tests using the flat indenter were pressed into a flattened wedge of ice. The initial contact area was not the full indenter area. Final contact area was dependent upon the depth reached during indentation, as well as the extent of fracturing and deformation; for low speed tests it is possible the ice deformed continuously, coming into further contact with the indenter and increasing the contact

area. For high speed tests, it is more likely that the ice on the periphery simply fractures, reducing the amount of contact area instead. Under these conditions, the initial contact diameter seems the most suitable metric by which to define the normalized velocity.

This is not the case for the spherical end-cap indentations, as a flat ice surface was used. The initial contact area would therefore be infinitesimal, and is not a useful metric by which to define the normalized velocity. The final contact region again depends upon the depth of the indentation and the extent of fracture. In this case, the final contact diameter provides the most suitable metric for defining the normalized velocity.

The geometry used for simulations was designed to model a spherical end-cap indentation after initial contact and fracture occurs. It therefore closely resembles the late stages of such a test, with practically the full contact area already achieved. Since the model does not include fracture behaviour, the contact area will continue to increase during indentation. The effect is relatively minor, and the benefits of the extended indenter outweigh the cons; nodes from the ice mesh would otherwise creep around the indenter surface, giving the mistaken impression that the ice passed through the indenter. The diameter of the groove in the ice is used to define the normalized velocities for these simulations.

Indenter velocities over a range of three orders of magnitude were simulated. The examined velocities and their corresponding normalized velocities,  $v_n$ , are listed in Table 6.2. These velocities were chosen to match both the normalized velocities examined in the indentation experiments described in O'Rourke et al. (2015) as well as the velocity used in simulations by earlier investigators (Jordaan et al., 2016; Li,

Table 6.2: Indentor velocities simulated;  $v$  represents the true velocity,  $v_n$  the normalized velocity.

$v$ (mm/s)	68	6.8	0.68
$v_n$ ( $s^{-1}$ )	0.34	0.034	0.0034

2002; Xiao, 1997).

The resulting load traces can be seen in Figure 6.6. The ice transitions to creep behaviour with decreasing velocity, as seen in the reduction in the magnitude of the load drop for the 0.68 mm/s indentor velocity simulation. It should be noted that the maximum loads observed in the high speed tests may be excessive; in a true indentation experiment, fracture may occur prior to reaching these loads, as noted in Turner et al. (2015).

The simulations produced the expected damage layer evolution, with a thin, highly damaged layer observed in the high speed test and a disperse damage zone produced by the low speed creep test, as shown in Figure 6.7 (Note that a high-pressure damage exponent of at least  $r_2 = 10$  is required to produce this behaviour). These results compare well to recent laboratory-scale experiments (Kavanagh et al., 2015; O'Rourke et al., 2015; Turner et al., 2015) when the normalized velocity is taken into account, as seen in Figure 6.8.

The surface stresses and damage distributions during layer development were also examined for both the low- and high-speed simulations. For both speeds, the surface stresses are initially parabolic, with the minimum stress occurring near the centre of

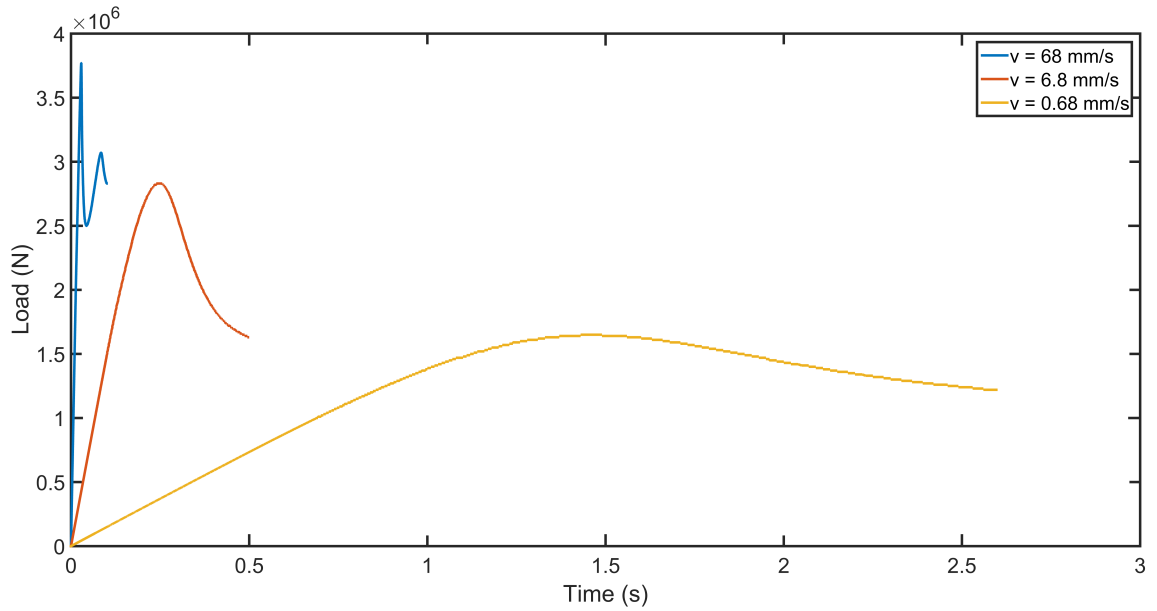


Figure 6.6: Load traces for examined indenter velocities. Relevant parameters include: 1) used calibration values of Xiao; 2) no elastic damage was implemented, and; 3) the high-pressure damage exponent,  $r_2$ , equals 10.

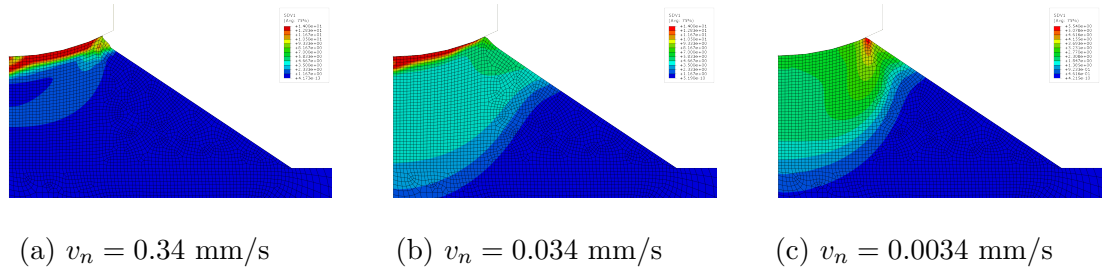


Figure 6.7: Damage layer development at approximately peak load for high, medium, and low indenter velocities. The layer becomes highly localized at high velocities, similar to experimental indentation results.

the indenter and the maximum at the edge, as expected from the geometry of the simulation.

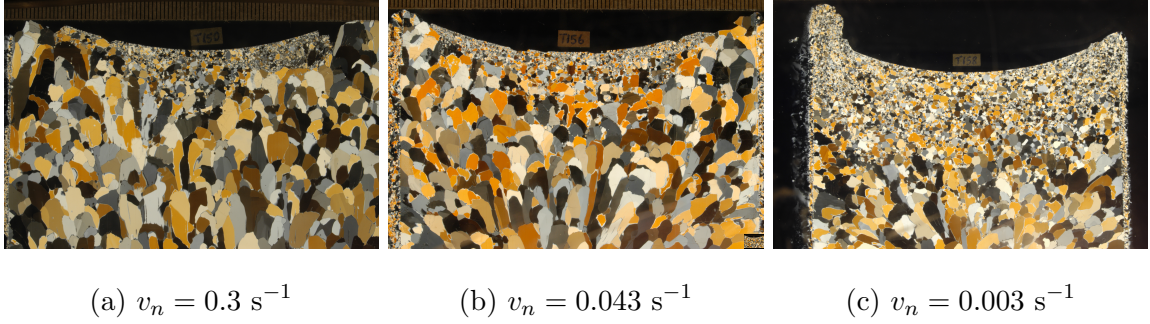


Figure 6.8: Thin sections for normalized velocities of 0.3, 0.043, and  $0.003 \text{ s}^{-1}$  under polarized light.

Simulation results begin to differ as damage accrues under the edge of the indenter; for the high-speed test, the material at the edge becomes unable to support shear stress, leading to a drop in von Mises stress and a corresponding increase in hydrostatic pressure. This process spreads from the edge towards the centre of the indenter, with maximum load occurring when approximately half the surface can no longer support shear stress. Damage also begins to accrue at the centre of the indenter at this time, which may also influence the timing of the load drop. The full damage layer develops within  $0.003 \text{ s}$  of the peak load, corresponding to the complete collapse of shear strength within the layer. It is reasonable to believe that the layer would be extruded from beneath the indenter at this point during a true indentation experiment, after which the cycle would begin anew. This series of developments is shown in Figures 6.9; the load trace is provided for convenience.

It should be noted that the stresses observed are significantly higher than those observed by Li (2002) under similar conditions. This can be explained by a combination of factors: firstly, a much finer mesh is used here, which localizes the surface loads into a smaller area and leads to stresses approximately  $10 \text{ MPa}$  higher, and;

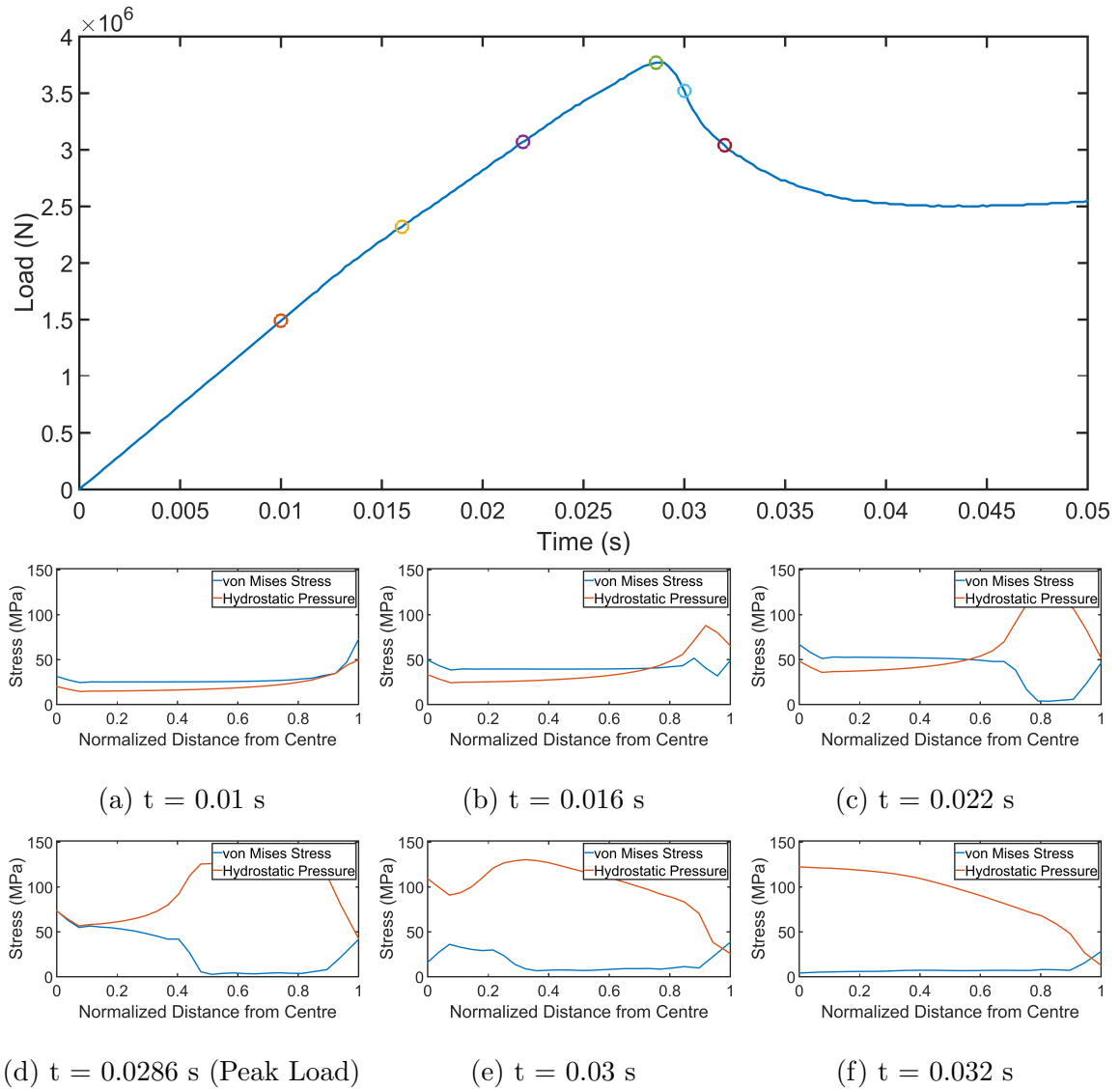


Figure 6.9: Development of surface stresses over the course of indentation simulation with indenter velocity of 68 mm/s. Note that the slightly higher stresses at the centre of the indenter are an anomaly, likely due to the constraints imposed at this location. secondly, some form of elastic damage was implemented in the work of Li, which drastically reduces the observed stresses.

The observed softening in the layer is related to the flux of energy into the  $hpz$ , as

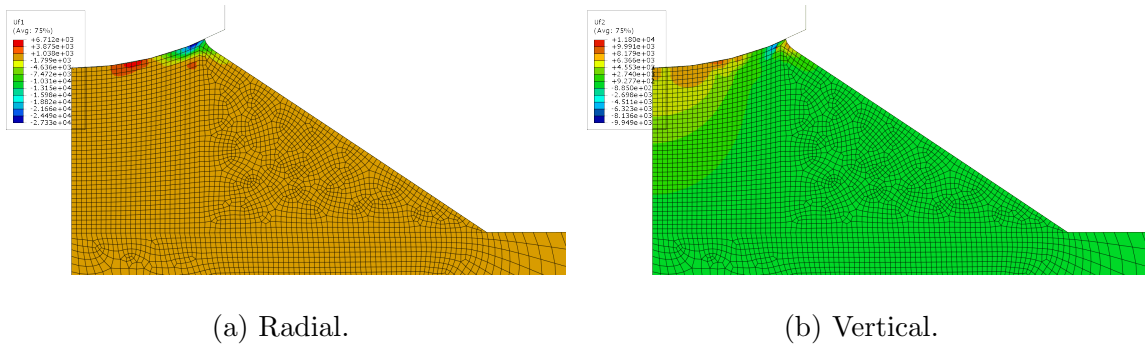


Figure 6.10: Energy at peak load. Energy is seen to flow into undamaged region in surface layer; majority of ice left unstrained and undamaged.

shown in Figures 6.10. The majority of the energy is absorbed in the layer, with little energy flowing into the remainder of the ice; this explains why the latter region is relative undamaged. Note that the results differ slightly from the work of Li (2002), due simply to the change in geometry; the ice at the edge of the *hpz* under a spherical-end cap indenter flows out and up, which cannot occur under a flat indenter.

Similar surface behaviour is observed for the low-speed simulation, with two major differences: 1) the surface damage is entirely microcracking based, and 2) runaway damage does not occur, so the complete collapse of shear strength is not observed. This is seen in Figures 6.11, where the von Mises stress is still comparable to the hydrostatic pressure post-peak load.

To confirm that layer development is indeed dependent upon normalized velocity, two additional ice geometries were examined, one with half the contact radius, the other with double, as shown in Figures 6.12. The radius of curvatures of the indentors and the indenter velocities were also modified by these ratios. The simulations were found to produce similar behaviour at a given normalized velocity, no matter the scale

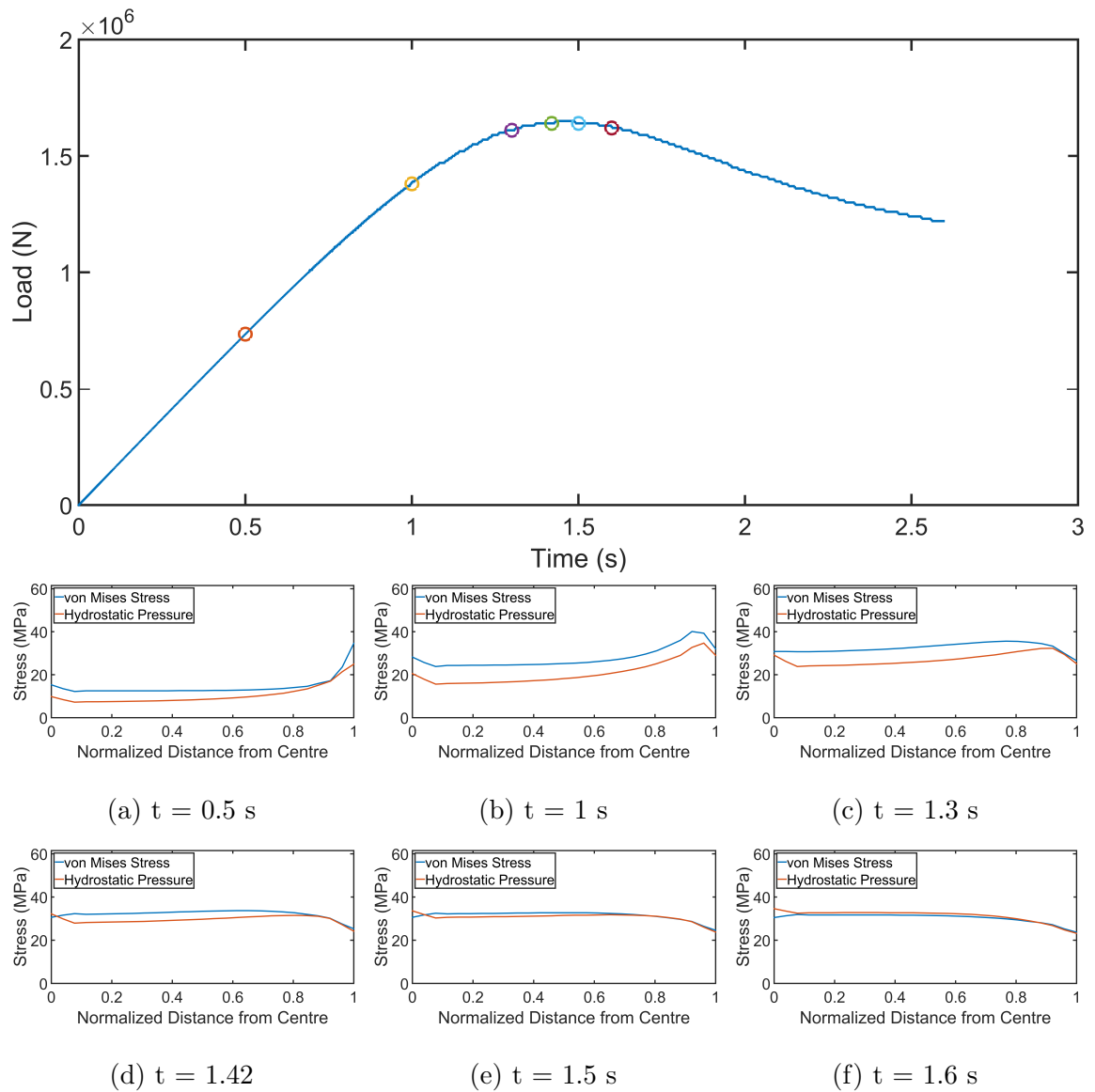


Figure 6.11: Development of surface stresses over the course of indentation simulation with indenter velocity of 0.68 mm/s. Note that the slightly higher stresses at the centre of the indenter are an anomaly, likely due to the constraints imposed at this location.

of the interaction; the ratio of layer depth to indenter radius for the examined cases were found to be approximately equal to four, as seen in Figures 6.13 and 6.14.

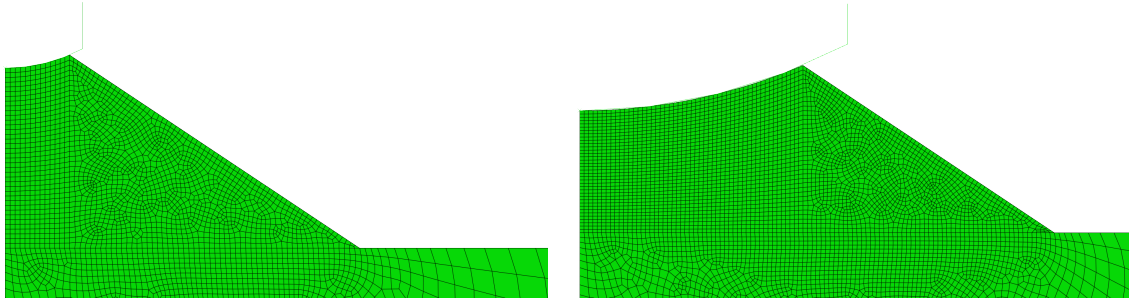


Figure 6.12: Scaled ice geometries.

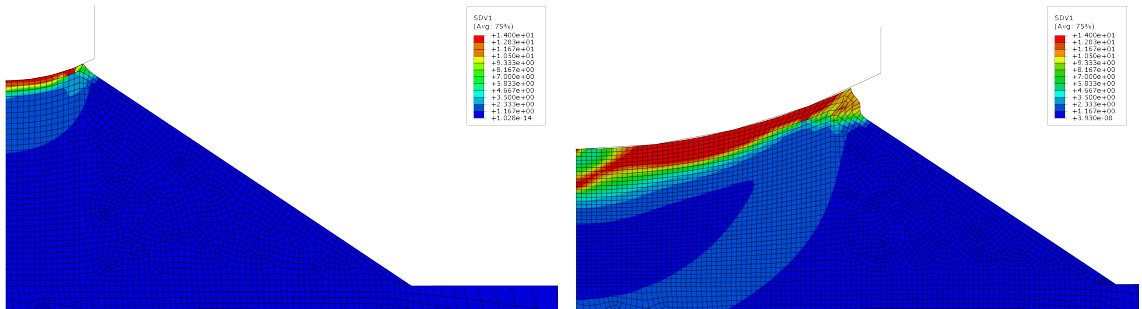


Figure 6.13: Layer development,  $v_n = 0.34 \text{ s}^{-1}$ .

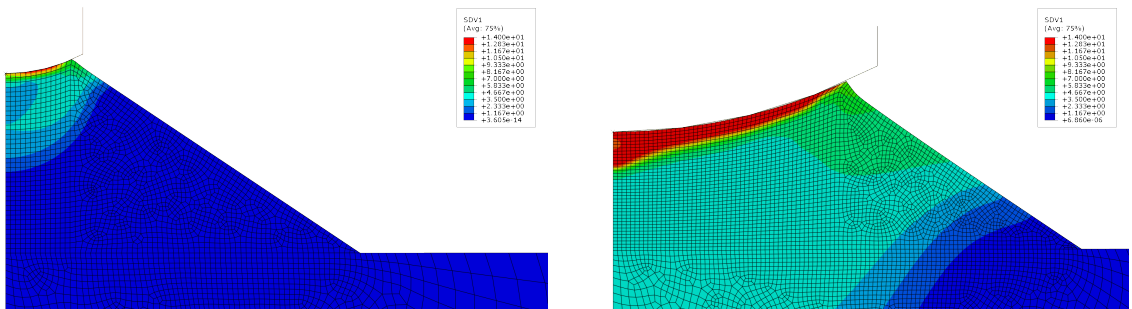


Figure 6.14: Layer development,  $v_n = 0.034 \text{ s}^{-1}$ .

## 6.2 Further Development

Numerous additions and modifications to the constitutive model developed by previous investigators were implemented and examined in this study in an effort to improve both our understanding of the processes involved in an ice-structure interaction as well as the estimation of the loads produced. An indenter velocity of 68 mm/s, ( $v_n = 0.34 \text{ s}^{-1}$ ), is enforced for each simulation, to match the work of previous investigators. The results of these simulations are summarized in the following sections.

### 6.2.1 Recalibration of Microcracking Damage Function

Recalibration of the pressure-dependent microcracking damage function,  $f_1(p)$ , was undertaken to remove its dependence upon the cut-off pressure,  $p_c$ , which is likely to be highly dependent upon the environmental temperature. The triaxial data of Meglis et al. (1999) were used to produce the necessary fit parameters, which are presented in Table 4.1.

The recalibrated damage function was found to produce results nearly identical to those of Xiao (1997), with only minor differences in damage development and indenter load, as shown in Figures 6.15 and 6.16. With this calibration, the damage function should now be applicable for all combinations of temperature and pressure, and was then used for all further simulations.

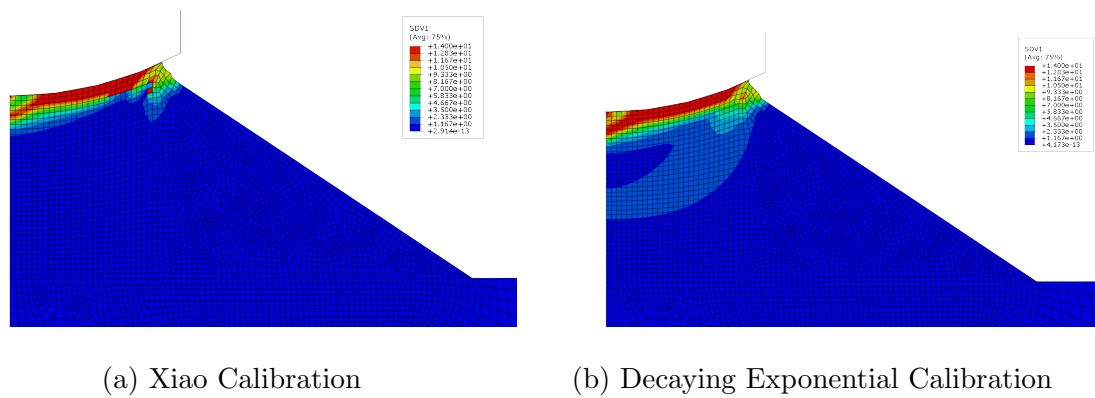


Figure 6.15: Damage layer development for recalibrated and original  $f_1(p)$  at approximately peak load.

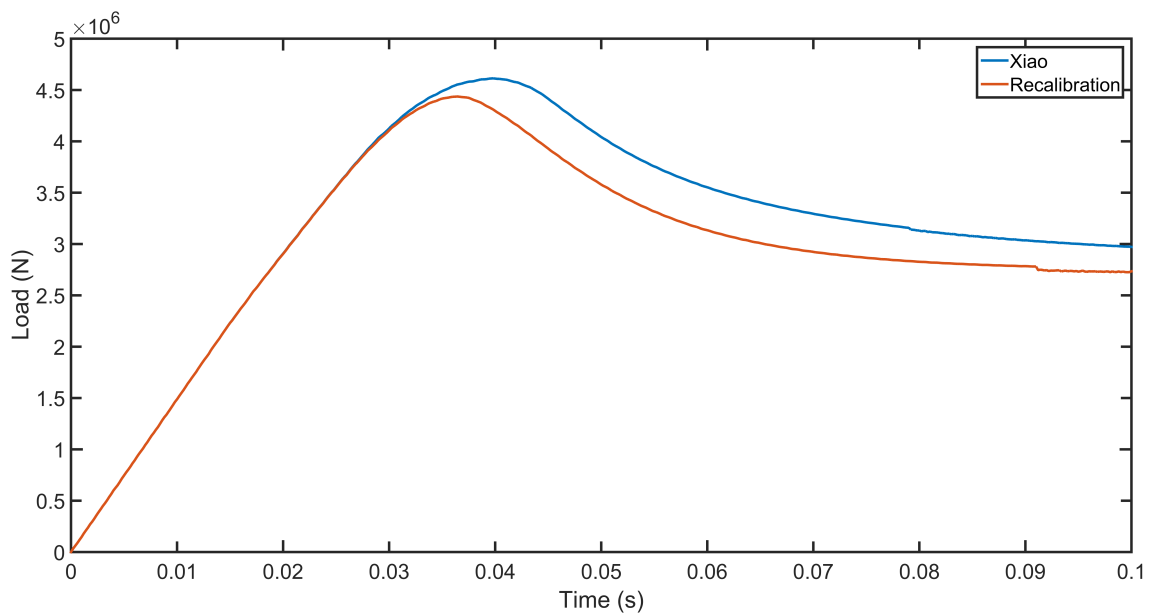


Figure 6.16: Comparison of indenter loads produced by recalibrated and Xiao (1997)  $f_1(p)$ .

## 6.2.2 Power Law Breakdown

Power law breakdown is known to occur under uniaxial conditions for applied stresses of up to approximately 10 MPa, but appears to be suppressed under triaxial compression, as discussed in Section 4.4. To investigate this behaviour, the secondary creep rate of Xiao (1997) and others was modified to include a pressure-dependent sinh function, as described by Equations 4.68 and 4.69.

The effects of this addition were examined within a series of simulations with different normalization pressures,  $p_n$ . The limits of the function  $\alpha(p)$  provide a baseline for comparison; the lower limit reduces to the standard power law behaviour, while the other corresponds to the pressure-independent application of power law breakdown, with  $\alpha(p) = 0.27$  in this formulation. The indiscriminate application of power law breakdown leads to a drastic increase in secondary creep, which, in turn, significantly reduces the applied stress, as seen in Figures 6.17; this produces behaviour similar to the effect of increasing the power law exponents for delayed elastic ( $n$ ) and secondary creep ( $m$ ) deformation or significantly reducing the indentation velocity, as discussed in Section 6.1.2. It is clear that the parameters involved in ice deformation are all intimately linked, with multiple avenues to the same result.

Between these extremes, a number of normalization constants were implemented to examine the effects of power law breakdown on regions of varying hydrostatic pressure. The effect of increasing the normalization constant on the indenter load can be seen in Figure 6.18. Low values are seen to be practically identical to pure power law behaviour, as expected. The loading traces begins to diverge from power law behaviour as the normalization constant approaches a value of ten; exponential

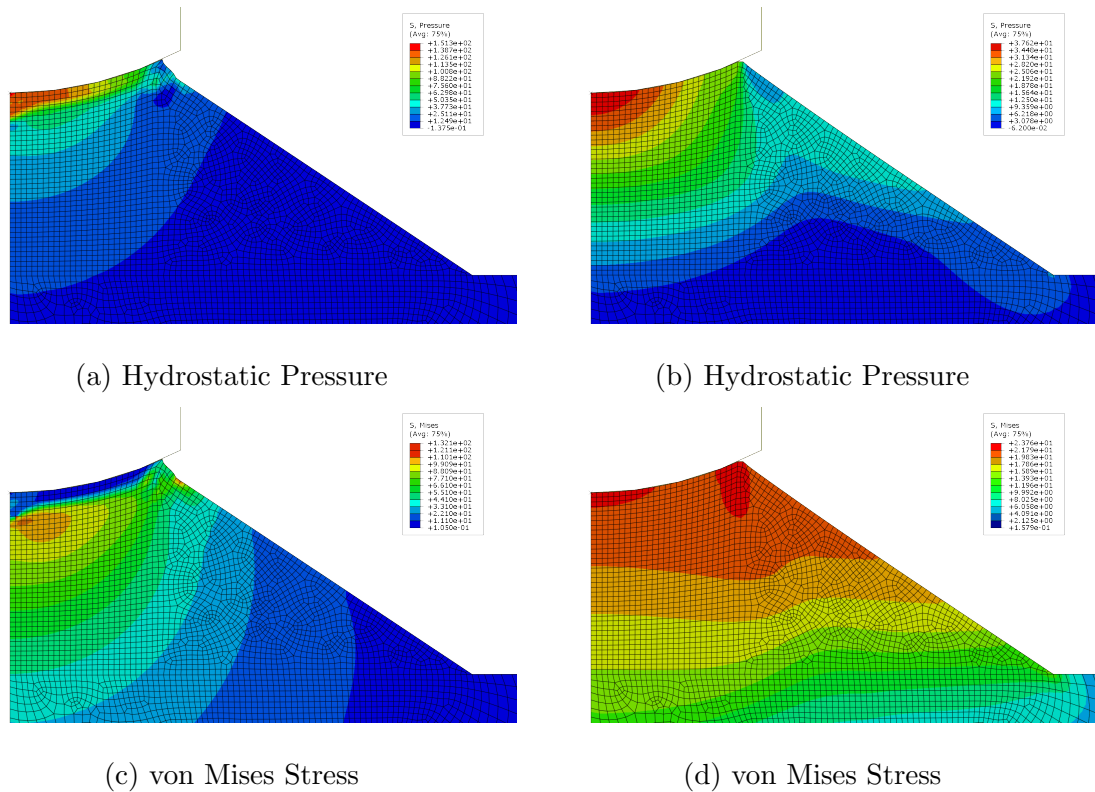


Figure 6.17: Stress conditions near peak-load with (right) and without (left) power law breakdown. A value of  $r_2 = 10$  was used to ensure a significant load drop under power law conditions.

behaviour in low-pressure regions has begun to slightly alter the stress distributions in the peripheral regions.

A qualitative difference in behaviour has occurred by the time the normalization constant has reached a value of twenty; the peak load has been delayed due to the decrease in stress brought on by higher secondary creep strain, and the magnitude of the load drop has decreased due to the corresponding change in damage distribution, as shown in Figures 6.19. At still higher normalization constants the deformation behaviour closely resembles pure exponential behaviour, and is of little interest. Given

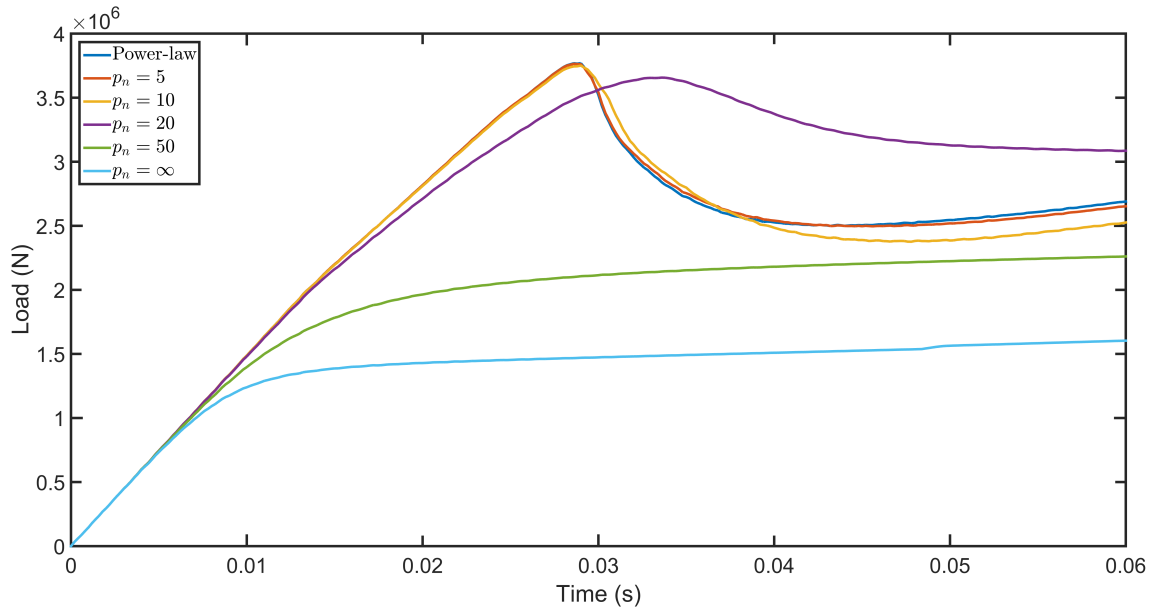


Figure 6.18: Resulting indenter load from varying normalization constants for power law breakdown.

that there is little evidence for power law breakdown at the pressure observed within high-pressure zones, any normalization constant that affects that region should be avoided. Thus, a value of between ten and twenty is recommended; any lower and the implementation is virtually pointless, any higher and power law breakdown is no longer suppressed within the *hpz*.

### 6.2.3 High-Shear Elastic Failure

The recent study described in Chapter 3 showed that there may exist a limit to the amount of shear stress a triaxially confined ice specimen can support elastically. This limit was found to decrease slightly as confining pressure was increased from mid-to-high levels, which is consistent with a decrease in strength with confining pressure that

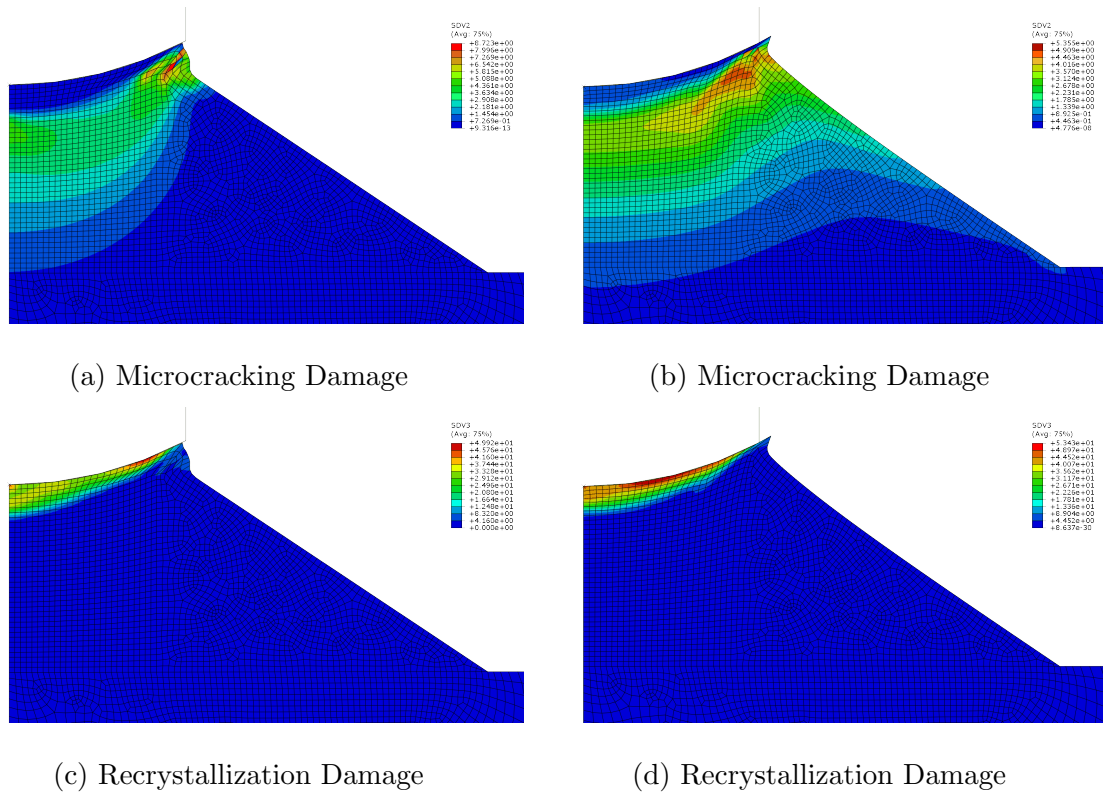


Figure 6.19: Damage distributions with (right) and without (left) power law breakdown. Microcracking damage can be seen to have spread throughout the sloped region, where confinement is practically non-existent, with the addition of power law breakdown.

has been found in other studies (Jones and Chew, 1983). Finite element simulations produce von Mises stresses that at times greatly exceed this limit. In an attempt to replicate this behaviour, a limit to the von Mises stress of each element of 26.0 MPa was applied. To accomplish this, all stresses were scaled by a factor of 26.0/s whenever the von Mises stress was found to be greater than 26.0 MPa.

The results of this restriction on previously examined simulation conditions differ greatly from the observed experimental evidence; applying the limit element-by-

element prevents the formation of a damage layer, as the stress is dispersed throughout a much larger region with the ice sample, and instead produces a radial layer of microcracking damage starting from the edge of the indenter, as shown in Figures 6.20 and 6.21.

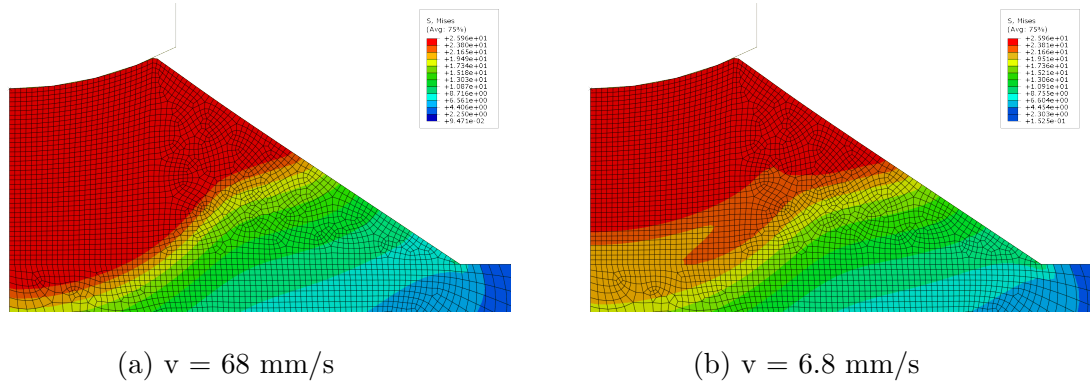


Figure 6.20: von Mises stress distribution for two different indenter velocities when von Mises stress is limited to 26.0 MPa.

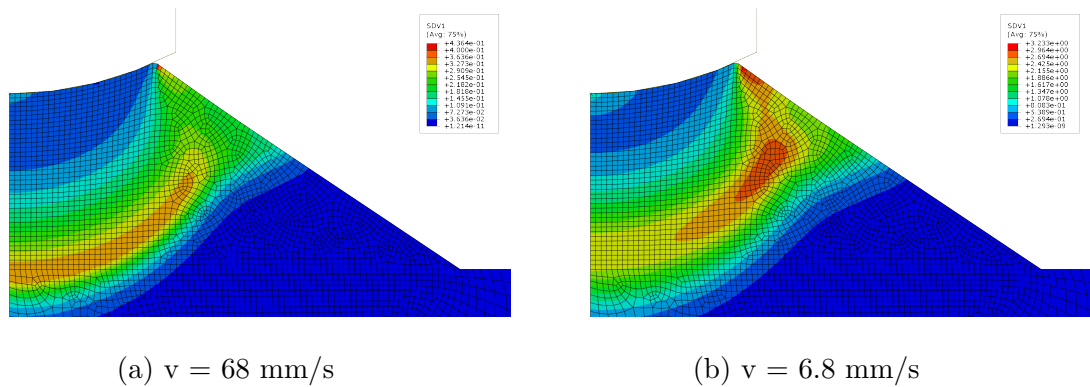


Figure 6.21: Damage distribution for two different indenter velocities when von Mises stress is limited to 26.0 MPa.

This implementation produces behaviour that is similar to plastic deformation, as can be seen in the load traces for the two velocities shown in 6.22; the resulting indenter loads are practically identical when plotted versus indentation depth, as would be the case for general elastic-plastic materials. Combined with the lack of layer development, it is clear that this implementation does not reproduce experimental results.

To effectively reproduce the results observed in triaxial experiments, the von Mises stress limit should be applied at the ice-indenter interface (likely as a load limit on the indenter) instead of the element-by-element method presented here. This would allow for the development of excessive stress in single elements without violating the stress limit at the boundary. The author is unaware of any method with which to enforce such a limit using Abaqus at this time.

In an attempt to sidestep this problem, the von Mises stress limit was re-imagined; rather than applying a hard limit to the applied stress, any element which exceeded the stress limit was instead assumed to immediately reach an excessive level of microcracking damage, drastically reducing the elastic modulus. In this case, the damage was assumed to immediately reach the damage cap of 14, which represents a reduction in elastic modulus by a factor of 15 and an increase in the delayed elastic and viscous strain rates of  $e^{14} = 1.2 \times 10^6$ , which was hypothesized to produce effects comparable to elastic failure. It should be noted that this requires that microcracking elastic damage be assumed.

The resulting load trace for these conditions is presented in Figure 6.23; the standard result when the elastic failure limit is not included is provided for comparison. The new limit is seen to produce a sharp load drop almost immediately, reaching less

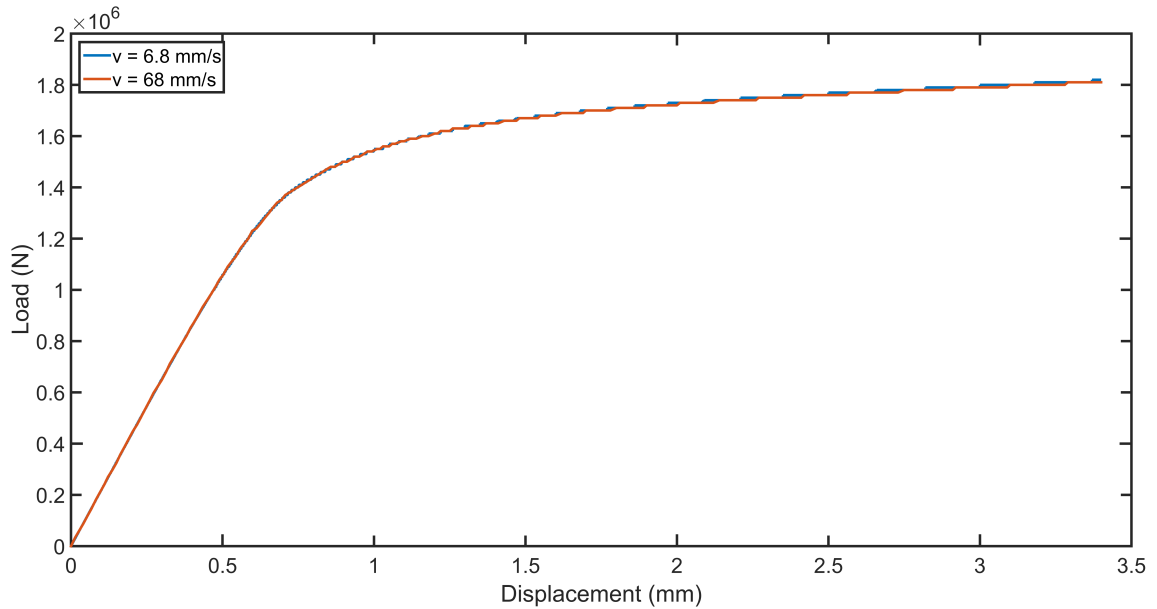


Figure 6.22: Load vs. indentation depth for two different indenter velocities when von Mises stress is limited to 26.0 MPa.

than a third of the maximum load observed without the elastic failure limit. The corresponding damage layers both before and after the load drop are provided in Figures 6.24; the layer is observed to increase in size dramatically within these 0.002 s, particularly at the centre of the indenter.

These results contradict experimental evidence in several ways. Firstly, layer development is a continuous process, characterized by the continuous expansion (and removal) of damage with increasing indentation. Secondly, many indentation experiments produce layers that are thinnest at the centre, with large, undamaged grains below. It would seem that this implementation is excessive in its application of damage; a more controlled reduction in elastic modulus may produce results more consistent with experiments.

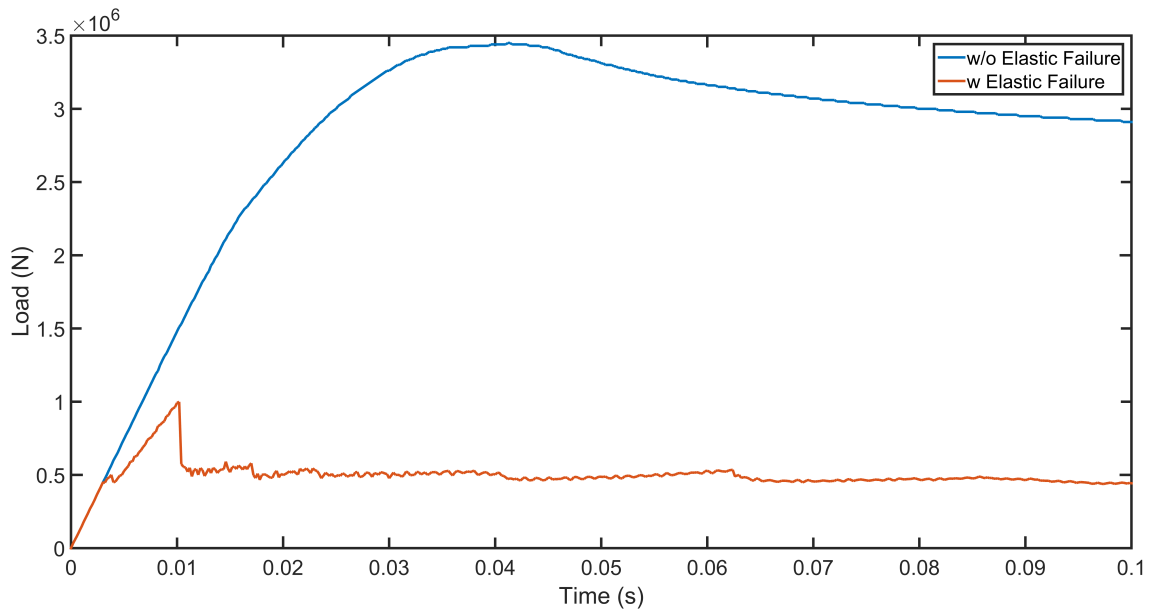


Figure 6.23: Load traces with and without elastic failure assuming microcracking elastic damage.

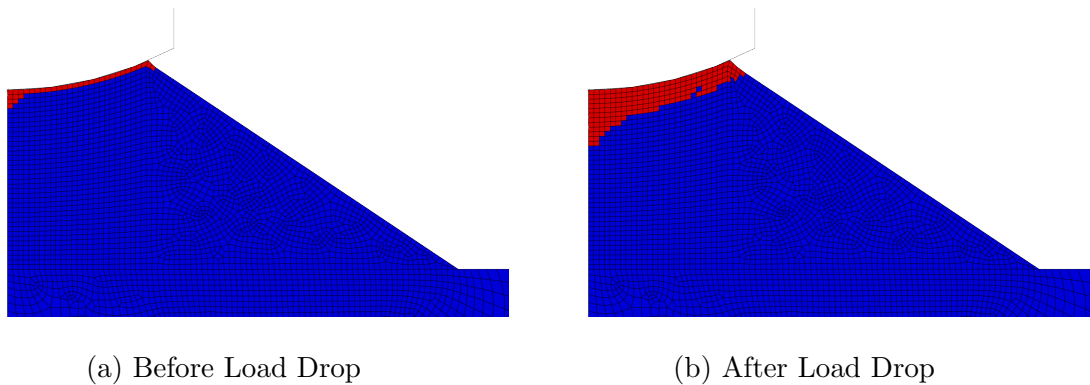


Figure 6.24: Damage layers before and after load drop when elastic failure is assumed.

In a final attempt to model the observed high-shear elastic failure, the reduction in elastic modulus due to exceeding the von Mises stress limit was separated from the effects of microcracking and dynamic recrystallization damage. Two implementations

were investigated: the first scaled the elastic modulus by  $s^m/s$  during any time step where  $s$  exceeded  $s_m$ , while the second simply reduced the elastic modulus a single time, by a factor of 100. The resulting load traces are plotted in Figure 6.25, with the load during the corresponding constant elastic modulus test plotted for comparison. Both results are seen to conform closely to those of the constant elastic modulus test, producing results consistent with experimental indentation tests. Layer development is also maintained, and does not differ significantly from comparison tests. Given these results, reducing the elastic modulus separately would appear to be the most viable method with which to implement high-shear elastic failure. Note that this directly contradicts the assumption of constant elastic properties made in Section 6.1.1; further theoretical and experimental verification is required in order to fully resolve this issue.

#### 6.2.4 Non-Linear High-Pressure Damage Exponent

The possible existence of a non-linear high-pressure damage exponent,  $r_2$ , was intuited from the triaxial data of earlier investigators (Barrette and Jordaan, 2003; Meglis et al., 1999; Xiao, 1997), who had difficulty accurately measuring and estimating its value from experimental data. To investigate this behaviour, a damage-dependent  $r_2$  value was implemented in the following form:

$$r_2 = r_0 e^{S_2/S_0} \quad (6.28)$$

where  $r_0$  is the initial damage exponent and  $S_0$  is a normalization constant. A range of initial damage exponents was examined, beginning with the calibration values of  $r_2$  up to a maximum of  $r_2 = 10$ , which had earlier been found to be the point where a

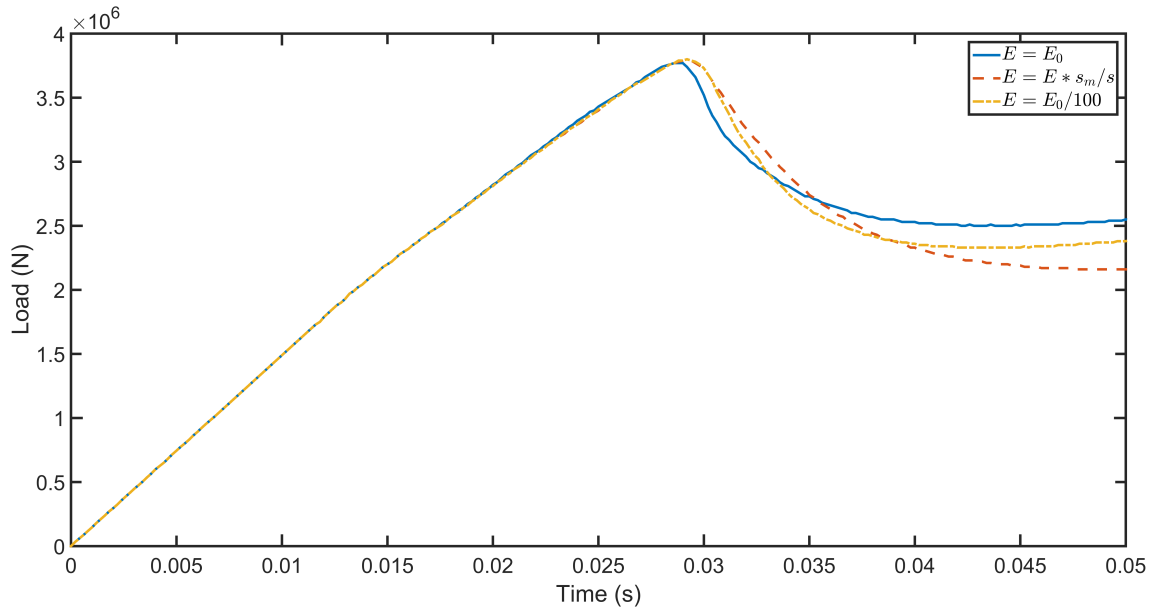
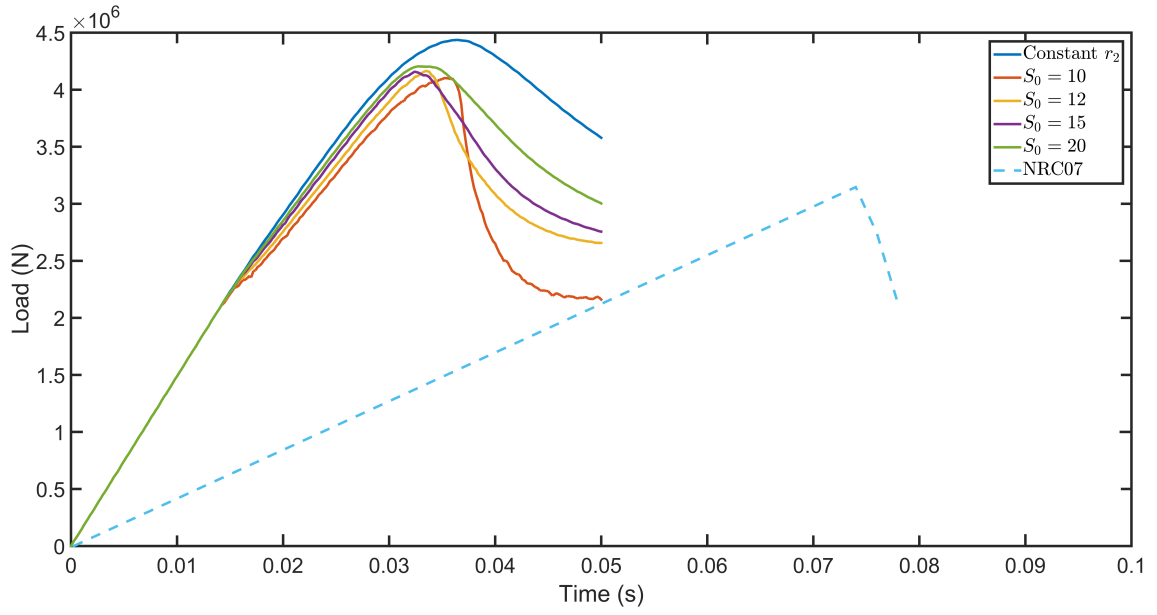


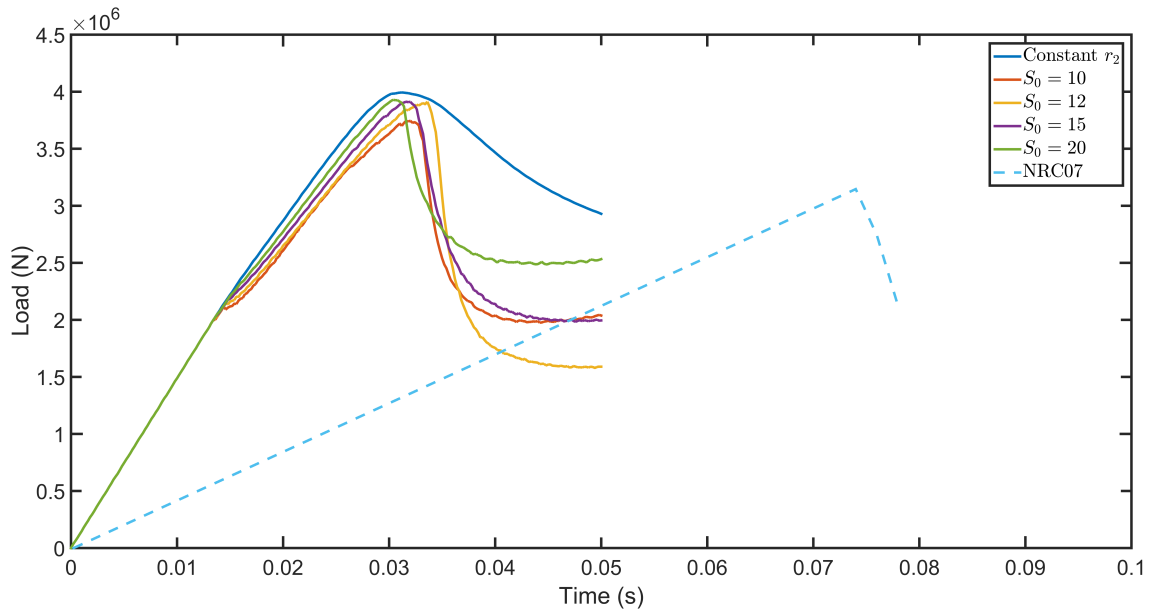
Figure 6.25: Load traces with high-shear elastic failure separated from effect of damage.

significant load drop and a highly localized damage layer had developed for a constant  $r_2$  value. The loading results for the series of indentation simulations are provided in Figures 6.26.

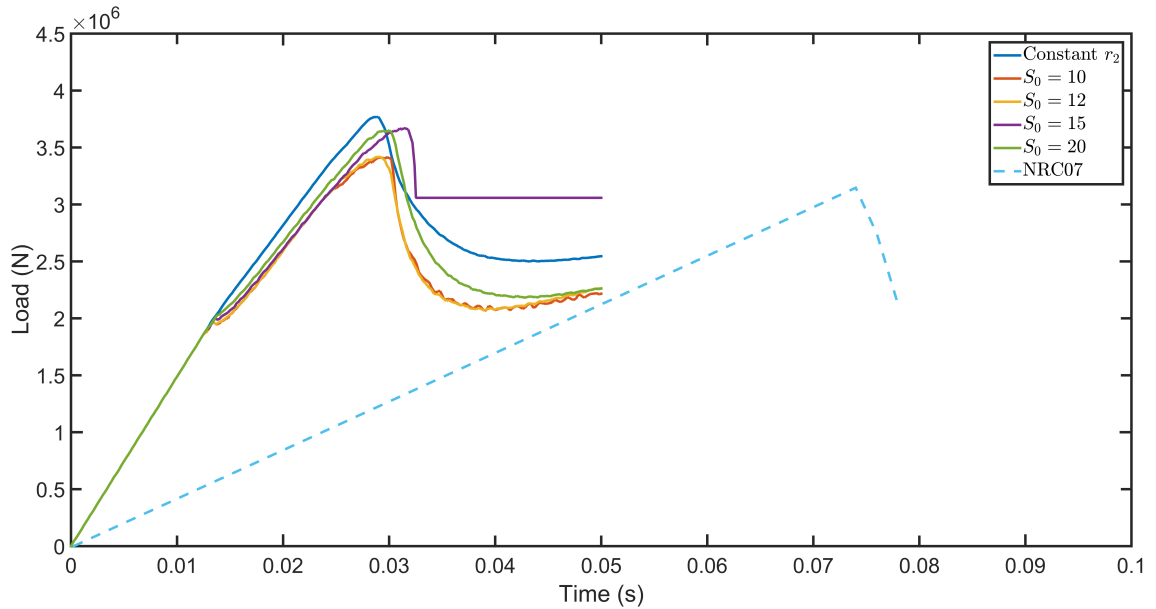
The addition of a non-linear  $r_2$  exponent is seen to produce an incredibly sheer load drop for sufficiently small normalization constants, as seen in all three cases; higher values of  $S_0$  are seen to produce results that are very similar to those for a constant  $r_2$  value. The normalization constant required decreases with decreasing  $r_0$ , as would be expected; higher values of  $r_2$  already produce significant load drops, as seen in the case of  $r_0 = 10$ . It is therefore recommended to use a non-linear  $r_2$  formulation only in the case of lower values of  $r_0$ . Note that the magnitudes of the observed load drops are noticeably larger than that observed in test NRC07; this can



(a)  $r_0 = 5$



(b)  $r_0 = 7$



(c)  $r_0 = 10$

Figure 6.26: Load traces produced for non-linear and constant  $r_2$  values with different initial damage exponents and normalization constants. The first load cycle from test NRC07 (Frederking et al., 1990) is provided for comparison. Note that in the few cases where the simulations failed prior to completion the load was extrapolated simply as a constant.

be attributed to the lack of refreezing within the numerical model.

The damage layers produced under these circumstances are extremely localized, as seen in Figure 6.27; the  $r_2$  exponent increases in a run-away manner, as increasing  $S_2$  damage leads to a higher damage rate under this formulation. This leads to the formation of regions with a significant damage gradient, as regions of microcracking will remain relatively undamaged by comparison.

Given the observed load drops, this formulation appears to be a worthwhile avenue

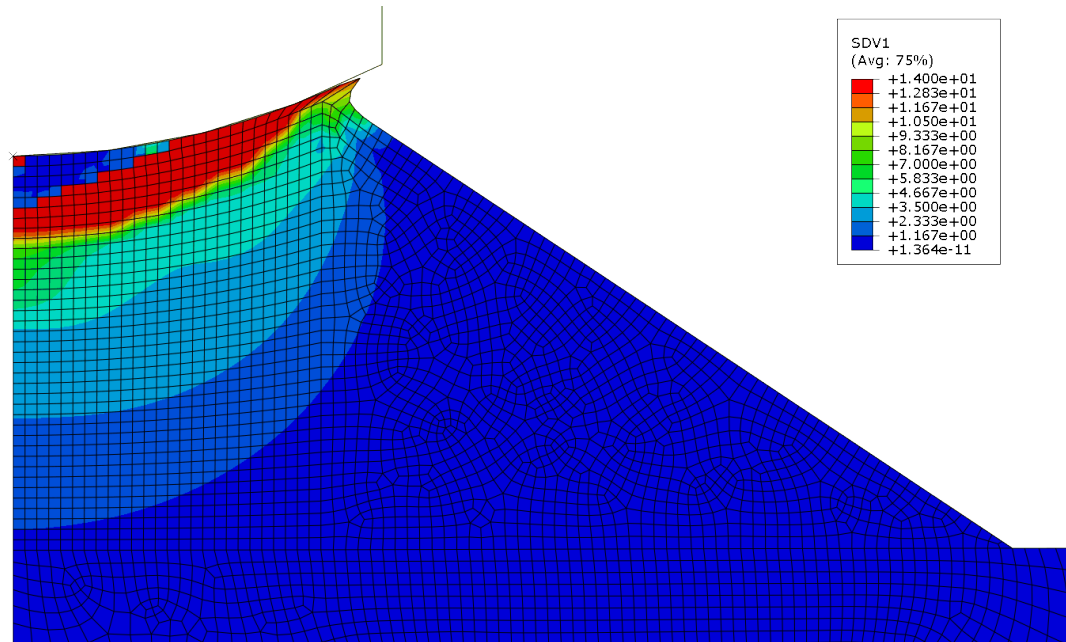


Figure 6.27: Total damage produced by non-linear  $r_2$  value at peak load. Values of  $r_0 = 5$  and  $S_0 = 10$  were used in this case. The damage is seen to be highly localized, with very little damage accruing outside the layer.

for further investigation; experimental and theoretical validation is recommended.

### 6.2.5 Temperature-Dependent Damage Model

The effect of temperature on the deformation of ice has been shown to be practically equivalent to the application of hydrostatic pressure, with some minor deviations due to the existence of stress concentrations at grain boundaries within polycrystalline ice; in this study, these deviations were assumed to be negligible. A pressure-temperature damage function was developed to transform the pressure at some environmental temperature to the corresponding pressure at the reference temperature,  $T = -10^\circ\text{C}$ . This pressure was then used in the high-pressure damage function,  $f_2(p)$ , described

throughout this work. Temperatures lower than  $-10\text{ }^{\circ}\text{C}$  would thus produce less recrystallization damage, with the opposite occurring at higher temperatures, as is observed in indentation experiments.

To examine the effect of this pressure-temperature damage function, several simulations were run at environmental temperatures of  $-5$ ,  $-10$ , and  $-15\text{ }^{\circ}\text{C}$ . Two indenter velocities ( $68$  and  $6.8\text{ mm/s}$ ) were examined, to observe the interrelation between the two parameters. An attempt to apply the shift function of earlier investigators, based on rate theory and experimental results, was also made. However, the transition to a higher activation energy at temperatures above  $-8\text{ }^{\circ}\text{C}$  was found to interfere with the functioning of the model; this can be seen in the load traces of Figure 6.28, wherein the simulation at  $-5\text{ }^{\circ}\text{C}$  is seen to fail early. The rate theory-based approach was thus suppressed in favour of using the pressure-temperature damage function approach.

The pressure-temperature damage function was found to produce results that are consistent with experimental evidence at high indenter velocities; the damage layer increases in size with temperature, while the amount of microcracking decreases significantly, as was observed in Figure 2.14 in Section 2.6.3. The microcracking that does occur is observed to form shear “rings” that move closer to the ice-indenter interface with increasing temperature.

The low velocity results are more difficult to interpret; the above trends still apply, but the low temperature simulation is seen to produce a damage zone similar to a creep test instead of a damage layer with significant microcracking, indicating that there may be a relation between environmental temperature and the onset velocity of creep behaviour. These results are all presented in Figures 6.29. The results are separated into  $S_1$  and  $S_2$  damage in Figures 6.30 and 6.31, respectively.

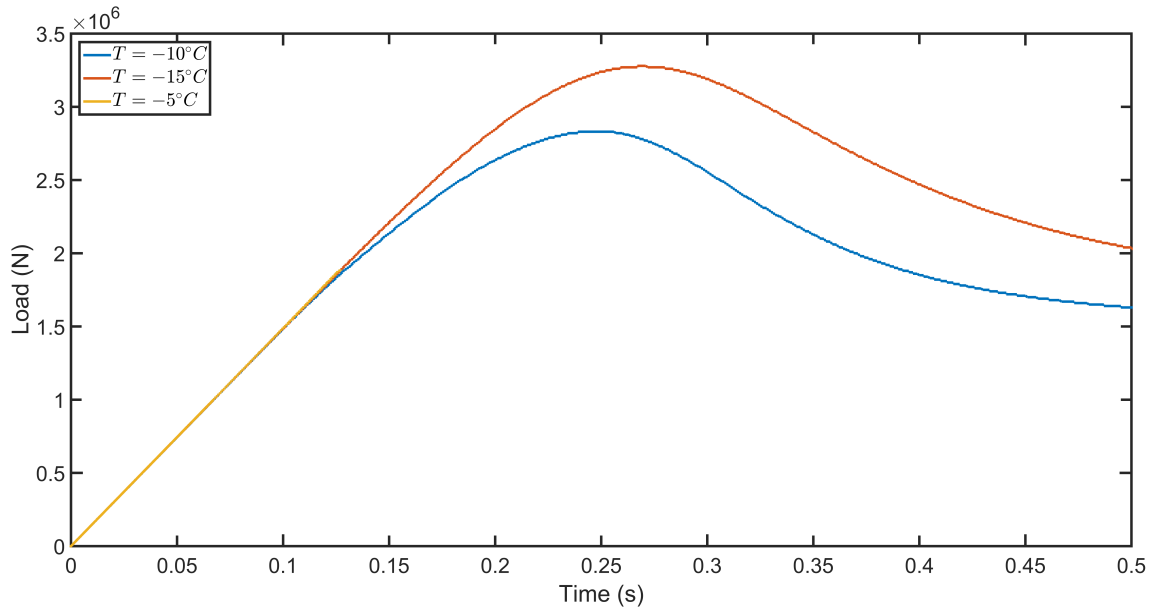


Figure 6.28: Load traces at temperatures of -5, -10, and -15 °C with rate theory-based shift function included.

The corresponding load traces are provided in Figures 6.32. The model produces the expected load drop, and, unlike the activation energy based shift function, produces larger loads at lower temperatures, consistent with experimental evidence, as shown in Figure 6.33. Anomalous behaviour is observed in two cases: for the high-speed, low temperature simulation, the load drop is unexpectedly gentle, providing further evidence for a link between the extent of dynamic recrystallization and the steepness of the load drop, and; the low-speed, high temperature simulation produced a significantly lower maximum load well before the formation of the full damage layer. This is related to the stress conditions associated with this indenter velocity; lower velocities produce lower pressures, leading to the accumulation of little dynamic recrystallization at -10 °C. Thus, there is little difference between the -15 and -10 °C

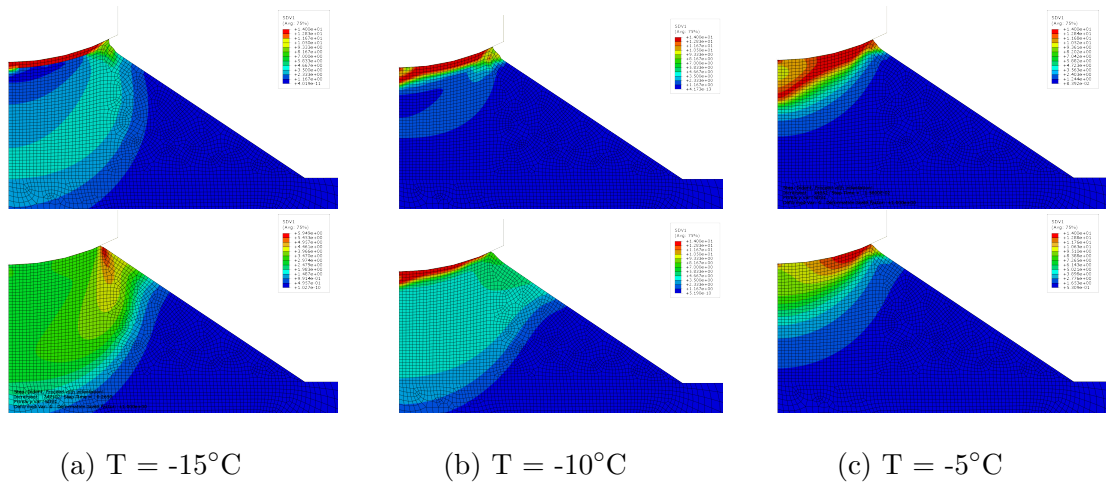


Figure 6.29: Damage layers at temperatures from -15 to -5 °C near peak-load. The top layer of figures were taken from simulations with an indenter velocity of 68 mm/s, while the bottom layer were taken from simulations with an indenter velocity of 6.8 mm/s

simulations, as microcracking dominates both. When the temperature is increased, dynamic recrystallization becomes more prominent, leading to a significant decrease in ice strength. It should be noted that fracture becomes much more likely at colder temperatures, as the loads required to produce microstructural damage become greater than those required to initiate failure through fracture.

It must be noted once again that the pressure-temperature damage function is currently only valid for  $\Delta T_m = [-10, 0]$  and  $T_h = [0.9634, 1]$  due to the environmental temperature of the experiments used to calibrate the models of Xiao (1997) and Li (2002). A series of triaxial compression experiments at -22 °C and hydrostatic pressures ranging up to 220 MPa are required to produce a complete master curve for the pressure-temperature damage function.

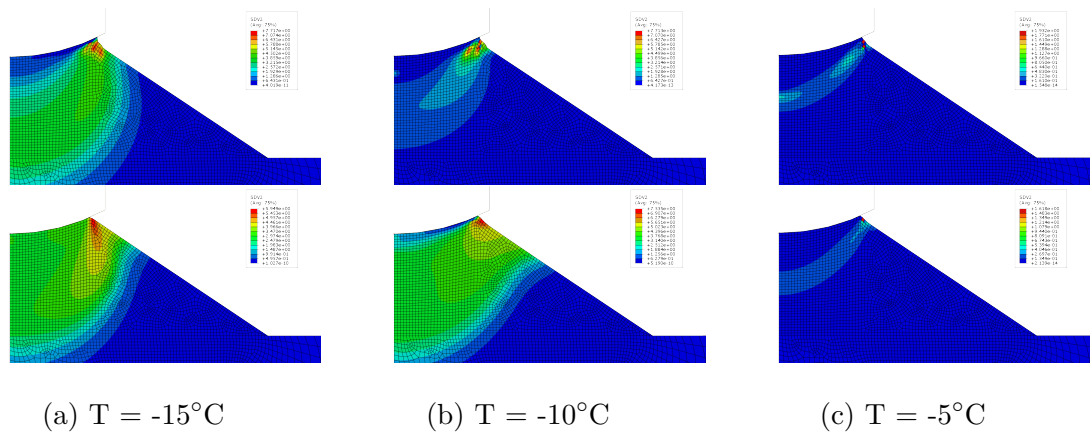


Figure 6.30: Microcracking damage layers at temperatures from -15 to -5 °C near peak-load. The top layer of figures were taken from simulations with an indenter velocity of 68 mm/s, while the bottom layer were taken from simulations with an indenter velocity of 6.8 mm/s

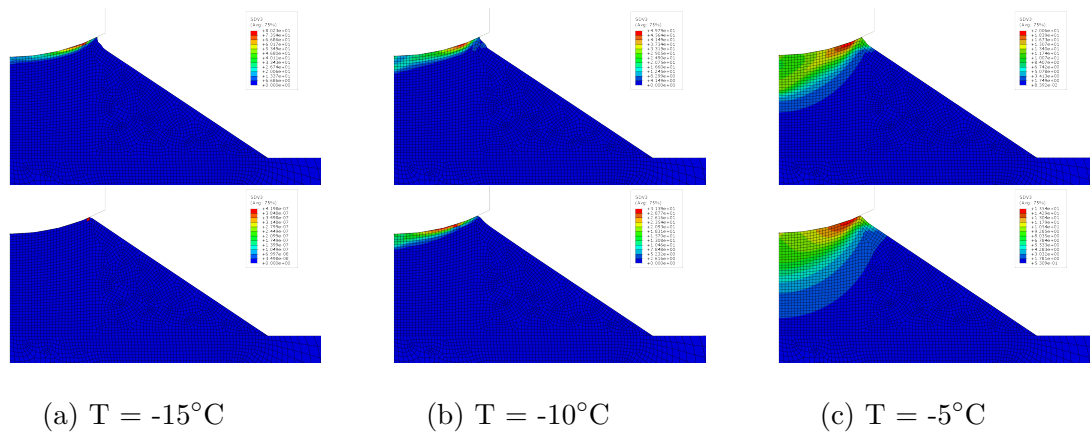
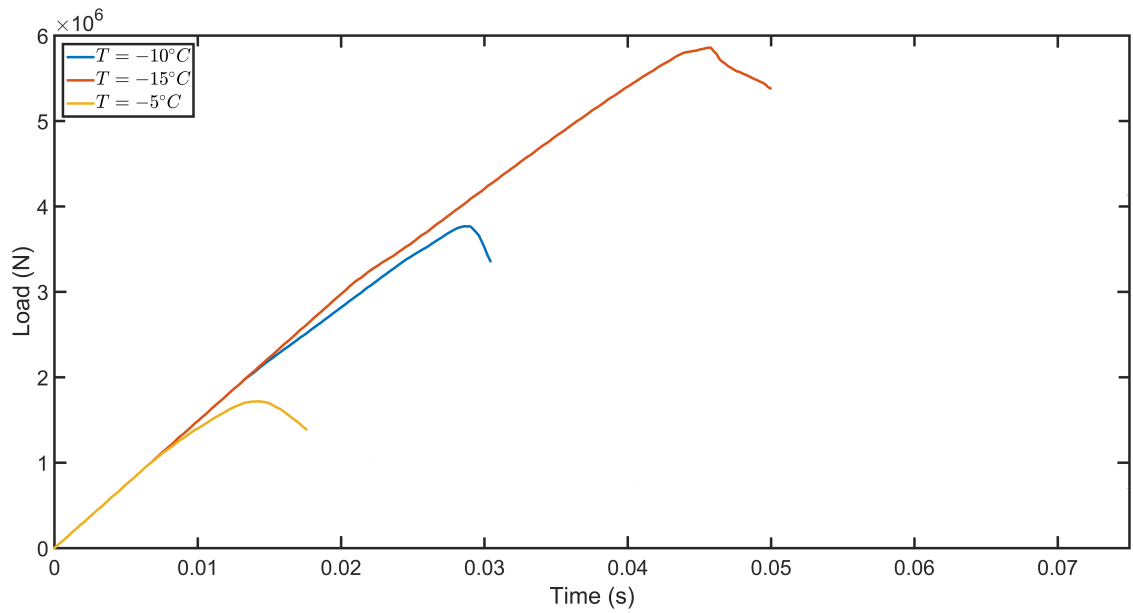
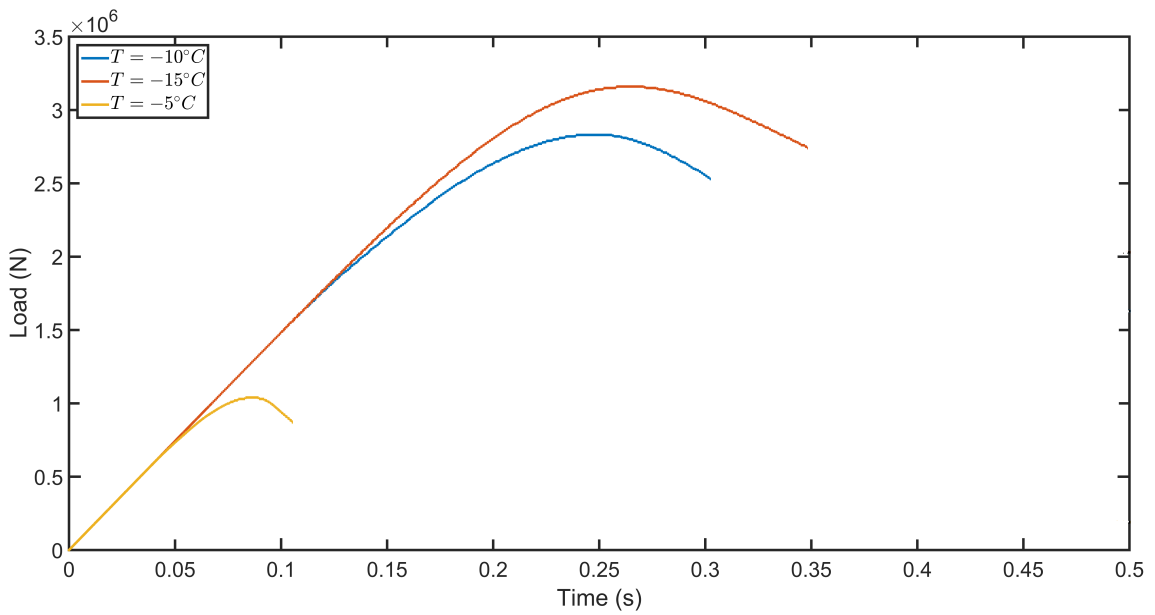


Figure 6.31: Recrystallization damage layers at temperatures from -15 to -5 °C near peak-load. The top layer of figures were taken from simulations with an indenter velocity of 68 mm/s, while the bottom layer were taken from simulations with an indenter velocity of 6.8 mm/s



(a)  $v = 68 \text{ mm/s}$



(b)  $v = 6.8 \text{ mm/s}$

Figure 6.32: Load traces produced for three temperatures and two indenter velocities.

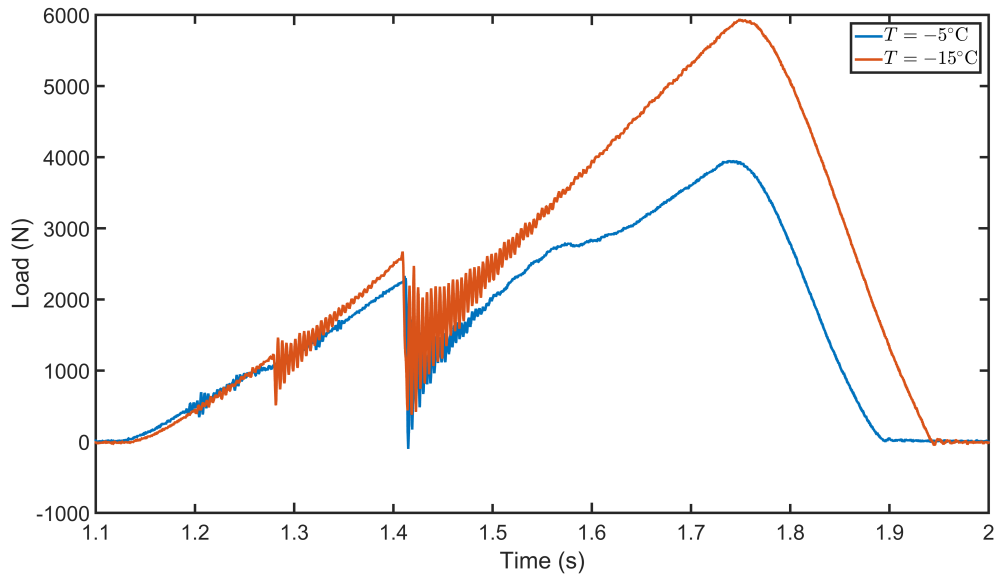


Figure 6.33: Experimental load traces at temperatures of -5 and -15 °C. The low temperature test reaches significantly higher loads. Figure recreated from the data of Browne (2012). The displacement rate for both tests was 4 mm/s, with a 40 mm diameter indenter.

### 6.3 Summary of Results

Numerous potential modifications to the constitutive model of ice were implemented and their results examined via a finite element analysis of a standard ice indentation experiment. The results are summarized here for ease of reference:

1. The role of elastic properties was examined to determine whether elastic damage plays a significant role in *hpz* behaviour. Constant elastic properties were found to produce the largest load drops, a common feature in *hpz* behaviour for the indenter velocities studied. Constant elastic properties were therefore used as

the baseline for further study.

2. Increasing values of the high-pressure damage exponent,  $r_2$ , were examined as a comparison to the work of Xiao (1997) and were found to produce equivalent results; larger, sheerer load drops are observed with increasing values of  $r_2$ . A value of  $r_2$  of at least 7 is recommended based on this work.
3. A brief examination of the damage accumulation in the Kelvin spring used to describe delayed elastic behaviour was made. Both the constant Poisson's ratio formulation and the microcracking based form of Kachanov were examined; little difference between the two was observed. The Kachanov model was chosen as a baseline, due to its solid theoretical grounds.
4. The effect of indenter velocity was examined. The model behaviour was found to correlate well with experimental evidence, with low speed simulations produce a large damage zone and high speed tests producing a highly localized damage layer. This behaviour was also found to scale with changes in geometry when a normalized velocity was enforced, similar to experimental results. A normalized velocity of  $0.34 \text{ s}^{-1}$  ( $v = 68 \text{ mm/s}$ ) is used for further simulations.
5. The recalibrated microcracking damage function,  $f_1(p)$ , was found to produce results similar to those obtained by the earlier quadratic model. It was used for further simulations to avoid the temperature dependence of the earlier function.
6. The effect of power law breakdown was examined under a range of normalization constants. Low values of this constant were found to produce practically pure power law loading behaviour; allowing power law breakdown to occur in

regions of low stress has little effect upon *hpz* behaviour, which controls loading. Implementing power law breakdown over an increasingly wide range of pressures, the loading traces were found to slowly transition to plastic-like load plateaus, contradicting experimental evidence. A low value for the normalizing constant is thus recommended.

7. Several modifications were made in an effort to implement the high-shear elastic failure observed in the experiments of 3, including:
  - (a) A limit of 26 MPa on the von Mises stress, which was found to produce plastic loading behaviour and was thus discarded.
  - (b) A drastic increase in microcracking damage at  $s = 26$  MPa, which was found to produce exaggerated loading behaviour, with a sudden, shear load drop occurring at loads much lower than expected. This model was also discarded.
  - (c) A decrease in elastic modulus, either continuous or sudden, was found to produce loading behaviour similar to experimental evidence, with a larger load drop observed than the model where a constant elastic modulus is assumed. This method is recommended for further examination.
8. A non-linear high-pressure damage exponent,  $r_2$ , was briefly examined and found to produce highly shear load drops, similar to those observed during saw-tooth loading. This seems like a promising avenue for further examination.
9. The effect of implementing the temperature-dependent damage function was examined with and without the use of the standard rate-based shift function.

The addition of the shift function was found to produce numerical instabilities at high temperatures, and was not considered further. The temperature-dependent damage function was found to produce results consistent with experimental evidence, with larger loads (and load drops) observed at lower temperatures, and damage layers of increasing thickness with increasing temperature. Further examination is advised.

# Chapter 7

## Conclusions

The present study examined the role of damage processes during the deformation of viscoelastic materials, particularly ice. It focused primarily upon the deformation behaviour of ice under triaxial compression, particularly with regards to the development and failure of high-pressure zones, which provide the majority of the structural load during an ice-structure interaction.

The development of the constitutive damage model of Jordaan and others was reviewed, and modifications to the theory have been described and examined. Triaxial compression tests and both medium- and laboratory-scale indentation experiments on ice performed by previous investigators have been described and the results used for comparison. An exploratory series of triaxial tests at high stress differences ( $\sigma_1 - \sigma_3$ ) was performed and described. The results show a clear limit to the stress difference ice is capable of supporting elastically (approximately 26 MPa), even under high confining pressures (40, 45, and 60 MPa). Though interesting, this result has yet to be connected to *hpz* behaviour, where stresses can exceed 100 MPa; its effect upon

design criteria is therefore currently unknown. If such a link can be established, these results could prove quite useful in the development of failure tools for use in the design of future offshore structures and ships, as they provide a possible limit to the amount of load ice can sustain during an interaction.

Thin sections of the tested samples provide clear evidence of dynamic recrystallization in the regions near the resulting shear faults, with significantly less damage in regions further from the fault; here, microcracking is more evident, though microcracking damage in general is suppressed under these confining pressures.

A wide range of finite-element simulations were performed based on the modifications made to the constitutive model and their results presented, focused primarily on the region of high-pressure at the centre of an indentation. The multi-axial constitutive theory for viscoelastic materials upon which the study was based was derived from continuum damage theory coupled with Glen's power law relationship. The changes in material microstructure (damage) brought on by deformation have been modelled via a finite collection of state variables, which represent the average effect of damage within a region. The damage evolution model is based on the approach of Schapery, the re-calibration of which was accomplished using numerous constant load triaxial tests of previous investigators.

This study has re-examined the effect of numerous parameters on the deformation behaviour of ice, including: elastic damage, both with and without high-pressure damage, as well as the case of constant elastic properties; the formulation used for elastic damage, primarily those of Kachanov (1993) and Moore et al. (2013); the high-pressure damage exponent,  $r_2$ , and; the normalized velocity,  $v_n$ .

It was found that, while high-pressure elastic damage was required to reproduce

the surface layer of earlier investigators using their calibration parameters, no corresponding load drop was observed. Both the microcracking elastic damage model and the model with constant elastic properties produced the desired load drop, but resulted in a diagonal band of damage using the calibration parameters of Xiao (1997) and Li (2002). Increasing the high-pressure damage exponent,  $r_2$ , was found to both localize damage into the expected layer and produce an abrupt load drop, indicating that the calibration values are not a good indicator of the true value of  $r_2$  within a *hpz*, likely due to the smearing (or averaging) of results over the entire contact area.

The increased  $r_2$  values were found to not reproduce the load drop under the high-pressure elastic damage formulation, instead producing a series of plastic-like load plateaus. Since the load drop was most significant under constant elastic properties, these conditions were focused on during further simulations. Under these conditions, the difference between the Kachanov and constant Poisson's ratio elastic damage formulations was practically non-existent, and was not further investigated.

Finally, increasing indenter velocity was found to produce the expected results, with the damage layer becoming more and more localized with increasing velocity. High speed tests were found to reach indenter loads much larger than those observed during indentation experiments due to the absence of spalling failure.

All formulations produce unexpected behaviour at high damage; highly damaged elements cannot support shear stress under these formulations, producing a von Mises stress of nearly zero and high surface pressures. This is theoretically consistent with the constitutive model; since the delayed elastic, viscous, and volumetric strain rates increase with damage, the elastic component must decrease in response to maintain an approximately constant total strain rate.

This study modified and investigated the following aspects of the constitutive model: the exponential function used to describe high-pressure damage was converted to a geometric or normalized exponential; power law breakdown was implemented within regions of low confining pressure; a non-linear high-pressure exponent was examined; an attempt to model high-shear elastic failure was made, and; a pressure-temperature shift function for the description of deformation at temperatures other than the reference temperature,  $T_0 = -10^\circ\text{C}$ , was implemented.

The use of the normalized exponential or geometric damage function was found to simply reduce the damage rate slightly, producing results that were qualitatively identical to those of the previous exponential function. The effects of implementing power law breakdown were found to differ depending upon the normalization constant used. The main effect was to increase the amount of secondary creep for a given von Mises stress, leading to a general reduction in the applied stress, similar to the effect of decreasing indenter velocity or increasing the power for the secondary creep rate.

The implementation of a non-linear high-pressure damage exponent was found to produce a highly shear load drop, as observed in many indentation experiments during cyclic loading. The localization of the damage layer was found to dramatically increase, with a sharp separation between damaged and undamaged regions.

Multiple implementations of the high-shear elastic stress limit observed in the recent test series were examined: applying the limit element-by-element led to plastic-like deformation, instead of the desired load drop, and should be avoided. Applying the limit globally, at the rigid indenter, may reproduce the desired results, but it is currently unclear whether Abaqus is capable of applying such a limit. Another attempt to model the high-shear limit was made assuming that reaching the limit

produced significant damage, leading to the collapse of the element. This produced a shear load drop, but it was both significantly smaller and occurred much sooner than expected; the applied damage was too excessive to reproduce experimental results. Finally, reducing the elastic modulus separately from viscous damage produced promising indentation results; both the load drop and damage layer development were maintained, while reducing the effect of the elastic properties on the simulation, as the observed high-shear elastic failure would indicate. Further investigation is recommended.

The pressure-temperature shift function was found to produce results consistent with experimental evidence; the damage layer was found to contain higher levels of recrystallization damage and extend deeper into the ice sample with increasing temperature, while also suppressing the development of microcracking damage. The addition of the rate theory-based shift function used by earlier investigators was found to interact poorly with the pressure-temperature shift function, causing a numerical instability which prevented the solution from converging. This function was suppressed in favour of the pressure-temperature shift function, as it had never satisfactorily accounted for the transition to a new deformation regime at high temperatures and pressures.

Based on the results of the experiments and simulations described here, some general conclusions can be made:

1. Confined ice samples appear to have a mean failure stress difference of 26.0 MPa with a standard deviation of only 1.6 MPa. The minor differences between tests are likely due to changes in confining pressure, with the stress at failure steadily

decreasing with increasing confining pressure. The loading rate appears to have no bearing upon the observed failure stress or the strain rate post-failure.

2. The use of constant elastic properties produces both the largest and steepest load drops, similar to those observed in indentation experiments. This conflicts with the long-known detrimental effects of microcracking damage on the elastic properties of materials, indicating that perhaps high-pressure damage “heals” the damage done by microcracking within a *hpz*, which is the determining factor in indentation behaviour.
3. Power law breakdown is suppressed by confining pressure, and is thus relegated to the peripheral regions of an indentation where microcracking dominates, having little effect on the bulk behaviour of an ice-structure interaction.
4. A non-linear, damage-dependent  $r_2$  value was found to produce a dramatically sheerer load drop and a highly localized damage layer. This seems like a promising avenue for further examination.
5. The pressure-temperature shift function is consistent with experimental evidence, but is incompatible with the rate theory-based shift function. The pressure-temperature shift function is preferred, as the rate theory-based shift function does not effectively model the transition to a new deformation regime at higher temperatures and pressures.

Finally, several areas for further study are recommended based on the results discussed throughout this work:

1. The exploratory series of high-shear, high confining pressure experiments outlined in this study should be extended; five data points are insufficient to judge the validity of the results. It is recommended that the full range of confining pressures (low-to-high) be examined, to illustrate the relation between failure stress and confining pressure.
2. The pressure-temperature shift function would benefit from a series of triaxial experiments at  $-22^{\circ}\text{C}$ , at the full range of confining pressures under which pressure melting is possible. This would provide a master damage rate curve that covered all temperatures and pressures of interest.
3. The Abaqus VUMAT code is designed to update stress based on the elastic strain, represented by  $\dot{\sigma}_{ij} = \dot{K}_{ijkl}\epsilon_{kl}^e + K_{ijkl}\dot{\epsilon}_{kl}^e$ . For the case where the elastic properties have collapsed, this will produce a stress of zero, when instead the viscous components should continue supporting stress of some form. Modifying the code to account for this edge case is recommended, and may provide a method to successfully describe the high-shear elastic failure observed in this study.
4. The constitutive relations described hold only for a single load cycle, as, unlike an actual indentation experiment, highly damaged material is not ejected from the interaction area. Some combination of element deletion, re-meshing, and damage healing are likely necessary to model multiple cycles, and would provide an interesting avenue for improvement to the constitutive model.
5. Not only are high stresses produced during an interaction, but large amounts of

heat as well, as discussed in Turner et al. (2015) and elsewhere. This will have an effect on the deformation behaviour in the region, as a higher temperature will reduce the pressure necessary to induce pressure melting. The heat distribution is seemingly random, but is likely highly dependent upon the pressure distribution at the ice surface, as well as the location of spalling fracture. A study of heat transfer processes during an interaction would be highly valuable.

6. Finally, it should be noted that damage development alone does not fully describe an ice-structure interaction; fracture plays a role in the deformation behaviour of ice at most loading rates of interest, as noted by Jordaan and Xiao (1992). Large, time-dependent fractures are observed to occur at low loading rates, while spalling fractures, localized to the edges of the *hpzs*, dominate at high loading rates. A combined fracture and damage analysis is therefore necessary to accurately describe these interactions.

Overall, the results outlined in this thesis provide significant insight into *hpz* behaviour, outlining several promising avenues for further research while examining the weaknesses of others. This improved understanding of *hpz* behaviour can be translated directly into a better estimation of the local pressures produced by an ice-structure interaction, a key aspect of offshore structure design. Continued research into *hpz* behaviour, concurrent with the development of the presented continuum damage model, is believed to be essential to improving local pressure estimates.

# Bibliography

- Abdel-Tawab, K. and Rodin, G. J. (1995). Inelastic effects in fracture of columnar-grained ice. In *Ice Mechanics -1995*, pages 49–63. AMSE AMD-Vol. 207.
- Alberty, R. (2009). Use of legendre transforms in chemical thermodynamics (iupac technical report). *The Scientific Journal of IUPAC*, 73(8):1349 – 1380.
- Arrhenius, S. (1889). Über die Reaktionsgeschwindigkeit bei der Inversion von Rohrzucker durch Säuren. *Z. Phys. Chem.*, 4:226.
- Atkins, A. and Mai, Y. (1985). *Elastic and plastic fracture: metals, polymers, ceramics, composites, biological materials*. Ellis Horwood series in mechanical engineering. Ellis Horwood.
- Barenblatt, G. (1962). The mathematical theory of equilibrium cracks in brittle fracture. *Advances in Applied Mechanics*, 7:55 – 129.
- Barnes, P., Tabor, D., and Walker, J. C. F. (1971). The friction and creep of polycrystalline ice. *Proceedings of the Royal Society of London A: Mathematical, Physical and Engineering Sciences*, 324(1557):127–155.

- Barrette, P. D. (2014). Ice-structure interaction and high pressure zones: Analysis of experimental data and constitutive modeling of ice. Progress Report.
- Barrette, P. D. and Jordaan, I. J. (2001). Creep of ice and microstructural changes under confining pressure. In Murakami, S. and Ohno, N., editors, *IUTAM Symposium on Creep in Structures*, volume 86 of *Solid Mechanics and its Applications*, pages 479–488. Springer Netherlands.
- Barrette, P. D. and Jordaan, I. J. (2003). Pressure-temperature effects on the compressive behavior of laboratory-grown and iceberg ice. *Cold Regions Science and Technology*, 36(1–3):25 – 36.
- Barrette, P. D., Pond, J., and Jordaan, I. J. (2002). Ice damage and layer formation: in small scale indentation experiments. In *Ice in the Environment, Proceedings of the 16th International Symposium on Ice, IAHR, Dunedin, New Zealand*, volume **3**, pages 246–253.
- Becker, R. (1925). Thermische inhomogenitäten. *Z. Phys. Bd*, 26:919.
- Biot, M. (1954). Theory of stress-strain relations in anisotropic viscoelasticity and relaxation phenomena. *Journal of Applied Physics*, 25(11):1385–1391.
- Biot, M. A. (1955). Variational principles in irreversible thermodynamics with application to viscoelasticity. *Phys. Rev.*, 97:1463–1469.
- Blair, S. (1987). *Mechanical properties of first-year sea ice at intermediate strain rates*.

- Blenkarn, K. A. (1970). Measurement and analysis of ice forces on cook inlet structures. In *Proc. 2nd Offshore Technology Conference, Houston, TX*, volume **2**, pages 365–378.
- Bridgman, P. (1950). The thermodynamics of plastic deformation and generalized entropy. *Reviews of Modern physics*, 22(1):56.
- Brown, T. G. (2001). Four years of ice force measurements on the Confederation Bridge. In *Proc. 16th Conference on Port and Ocean Engineering under Arctic Conditions (POAC), Ottawa*, volume **1**, pages 285–298.
- Browne, T. (2012). Analysis of Compressive Ice Failure during Ice-structure Interaction. M.Eng Thesis, Memorial University of Newfoundland, St. John’s, Canada.
- Browne, T., Taylor, R., Jordaan, I., and Görtner, A. (2013). Small-scale ice indentation tests with variable structural compliance. *Cold Regions Science and Technology*, 88(0):2 – 9.
- Budiansky, B. and O’Connell, R. J. (1976). Elastic moduli of a cracked solid. *International Journal of Solids and Structures*, 12(2):81 – 97.
- Cherepanov, G. P. (1967). Crack propagation in continuous media. *Journal of Applied Mathematics and Mechanics*, 31(3):503 – 512.
- Coleman, B. D. and Gurtin, M. E. (1967). Thermodynamics with internal state variables. *The Journal of Chemical Physics*, 47(2):597–613.
- Conrad, H. and Wiedersich, H. (1960). Activation energy for deformation of metals at low temperatures. *Acta Metallurgica*, 8(2):128 – 130.

- Cowper, B. and Edgecombe, M. (1987). *The 1985 global ice impact tests on the USCG Polar sea*. Transport Canada Development Centre.
- da Costa Andrade, E. N. (1910). On the viscous flow in metals, and allied phenomena. *Proceedings of the Royal Society of London A: Mathematical, Physical and Engineering Sciences*, 84(567):1–12.
- De Groot, S. R. (1951). *Thermodynamics of irreversible processes*, volume 336. North-Holland Amsterdam.
- Debenedetti, P. (1996). *Metastable liquids: Concepts and principles*. Princeton, N.J.: Princeton University Press, first edition.
- Dempsey, J. P. (1996). Scale effects on the fracture of ice. In *The Johannes Weertman Symposium*, pages 351–361, 1996. The Minerals, Metals, and Materials Society.
- Derradji-Aouat, A. (1992). *Mathematical modelling of monotonic and cyclic behaviour of polycrystalline fresh water ice*. PhD Thesis, University of Ottawa, Ottawa, Canada.
- Derradji-Aouat, A. (2000). A unified failure envelope for isotropic fresh water ice and iceberg ice. In *ETCE/OMAE 2000 Joint Conference, New Orleans, Louisiana*.
- Derradji-Aouat, A. (2003). Multi-surface failure criterion for saline ice in the brittle regime. *Cold Regions Science and Technology*, 36(1):47 – 70.
- Derradji-Aouat, A., Sinha, N. K., and Evgin, E. (2000). Mathematical modelling of monotonic and cyclic behaviour of fresh water columnar grained s-2 ice. *Cold Regions Science and Technology*, 31(1):59 – 81.

- Dorn, J. (1957). The spectrum of activation energies for creep. *Creep and Recovery, Am. Soc. for Metals, Cleveland, Ohio*, pages 255—283.
- Dugdale, D. (1960). Yielding of steel sheets containing slits. *Journal of the Mechanics and Physics of Solids*, 8(2):100 – 104.
- Durham, W. B., Heard, H. C., and Kirby, S. H. (1983). Experimental deformation of polycrystalline h<sub>2</sub>o ice at high pressure and low temperature: Preliminary results. *Journal of Geophysical Research: Solid Earth*, 88(S01):B377–B392.
- Edgecombe, M., St. John, J., Liljeström, G., and Ritch, A. (1992). *Full scale measurement of hull-ice impact loads and propulsion machinery response onboard I/B Oden during the 1991 international Arctic ocean expedition*. Canadian Coast Guard Northern.
- Eshelby, J. (1956). The continuum theory of lattice defects. *Solid State Physics*, 3:79 – 144.
- Eshelby, J. D. (1951). The force on an elastic singularity. *Philosophical Transactions of the Royal Society of London A: Mathematical, Physical and Engineering Sciences*, 244(877):87–112.
- Eyring, H. (1935). The activated complex in chemical reactions. *The Journal of Chemical Physics*, 3(2):107–115.
- Eyring, H. (1936). Viscosity, plasticity, and diffusion as examples of absolute reaction rates. *The Journal of Chemical Physics*, 4(4):283–291.

- Eyring, H. and Polanyi, M. (1931). Über Einfache Gasreaktionen. *Z. Phys. Chem. B*, 12:279–311.
- Findley, W. N. and Davis, F. A. (2013). *Creep and relaxation of nonlinear viscoelastic materials*. Courier Corporation.
- Findley, W. N., Lai, J. S., and Onaran, K. (1976). *Creep and relaxation of nonlinear viscoelastic materials*. North-Holland.
- Fischer-Cripps, A. (2000). *Introduction to Contact Mechanics*. Mechanical Engineering Series. Springer New York.
- Frederking, R., Jordaan, I., and McCallum, J. (1990). Field tests on ice indentation at medium scale, Hobson’s Choice ice island. In *Proc. 10th International IAHR Symposium on Ice, Espoo, Finland*, volume **2**, pages 931–944.
- Gagnon, R. (1994a). Generation of melt during crushing experiments on freshwater ice. *Cold Regions Science and Technology*, 22(2):385–398.
- Gagnon, R. (1994b). Melt layer thickness measurements during crushing experiments on freshwater ice. *Journal of Glaciology*, 40(134):119–124.
- Gagnon, R. (2008). High-speed imaging of mechanisms responsible for sawtooth cyclic loading during ice crushing. In *Proceedings of IAHR 2008, Vancouver, Canada*.
- Gagnon, R. (2011). A numerical model of ice crushing using a foam analogue. *Cold Regions Science and Technology*, 65(3):335 – 350.
- Gagnon, R. and Sinha, N. (1991). Energy dissipation through melting in large scale indentation experiments on multi-year sea ice. In *Proceedings of the 10th Inter-*

- national Conference on Offshore Mechanics and Arctic Engineering, Stavanger, Arctic/Polar Technology*, volume 4, pages 157–161.
- Garofalo, F. (1963). An empirical relation defining the stress dependence of minimum creep rate in metals. In *Trans. Metal. Soc. AIME*, volume 227, pages 351—356.
- Glen, I. and Blount, H. (1984). Measurement of ice impact pressures and loads onboard CCGS Louis S. St. Laurent. In *Proc, 3rd Offshore Mechanics and Arctic Engineering Symposium, ASME, New Orleans, LA*, volume 3, pages 246–252.
- Glen, J. W. (1955). The creep of polycrystalline ice. *Proceedings of the Royal Society of London A: Mathematical, Physical and Engineering Sciences*, 228(1175):519–538.
- Gold, L. W. (1973). Activation energy for creep of columnar-grained ice. *Symposium on the Physics and Chemistry of Ice*, pages P.362–364.
- Green, A. E. and Rivlin, R. S. (1957). The mechanics of non-linear materials with memory. *Archive for Rational Mechanics and Analysis*, 1(1):1–21.
- Griffith, A. A. (1921). The phenomena of rupture and flow in solids. *Philosophical Transactions of the Royal Society of London A: Mathematical, Physical and Engineering Sciences*, 221(582-593):163–198.
- Haefeli, R., Jaccard, C., and De Quervain, M. (1968). Deformation of polycrystalline ice under combined uniaxial and hydrostatic pressure. *General Assembly of Bern*, (79):341–344.
- Hirsch, P. B. and Warrington, D. H. (1961). The flow stress of aluminium and copper at high temperatures. *Philosophical Magazine*, 6(66):735–768.

- Horii, H. and Nemat-Nasser, S. (1983). Overall moduli of solids with microcracks: Load-induced anisotropy. *Journal of the Mechanics and Physics of Solids*, 31(2):155 – 171.
- Irwin, G. R. (1958). *Fracture*, pages 551–590. Springer Berlin Heidelberg, Berlin, Heidelberg.
- Jefferies, M. and Wright, W. (1988). Dynamic response of Molikpaq to ice-structure interactions. In *Proc. 7th International Conference on Offshore Mechanics and Arctic Engineering (OMAE), Houston, Texas*, volume 4, pages 201–220.
- Johnston, M., Croasdale, K. R., and Jordaan, I. J. (1998). Localized pressures during ice-structure interaction: relevance to design criteria. *Cold Regions Science and Technology*, 27(2):105–117.
- Jonas, J. J., Sellars, C. M., and Tegart, W. J. M. (1969). Strength and structure under hot-working conditions. *Metallurgical Reviews*, 14(1):1–24.
- Jones, S. J. (1978). Triaxial testing of polycrystalline ice. In *Proceedings of the 3rd International Conference on Permafrost*, pages 671–674.
- Jones, S. J. (1982). The confined compressive strength of polycrystalline ice. *Journal of Glaciology*, 28:171–177.
- Jones, S. J. and Chew, H. A. M. (1983). Creep of ice as a function of hydrostatic pressure. *The Journal of Physical Chemistry*, 87(21):4064–4066.
- Jordaan, I., O'Rourke, B., Turner, J., Moore, P., and Ralph, F. (2016). Estimation

- of ice loads using mechanics of ice failure in compression. In *Offshore Technology Conference*.
- Jordaan, I. and Pond, J. (2001). *Scale Effects and Randomness in the Estimation of Compressive Ice Loads*, pages 43–54. Springer Netherlands, Dordrecht.
- Jordaan, I. J. (2001). Mechanics of ice-structure interaction. *Engineering Fracture Mechanics*, 68:1923–1960.
- Jordaan, I. J. and Barrette, P. D. (2014). Mechanics of Dynamic Ice Failure against Vertical Structures. In *ASME 2014, Volume 10. San Francisco, California, USA, June 8–13*, volume **10**.
- Jordaan, I. J., Li, C., Barrette, P., Duval, P., and Meyssonier, J. (2005). Mechanisms of ice softening under high pressure and shear. In *POAC 2005, Potsdam, N.Y., Proceedings*, volume **1**, pages 249–259.
- Jordaan, I. J., Matskevitch, D. G., and Meglis, I. L. (1999). Disintegration of ice under fast compressive loading. *International Journal of Fracture*, 97(1-4):279–300.
- Jordaan, I. J. and McKenna, R. F. (1988a). Constitutive relations for the creep of ice. In *For International Association for Hydraulic Research (IAHR) Symposium on Ice, Sapporo, Japan*, volume **3**, pages 47–58.
- Jordaan, I. J. and McKenna, R. F. (1988b). Modelling of progressive damage in ice. In *For International Association for Hydraulic Research (IAHR) Symposium on Ice, Sapporo, Japan*, volume **2**, pages 585–624.

- Jordaan, I. J. and McKenna, R. F. (1991). Processes of deformation and fracture of ice in compression. In Jones, S., Tillotson, J., McKenna, R., and Jordaan, I., editors, *Ice-Structure Interaction*, International Union of Theoretical and Applied Mechanics, pages 283–309. Springer Berlin Heidelberg.
- Jordaan, I. J., McKenna, R. F., Duthinh, D., Fuglem, M. K., Kennedy, K. P., Maes, M. A., and Marshall, A. (1990). Development of New Ice Load Models, report for Canada Oil and Gas Lands Administration (COGLA) by (C-CORE), Memorial University, St. John's, Nfld.
- Jordaan, I. J., Stone, B. M., McKenna, R. F., and Fuglem, M. K. (1992a). Effect of microcracking on the deformation of ice. *Canadian Geotechnical Journal*, 29(1):143–150.
- Jordaan, I. J., Stone, B. M., McKenna, R. F., and Fuglem, M. K. (1992b). Effect of microcracking on the deformation of ice. *Canadian Geotechnical Journal*, 29(1):143–150.
- Jordaan, I. J. and Xiao, J. (1992). Interplay between damage and fracture in ice-structure interaction. In *IAHR 92, Proceedings of the 11th International Symposium on Ice, Banff, Alta.*, volume **3**, pages 1448–1467.
- Kachanov, L. (1958). On the creep rupture time. *Izvv. An SSSR, Otd. Tekhn. Nauk*, (8):26–31.
- Kachanov, M. (1993). Elastic solids with many cracks and related problems. volume 30 of *Advances in Applied Mechanics*, pages 259 – 445. Elsevier.

- Kalifa, P., Ouillon, G., and Duval, P. (1992). Microcracking and the failure of polycrystalline ice under triaxial compression. *Journal of Glaciology*, 38:65–76.
- Kanninen, M. F. and Popelar, C. L. (1985). Advanced fracture mechanics.
- Kauzmann, W. (1941). Flow of solid metals from the standpoint of the chemical-rate theory. *Trans. AIME*, 143:57–83.
- Kavanagh, M. (2018). *Time-Dependent Aspects of Fracture in Ice*. PhD Thesis, Manuscript in preparation, Memorial University of Newfoundland, St. John’s, Nfld.
- Kavanagh, M., O’Rourke, B., Jordaan, I., and Taylor, R. (2015). Observations on the time-dependent fracture of ice. In *ASME 2015 34th International Conference on Ocean, Offshore and Arctic Engineering*, volume 8.
- Keegan, M. H., Nash, D. H., and Stack, M. M. (2013). On erosion issues associated with the leading edge of wind turbine blades. *Journal of Physics D: Applied Physics*, 46(38):383001.
- Kestin, J. and Rice, J. R. (1970). *PARADOXES IN THE APPLICATION OF THERMODYNAMICS TO STRAINED SOLIDS*. Mono Book Corp.
- Krausz, A. (1970). A rate theory analysis of the temperature dependence dislocation velocity. *Materials Science and Engineering*, 6(4):260 – 264.
- Krausz, A. and Eyring, H. (1975). *Deformation kinetics*. Wiley.
- Kuon, L. G. and Jonas, J. J. (1973). Effect of strain rate and temperature on the microstructure of polycrystalline ice. In *Proc. from the Symposium on the Physics and Chemistry of Ice, Ottawa, Canada*.

- Laidler, K. J. (1965). *Chemical Kinetics (2nd Ed.)*. McGraw-Hill, New York.
- Lehmann, T.-Ø. (2010). Prediction of the response from ice forces to a lighthouse structure: Reanalysis of the Nygrån lighthouse collapse incident in the light of new design codes. M.Eng Thesis.
- Li, C. (2002). Finite element analysis of ice-structure interaction with a viscoelastic model coupled with damage mechanics. M.Eng Thesis, Memorial University of Newfoundland, St. John's, Canada.
- Li, C., Jordaan, I., and Barrette, P. (2003). Damage and microstructural changes in ice in compression during interaction with structures. *Key Engineering Materials*, 251–252:431–436.
- Li, C., Jordaan, I., and Barrette, P. (2005). Strain localization and fracture cylindrical ice specimens under confining pressure. In *Proceedings of 18th International Conference on Port and Ocean Engineering under Arctic Conditions*, volume 1, pages 213–224.
- Liebowitz, H. (1968). *Fracture, an advanced treatise*. Number v. 2 in Fracture, an Advanced Treatise. Academic Press.
- Liu, B. (1994). Numerical modelling of medium scale indentation tests. M.Eng Thesis, Memorial University of Newfoundland, St. John's, Canada.
- Määttänen, M. (1978). *On conditions for the rise of self-excited ice induced autonomous oscillations in slender marine pile structures*. Dissertation from Helsinki University of Technology: Teknillinen Korkeakoulu.

- Mae, S. and Azuma, N. (1989). Ice sheet dynamics and rheology of ice under hydrostatic pressure. In Karato, S. and Toriumi, M., editors, *Rheology of solids and of the Earth*, pages 209–222. Oxford University Press, N.Y.
- Makin, M. J. (1964). The thermal activation of slip in neutron irradiated copper. *Philosophical Magazine*, 9(97):81–98.
- Malvern, L. (1969). *Introduction to the mechanics of a continuous medium*. Prentice-Hall series in engineering of the physical sciences. Prentice-Hall.
- Masterson, D., Frederking, R., Jordaan, I., and Spencer, P. (1993). Description of multi-year ice indentation tests at hobson’s choice ice island – 1990. In *12th International Conference on Offshore Mechanics and Arctic Engineering, Glasgow*, volume 4, pages 145–155.
- Meaney, R., Kenny, S., and Sinha, N. (1991). Medium-scale ice-structure interaction: Failure zone characterization. In *Proceedings Port and Ocean Engineering under Arctic Conditions, POAC’91, St. John’s, Canada*, volume 1, pages 126–140.
- Meglis, I., Melanson, P., and Jordaan, I. (1999). Microstructural change in ice: II. Creep behavior under triaxial stress conditions. *Journal of Glaciology*, pages 438–448.
- Melanson, P. (1998). Damage and microstructural change in laboratory grown ice under high pressure zone conditions. M.Eng Thesis, Memorial University of Newfoundland, St. John’s, Canada.
- Melanson, P., Meglis, I., and Jordaan, I. (1999a). Modelling of damage in ice. In *Ice*

- in surface waters. Proc. 14th Int. Symp. on Ice, A.A. Balkema, Brookfield*, pages 979–988.
- Melanson, P., Meglis, I., Jordaan, I., and Stone, B. (1999b). Microstructural change in ice: I. Constant deformation-rate tests under triaxial stress conditions. *Journal of Glaciology*, pages 417–422.
- Mellor, M. and Testa, R. (1969). Effect of temperature on the creep of ice. *Journal of Glaciology*, 8:131–145.
- Mizuno, Y. (1992). High temperature creep of polycrystalline ice under hydrostatic pressure. In Maeno, N. and Hondoh, T., editors, *Physics and Chemistry of Ice*, pages 434–439. Hokkaido University Press, Sapporo.
- Mizuno, Y. (1998). Effect of hydrostatic confining pressure on the failure mode and compressive strength of polycrystalline ice. *The Journal of Physical Chemistry B*, 102(2):376–381.
- Moore, P. F., Jordaan, I. J., and Taylor, R. S. (2013). Explicit finite element analysis of compressive ice failure using damage mechanics. In *Proceedings of the 22nd International Conference on Port and Ocean Engineering under Arctic Conditions*.
- Morsy, U. and Brown, T. (1996). Three-dimensional non-linear finite element model for the Molikpaq, Gulf’s mobile caisson. *Computers & Structures*, 60(4):541 – 560.
- Nabarro, F. (2004). Do we have an acceptable model of power-law creep? *Materials Science and Engineering: A*, 387–389:659 – 664. 13th International Conference on the Strength of Materials.

- Nadreau, J. and Michel, B. (1986a). Secondary creep in confined ice samples. In *Proc. 8th IAHR Conf., Iowa City*, volume 1, pages 307–318.
- Nadreau, J. and Michel, B. (1986b). Yield envelope for confined ice. In *Proc. 1st Int. Conf. Ice Technology*, pages 25–36.
- Nordell, B. (1990). Measurement of P-T coexistence curve for ice-water mixture. *Cold Regions Science and Technology*, 19(1):83–88.
- Onsager, L. (1931). Reciprocal relations in irreversible processes. i. *Phys. Rev.*, 37:405–426.
- O’Rourke, B., Jordaan, I., Taylor, R., and Gürtner, A. (2015). Spherical indentation of confined ice specimens at small scales. In *ASME 2015 34th International Conference on Ocean, Offshore and Arctic Engineering*, volume 8.
- O’Rourke, B. J., Jordaan, I. J., Taylor, R. S., and Gürtner, A. (2016a). Experimental investigation of oscillation of loads in ice high-pressure zones, part 1: Single indenter system. *Cold Regions Science and Technology*, 124:25 – 39.
- O’Rourke, B. J., Jordaan, I. J., Taylor, R. S., and Gürtner, A. (2016b). Experimental investigation of oscillation of loads in ice high-pressure zones, part 2: Double indenter system — coupling and synchronization of high-pressure zones. *Cold Regions Science and Technology*, 124:11 – 24.
- Orowan, E. (1936). Zur kristallplastizität. v. *Zeitschrift für Physik*, 98(5):382–387.
- Orowan, E. (1940). Problems of plastic gliding. *Proceedings of the Physical Society*, 52:8–22.

- Osborne, P. (1963). Thermal activation energies for the low temperature deformation of metals. *Acta Metallurgica*, 11(8):998 – 999.
- Pathria, R. (1972). *Statistical Mechanics*. International series of monographs in natural philosophy, v. 45. Elsevier Science & Technology Books.
- Podgornik, R. (2011). Water and life: the unique properties of h(2)o: Ruth m. lyndenbell, simon conway morris, john d. barrow, john l. finney and charles harper (eds). crc press; 1 edition, 2010. *J Biol Phys*, 37(2):163–165. 9217[PII].
- Pounder, E., Jacobs, J., and Wilson, J. (1965). *The Physics of Ice*. The Commonwealth and international library of science, technology, engineering, and liberal studies. Geophysics division). Elsevier Science.
- Raj, R. and Ashby, M. (1971). On grain boundary sliding and diffusional creep. *Metallurgical Transactions*, 2(4):1113–1127.
- Ree, T. and Eyring, H. (1955). Theory of Non-Newtonian Flow. I. Solid Plastic System. *Journal of Applied Physics*, 26:793–800.
- Ree, T. and Eyring, H. (1958). The relaxation theory of transport phenomena. In Eirich, F. R., editor, *Rheology, Theory and Applications, Vol II*, pages 83–144. New York.
- Rice, J. (1971). Inelastic constitutive relations for solids: An internal-variable theory and its application to metal plasticity. *Journal of the Mechanics and Physics of Solids*, 19(6):433 – 455.

- Rice, J. (1977). *Thermodynamics of the Quasi-static Growth of Griffith Cracks*. Technical report (Brown University. Division of Engineering). Division of Engineering, Brown University.
- Rice, J. R. (1968). A path independent integral and the approximate analysis of strain concentration by notches and cracks. *ASME, J. Appl. Mech*, 35(2):379–386.
- Rigsby, G. P. (1958). Effect of hydrostatic pressure on velocity of shear deformation on single ice crystals. *Journal of Glaciology*, 3:271–278.
- Riska, K., Rantala, H., and Joensuu, A. (1990). Full scale observations of ship-ice impact. Report M-97, Helsinki University of Technology.
- Rist, M. A., Murrell, S. A. F., and Sammonds, P. R. (1988). Experimental results on the failure of polycrystalline ice under triaxial stress conditions. In *Proc. 9th IAHR Conf., Sapporo*, pages 118–127.
- Sammonds, P. and Murrell, S. (1989). A laboratory investigation of the fracture of multi-year sea ice under triaxial stresses at  $-20^{\circ}\text{C}$  and  $-40^{\circ}\text{C}$ . In *Proc. 10th POAC Conf., Luleå*, volume 1, pages 279–288.
- Sammonds, P., Murrell, S., and Rist, M. (1989). Fracture of multi-year sea ice under triaxial stresses: Apparatus description and preliminary results. *Journal of Offshore Mechanics and Arctic Engineering*, 111:258–263.
- Sammonds, P. R., Murrell, S. A. F., and Rist, M. A. (1998). Fracture of multiyear sea ice. *Journal of Geophysical Research: Oceans*, 103(C10):21795–21815.

- Sanderson, T. J. O. (1988). *Ice mechanics: risks to offshore structures*. Graham and Trotman, London.
- Santaoja, K. (1990). *Mathematical Modelling of Deformation Mechanisms in Ice*. Technical research centre of Finland, research reports. na.
- Schapery, R. (1962). A simple collocation method for fitting viscoelastic models to experimental data.
- Schapery, R. (1981). On Viscoelastic Deformation and Failure Behaviour of Composite Materials with Distributed Flaws. In *Advances in Aerospace Structure and Materials, ASME*, pages 5–20.
- Schapery, R. (1984). Correspondence principles and a generalized integral for large deformation and fracture analysis of viscoelastic media. *International Journal of Fracture*, 25(3):195–223.
- Schapery, R. (1990). A theory of mechanical behavior of elastic media with growing damage and other changes in structure. *Journal of the Mechanics and Physics of Solids*, 38(2):215 – 253.
- Schapery, R. (1991). Models for the deformation behavior of viscoelastic media with distributed damage and their applicability to ice. In Jones, S., Tillotson, J., McKenna, R., and Jordaan, I., editors, *Ice-Structure Interaction*, International Union of Theoretical and Applied Mechanics, pages 191–230. Springer Berlin Heidelberg.

- Schapery, R. (1997a). Nonlinear viscoelastic and viscoplastic constitutive equations based on thermodynamics. *Mechanics of Time-Dependent Materials*, 1(2):209–240.
- Schapery, R. (1997b). Thermoviscoelastic constitutive equations for polycrystalline ice. *Journal of Cold Regions Engineering*, 11(2):146–157.
- Schapery, R. A. (1966). A theory of nonlinear thermoviscoelasticity based on irreversible thermodynamics. In *Proc. 5th U.S. Nat. Cong. Appl. Mech., ASME*, page 511–530.
- Schapery, R. A. (1969). On the characterization of nonlinear viscoelastic materials. *Polymer Engineering & Science*, 9(4):295–310.
- Scheffer, F. E. C. and Kohnstamm, P. (1911). Thermodynamic potential and velocities of reaction. *Verlag Akad. Wetensch. Amsterdam*, 19:878.
- Schoeck, G. (1965). The activation energy of dislocation movement. *physica status solidi (b)*, 8(2):499–507.
- Seeger, A. (1958). Kristallplastizität. *Handbuch der Physik*, 7:1–210.
- Simonson, E., Jones, A., and Green, S. (1974). *High Pressure Mechanical Properties of Three Frozen Materials*.
- Singh, S. K. (1993). *Mechanical behavior of viscoelastic material with changing microstructure*. PhD Thesis, Memorial University of Newfoundland, St. John's, NL.
- Singh, S. K. and Jordaan, I. J. (1996). Triaxial tests on crushed ice. *Cold Regions Science and Technology*, 24(2):153 – 165.

- Singh, S. K., Jordaan, I. J., Xiao, J., and Spencer, P. A. (1995). The Flow Properties of Crushed Ice. *Journal of Offshore Mechanics and Arctic Engineering*, 117(4):276–282.
- Sinha, N. (1978). Rheology of columnar-grained ice. *Experimental Mechanics*, 18(12):464–470.
- Sinha, N. (1982). Delayed elastic strain criterion for first cracks in ice. In Vermeer, P. and Luger, H., editors, *Symp. on the Deformation and Failure of Granular Materials*, pages 323–330. IUTAM.
- Stone, B., Jordaan, I., Jones, S., and McKenna, R. (1989). Damage of isotropic polycrystalline ice under moderate confining pressures. In *Proceedings of the 10th. International Conference on Port and Ocean Engineering under Arctic Conditions*, volume 1, pages 408–419.
- Stone, B. M., Jordaan, I. J., Xiao, J., and Jones, S. J. (1997). Experiments on the damage process in ice under compressive states of stress. *Journal of Glaciology*, 43:11–25.
- Suzuki, T. and Kojima, H. (1966). Dislocation motion in silicon crystals as measured by the lang x-ray technique. *Acta Metallurgica*, 14(8):913 – 924.
- Taylor, R., Frederking, R., and Jordaan, I. J. (2008). The nature of high pressure zones in compressive ice failure. In *Proceedings 19th IAHR Symposium on Ice, Vancouver, British Columbia, Canada*.

- Taylor, R. and Jordaan, I. (2015). Probabilistic fracture mechanics analysis of spalling during edge indentation in ice. *Engineering Fracture Mechanics*, 134:242 – 266.
- Timoshenko, S. and Goodier, J. (1951). *Theory of elasticity*. Engineering societies monographs. McGraw-Hill, New York, 2d ed. edition.
- Turner, J., O'Rourke, B., Jordaan, I., and Taylor, R. (2015). Surface temperature fluctuations in ice indentation tests. Draft submitted for OMAE 2015, Paper No. OMAE2015-41953.
- van't Hoff, J. H. (1884). *Etudes de Dynamique Chimique*. F. Muller.
- Wax, J.-F., Albaki, R., and Bretonnet, J.-L. (2001). Temperature dependence of the diffusion coefficient in liquid alkali metals. *Phys. Rev. B*, 65:014301.
- Wells, J., Jordaan, I., Derradji-Aouat, A., and Taylor, R. (2011). Small-scale laboratory experiments on the indentation failure of polycrystalline ice in compression: Main results and pressure distribution. *Cold Regions Science and Technology*, 65(3):314 – 325.
- Willis, J. (1967). A comparison of the fracture criteria of Griffith and Barenblatt. *Journal of the Mechanics and Physics of Solids*, 15(3):151 – 162.
- Xiao, J. (1991). Finite element modelling of damage processes in ice-structure interaction. Copyright - Copyright UMI - Dissertations Publishing 1991; Last updated - 2014-01-21; First page - n/a.
- Xiao, J. (1997). *Damage and fracture of brittle viscoelastic solids with application to*

- ice load models*. PhD Thesis, Memorial University of Newfoundland, St. John's, Nfld.
- Xiao, J. and Jordaan, I. J. (1996). Application of damage mechanics to ice failure in compression. *Cold Regions Science and Technology*, 24(3):305 – 322.
- Xiao, J., Jordaan, I. J., McKenna, R. F., and Frederking, R. M. W. (1991). Finite element modelling of spherical indentation tests on ice. In *11th International Conference on Port and Ocean Engineering under Arctic Conditions*, volume 1, pages 471–485.
- Yue, Q. and Bi, X. (2000). Iceinduced jacket structure vibrations in bohai sea. *Journal of Cold Regions Engineering*, 14(2):81–92.
- Zener, C. and Hollomon, J. H. (1944). Effect of strain rate upon plastic flow of steel. *Journal of Applied Physics*, 15(1):22–32.

# Appendix A

## Validation of Model

Single element triaxial creep-relaxation cycles were used to validate the Abaqus implementation of the constitutive model, as described in Chapter 5. The relevant parameters that are consistent between each cycle are: a confining pressure,  $P_c = 30$  MPa, applied over a total time of  $t = 40$  s; an additional axial stress of  $\Delta\sigma_1 = 12$  MPa applied until time  $t_1 = 20$ , then reduced to  $\Delta\sigma_2 = 0$  MPa for the remainder of the simulation.

These values were chosen for three reasons: first, the low confining pressure allowed for the examination of the microcracking damage function, which disappears at higher confining pressures; secondly, three of the high pressure damage functions are identical at the reference von Mises stress ( $s_0^s = 15$  MPa), so another value for  $\Delta\sigma_1$  had to be chosen so that comparison was possible; and lastly,  $\Delta\sigma_2 = 0$  MPa was chosen to ensure that delayed elastic recovery was occurring as the numerical singularity at  $s = 0$  was approached.

Numerous simulations were run to test a variety of models, including those: with

and without damage; with and without elastic damage; with microcracking elastic damage only; with one of four types of high-pressure damage: power-law, exponential, normalized exponential, or geometric; with the damage calibrations of either Xiao (1997) or Li (2002); and with one of three elastic damage formulations: constant  $\nu$ , constant  $K$ , or Kachanov's, for a total of 85 combinations of parameters.

The results produced by the Abaqus VUMAT simulations match the expected theoretical results in almost every case. Those simulations that do not match do so not because of theoretical inconsistencies, but due to Abaqus itself having difficulty modelling a step decrease in stress, a common deficiency in numerical models.

The results for each combination of parameters can be found in the following Tables and Figures.

Table A.1: Triaxial validation results for case of no damage. Note that  $_{11}$  indicates the axial direction,  $_{22}$  the lateral.

		Theory	VUMAT
$\epsilon_{11}^e$	$t = 20$	$2.53 \times 10^{-3}$	$2.53 \times 10^{-3}$
	$t = 40$	$1.26 \times 10^{-3}$	$1.26 \times 10^{-3}$
$\epsilon_{22}^e$	$t = 20$	$8.84 \times 10^{-4}$	$8.84 \times 10^{-4}$
	$t = 40$	$1.26 \times 10^{-3}$	$1.26 \times 10^{-3}$
$e^d$	$t = 20$	$1.19 \times 10^{-3}$	$1.19 \times 10^{-3}$
	$t = 40$	$6.88 \times 10^{-5}$	$6.99 \times 10^{-5}$
$e^c$	$t = 20$	$2.63 \times 10^{-3}$	$2.62 \times 10^{-3}$
	$t = 40$	$2.63 \times 10^{-3}$	$2.62 \times 10^{-3}$
$\epsilon_{11}^t$	$t = 20$	$4.92 \times 10^{-3}$	$4.92 \times 10^{-3}$
	$t = 40$	$2.92 \times 10^{-3}$	$2.92 \times 10^{-3}$
$\epsilon_{22}^t$	$t = 20$	$-5.35 \times 10^{-4}$	$-5.33 \times 10^{-4}$
	$t = 40$	$2.14 \times 10^{-4}$	$2.14 \times 10^{-4}$

Table A.2: Total damage using the calibrations of Xiao (1997) and Li (2002).

		Xiao		Li	
		Theory	VUMAT	Theory	VUMAT
$S_1$	$t = 20$	$3.06 \times 10^{-2}$	$3.05 \times 10^{-2}$	$8.36 \times 10^{-1}$	$8.35 \times 10^{-1}$
	$t = 40$	$3.07 \times 10^{-2}$	$3.07 \times 10^{-2}$	$8.39 \times 10^{-1}$	$8.40 \times 10^{-1}$
$S^p$	$t = 20$	$2.37 \times 10^{-1}$	$2.37 \times 10^{-1}$	$9.14 \times 10^{-1}$	$9.13 \times 10^{-1}$
	$t = 40$	$2.38 \times 10^{-1}$	$2.38 \times 10^{-1}$	$9.17 \times 10^{-1}$	$9.18 \times 10^{-1}$
$S^e$	$t = 20$	1.43	1.43	1.36	1.36
	$t = 40$	1.78	1.78	1.48	1.48
$S^{ne}$	$t = 20$	$4.80 \times 10^{-1}$	$4.80 \times 10^{-1}$	1.01	1.00
	$t = 40$	$4.82 \times 10^{-1}$	$4.82 \times 10^{-1}$	1.01	1.01
$S^g$	$t = 20$	$4.98 \times 10^{-1}$	$4.97 \times 10^{-1}$	1.01	1.01
	$t = 40$	$5.00 \times 10^{-1}$	$5.00 \times 10^{-1}$	1.02	1.02

Table A.3: Elastic strain with damage using the calibrations of Xiao (1997) and Li (2002).

			Xiao		Li	
			Theory	VUMAT	Theory	VUMAT
$\epsilon_{11}^e(S_1)$	$\nu = \nu_0$	$t = 20$	$2.60 \times 10^{-3}$	$2.61 \times 10^{-3}$	$4.64 \times 10^{-3}$	$4.64 \times 10^{-3}$
		$t = 40$	$1.30 \times 10^{-3}$	$1.30 \times 10^{-3}$	$2.32 \times 10^{-3}$	$2.32 \times 10^{-3}$
	$K = K_0$	$t = 20$	$2.57 \times 10^{-3}$	$2.57 \times 10^{-3}$	$3.58 \times 10^{-3}$	$3.59 \times 10^{-3}$
		$t = 40$	$1.26 \times 10^{-3}$	$1.26 \times 10^{-3}$	$1.26 \times 10^{-3}$	$1.27 \times 10^{-3}$
	Kachanov	$t = 20$	$2.75 \times 10^{-3}$	$2.75 \times 10^{-3}$	$8.63 \times 10^{-3}$	$8.56 \times 10^{-3}$
		$t = 40$	$1.42 \times 10^{-3}$	$1.42 \times 10^{-3}$	$5.55 \times 10^{-3}$	$5.60 \times 10^{-3}$
$\epsilon_{22}^e(S_1)$	$\nu = \nu_0$	$t = 20$	$9.11 \times 10^{-4}$	$9.11 \times 10^{-4}$	$1.62 \times 10^{-3}$	$1.62 \times 10^{-3}$
		$t = 40$	$1.30 \times 10^{-3}$	$1.30 \times 10^{-3}$	$2.32 \times 10^{-3}$	$2.32 \times 10^{-3}$
	$K = K_0$	$t = 20$	$8.65 \times 10^{-4}$	$8.65 \times 10^{-4}$	$3.56 \times 10^{-4}$	$3.53 \times 10^{-4}$
		$t = 40$	$1.26 \times 10^{-3}$	$1.26 \times 10^{-3}$	$1.26 \times 10^{-3}$	$1.26 \times 10^{-3}$
	Kachanov	$t = 20$	$1.04 \times 10^{-3}$	$1.04 \times 10^{-3}$	$5.10 \times 10^{-3}$	$5.06 \times 10^{-3}$
		$t = 40$	$1.42 \times 10^{-3}$	$1.42 \times 10^{-3}$	$5.55 \times 10^{-3}$	$5.59 \times 10^{-3}$
$\epsilon_{11}^e(S^p)$	$\nu = \nu_0$	$t = 20$	$3.13 \times 10^{-3}$	$3.13 \times 10^{-3}$	$4.84 \times 10^{-3}$	$4.83 \times 10^{-3}$
		$t = 40$	$1.56 \times 10^{-3}$	$1.57 \times 10^{-3}$	$2.42 \times 10^{-3}$	$2.42 \times 10^{-3}$
	$K = K_0$	$t = 20$	$2.83 \times 10^{-3}$	$2.83 \times 10^{-3}$	$3.68 \times 10^{-3}$	$3.68 \times 10^{-3}$
		$t = 40$	$1.26 \times 10^{-3}$	$1.26 \times 10^{-3}$	$1.26 \times 10^{-3}$	$1.27 \times 10^{-3}$
	Kachanov	$t = 20$	$4.26 \times 10^{-3}$	$4.24 \times 10^{-3}$	$9.19 \times 10^{-3}$	$9.10 \times 10^{-3}$
		$t = 40$	$2.48 \times 10^{-3}$	$2.47 \times 10^{-3}$	$5.95 \times 10^{-3}$	-1.05
Continued on next page						

Table A.3 – Continued from previous page

			Xiao		Li	
			Theory	VUMAT	Theory	VUMAT
$\epsilon_{22}^e(S^p)$	$\nu = \nu_0$	$t = 20$	$1.09 \times 10^{-3}$	$1.09 \times 10^{-3}$	$1.69 \times 10^{-3}$	$1.69 \times 10^{-3}$
		$t = 40$	$1.56 \times 10^{-3}$	$1.56 \times 10^{-3}$	$2.42 \times 10^{-3}$	$2.42 \times 10^{-3}$
	$K = K_0$	$t = 20$	$7.34 \times 10^{-4}$	$7.34 \times 10^{-4}$	$3.07 \times 10^{-4}$	$3.03 \times 10^{-4}$
		$t = 40$	$1.26 \times 10^{-3}$	$1.26 \times 10^{-3}$	$1.26 \times 10^{-3}$	$1.26 \times 10^{-3}$
	Kachanov	$t = 20$	$2.08 \times 10^{-3}$	$2.08 \times 10^{-3}$	$5.49 \times 10^{-3}$	$5.44 \times 10^{-3}$
		$t = 40$	$2.48 \times 10^{-3}$	$2.47 \times 10^{-3}$	$5.95 \times 10^{-3}$	-2.32
$\epsilon_{11}^e(S^e)$	$\nu = \nu_0$	$t = 20$	$6.15 \times 10^{-3}$	$6.15 \times 10^{-3}$	$5.97 \times 10^{-3}$	$5.97 \times 10^{-3}$
		$t = 40$	$3.51 \times 10^{-3}$	$3.51 \times 10^{-3}$	$3.13 \times 10^{-3}$	$3.13 \times 10^{-3}$
	$K = K_0$	$t = 20$	$4.34 \times 10^{-3}$	$4.36 \times 10^{-3}$	$4.25 \times 10^{-3}$	$4.27 \times 10^{-3}$
		$t = 40$	$1.26 \times 10^{-3}$	$1.27 \times 10^{-3}$	$1.26 \times 10^{-3}$	$1.27 \times 10^{-3}$
	Kachanov	$t = 20$	$1.30 \times 10^{-2}$	$1.28 \times 10^{-2}$	$1.25 \times 10^{-2}$	$1.23 \times 10^{-2}$
		$t = 40$	$1.03 \times 10^{-2}$	$1.10 \times 10^{-2}$	$8.82 \times 10^{-3}$	$9.52 \times 10^{-3}$
$\epsilon_{22}^e(S^e)$	$\nu = \nu_0$	$t = 20$	$2.15 \times 10^{-3}$	$2.15 \times 10^{-3}$	$2.09 \times 10^{-3}$	$2.08 \times 10^{-3}$
		$t = 40$	$3.51 \times 10^{-3}$	$3.51 \times 10^{-3}$	$3.13 \times 10^{-3}$	$3.13 \times 10^{-3}$
	$K = K_0$	$t = 20$	$-2.15 \times 10^{-5}$	$-3.02 \times 10^{-5}$	$2.36 \times 10^{-5}$	$1.53 \times 10^{-5}$
		$t = 40$	$1.26 \times 10^{-3}$	$1.26 \times 10^{-3}$	$1.26 \times 10^{-3}$	$1.26 \times 10^{-3}$
	Kachanov	$t = 20$	$8.11 \times 10^{-3}$	$8.11 \times 10^{-3}$	$7.75 \times 10^{-3}$	$7.67 \times 10^{-3}$
		$t = 40$	$1.03 \times 10^{-2}$	$1.10 \times 10^{-2}$	$8.82 \times 10^{-3}$	$9.51 \times 10^{-3}$
Continued on next page						

Table A.3 – Continued from previous page

			Xiao		Li	
			Theory	VUMAT	Theory	VUMAT
$\epsilon_{11}^e (S^{ne})$	$\nu = \nu_0$	$t = 20$	$3.74 \times 10^{-3}$	$3.74 \times 10^{-3}$	$5.07 \times 10^{-3}$	$5.06 \times 10^{-3}$
		$t = 40$	$1.87 \times 10^{-3}$	$1.87 \times 10^{-3}$	$2.54 \times 10^{-3}$	$2.54 \times 10^{-3}$
	$K = K_0$	$t = 20$	$3.13 \times 10^{-3}$	$3.14 \times 10^{-3}$	$3.80 \times 10^{-3}$	$3.81 \times 10^{-3}$
		$t = 40$	$1.26 \times 10^{-3}$	$1.27 \times 10^{-3}$	$1.26 \times 10^{-3}$	$1.27 \times 10^{-3}$
	Kachanov	$t = 20$	$6.03 \times 10^{-3}$	$6.00 \times 10^{-3}$	$9.86 \times 10^{-3}$	$9.76 \times 10^{-3}$
		$t = 40$	$3.73 \times 10^{-3}$	$3.72 \times 10^{-3}$	$6.42 \times 10^{-3}$	$6.95 \times 10^{-3}$
$\epsilon_{22}^e (S^{ne})$	$\nu = \nu_0$	$t = 20$	$1.31 \times 10^{-3}$	$1.31 \times 10^{-3}$	$1.77 \times 10^{-3}$	$1.77 \times 10^{-3}$
		$t = 40$	$1.87 \times 10^{-3}$	$1.87 \times 10^{-3}$	$2.54 \times 10^{-3}$	$2.54 \times 10^{-3}$
	$K = K_0$	$t = 20$	$5.81 \times 10^{-4}$	$5.79 \times 10^{-4}$	$2.49 \times 10^{-4}$	$2.45 \times 10^{-4}$
		$t = 40$	$1.26 \times 10^{-3}$	$1.26 \times 10^{-3}$	$1.26 \times 10^{-3}$	$1.26 \times 10^{-3}$
	Kachanov	$t = 20$	$3.30 \times 10^{-3}$	$3.29 \times 10^{-3}$	$5.95 \times 10^{-3}$	$5.90 \times 10^{-3}$
		$t = 40$	$3.73 \times 10^{-3}$	$3.71 \times 10^{-3}$	$6.42 \times 10^{-3}$	$6.95 \times 10^{-3}$
$\epsilon_{11}^e (S^g)$	$\nu = \nu_0$	$t = 20$	$3.78 \times 10^{-3}$	$3.78 \times 10^{-3}$	$5.08 \times 10^{-3}$	$5.08 \times 10^{-3}$
		$t = 40$	$1.89 \times 10^{-3}$	$1.89 \times 10^{-3}$	$2.55 \times 10^{-3}$	$2.55 \times 10^{-3}$
	$K = K_0$	$t = 20$	$3.16 \times 10^{-3}$	$3.16 \times 10^{-3}$	$3.80 \times 10^{-3}$	$3.82 \times 10^{-3}$
		$t = 40$	$1.26 \times 10^{-3}$	$1.27 \times 10^{-3}$	$1.26 \times 10^{-3}$	$1.27 \times 10^{-3}$
	Kachanov	$t = 20$	$6.16 \times 10^{-3}$	$6.13 \times 10^{-3}$	$9.91 \times 10^{-3}$	$9.81 \times 10^{-3}$
		$t = 40$	$3.82 \times 10^{-3}$	$3.81 \times 10^{-3}$	$6.45 \times 10^{-3}$	$6.91 \times 10^{-3}$
Continued on next page						

Table A.3 – Continued from previous page

			Xiao		Li	
			Theory	VUMAT	Theory	VUMAT
$\epsilon_{22}^e(S^g)$	$\nu = \nu_0$	$t = 20$	$1.32 \times 10^{-3}$	$1.32 \times 10^{-3}$	$1.78 \times 10^{-3}$	$1.78 \times 10^{-3}$
		$t = 40$	$1.89 \times 10^{-3}$	$1.89 \times 10^{-3}$	$2.55 \times 10^{-3}$	$2.54 \times 10^{-3}$
	$K = K_0$	$t = 20$	$5.70 \times 10^{-4}$	$5.68 \times 10^{-4}$	$2.45 \times 10^{-4}$	$2.41 \times 10^{-4}$
		$t = 40$	$1.26 \times 10^{-3}$	$1.26 \times 10^{-3}$	$1.26 \times 10^{-3}$	$1.26 \times 10^{-3}$
	Kachanov	$t = 20$	$3.39 \times 10^{-3}$	$3.38 \times 10^{-3}$	$5.98 \times 10^{-3}$	$5.93 \times 10^{-3}$
		$t = 40$	$3.82 \times 10^{-3}$	$3.80 \times 10^{-3}$	$6.45 \times 10^{-3}$	$6.90 \times 10^{-3}$

Table A.4: Delayed elastic equivalent strain with damage using the calibrations of Xiao (1997) and Li (2002). Note that the results for  $\nu = \nu_0$  are identical to the  $K = K_0$  results.

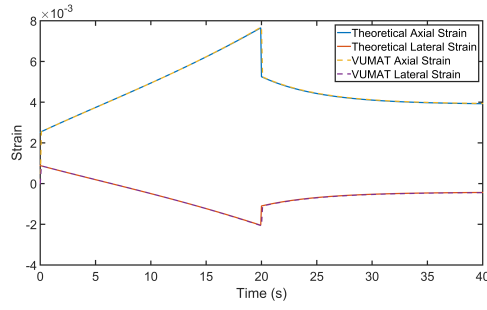
			Xiao		Li	
			Theory	VUMAT	Theory	VUMAT
$e^d(S_1)$	$\nu = \nu_0$	$t = 20$	$1.22 \times 10^{-3}$	$1.22 \times 10^{-3}$	$1.96 \times 10^{-3}$	$1.95 \times 10^{-3}$
		$t = 40$	$6.94 \times 10^{-5}$	$7.14 \times 10^{-5}$	$5.31 \times 10^{-5}$	$5.62 \times 10^{-5}$
	Kachanov	$t = 20$	$1.23 \times 10^{-3}$	$1.23 \times 10^{-3}$	$2.34 \times 10^{-3}$	$2.33 \times 10^{-3}$
		$t = 40$	$7.47 \times 10^{-5}$	$7.68 \times 10^{-5}$	$1.58 \times 10^{-4}$	$1.62 \times 10^{-4}$
$e^d(S^p)$	$\nu = \nu_0$	$t = 20$	$1.39 \times 10^{-3}$	$1.39 \times 10^{-3}$	$2.03 \times 10^{-3}$	$2.03 \times 10^{-3}$
		$t = 40$	$7.41 \times 10^{-5}$	$7.65 \times 10^{-5}$	$4.83 \times 10^{-5}$	$5.15 \times 10^{-5}$
	Kachanov	$t = 20$	$1.51 \times 10^{-3}$	$1.51 \times 10^{-3}$	$2.46 \times 10^{-3}$	$2.44 \times 10^{-3}$
		$t = 40$	$1.16 \times 10^{-4}$	$1.18 \times 10^{-4}$	$1.55 \times 10^{-4}$	$1.58 \times 10^{-4}$
$e^d(S^e)$	$\nu = \nu_0$	$t = 20$	$2.61 \times 10^{-3}$	$2.61 \times 10^{-3}$	$2.53 \times 10^{-3}$	$2.53 \times 10^{-3}$
		$t = 40$	$1.05 \times 10^{-5}$	$1.39 \times 10^{-5}$	$1.85 \times 10^{-5}$	$2.18 \times 10^{-5}$
	Kachanov	$t = 20$	$3.32 \times 10^{-3}$	$3.31 \times 10^{-3}$	$3.19 \times 10^{-3}$	$3.17 \times 10^{-3}$
		$t = 40$	$7.52 \times 10^{-5}$	$8.10 \times 10^{-5}$	$1.03 \times 10^{-4}$	$9.79 \times 10^{-5}$
$e^d(S^{ne})$	$\nu = \nu_0$	$t = 20$	$1.61 \times 10^{-3}$	$1.61 \times 10^{-3}$	$2.13 \times 10^{-3}$	$2.13 \times 10^{-3}$
		$t = 40$	$7.05 \times 10^{-5}$	$7.33 \times 10^{-5}$	$4.26 \times 10^{-5}$	$4.58 \times 10^{-5}$
	Kachanov	$t = 20$	$1.84 \times 10^{-3}$	$1.83 \times 10^{-3}$	$2.60 \times 10^{-3}$	$2.58 \times 10^{-3}$
		$t = 40$	$1.47 \times 10^{-4}$	$1.51 \times 10^{-4}$	$1.50 \times 10^{-4}$	$1.48 \times 10^{-4}$
Continued on next page						

Table A.4 – Continued from previous page

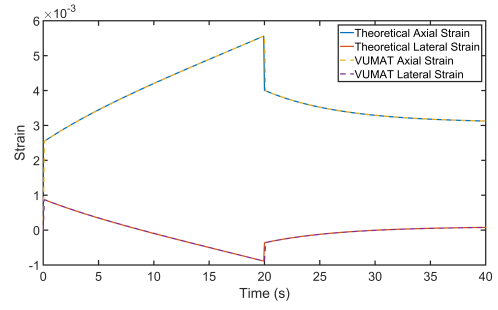
			Xiao		Li	
			Theory	VUMAT	Theory	VUMAT
$e^d(S^g)$	$\nu = \nu_0$	$t = 20$	$1.63 \times 10^{-3}$	$1.63 \times 10^{-3}$	$2.14 \times 10^{-3}$	$2.14 \times 10^{-3}$
		$t = 40$	$7.00 \times 10^{-5}$	$7.27 \times 10^{-5}$	$4.22 \times 10^{-5}$	$4.54 \times 10^{-5}$
	Kachanov	$t = 20$	$1.86 \times 10^{-3}$	$1.86 \times 10^{-3}$	$2.61 \times 10^{-3}$	$2.59 \times 10^{-3}$
		$t = 40$	$1.49 \times 10^{-4}$	$1.52 \times 10^{-4}$	$1.49 \times 10^{-4}$	$1.46 \times 10^{-4}$

Table A.5: Viscous equivalent strain with damage using the calibrations of Xiao (1997) and Li (2002).

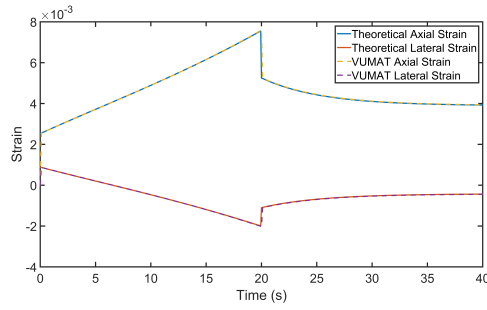
		Xiao		Li	
		Theory	VUMAT	Theory	VUMAT
$e^c(S_1)$	$t = 20$	$2.67 \times 10^{-3}$	$2.66 \times 10^{-3}$	$4.11 \times 10^{-3}$	$4.09 \times 10^{-3}$
	$t = 40$	$2.67 \times 10^{-3}$	$2.67 \times 10^{-3}$	$4.13 \times 10^{-3}$	$4.13 \times 10^{-3}$
$e^c(S^p)$	$t = 20$	$2.96 \times 10^{-3}$	$2.95 \times 10^{-3}$	$4.29 \times 10^{-3}$	$4.27 \times 10^{-3}$
	$t = 40$	$2.97 \times 10^{-3}$	$2.97 \times 10^{-3}$	$4.31 \times 10^{-3}$	$4.32 \times 10^{-3}$
$e^c(S^e)$	$t = 20$	$5.85 \times 10^{-3}$	$5.83 \times 10^{-3}$	$5.60 \times 10^{-3}$	$5.57 \times 10^{-3}$
	$t = 40$	$5.89 \times 10^{-3}$	$5.90 \times 10^{-3}$	$5.63 \times 10^{-3}$	$5.67 \times 10^{-3}$
$e^c(S^{me})$	$t = 20$	$3.37 \times 10^{-3}$	$3.36 \times 10^{-3}$	$4.52 \times 10^{-3}$	$4.50 \times 10^{-3}$
	$t = 40$	$3.38 \times 10^{-3}$	$3.38 \times 10^{-3}$	$4.55 \times 10^{-3}$	$4.58 \times 10^{-3}$
$e^c(S^g)$	$t = 20$	$3.40 \times 10^{-3}$	$3.39 \times 10^{-3}$	$4.54 \times 10^{-3}$	$4.52 \times 10^{-3}$
	$t = 40$	$3.42 \times 10^{-3}$	$3.41 \times 10^{-3}$	$4.57 \times 10^{-3}$	$4.60 \times 10^{-3}$



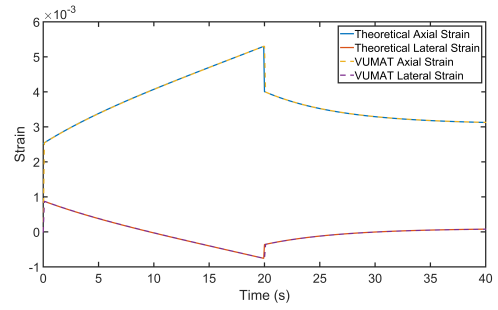
(a)  $E(S) = E(S_1 + S_2)$



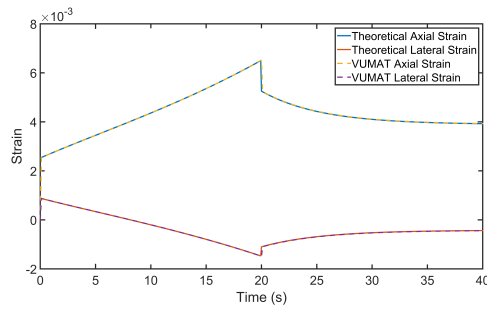
(b)  $E(S) = E(S_1 + S_2)$



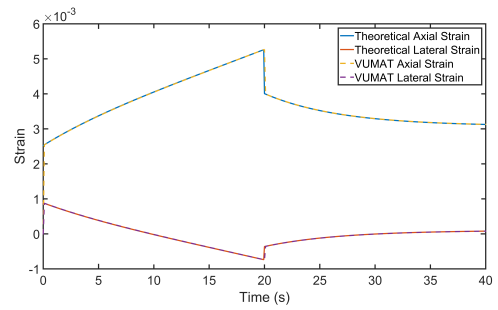
(c)  $E(S) = E(S_1)$



(d)  $E(S) = E(S_1)$

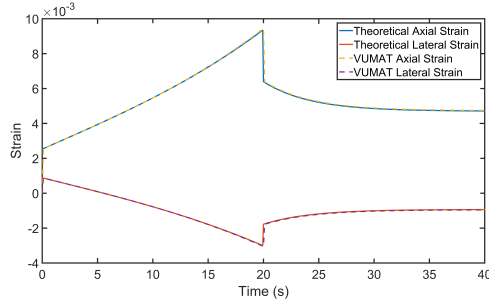


(e)  $E(S) = E_0$

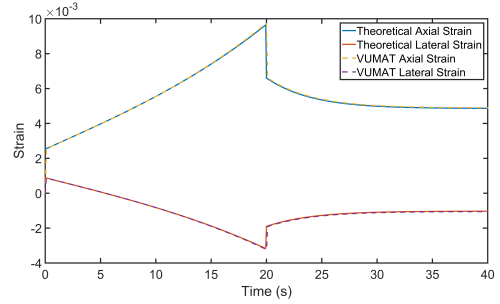


(f)  $E(S) = E_0$

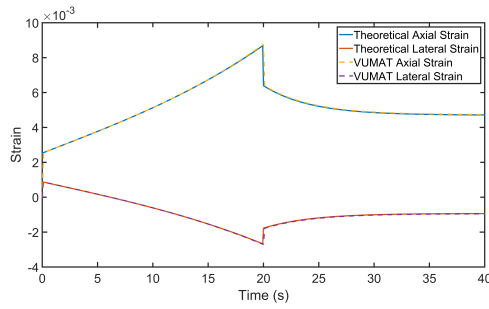
Figure A.1: Comparison of total strains with the constant bulk modulus elastic damage formulation and power-law high-pressure damage. (a),(c), and (e) use the damage calibration of Li (2002), the remainder Xiao (1997). Note that full elastic damage is represented by  $E(S) = E(S_1 + S_2)$ , microcracking elastic damage by  $E(S) = E(S_1)$ , and no elastic damage by  $E(S) = E_0$ .



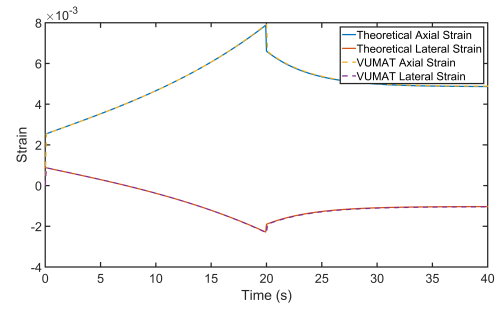
(a)  $E(S) = E(S_1 + S_2)$



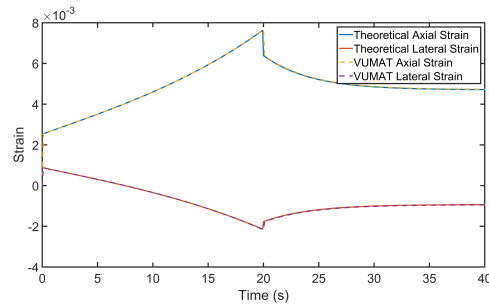
(b)  $E(S) = E(S_1 + S_2)$



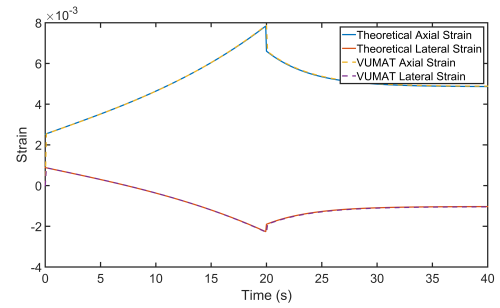
(c)  $E(S) = E(S_1)$



(d)  $E(S) = E(S_1)$

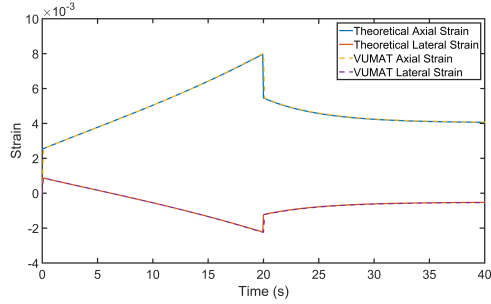


(e)  $E(S) = E_0$

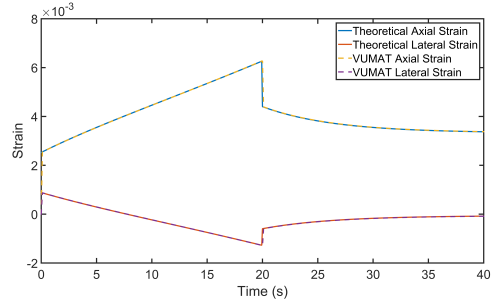


(f)  $E(S) = E_0$

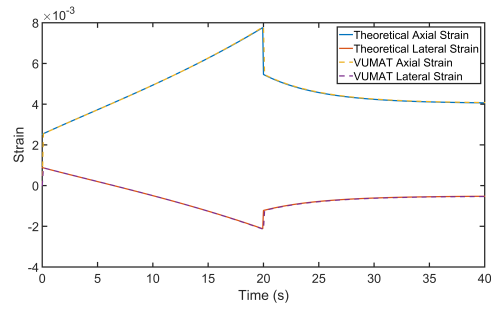
Figure A.2: Comparison of total strains with the constant bulk modulus elastic damage formulation and exponential high-pressure damage. (a),(c), and (e) use the damage calibration of Li (2002), the remainder Xiao (1997).



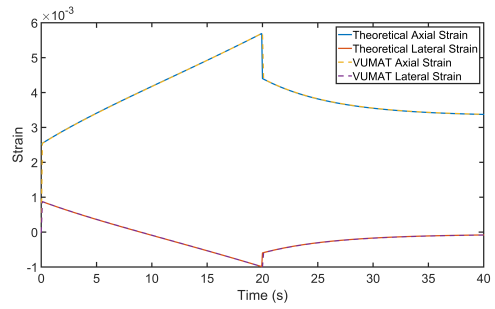
(a)  $E(S) = E(S_1 + S_2)$



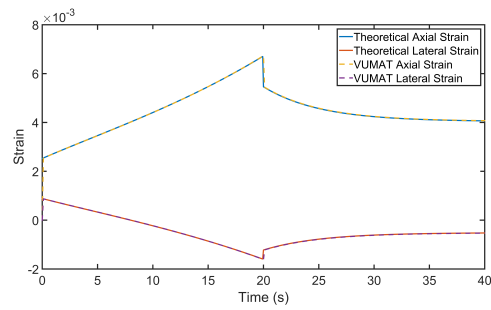
(b)  $E(S) = E(S_1 + S_2)$



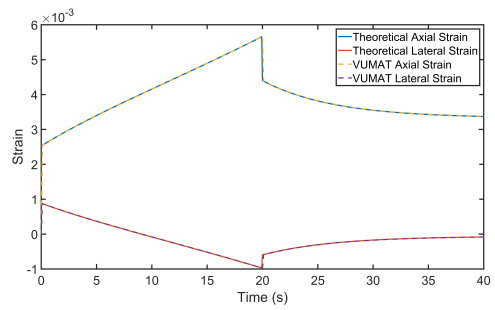
(c)  $E(S) = E(S_1)$



(d)  $E(S) = E(S_1)$

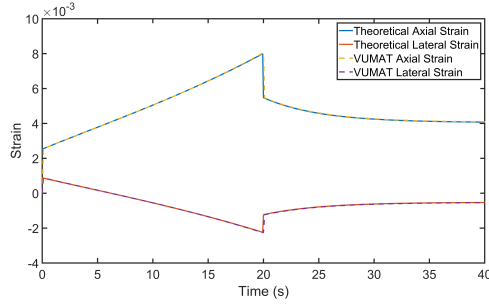


(e)  $E(S) = E_0$

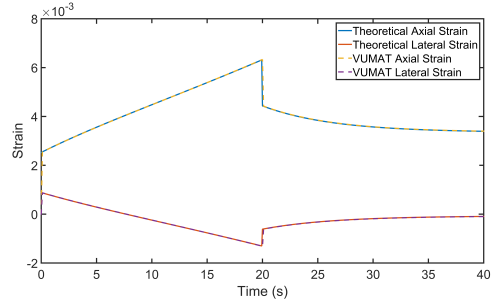


(f)  $E(S) = E_0$

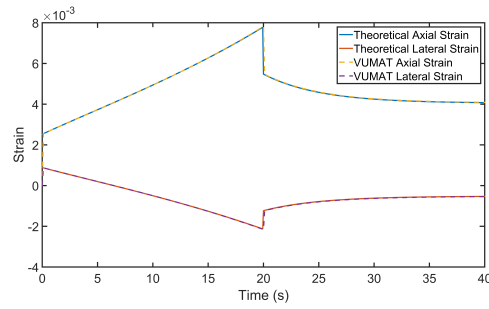
Figure A.3: Comparison of total strains with the constant bulk modulus elastic damage formulation and normalized exponential high-pressure damage. (a),(c), and (e) use the damage calibration of Li (2002), the remainder Xiao (1997).



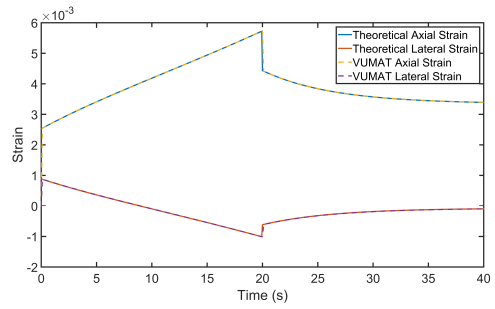
(a)  $E(S) = E(S_1 + S_2)$



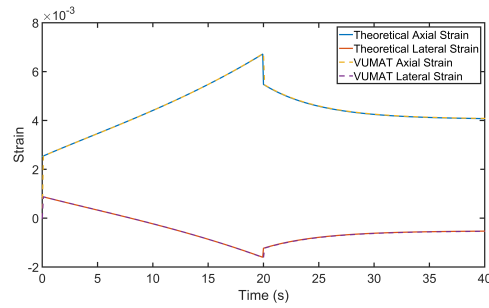
(b)  $E(S) = E(S_1 + S_2)$



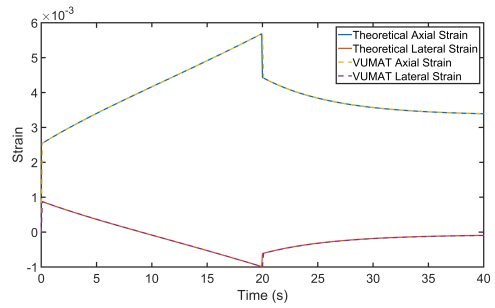
(c)  $E(S) = E(S_1)$



(d)  $E(S) = E(S_1)$

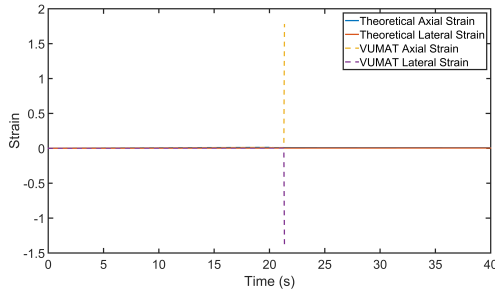


(e)  $E(S) = E_0$

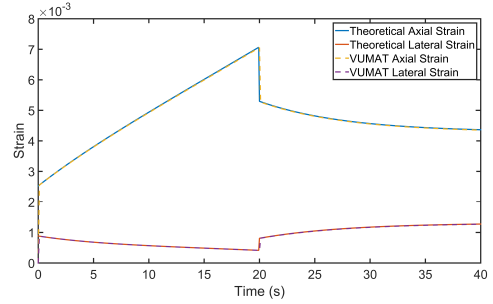


(f)  $E(S) = E_0$

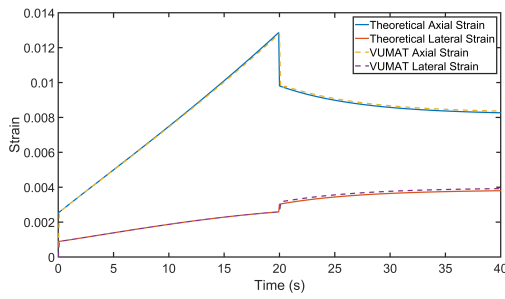
Figure A.4: Comparison of total strains with the constant bulk modulus elastic damage formulation and geometric high-pressure damage. (a),(c), and (e) use the damage calibration of Li (2002), the remainder Xiao (1997).



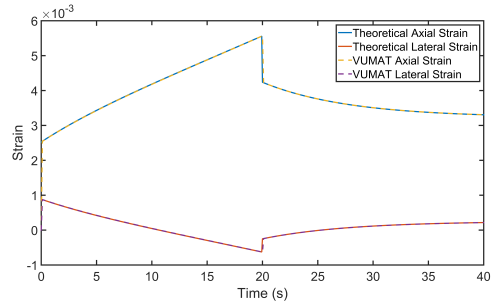
(a)  $E(S) = E(S_1 + S_2)$



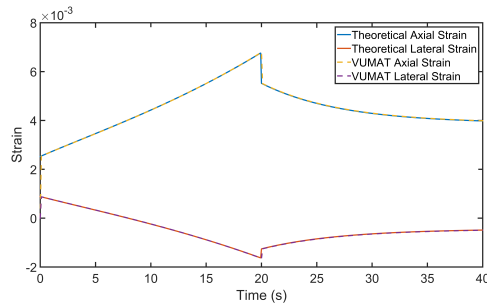
(b)  $E(S) = E(S_1 + S_2)$



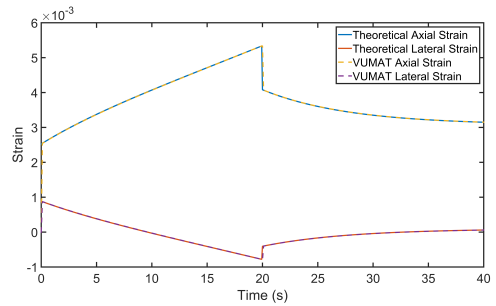
(c)  $E(S) = E(S_1)$



(d)  $E(S) = E(S_1)$

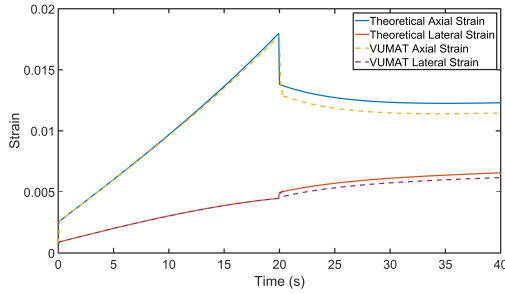


(e)  $E(S) = E_0$

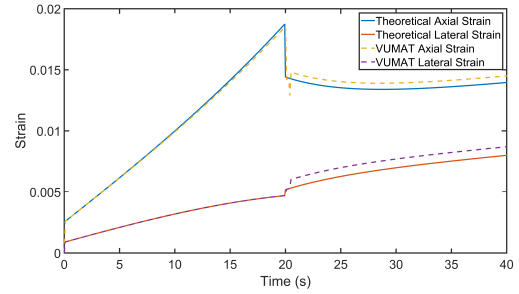


(f)  $E(S) = E_0$

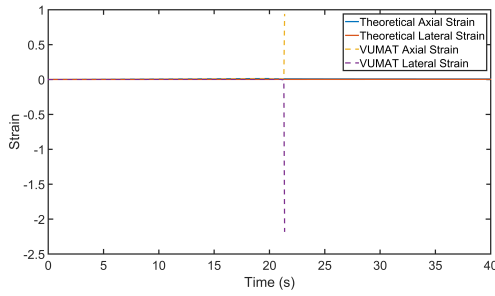
Figure A.5: Comparison of total strains with the Kachanov elastic damage formulation and power-law high-pressure damage. (a),(c), and (e) use the damage calibration of Li (2002), the remainder Xiao (1997).



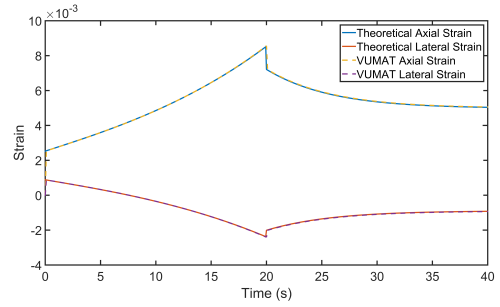
(a)  $E(S) = E(S_1 + S_2)$



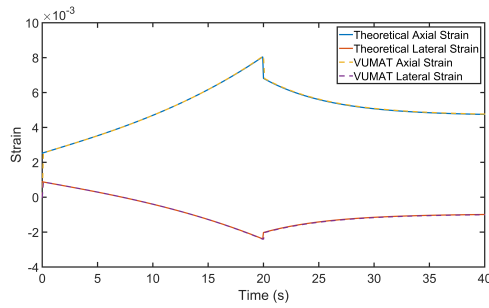
(b)  $E(S) = E(S_1 + S_2)$



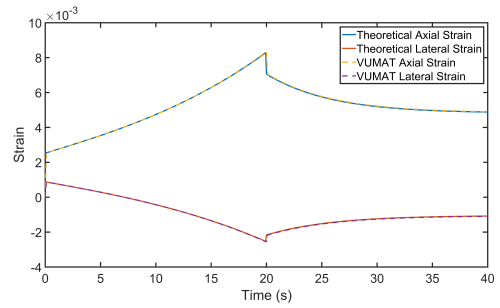
(c)  $E(S) = E(S_1)$



(d)  $E(S) = E(S_1)$

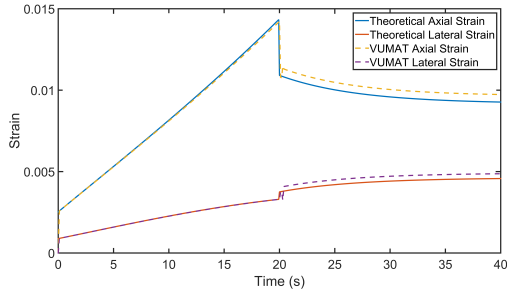


(e)  $E(S) = E_0$

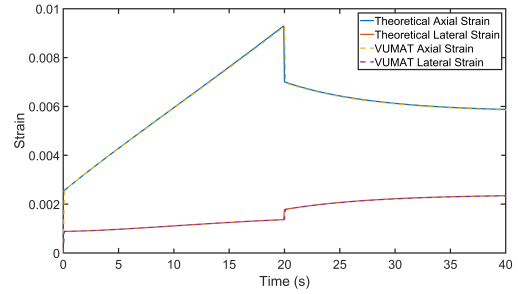


(f)  $E(S) = E_0$

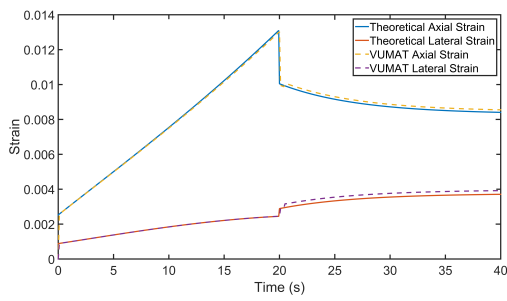
Figure A.6: Comparison of total strains with the Kachanov elastic damage formula and exponential high-pressure damage. (a),(c), and (e) use the damage calibration of Li (2002), the remainder Xiao (1997).



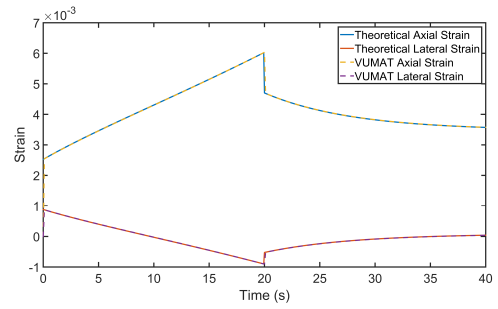
(a)  $E(S) = E(S_1 + S_2)$



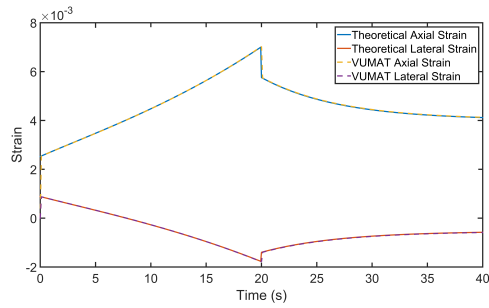
(b)  $E(S) = E(S_1 + S_2)$



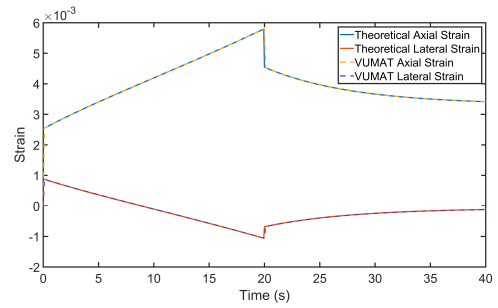
(c)  $E(S) = E(S_1)$



(d)  $E(S) = E(S_1)$

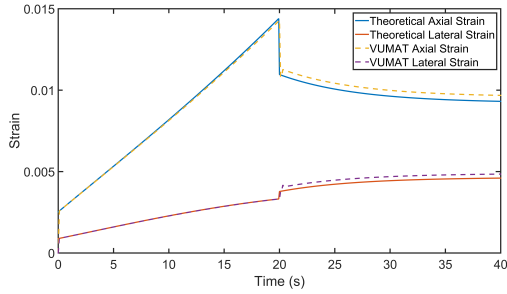


(e)  $E(S) = E_0$

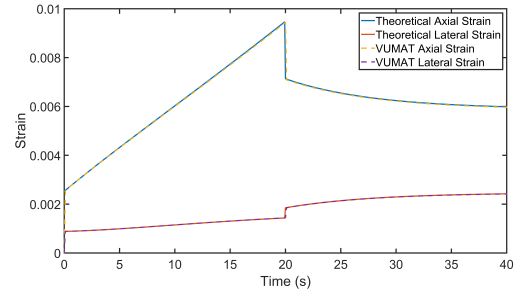


(f)  $E(S) = E_0$

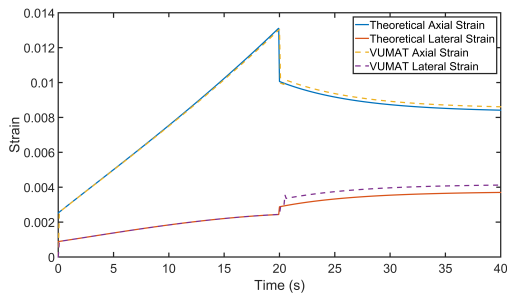
Figure A.7: Comparison of total strains with the Kachanov elastic damage formulation and normalized exponential high-pressure damage. (a),(c), and (e) use the damage calibration of Li (2002), the remainder Xiao (1997).



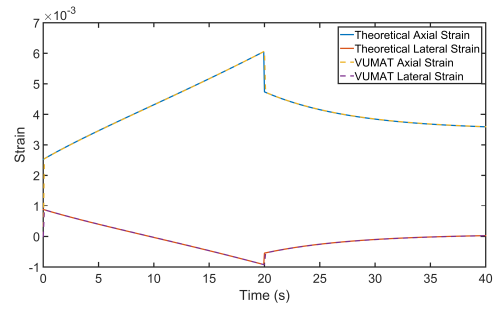
(a)  $E(S) = E(S_1 + S_2)$



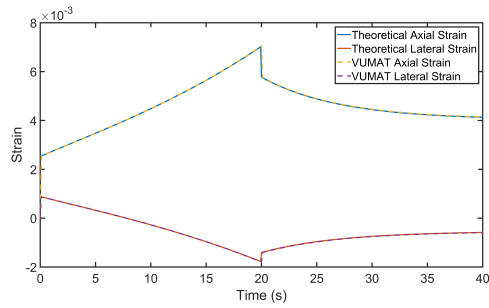
(b)  $E(S) = E(S_1 + S_2)$



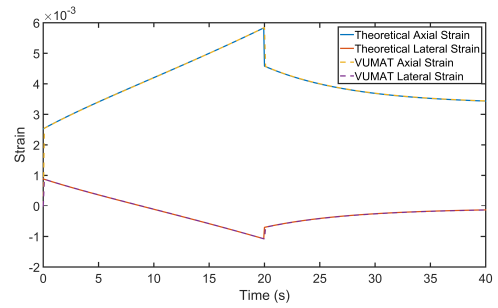
(c)  $E(S) = E(S_1)$



(d)  $E(S) = E(S_1)$

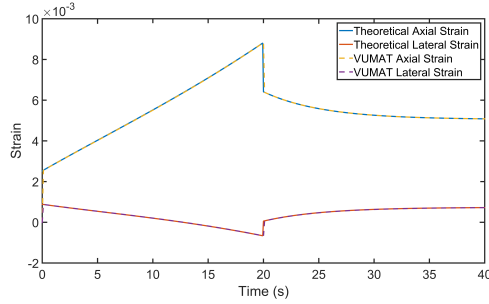


(e)  $E(S) = E_0$

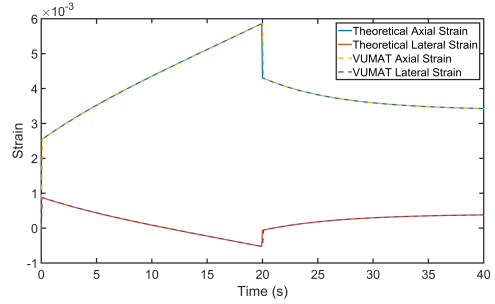


(f)  $E(S) = E_0$

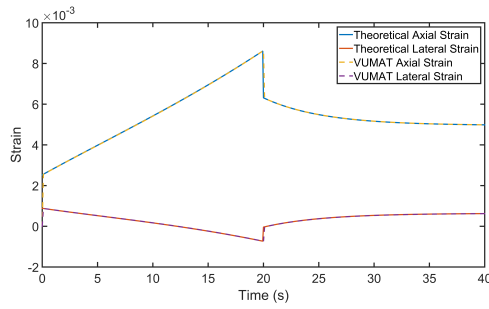
Figure A.8: Comparison of total strains with the Kachanov elastic damage formulation and geometric high-pressure damage. (a),(c), and (e) use the damage calibration of Li (2002), the remainder Xiao (1997).



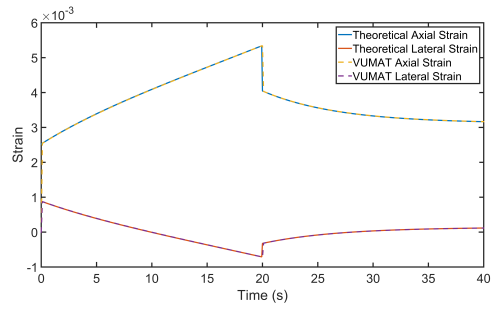
(a)  $E(S) = E(S_1 + S_2)$



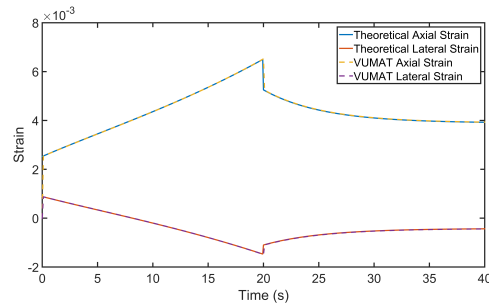
(b)  $E(S) = E(S_1 + S_2)$



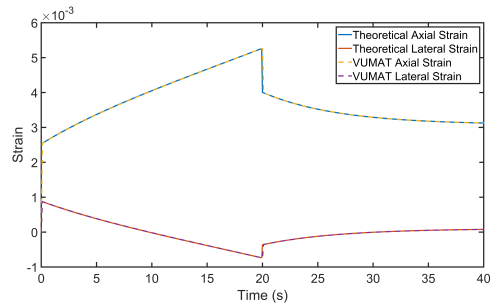
(c)  $E(S) = E(S_1)$



(d)  $E(S) = E(S_1)$

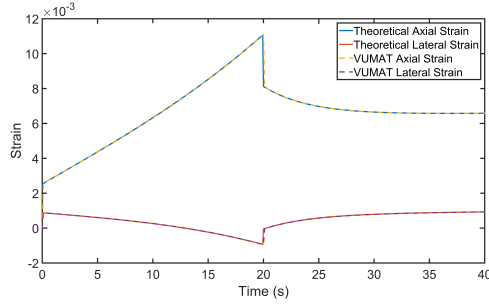


(e)  $E(S) = E_0$

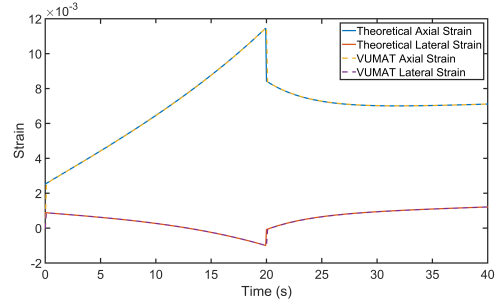


(f)  $E(S) = E_0$

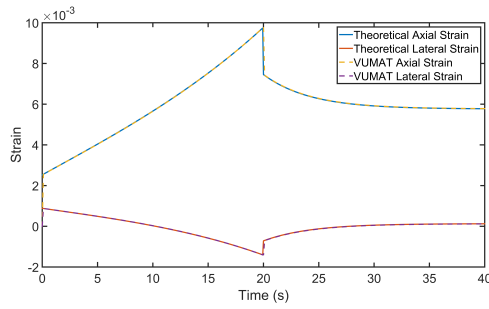
Figure A.9: Comparison of total strains with the constant Poisson's ratio elastic damage formulation and power-law high-pressure damage. (a),(c), and (e) use the damage calibration of Li (2002), the remainder Xiao (1997).



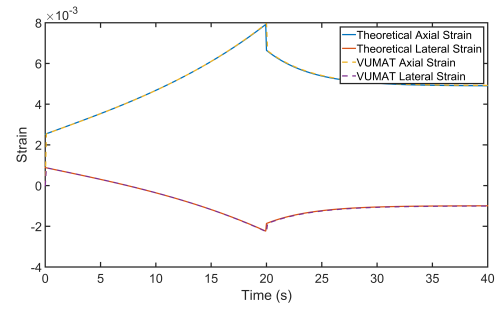
(a)  $E(S) = E(S_1 + S_2)$



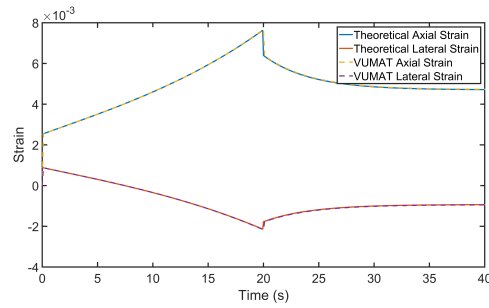
(b)  $E(S) = E(S_1 + S_2)$



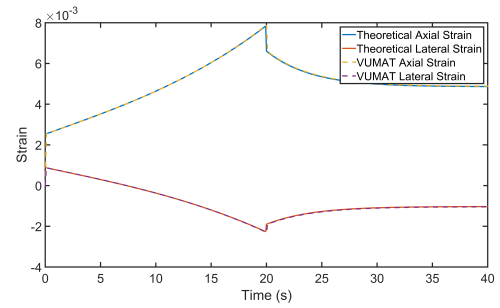
(c)  $E(S) = E(S_1)$



(d)  $E(S) = E(S_1)$

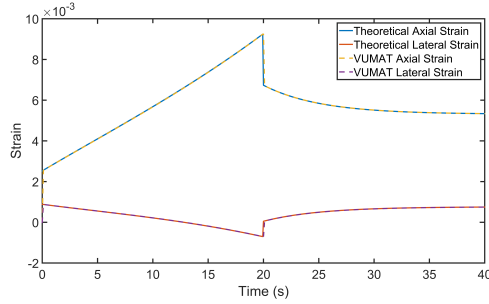


(e)  $E(S) = E_0$

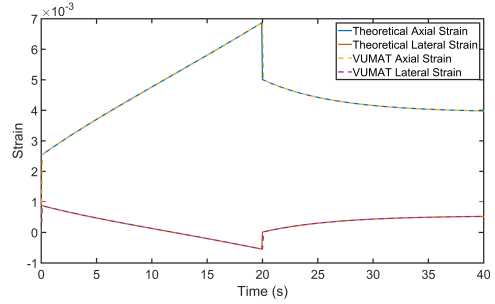


(f)  $E(S) = E_0$

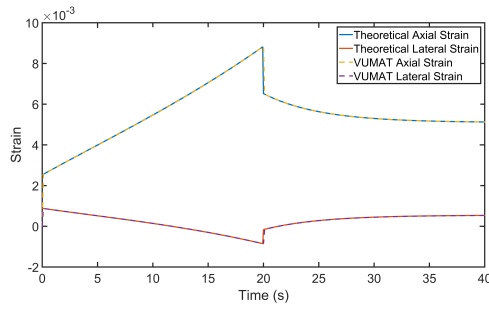
Figure A.10: Comparison of total strains with the constant Poisson's ratio elastic damage formulation and exponential high-pressure damage. (a),(c), and (e) use the damage calibration of Li (2002), the remainder Xiao (1997).



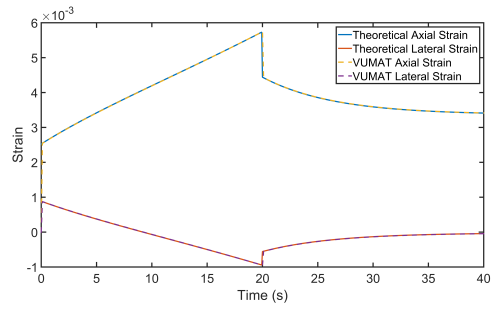
(a)  $E(S) = E(S_1 + S_2)$



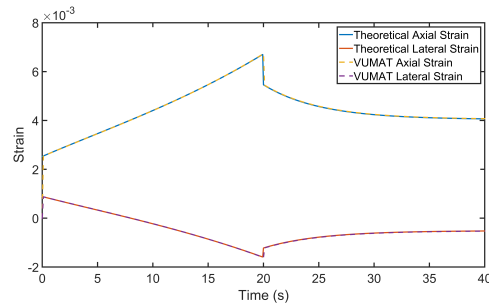
(b)  $E(S) = E(S_1 + S_2)$



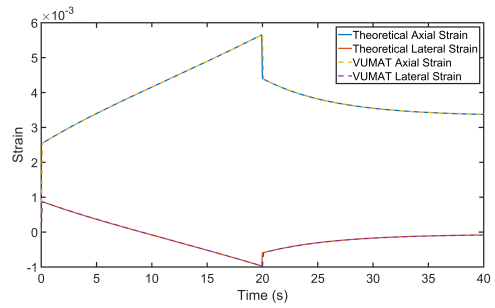
(c)  $E(S) = E(S_1)$



(d)  $E(S) = E(S_1)$

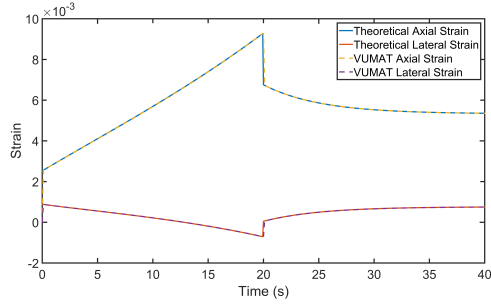


(e)  $E(S) = E_0$

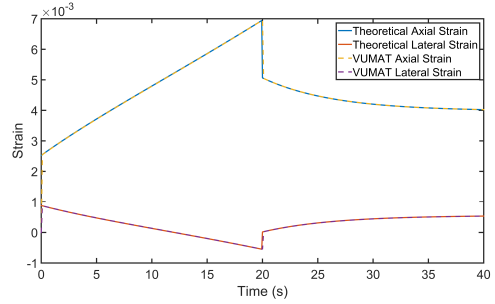


(f)  $E(S) = E_0$

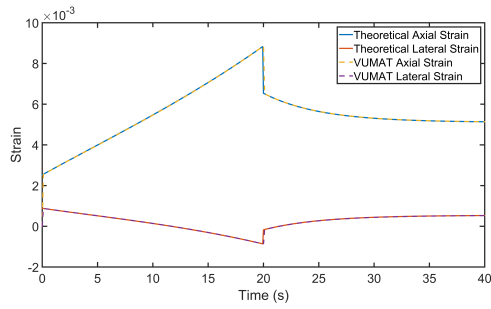
Figure A.11: Comparison of total strains with the constant Poisson's ratio elastic damage formulation and normalized exponential high-pressure damage. (a),(c), and (e) use the damage calibration of Li (2002), the remainder Xiao (1997).



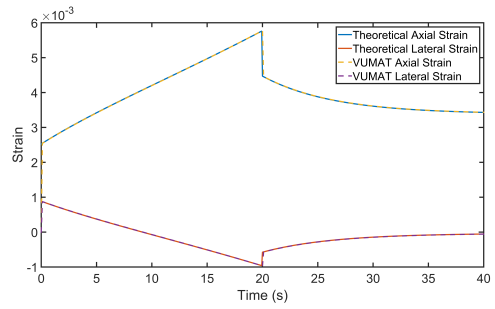
(a)  $E(S) = E(S_1 + S_2)$



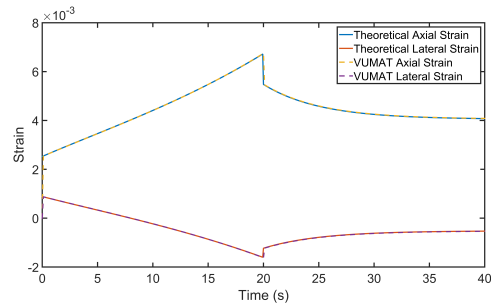
(b)  $E(S) = E(S_1 + S_2)$



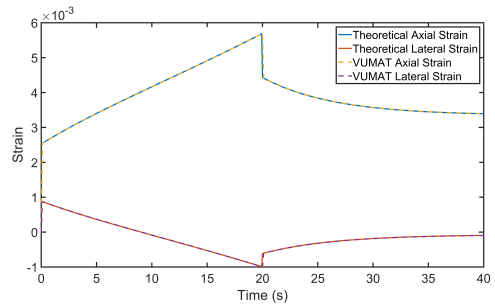
(c)  $E(S) = E(S_1)$



(d)  $E(S) = E(S_1)$

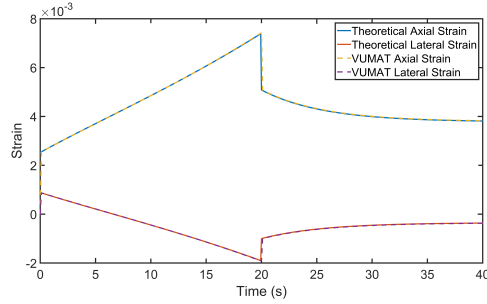


(e)  $E(S) = E_0$

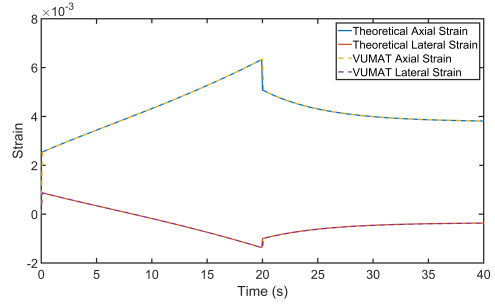


(f)  $E(S) = E_0$

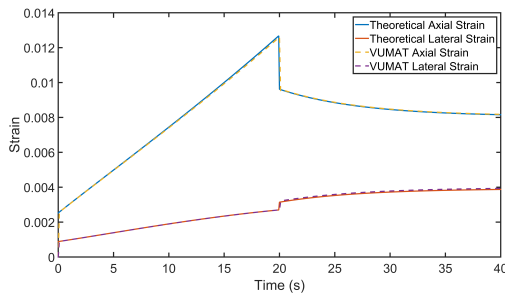
Figure A.12: Comparison of total strains with the constant Poisson's ratio elastic damage formulation and geometric high-pressure damage. (a),(c), and (e) use the damage calibration of Li (2002), the remainder Xiao (1997).



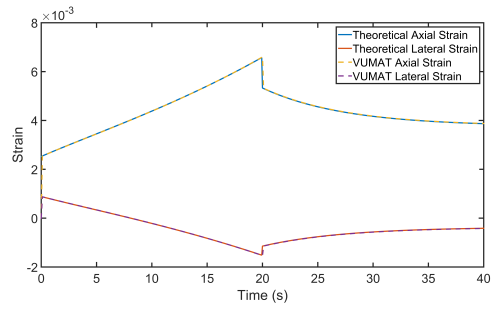
(a)  $K = K_0$



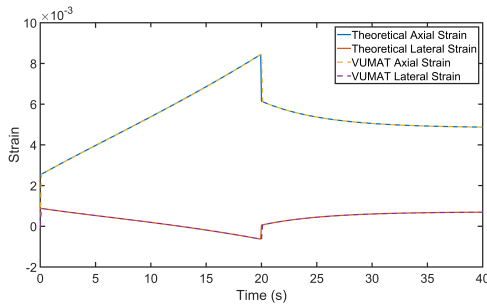
(b)  $K = K_0$



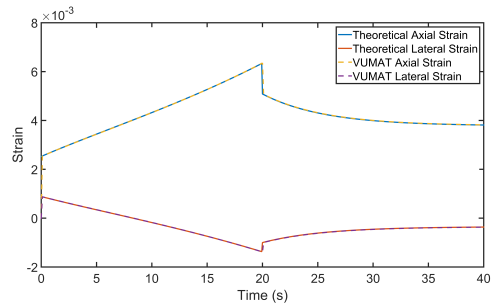
(c) Kachanov



(d) Kachanov

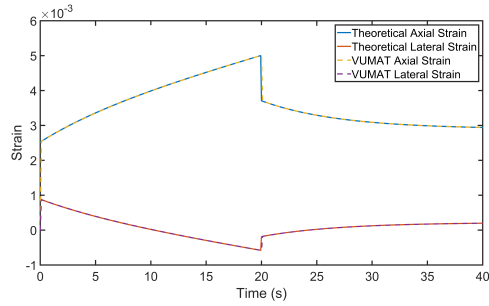


(e)  $\nu = \nu_0$

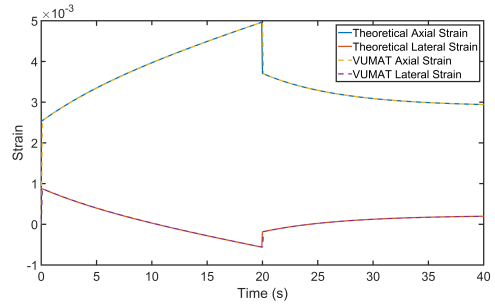


(f)  $\nu = \nu_0$

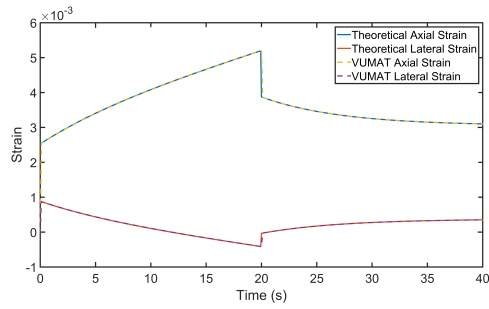
Figure A.13: Comparison of total strains with microcracking damage only using the calibration of Li (2002). (a),(c), and (e) included full elastic damage, the remainder no elastic damage.



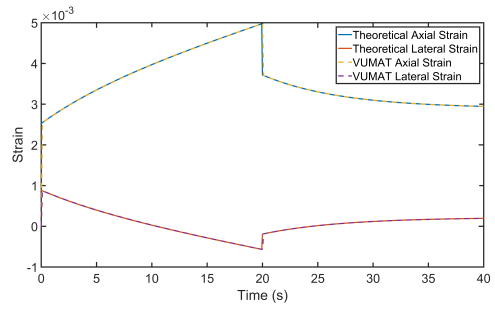
(a)  $K = K_0$



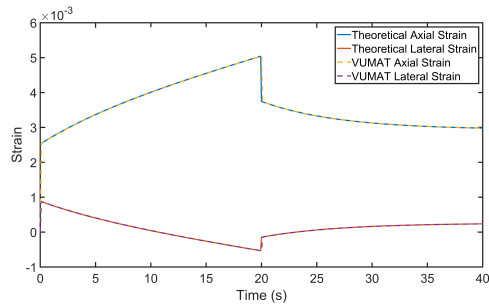
(b)  $K = K_0$



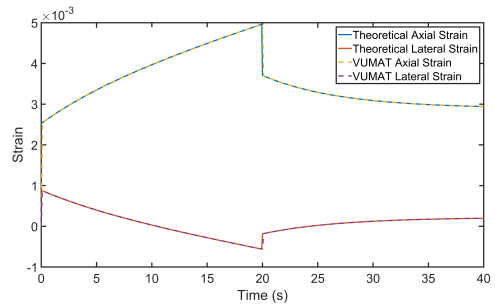
(c) Kachanov



(d) Kachanov



(e)  $\nu = \nu_0$



(f)  $\nu = \nu_0$

Figure A.14: Comparison of total strains with microcracking damage only using the calibration of Xiao (1997). (a),(c), and (e) included full elastic damage, the remainder no elastic damage.